

SELF-INSCRIPTION OF COMPLEX,
FUNCTIONAL 3-D STRUCTURES WITH
SELF-TRAPPED LIGHT BEAMS

SELF-INSCRIPTION OF COMPLEX, FUNCTIONAL 3-D STRUCTURES WITH SELF-TRAPPED LIGHT BEAMS

BY

OSCAR ALEJANDRO HERRERA CORTES, BACHELOR'S IN SCIENCE (CHEMISTRY)

A Thesis

Submitted to the School of Graduate

Studies

In Partial Fulfilment of the Requirements

For the Degree

Doctor of Philosophy

McMaster University

© Copyright by Oscar Alejandro Herrera Cortes, 2022.

DOCTOR OF PHILOSOPHY (2022)

Chemistry and Chemical Biology

McMaster University

Hamilton, Ontario, Canada

TITLE: Self-Inscription of Complex, Functional 3-D Structures with Self-Trapped Light Beams

AUTHOR: Oscar Alejandro Herrera Cortes, bachelor's in science (Chemistry) (National Autonomous University of Mexico)

SUPERVISOR: Professor Kalaichelvi Saravanamuttu

NUMBER OF PAGES: xxx and 151

Abstract

The behavior and dynamics of light waves in soft light-responsive polymers was studied. We used the properties of these beams to develop three routes to functional 3-D structures which would be impossible to fabricate through conventional lithography. The method to obtain functional 3-D structures, known as Prismatic 3-D printing, exploits the fact the divergence of beams can be controlled through the rate of photopolymerization which is intensity-dependent, to rapidly 3-D objects. Here, we employ segmentation algorithms to deconstruct a mesh of the desired object into prisms, which are then inscribed in a single step by self-trapped beams to generate a wide range of complex architectures within seconds. Such prisms can be assembled in situ or as a form of post-processing. Each of these prismatic elements has a higher refractive index than their surroundings and they are also continuous along the propagation front direction. These two properties make each prismatic element light-guiding. Taking advantage of this function obtained through our method, remote-controllable waveguide architectures including planar slab waveguide, individual and small arrays of cylindrical waveguides as well as waveguide lattices ($>10\ 000\ \text{cm}^{-2}$) made of electroactive hydrogels were printed using self-trapped beams. By applying and varying external electric fields, we can then dynamically control the bending, angular orientation and rotation (up to 360°) of these pliant light-guiding structures. Reminiscent of the camouflaging techniques of certain marine creatures, this allows precise, remote control of the waveguided light output. Finally, we examined the propagation dynamics and structures inscribed by vortex beams in photopolymerizable systems and showed that they elicited rotation along their propagation paths and ultimately collapsed into self-trapped filaments. The sense of rotation was commensurate with the topological charge of the vortex while the rotation rate was proportional to the intensity of the beam output.

Acknowledgments

I would like to thank my supervisor Dr. Kalaichelvi Saravanamuttu for giving me the opportunity to be part of her research group. Her guidance and support inside and outside the lab have been extremely important to me during these years. I specially want to thank Dr. Saravanamuttu for giving me the opportunity to propose and try new ideas. This freedom is exactly what I was looking for when I decided to join the group. I would like to thank the members of my committee, Dr. Karen Volke and Dr. Duncan O'Dell for their time and suggestions. I specially want to thank Dr. Denish Kumar for his training during the internship I carried out before starting my doctoral studies and to Dr. Derek Morim for his training during my first year of my PhD, for all the conversation and exchange of ideas during the years. I also want to thank current and past members of our research group including Kathryn Benincasa, Matthew R. Ponte, Kevin Vaughan, Jaimini Patel, Fariha Mahmood, Alex Hudson, Hao Lin, Yi Pan, Natalie Blanchard, Kevin Vaughan, and Dusan. I also want to thank MITACS and CONACYT (National Council of Science and Technology of Mexico) for the scholarships provided. I also want to thank Araceli Martinez, my biology high school teacher. You opened the door of a fascinating world that was unknown to me at that time. I want to thank Dr. Jorge Peon, my undergraduate thesis supervisor. I learned a lot in your group. The experience I gained there was fundamental during graduate school. Finally, I want to thank my family, especially my parents Martha and Juan and my sister Tete. I also want to thank Angel, Xavier, Victoria Lila and Kevin. I was so lucky I was born into this family. I know my life would have been very different otherwise.

Table of content

Abstract	iii
Acknowledgments	iv
List of Figures	xi
List of Tables	xxxi
List of Abbreviations and symbols	xxxii
1 Introduction	1
1.1 Light propagation in Nonlinear Media.....	1
1.2 Types of Nonlinear Materials.....	2
1.2.1 Third order nonlinear materials.....	3
1.2.2 Second-order nonlinear materials.....	3
1.2.3 Photorefractivematerials.....	4
1.2.4 Liquid crystals	5
1.2.5 Photopolymerization reactions.....	5
1.3 Photopolymerizationreactionmechanisms.....	7
1.3.1 Free-radical photopolymerization.....	8
1.3.2 Cationic photopolymerization.....	9
1.4 Self-trapped beams.....	12

1.4.1 Self-trapping of coherent beams.....	12
1.4.2 Self-trapping of incoherent beams.....	20
1.5 Volumetric 3-D printing.....	25
1.6 3-D printing with functional materials.....	33
1.7 Electroactive hydrogels.....	34
1.8 Vortex beams.....	38
1.9 Contributions.....	47
1.10 References.....	48
2 Decomposition and 3D Printing of Volumetric Prismatic Elements using Nonlinear Optochemical Waves.....	60
2.1 Abstract.....	60
2.2 Introduction.....	60
2.3 Results and Discussion.....	64
2.3.1 Prismatic Printing Process and Calibration.....	64
2.3.2 Decomposition of Objects into Prismatic Elements.....	67
2.3.3 Printing of Intersecting Prismatic Elements.....	71
2.3.4 Printing Prisms Embedded with Microscopic Waveguide Arrays.....	76
2.4 Conclusions and Outlook.....	80
2.5 Methods.....	81

2.5.1 Materials.....	81
2.5.2 Preparation of photopolymer.....	81
2.5.3 Optical Apparatus and Imaging.....	81
2.5.4 Structural characterization of prisms with waveguide circuitry.....	82
2.5.5 Optical characterization of the channel waveguides.....	82
2.5.6 Post-Processing of Structures.....	82
2.5.7 Decomposition of Mesh.....	83
2.5.8 SLA Printing.....	83
2.6 Acknowledgements.....	83
2.7 References.....	83
2.8 SUPPLEMENTARY INFORMATION	86
2.8.1 Experimental Methods	86
2.8.1.1 Materials.....	86
2.8.1.2 Preparation of photopolymer resins.....	87
2.8.2 Post-Processing of Structures.....	87
2.8.3 SLA Printing.....	87
2.8.4 Optical Assembly for Self-Trapping Experiments.....	88
2.8.5 Calibration of Intensity by Printing Cylinders.....	88
2.8.6 Optical and Structural Characterization of Waveguides.....	89

2.8.7 Decomposition and Printing of Objects.....	89
3 Dynamic, remote-controllable bioinspired electroactive hydrogel waveguide architectures.....	95
3.1 Abstract.....	95
3.2 Introduction.....	95
3.3 Horizontal Right-Left beam manipulation with slab electroactive hydrogels inspired by deep sea angler fish lure.....	99
3.4 Cilia-inspired array of cylindric electroactive waveguides.....	106
3.5 Hydrogel waveguide array inspired by squid skin.....	108
3.6 Multidirectional bending of cylindric hydrogel waveguides.....	113
3.7 Conclusions and Outlook.....	116
3.8 References.....	116
3.9 SUPPLEMENTARY INFORMATION.....	119
3.9.1 Resin formulations.....	119
3.9.2 3D printing of slab hydrogel waveguides and micro-patterned prisms with channel waveguides.....	119
3.9.3 Horizontal Right to Left beam manipulation with slab electroactive hydrogels.....	120
3.9.4 Calculation of bending angles.....	121
3.9.5 Beam Propagation Method (BPM) simulations of light propagation in slab hydrogel waveguides.....	122

3.9.6 Horizontal Right-Left beam manipulation with slab electroactive hydrogels.....	123
3.9.7 Vertical right-left bending beam manipulation with slab electroactive hydrogels.....	124
3.9.8 Horizontal Right-Left beam manipulation with micro-patterned prisms with channel waveguides.....	125
3.9.9 Structural characterization of prisms with micro-channel waveguides.....	125
3.9.10 Tracking and intensity quantification of micro-beams within a hydrogel waveguide lattice.....	126
3.9.11 References.....	127
3.9.12 Multidirectional bending of cylindric hydrogel waveguides.....	127
3.9.13 Trajectory of the end of a cylindric hydrogel waveguide during.....	129
4 Dynamics of a vortex beam in a medium undergoing cationic photopolymerization.....	130
4.1 Abstract.....	130
4.2 Introduction.....	130
4.3 Results and Discussion.....	133
4.4 Conclusions and Outlook.....	137
4.5 References.....	138
4.6 SUPPLEMENTARY INFORMATION	140
4.7 Methods	140
4.8 Materials.....	140

4.9 Preparation of photopolymer.....	140
5 Conclusions and future work.....	143
5.1.1 Prismatic 3-D printing.....	143
5.1.2 Electroactive hydrogel waveguide architectures.....	144
5.1.3 Dynamics of a vortex beam in a medium undergoing cationic photopolymerization...147	
5.1.4 General conclusions.....	147
5.2 Future work and outlook.....	148
5.2.1 Prismatic 3-D Printing.....	148
5.2.2 Electroactive waveguides.....	148
5.2.3 Vortex beams in photopolymerizable media.....	150
5.3 References.....	150

List of Figures

Figure 1.1 A self-trapped (right) beam is produced when the natural diffraction of light (left) is counteracted by the focusing effect (middle) originated by the refractive index change (Δn) in a nonlinear medium. Reprinted with permission from Biria, S.; Morim, D. R.; Tsao, F. A.; Saravanamuttu, K.; Hosein, I. D. Coupling nonlinear optical waves to photoreactive and phase-separating soft matter: Current status and perspectives. *Chaos* **2017**, *27*, 104611. Copyright 2017 AIP Publishing.....2

Figure 1.2 General evolution of the refractive index change in a photopolymerizable sample. Reproduced with permission from Kewitsch, A. S.; Yariv, A. Self-focusing and self-trapping of optical beams upon photopolymerization. *Opt. Lett.* **1996**, *21*, 24-26. Copyright 1996 Optical Society of America.....7

Figure 1.3 a) Photolysis of initiators Irgacure 184 (1-Hydroxycyclohexyl phenyl ketone) and Irgacure 819 (Bis(2,4,6-trimethylbenzoyl)-phenylphosphineoxide). Example of an initiation step. A radical attack the carbon-carbon double bond creating a new radical one monomer longer. b) General steps in any radical polymerization reaction.....8

Figure 1.4 Radical photopolymerization of 3-(trimethoxysilyl)propyl methacrylate using Irgacure[®] 784.....9

Figure 1.5 Basic steps in a cationic polymerization. The initial step involves the protonation of the monomer. This new cation keeps adding more monomer until all monomer is depleted or until the growing chain reacts with a contaminant.....10

Figure 1.6 (1) and (2) show the generation of a cation R^+ assisted by a photosensitizer that produces radicals upon absorption of light. (3) Light absorption and proton abstraction of a

monomer/solvent molecule by a diaryliodonium salt. (4), (5) and (6) shows the reactions that are part of the mechanism to explain the acceleration of a photopolymerization reactions when alcohols are used with a diaryliodonium salt photoinitiator. (8) show the propagation mechanism of ring-opening polymerization. (9), (10) and (11) show some of the reactions that lead to termination in ring-opening polymerization.....11

Figure 1.7 Time evolution of the 3-D intensity profile of an incoherent white beam traveling in a crystal. At $t = 0$ s, the width of the beam at the entrance and exit faces of the sample are 14 and 82 μm , respectively. After 180 min, the width of the beam at the exit face reduced to 12 μm .
.....13

Figure 1.8. Evolution of the self-trapping process of a blue laser beam ($\lambda=488$ nm) in a photopolymerizable medium. As photopolymerization takes place, a permanent optical waveguide is formed in the medium with a core diameter of 100 μm and a length of 40 mm.....14

Figure 1.9 Polymeric waveguide obtained through photopolymerization by a self-trapped beam connecting two optical fibers placed 1 mm apart. Reprinted with permission from Dorkenoo, K.; Crégut, O.; Mager, L.; Gillot, F.; Carre, C.; Fort, A. Quasi-solitonic behavior of self-written waveguides created by photopolymerization. *Opt. Lett.* 2002, 27, 1782–1784. Copyright 2002 Optical Society of America.....15

Figure 1.10 A) Temporal evolution at the exit face of the 2-D intensity profile of a green laser beam at 1.6×10^2 traveling through a sample 6 mm long that contains 3-(trimethoxysilyl)propyl methacrylate (left). Image (a) shows the 2-D intensity profile of the beam under linear conditions. Images (b)-(r) were acquired after 3 s, 27 s, 30 s, 30 s, 32 s, 35 s, 41 s, 47 s, 55 s, 57 s, 61 s, 116 s,

123 s, 129 s, 134 s, 141 s, 156 s and 163 s. B) Representation of the three typical results obtained at the three different intensity regimes observed during the nonlinear propagation of a green laser beam in the organosiloxane sample (Left). The low intensity regime is dominated by self-trapping. Self-diffraction rings and beam filamentation are observed at mid- and high intensities. C) Optical micrographs (x,z and x,y) of a waveguide obtained in a organosiloxane sample 6 mm long at $1.6 \times 10^{-2} \text{ W/cm}^2$. At the right, the 2-D intensity profile of a probe laser beam is shown. Reprinted with permission from Villafranca, A. B.; Saravanamuttu, K. An experimental study of the dynamics and temporal evolution of self-trapped laser beams in a photopolymerizable organosiloxane. *J. Phys. Chem. C* 2008, 112, 17388–17396. Copyright 2008, American Chemical Society.....16

Figure 1.11 a) Representation of the linear propagation of a beam pair (A and B) under linear (left) and nonlinear conditions in which self-trapping and spiraling takes place. Time evolution of the beam output of the beam pair traveling through an organosiloxane sample at b) $\theta = 0.70^\circ$, c) 0.23° , and d) 0.86° . Centers of the beams under linear conditions are highlighted with white dots. The trajectories of each beam at these angles under linear conditions are shown at the left in b-d. Reprinted with permission from Morim, D. R.; Bevern, D.; Vargas-Baca, I.; Saravanamuttu, K. 3-D Spiraling Self-Trapped Light Beams in Photochemical Systems. *J. Phys. Chem. Lett.* 2019, 10, 5957–5962. Copyright 2019, American Chemical Society.....18

Figure 1.12 Photoisomerization reaction of merocyanine substituents in a methylenebis(acrylamide) cross-linked p(AAm-co-AAc) hydrogel. Upon absorption of visible light, the merocyanine moieties switch to their closed-ring spiropyran form (top). This chemical change increases the hydrophobicity in the irradiated area which causes the water in the irradiated zone to be expelled which leads to a contraction of the hydrogel network. The refractive index

change originated by such contraction produces a temporal waveguide. The graph shows the peak intensities of two self-trapped beams separated by 200 μm while they interact remotely. The 2-D intensity profile of the beams at selected times is shown at the bottom right. When both beams are launched simultaneously, they self-trap, increasing their intensity (from an initial value of 1) to 12 and 9 (beam 1 and beam 2, respectively) with the final width of both beams being $\sim 40 \mu\text{m}$ (region A). When beam 2 was intentionally blocked, the intensity of beam 1 increased to 20 while its beam width decreased to 28 μm (region B). When beam 2 was launched again to the hydrogel, the peak intensity of beam 1 decreased to 5.3 while the size of the beam increased to $\sim 40 \mu\text{m}$ (region C). The opposite effect is observed when beam 1 is blocked and then reintroduced (region D). Reproduced with permission from Morim, D. R.; Meeks, A.; Shastri, A.; Tran, A.; Shneidman, A. V.; Yashin, V. V.; Mahmood, F.; Balazs, A. C.; Aizenberg, J.; Saravanamuttu, K. Opto-chemo-mechanical transduction in photoresponsive gels elicits switchable self-trapped beams with remote interactions. *Proc. Natl. Acad. Sci. U. S. A.* 2020, 117, 3953-3959. Copyright 2020 National Academy of Sciences.....19

Figure 1.13 Time evolution of the 1-D, 2-D and 3-D intensity profiles of a white beam with a width of 45 μm at the entrance face traveling through an organosiloxane sample 6 mm long. Section **a** shows the intensity profile of the beam at the entrance face. Section **b** shows the intensity profile of the beam at the exit face of the sample under linear conditions. The size of the beam increases to 268.5 μm due to diffraction with a relative intensity of 15.4 %. As polymerization and the increase of refraction index takes place, there is a 5.4-fold decrease in the beam's width and at least a 6.5-fold increase in the intensity of the beam before it slightly widens at the end of the experiment. However, the width of the beam remained smaller than its value under linear conditions. Reprinted with permission from Zhang, J.; Kasala, K.; Rewari, A.; Saravanamuttu, K.

Self-trapping of spatially and temporally incoherent white light in a photochemical medium. *J. Am. Chem. Soc.* **2006**, 128, 406–407., Copyright 2006, American Chemical Society.....21

Figure 1.14 Optical set up used to obtain a lattice by launching two orthogonal white beams to an organosiloxane sample. Capital letters show the direction of the beam propagation. The subscript in Y indicates the direction of the modulation. Only beam Y carried a modulation. The top images in B (a, b, and c) are a representation of the evolution of lattice formation. Under linear conditions, the modulation vanishes as the beam travels in the medium (a). Once the photopolymerization reaction takes place rectangular self-trapped filaments emerged (b) which eventually become unstable creating a lattice of self-trapped filaments (c). The bottom at B shows the time evolution of the experimental 2-D intensity profiles at the exit face of the lattice side in which the modulated beam is launched ([010] plane). C Scheme showing the fabrication of a lattices with primitive cubic symmetry using three perpendicular incoherent modulated beams. A and B were reprint (adapted) with permission from Burgess I. B.; Ponte M.; Saravanamuttu K. Spontaneous formation of 3-D optical and structural lattices from two orthogonal and mutually incoherent beams of white light propagating in a photopolymerisable material. *J. Mater. Chem.* 2008 18, 4133–4139. Copyright 2008, ROYAL SOCIETY OF CHEMISTRY. C was reproduced with permission from Ponte, M. R.; Welch, R.; Saravanamuttu, K. An optochemically organized nonlinear waveguide lattice with primitive cubic symmetry. *Opt. Express* 2013, 21, 4205-4214. Copyright 2013 Optical Society of America.....22

Figure 1.15 Free-standing array of flexible square lattice of micro-waveguides made of a silicone-based acrylate polymer. Reprinted with permission from ref. 85. Copyright 2018 WILEY-VCH Verlag GmbH & Co. KGaA, Weinheim. Scheme of a polymer film with a radial distribution of

micro-waveguides that focuses light or increases its divergence depending on its orientation. These films possess a field of view of 115° for wavelengths in the visible spectrum. Optical micrographs obtained through transmission microscopy of the highlighted red and blue area in the scheme of the polymer film are shown at the middle and bottom in the left rectangle. Reprint with permission from ref. 86. Copyright 2019 WILEY-VCH Verlag GmbH & Co. KGaA, Weinheim. 3-D lattice fabricated by launching five beams from different orientations. The top image in the rectangle at the right shows a representation of the resulting intersecting lattice while the bottom images show micrographs of such lattice. Reprinted with permission from ref. 87. Copyright 2018 WILEY-VCH Verlag GmbH & Co. KGaA, Weinheim.....24

Figure 1.16 The top rectangle shows the two processes the photoinitiator undergoes to trigger free radical polymerization. The first step consists of absorption of UV light to form a latent state with a lifetime of 6 s. The graph at the top shows the photoswitching kinetics. Irradiation for 145 s generates the latent state. Once the UV light is removed, the latent state decays with a lifetime of 6 s. The graph at the bottom shows the absorption spectrum of the photoinitiator in its spiropiran (black line) and merocyanine form (blue line). A representation of the set up used in xolography is shown at the bottom left. The blue area represents the sheet in which solidification takes place. Reprint with permission from ref. 95. Copyright 2020, Springer Nature Limited. The bottom left rectangle: Set up used in holographic volumetric 3-D printing. Three orthogonal patterned beams generated using subregions of an image were launched into the sample using 45° mirrors. A spatial light modulator was used to create the image. The 3 beams intersected inside the bath to form the target object. Reprint with permission from ref 96. Copyright 2017, American Association for the Advancement of Science. The bottom right rectangle: Set up used for Computed Axial Lithography printing. It consists of a Digital Light Projector, and a rotating stage immersed in a

fluid. Reprinted with permission from ref. 99. Copyright 2019, American Association for the Advancement of Science.....28

Figure 1.17. Optical set up employed in 3D NSCRIPT. A blue LED beam (I_1) is collimated by a planoconvex lens and then launched to an amplitude mask placed at the entrance face of a sample cell that contains the resin (P). The rest of the set up consists of a pair of planoconvex lens and a CCD camera used to monitor the intensity profile of the beam. Time evolution of the printing process of a cone monitored through side view pictures (middle). The resulting cone after being isolated and polished is shown at the bottom left. The gear at the bottom right was obtained in the same manner but using an amplitude mask that produces a beam with cross sectional profile of the gear. HAuCl_4 was added to the resin that, upon irradiation, produces gold nanoparticles. **b** Optical set up used to print the cup shown at the bottom right. Two counter-propagating beams were launched simultaneously to the sample, each of them patterned with the amplitude masks shown at the right. Each of the beams acquired the shape of the white area in the amplitude mask. The time evolution of the printing process of the cup was monitored by imaging the sample cell from the top of the set up. Reprinted with permission from Basker, D. K.; Cortes, O. A. H.; Brook, M. A.; Saravanamuttu, K. 3D Nonlinear Inscription of Complex Microcomponents (3D NSCRIPT): Printing Functional Dielectric and Metallodielectric Polymer Structures with Nonlinear Waves of Blue LED Light. *Adv. Mater. Technol.* **2017**, *2*, 1600236-n/a.30

Figure 1.18 Assembled catapult. All the components were obtained through 3D NSCRIPT except for the tension spring (k). Reprinted with permission from Basker, D. K.; Cortes, O. A. H.; Brook, M. A.; Saravanamuttu, K. 3D Nonlinear Inscription of Complex Microcomponents (3D NSCRIPT): Printing Functional Dielectric and Metallodielectric Polymer Structures with

Nonlinear Waves of Blue LED Light. *Adv. Mater. Technol.* **2017**, 2, 1600236-n/a. Copyright 2017 WILEY-VCH Verlag GmbH & Co. KGaA, Weinheim.....31

Figure 1.19 Components of Resing G used in SMaLL(left). The ring-opening reaction of the photochromic molecule (DAE530) used in this method produces an optically transparent solution upon absorption of visible light ($\lambda = 530 \text{ nm}$). The masking effect is clearly observed in the absorption spectra in the middle. Before the ring opening reaction of the photochromic molecule takes place, the absorption of the solution is dominated by the former. After this transformation, light can be absorbed by the photosensitizer. Printing process of a cone through the SMaLL principle (right). Reprinted with permission from ref. Dolinski, N. D.; Page, Z. A.; Callaway, E. B.; Eisenreich, F.; Garcia, R. V.; Chavez, R.; Bothman, D. P.; Hecht, S.; Zok, F. W.; Hawker, C. J. Solution Mask Liquid Lithography (SMaLL) for One-Step, Multimaterial 3D Printing. *Adv. Mater.* **2018**, 30, 1800364. Copyright 2018 WILEY-VCH Verlag GmbH & Co. KGaA, Weinheim.....32

Figure 1.20 a) “Walker” robot made of negatively charged monomers under the effect of an electric field. Reprint with permission from ref. Han, D.; Farino, C.; Yang, C.; Scott, T.; Browe, D.; Choi, W.; Freeman, J. W.; Lee, H. Soft Robotic Manipulation and Locomotion with a 3D Printed Electroactive Hydrogel. *ACS Appl. Mater. Interfaces* 2018, 10, 21, 17512-17518. Copyright 2018, American Chemical Society. b) Walking robot made of two legs. The purple leg is made of a hydrogel with positively charged monomers (right) while the grey leg (left) contains negatively charged monomers. In the initial configuration, the cathode is next to the positively charged hydrogel while the anode is next to the anionic hydrogel. Once an electric field is applied, both legs bend inward in opposite directions. The whole system moves toward the right since the anionic leg has a larger surface area than the cationic counterpart. Reversing the fields stretches the anionic leg toward the cathode while the cationic leg moves towards the anode but to a lesser

extent due to its higher friction force with the substrate which results in unidirectional motion of the two-leg robot. Reprinted with permission from ref. Morales, D.; Palleau, E.; Dickey, M. D.; Velev, O. D. Electro-actuated hydrogel walkers with dual responsive legs. *Soft Matter* 2014, 10, 1337.....35

Figure 1.21 a) Images of light of different wavelengths traveling through printed waveguides within tissue. Reprint from Feng, J.; Jiang, Q.; Rogin, P.; De Oliveira, P. W.; Del Campo, A. Printed Soft Optical Waveguides of PLA Copolymers for Guiding Light into Tissue. *ACS Appl. Mater. Interfaces* 2020, 12, 20287–20294. Copyright 2020 American Chemical Society. b) The top-left image is a representation of a continuum soft robot composed of an optical fiber wrapped with a ferromagnetic polymer jacket with hydrogel skin. The top-right image shows the experimental set up used to demonstrate steerable light delivery. The four images below show the magnetic soft robot initially traveling through a set of rings while directing light and then directing light towards specific areas (yellow dots). Reprinted with permission from Kim, Y.; Parada, G. A.; Liu, S.; Zhao, X. Ferromagnetic soft continuum robots. *Sci. Robot* 2019, 4, eaax7329.37

Figure 1.22 a) Phase surfaces of vortex beams with $l = 1, 2$ and 3 . b) Transverse profile of a vortex beam.....38

Figure 1.23 a) Beam profile at the exit face of a cell containing different concentrations of Rb atoms at a power of 20 mW at the entrance face. Detuning= 0.56 GHz. Concentrations ($10^{11}/\text{cm}^3$) in the first column from top to bottom: 0.03, 1.0, 2.1, 3.1. The concentrations in the second column also from top to bottom were 5.2, 6.2, 7.2 and $8.3 \cdot 10^{11} \text{ cm}^{-3}$. The separation and the rotation angle between the two solitons increases with the concentration of Rb atoms. Reprinted with permission

from Tikhonenko, V.; Christou, J.; Luther-Daves, B. Spiraling bright spatial solitons formed by the breakup of an optical vortex in a saturable self-focusing medium. *J. Opt. Soc. Am. B* **1995**, *12*, 2046-2052. Copyright 1995 Optical Society of America **b)** Modulation instability of vortex beams with $l = 1, 2, 3$ traveling through sodium vapor as the nonlinear medium with pulse energies of 76, 234 and 359 nJ respectively. The beams break into 2,4 and 6 filaments. **c)** When the pulse energy of these beams is increased to 9.1, 24.1 and 6.63 μJ for each topological charge ($l = 1, 2, 3$), they no longer break since the nonlinearity is immediately saturated. **b** and **c** were reprinted with permission from Bigelow, M. S.; Zerom, P.; Boyd, R. W. Breakup of Ring Beams Carrying Orbital Angular Momentum in Sodium Vapor. *Phys. Rev. Lett.* **2004**, *92*, 083902. Copyright 2004 American Physical Society.....41

Figure 1.24 a) Chiral structures obtained upon vortex irradiation of thin films made of tantalum, silver, silicon, and chromium/gold. Images (left to right) reprinted with permission from ref. 181,182,183 and 184. Copyright 2017 Optical Society of America. Copyright 2012 American Chemical Society. Copyright 2018 AIP Publishing. Copyright 2017 AIP Publishing. Chiral structures can also be obtained when the sample is irradiated from the substrate side rather than the film side. The top images in **b)** show the time evolution of a spin jet created upon irradiation of a viscous ink with a vortex beam. When the viscous ink is irradiated with a circularly polarized beam, scattered droplets are formed which confirms a vortex beam is necessary for the formation of the spin jet. Reprinted with permission from ref. 185. Copyright 2019 Optical Society of America.....43

Figure 1.25 a) Surface relief pattern generated with a vortex beam with $l=10$. Reprint with permission from ref. 166, Springer Nature **b)** Conch-shape reliefs created through the irradiation of a circularly polarized vortex beam with total angular momentum of ± 2 Reprinted with

permission from ref. 186, Springer Nature. c) Each column in the middle shows the time evolution of the fabrication of polymer fibers with $l = 0,1,2,4$ (left to right). Images of the fibers obtained in the experiments are shown on the top ($l = 0,2$) and bottom ($l = 1,4$). Reprinted with permission from ref. 187, Copyright © 2018 American Chemical Society45

Figure 1.26 a) Diagram of optical forces acting on a particle generated by a vortex beam. Force vectors are represented as bold black arrows while the narrow black arrows correspond to r and z components. b) Scheme of the model proposed to explain polymer fiber formation upon irradiation of a vortex beam based on a coarse-grained particle model. c) Simulated dynamics of a coarsened particle with $d = 50$ nm in a medium where the absorption is $\eta = 9.24 \times 10^3$ m⁻¹. The top graph shows the trajectory of the particle on the xy plane while the graph at the bottom shows the same trajectory of the particle on the yz plane (the z direction is compressed by 100 fold). Reprinted with permission from Lee, J.; Arita, Y.; Toyoshima, S.; Miyamoto, K.; Panagiotopoulos, P.; Wright, E. M.; Dholakia, K.; Omatsu, T. Photopolymerization with Light Fields Possessing Orbital Angular Momentum: Generation of Helical Microfibers. *ACS Photonics* 2018, 5, 4156–4163. Copyright 2019 Optical Society of America.....46

Figure 2.1 (a) Scheme of the optical assembly employed consisting of a blue LED ($\lambda = 460$ nm) and up to 3 amplitude masks (AM) placed at the transparent walls of the rotatable resin cell. Imaging of the optical profile at the exit face of the resin bath during the formation of cylinders was achieved with a planoconvex lens pair (L1, f.l. = 250 mm and L2, f.l. = 250 mm) and a CCD camera. (b) Side-view images of the growing cylinder with input width = 5 mm, length = 11 mm, intensity = 1.1 mW mm⁻² and scale bar = 2 cm. The sample cell consisted of a cut syringe with glass cover slips glued to each end. (c) Time evolution of the spatial intensity profile at the exit plane of the sample with a growing cylinder with input width = 2 mm, length = 11 mm (Scale bar

= 1 cm). (d) Final printed polymer cylinders with input width = 10 mm, length = 27 mm and obtained with an LED beam at incident intensities from left to right of 0.47 mW mm⁻², 1.1 mW mm⁻² and 1.9 mW mm⁻². Scale bar = 1 cm.....65

Figure 2.2 Flowchart depicting the decomposition steps that were carried out to convert mesh files into printable prismatic elements.68

Figure 2.3 (a) Decomposition of a house into 2 separate prismatic elements. (b) Separate printing of each element. (c) House constructed from glued fragments based on the identification of prisms.70

Figure 2.4 (a) Decomposition of an object into separate printable, prismatic elements based on the removal of triangular pyramid volumetric elements. (b) Separate in printing of each element. (c) House constructed from glued fragments based on the identification of prisms.71

Figure 2.5 (a) Decomposition of a runner using two degenerate methods and the fabrication of a runner. Scale bar = 1 cm. (b) The object was printed by first projecting light onto AM1 of the cell containing photopolymerizable resin, and then subsequently rotating the cell to AM2 and AM3 once each previous element was printed. (c) Images depicting a runner printed using SLA (left) and prismatic 3D printing (right). Scale bar = 1 cm.....73

Figure 2.6 Illustration of fragmented model from various meshes and the resulting printed objects.....75

Figure 2.7 a) Rectangular prism (Width x Height x Length= 4 x 8 x 3 mm) with waveguide circuitry. b) Optical micrographs of the entrance (right) and exit face (left) of a rectangular prism with waveguide circuitry. c) Near-Field view of a red LED beam that propagates through the

rectangular prism with waveguide circuitry at the exit face of the sample (left). A magnification of the filaments formed is shown in the middle. c) Far-Field view of a laser beam propagating through the same prism.....79

Figure 2.8 Decomposition steps that were carried out to identify a skull medallion mesh is a printable prismatic element and the resulting printed object that resulted. Scale bar = 1 cm. The skull medallion model is a reconstruction of the Mexican sculpture (right). Scale bar = 30 cm.....90

Figure 2.9 Decomposition steps that were carried out to convert a hockey player mesh into printable prismatic elements and the resulting printed object that resulted within 100 s. Scale bar = 1 cm.....90

Figure 2.10 Decomposition steps that were carried out to convert an inukshuk mesh into printable prismatic elements and the resulting printed object. Scale bar = 1 cm.....91

Figure 2.11 Decomposition steps that were carried out to convert a skyscraper mesh into printable prismatic elements and the resulting printed object. Scale bar = 1 cm.....91

Figure 2.12 Decomposition steps that were carried out to convert a house mesh into printable prismatic elements and the resulting printed object. Scale bar = 1 cm.....92

Figure 2.13 Amplitude masks used to print objects *in situ*.....92

Figure 2.14 Decomposition steps that were carried out to convert a skull mesh into printable prismatic elements and the resulting printed object. Scale bar = 1 cm.....93

Figure 2.15 Decomposition of a sprinting runner using two methods and the fabrication of the runner. Scale bar = 1 cm.....93

Figure 2.16 Decomposition of a starting runner using two methods and the fabrication of the runner.
Scale bar = 1 cm.....93

Figure 2.17 Decomposition of a lattice using 3 methods and the fabrication of the lattice in 3 steps with overlapping elements. Scale bar = 1 cm.....94

Figure 2.18 2-D and 3-D time evolution of the spatial intensity profile of an array of filaments generated with a periodic amplitude mask ($\Lambda = 80 \mu\text{m}$) with square apertures ($40 \times 40 \mu\text{m}$) during the printing process of a rectangular prism 3 mm long embedded with waveguide circuitry.....94

Figure 3.1 a) Slab waveguides were printed by launching a LED beam ($\lambda = 455 \text{ nm}$) through a rectangular or circular mask (top and middle images). The patterned beam was then launched to a cell containing resin **H4**. Micro-patterned prisms were printed by passing the same LED beam through a 2D periodic amplitude mask ($\Lambda = 80 \mu\text{m}$, $\approx 0.94 \text{ mW mm}^{-2}$) before being launched to the amplitude mask that defines the shape of the prism(bottom). In this case the cell contained resin **H6**. **b)** The LED beam induces localized free radical polymerization of acrylic acid monomers resulting in the formation of a prism hydrogel waveguide. **c)** Hydrogel prism 10 mm long (Width= 2 mm, Height= 10 mm). **d)** Optical up used to achieve horizontal right-left beam manipulation with electroactive rectangular waveguides. Samples glued to coverslips placed between two graphite electrodes were partially immersed in a phosphate buffer solution. A blue LED beam was launched to the top part of the sample. Optical profile at the exit face of the gel was monitored with a planoconvex lens pair (L1, f.l. = 250 mm and L2, f.l. = 250 mm) and a CCD camera. **e)** Bending mechanism in electroactive hydrogels. Counterions within the anionic network migrate towards the cathode when an electric field is applied but remain within the polymer to preserve the electroneutrality inside the gel. The concentration of ions at the cathode becomes

larger due to the gel permselectivity to cations (middle). This concentration gradient generates a higher osmotic pressure on the anode side than on the cathode. A positive pressure difference gives as result swelling on the anode side and bending (right) towards the cathode.....102

Figure 3.2. a) Top view and 2D beam output profile time evolution of a waveguide 10 mm long under the effect of an electric field ($\sigma = 1300 \text{ V/m}$) when irradiated with a blue LED ($\lambda = 455 \text{ nm}$). When the electric field is applied, the waveguide bends towards the cathode. At the same time, the beam traveling through the waveguide bends in the same direction. When the polarity of the electric field is reversed, the waveguide and the beam output move in the opposite direction. **b)** Time evolution of the bending angle and integrated intensity of the beam output **c)** As the waveguide bends away from the optical set up, the intensity on the detector decreases $\sim 92\%$ when the maximum bending angle θ_{max} is reached. On average, θ_{max} is $10^\circ \pm 2^\circ$104

Figure 3.3 a) Top view of the time evolution of a waveguide 9 mm long under the effect of an electric field ($\sigma = 520 \text{ V/cm}$) illuminated with a green laser ($\lambda = 520 \text{ nm}$). When the electric field is applied, the waveguide bends towards the cathode as in the horizontal configuration. When the polarity of the electric field is reversed after 180 s, the waveguide moves in the opposite direction. **b)** Time evolution of the bending angle when the polarity of the electric field is switched every 180 s before reaching equilibrium. A maximum bending angle of $10^\circ \pm 2^\circ$ is achieved. **c)** The intensity of the beam output decreases as it bends since light is guided away from the detector reaching a minimum of $\sim 23\%$ of its original value. The intensity of the beam output is fully recovered during the first 400 s when the polarity of the beam is inverted, and the cylinder points out directly at the camera.....105

Figure 3.4 Vertical right to left bending of an individual as well as square arrays of 4 (2 x 2) and 9 (3 x 3) cylindrical waveguides ($\sigma = 520$ V/cm) irradiated with an expanded green laser beam ($\lambda = 520$ nm). Graphs at the top show the time evolution of the bending angle of the individual cylinder and of cylinders 11 and 21 of the 2 x 2 array and, cylinders 12, 22 and 32 of the 3 x 3 array.....108

Figure 3.5 a) Hydrogel prism (H x L x W= 10 mm x 6 mm x 2.5 mm) with a waveguide lattice embedded. **b)** Side view, **c)** entrance and **d)** exit faces micrographs of the waveguide lattice. **e)** Time evolution of the hydrogel waveguide lattice under the effect of an electric field $\sigma = 350$ V/cm. The electric field was applied for 100 seconds to keep the lattice within the field of view of the CCD camera. After this period, the electric field was turn off for 60 seconds before inverting the field. The square light pattern generated by the lattice moves towards the cathode. **f)** Far field view of the light pattern generated by a hydrogel prism (H x L x W= 10 mm x 6 mm x 3.5 mm). The top image shows the hydrogel prism with the waveguide lattice embedded and the light pattern before the electric field was applied. The middle image shows the position of the pattern and the hydrogel lattice after applying the electric field for 240 s. The light pattern is clearly directed to the right. The bottom image shows how light is directed in the opposite direction 240 s after the polarity of the field was inverted.....110

Figure 3.6. Graphs showing the time evolution of the displacement and intensity of the nine waveguides highlighted in the image at the top right while. The electric field was applied for 100 in one direction before inverting its polarity. As the displacement graphs show, when the polarity was inverted, the waveguides does not bend to the same extend in the opposite. Unlike the intensity output of the slab waveguide, the intensity output of the micro-waveguides shows random fluctuations.....112

Figure 3.7. Multidirectional bending of cylindric waveguides illuminated with an expanded green laser ($\lambda=520\text{ nm}$). The top left shows an individual waveguide and arrays of 4 and 9 waveguides before the electric field is applied. Target angles are shown above each image. Target angles for the individual waveguide are shown at the right of each image of the individual waveguide. Going through each target angle in a sequence allows to rotate them.....114

Figure 3.8. a) The average bending curvature of the longest waveguide at θ_{max} is ~ 0.02 . Therefore, it can be assumed that the waveguide remains a straight line and that its length does not change during the experiment. **b)** Illustration of how the displacement of the waveguide Δx was calculated for horizontal and vertical bending. Subtracting the initial position of one of the edges of the beam from the of the edge after 10 seconds. Bending angles were obtained using the inversed sine function.....121

Figure 3.9 Beam propagation method simulations of a beam ($\lambda = 445\text{ nm}$) traveling through a slab waveguide $10,000\text{ }\mu\text{m}$ long ($\Delta n = 0.4$) oriented at $0\text{-}12^\circ$, 30° , 38° and 40° with respect to the x axis. Transverse (xy) cross sections of the beam output are shown. After 38° , the beam output does not follow the trajectory of the waveguide. Instead, the beam is guided at an angle smaller than the angle at which the waveguide is oriented.....122

Figure 3.10 Time evolution of the bending angle (left) and integrated intensity of the beam output (left) of slab waveguides 6 and 9 mm long (c). As the waveguide bends away from the optical set up, the intensity on the CCD camera decreases. The maximum bending angle θ_{max} for the waveguides 9 and 6 mm long is on average 10 ± 2 and 3 ± 2 . When θ_{max} is reached, the intensity decreases to ~ 22 and $\sim 75\%$ of its original value.....123

Figure 3.11 a) Top view of the set up to achieve vertical right-left and multidirectional bending of cylindric hydrogel waveguides (left). **b)** An example of the vectoral analysis carried out to combine the electric fields from both power supplies is shown at the right and bottom. To make the waveguide bend 60° taking as a reference a vertical line going through the center of the cage, the voltage from power supply 1 was set at 7.5 V producing a electric field pointing down of 260 V/m. Power supply 2 was set at 13 V with a horizontal field towards the right of 450 V/m. The combined electric field from both power supplies is 520 V/m. The same electric field (500 V/m) is obtained with an individual power supply is set at 15 V. **c)** All configurations used to direct the cylindric waveguide in a circular trajectory.....128

Figure 3.12 Polar plot of the position of a cylindric waveguide 10 mm long and its intensity output during a multidirectional bending experiment. The intensity of the waveguide output remains unchanged as it bends towards the first target angle (0°). Although times are not shown in the polar plot, the intensity of the waveguide output starts to decrease after 7 minutes due to damage within the hydrogel.....129

Figure 4.1 The optical assembly consists of a $\lambda/2$ waveplate (W1), a mirror (M), a neutral density filters (F1 & F2), a spiral phase plate (V), a focusing lens (L1), a sample stage (S), imaging lenses (L2 & L3) and a charge-coupled device camera (CCD).....133

Figure 4.2 Temporal evolution of the vortex beam with $l=-1$ at $I= 42.08 \text{ W/cm}^2$ in the epoxide system. The filament formed at the region of highest intensity rotates counter-clockwise around the beam axis.....135

Figure 4.3. a) Extent of the rotation $\Delta\theta$ as a function of intensity. **b)** Rate of rotation as a function of intensity. **c)** Polar plot showing the evolution of a rotating filament at $I= 42 \text{ W/cm}^2$. **d)**

Micrographs of the entrance and exit face of a polymer fiber obtained after irradiating an epoxide sample for 5 minutes at $I = 140 \text{ W/cm}^2$136

Figure 4.4. Temporal evolution of the vortex beam with $l = +1$ at $I = 42.08 \text{ W/cm}^2$ in the epoxide system. The filament formed at the region of highest intensity rotates counter-clockwise around the beam axis.....141

Figure 4.5 a) Typical result in a regular epoxide sample with $l = -1$ at $I = 140.27 \text{ W/cm}^2$ (top) and in a prepolymerized sample (bottom) at $I = 42.08 \text{ W/cm}^2$141

Figure 5.1. LED driven by a 9 V battery with a hydrogel prism acting as a part of the electronic circuit.....149

List of Tables

Table 2.1 Diameter at the entrance and exit face of cylinders fabricated with a beam 10 mm wide at 0.47, 1.1 and 1.9 mW mm ⁻² (3 replicates).....	89
Table 4.1 Area of a vortex beam with $l = -1$ at the exit face at $t = 0$ s (A_o) and before breaking up into filaments (A_f). The calculations were made for each of the intensities used by subtracting the area of the dark center from the area of the whole ring.....	142

List of Abbreviations and Symbols

Δn	Refractive index change
k_0	Free space wavenumber
n_0	Refractive index in vacuum
α	Attenuation coefficient, polarizability of a coarse-grained particle
E	Electric field
n_2, n'_2	Nonlinear refractive-index coefficient of a Kerr-type material
P	Polarization
ε_0	Vacuum permittivity
$\chi(n)$	Linear susceptibility of order n
E	Electric field, Young modulus
I	Intensity
ω	frequency of a beam
A	Amplitude function of a beam
$\delta\theta$	Phase difference factor
θ_1, θ_2	Phase factor of wave 1 and 2
KTP	Potassium titanyl phosphate
λ	Wavelength

LBO	Lithium triborate
SBN	strontium barium niobate
AC	Alternating current
DC	Direct current
c	Speed of light
LC	Liquid crystal
R	Molar fraction of a polymer (cm^3/mol), ideal gas constant
M	Polymer molecular weight
ρ	Density
U_0	Critical exposure required to initiate polymerization
Δn_s	Maximum refractive index change in a photopolymerizable medium
τ	Monomer radical lifetime
UV	Ultraviolet light
θ_A	Acceptance angle of a self-written waveguide
n_{core}	Refractive index of the core of a waveguide
n_{clad}	Refractive index of the cladding of a waveguide
a	core size of a waveguide
QTH	Quartz Tungsten Halogen

FOV	Field of View
LED	Light-emitting diode
CLIP	Continuous liquid interface production
CAL	Computed Axial Lithography
NSCRIPT	Nonlinear inscription of complex micro-components
SMaLL	Solution Mask Liquid Lithography
PEDOT:PSS	Poly(3,4-ethylenedioxythiophene: polystyrene sulfonate)
QD-LEDs	Quantum-dot light-emitting diodes
π_{ion}	Osmotic pressure difference
R	Gas constant
T	Temperature
C_i^h	Concentrations of ions inside a hydrogel network
C_i^s	Concentration of ions in a solution
$\Delta\pi_{ion}$	Osmotic pressure difference between two solid-liquid interfaces
π_n	Osmotic pressure
D	Thickness of a gel
E	Young's modulus
Y	Degree of bending

L	Length of a gel
SAM	Spin angular momentum
OAM	Orbital angular momentum
J	Total orbital angular momentum
l	Topological charge
s	Spin angular momentum
\hbar	Planck's constant
φ	Azimuthal angle
NLSE	Nonlinear Schrödinger Equation
\emptyset	Phase
$R(r)$	Radial soliton envelope
r	Radius
p	Perturbation
MI	Modulation Instability
F_{grad}	Gradient force
F_{scat}	Scattering force
t_p	Period of Pointing vector
S	Pointing vector

H	Magnetic field
C_{scat}	Scattering cross-section
ϵ_f	Dielectric constant of a fluid
ϵ_p	Dielectric constant of a coarse-grained particle
w_0	Beam waist
n_f	Refractive index of a fluid
C_{scat}	Scattering cross-section of a coarse-grained particle
k_f	Wavenumber of light in a liquid resin
η	Absorption coefficient of a resin
L_p	Period of the helix trajectory of a coarse-grained particle
d	Diameter of a coarse-grained particle
CT	Computed tomography
DLP	Digital light processing
DCPI	Dual-colour photoinitiator
SLA	Stereolithography
CQ	Camphorquinone
EDB	Ethyl p-dimethylamino benzoate
CCD	Charge-coupled device

HARP	Light-area rapid printing
DCPI	Dual-colour photoinitiator
PTP	Particle tracking program

1 Introduction

1.1 Light propagation in nonlinear media

The natural diffraction of light is affected when it travels in a medium undergoing a refractive index change (Δn). Depending on the magnitude and the sign of Δn and whether the change is local or non-local, three different effects often take place that modify the intensity or/and the special profile of a beam: self-focusing, self-trapping (soliton formation) and self-defocusing.¹ A self-focusing effect occurs when the refractive index change is positive and large enough to make a beam of light focused in the medium. When there is balance between the focusing effect and diffraction, the beam travels in the medium without changing its spatial or intensity profile. This entity confined within its own waveguide is known as self-trapped beam or soliton (Figure 1.1). When the refractive index change is negative, the beam broadens. This phenomenon is known as self-defocusing. The formation and propagation of a beam when these phenomena occur are described using the paraxial approximation and the nonlinear Schrödinger equation:^{2,3}

$$2ik_0n_0 \frac{\partial E}{\partial z} + \nabla_{\perp}^2 E + 2k_0^2 n_0 \Delta n E + ik_0 n_0 \alpha E = 0 \quad (1.1)$$

The first term in (1.1), $2ik_0n_0 \frac{\partial E}{\partial z}$, describes the beam propagation along the z-axis in the medium. The second term $\nabla_{\perp}^2 E$ describes the natural diffraction of the beam along the x and y axis while the third term accounts for the self-focusing effect due to the light-induced refractive index change Δn occurring in the medium. Finally, the last term accounts for the attenuation of the beam α by the medium. This thesis will focus on materials with a positive and permanent refractive index changes. Confining light while triggering permanent changes allows to transfer the pattern carried by the beam to the photo-responsive material as well as to study the effect of the refractive index change on the beam.

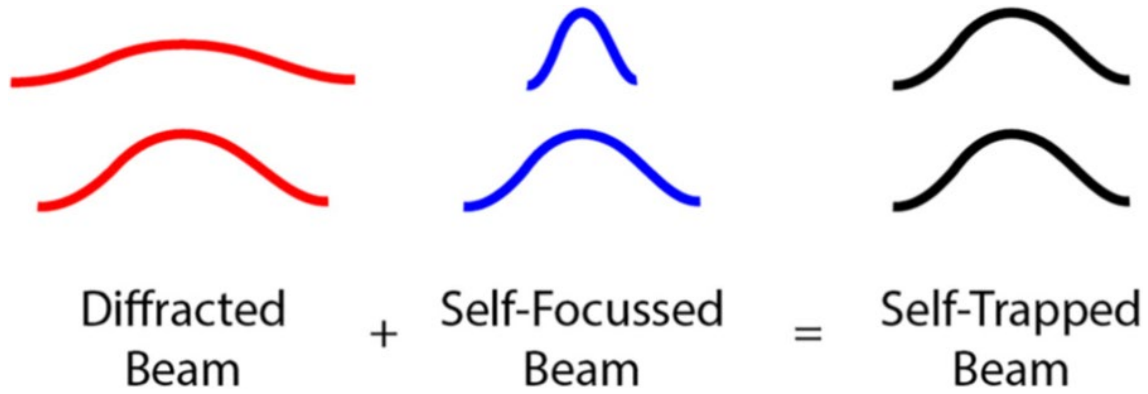


Figure 1.1 A self-trapped (right) beam is produced when the natural diffraction of light (left) is counteracted by the focusing effect (middle) originated by the refractive index change (Δn) in a nonlinear medium. Reprinted with permission from Biria, S.; Morim, D. R.; Tsao, F. A.; Saravanamuttu, K.; Hosein, I. D. Coupling nonlinear optical waves to photoreactive and phase-separating soft matter: Current status and perspectives. *Chaos* **2017**, *27*, 104611. Copyright 2017 AIP Publishing.³

1.2 Types of Nonlinear Materials

There are five kinds of materials that undergo refractive index changes in which self-focusing, and self-trapping have been observed: isotropic third order nonlinear media,⁴⁻⁸ second-order nonlinear crystals,⁹⁻¹³ liquid crystals,¹⁴⁻¹⁷ photorefractive materials,¹⁸⁻²¹ and photochemical systems.²²⁻³² It was initially thought that using coherent light was a requirement to induce a nonlinear response and that most nonlinear responses could be explained by expressing the susceptibility term χ in the equation that describes the electric polarization vector $P = \epsilon_0 \chi E$ as a power series:¹

$$P = \epsilon_0 [\chi^{(1)}E + \chi^{(2)}E^2 + \chi^{(3)}E^3 \dots] \quad (1.2)$$

where ϵ_0 is the free-space permittivity, $\chi^{(1)}$ corresponds to the first order linear susceptibility, $\chi^{(2)}$ and $\chi^{(3)}$ are the second- and third-order nonlinear susceptibility.

1.2.1 Third order nonlinear materials

A material with molecules oriented anisotropically tend to reorient themselves along the polarization direction of an intense optical field. A requirement for a material to exhibit a strong Kerr-type effect is a rotation axis for molecular symmetry. For these materials, $\chi^{(3)}$ is the only nonlinear term that is significant. The refractive index change in a Kerr-type material can be written as:¹

$$\Delta n = n_2 |E|^2 = n_2' I \quad (1.3)$$

Although Kerr-type media exhibit ultrafast response times (in the order of femtoseconds), they require high intensities that can only be achieved with high power lasers.

1.2.2 Second-order nonlinear materials.

The main mechanism causing the refractive index changes in non-resonant transparent optical media is electron-cloud distortion which is associated with the second order nonlinear susceptibility $\chi^{(2)}$. Such a change occurs when a beam of frequency ω and its second-harmonic wave 2ω are re-launched through a second-order nonlinear crystal meeting the amplitude requirements ($A(\omega) = \sqrt{2}A(2\omega)$) and phase-matching conditions between the two incident beams:¹

$$\Delta n^o(\omega) = \frac{\chi_{e,(l)}^2}{2n_0^o(\omega)} 2A(2\omega) \cos\delta\theta \quad (1.4)$$

$$\Delta n^e(2\omega) = \frac{\chi_{e,(l)}^2}{2n_0^e(2\omega)} \frac{A^2(\omega)}{A(2\omega)} \cos\delta\theta \quad (1.5)$$

$A(\omega)$ and $A(2\omega)$ are the amplitude functions of the beams, $\Delta n^o(\omega)$ and $\Delta n^e(2\omega)$ are the induced refractive-index changes for both the fundamental and second-harmonic generated beam, $\chi_{e,(l)}^2$ is

the second order susceptibility of the medium under type-I phase matching conditions (both beams having the same polarization), $\delta\theta$ is the phase difference factor $\delta\theta = 2\theta_1 - \theta_2$ where θ_1 and θ_2 are the initial phase wave factors. When $\delta\theta=2\theta_1 - \theta_2$ with θ_1 and θ_2 being the initial phase factors of the two waves. When $\delta\theta = 0$ or $2m\pi$, where m is an integer, there is a positive refractive index change which is a condition required to achieve self-focusing/self-trapping. Soliton formation,, in a second-order nonlinear crystal was demonstrated for the first time in a KTP (Potassium titanyl phosphate: orthorhombic system, space group Pna2₁) crystal in 1995 by launching a fundamental beam ($\lambda = 1064$ nm) and a second-harmonic generated beam ($\lambda = 532$ nm) through a 1-cm long sample.⁹ In the absence of the second-harmonic generated beam, the fundamental beam at the crystal entrance face was ~ 20 μm while at the exit face it increased to ≥ 80 μm . When the second-harmonic beam was launched in phase with the fundamental beam, the diameter of both beams got reduced to ~ 12.5 μm when the intensity of the fundamental beam was higher than 10 GW/cm². Similar results have also been obtained in the widely used LBO (Lithium triborate, LiB₃O₅: orthorhombic system, space group Pna2₁) crystal.^{13,33}

1.2.3 Photorefractive materials

Most photorefractive materials are crystals doped with an impurity that can be photo-excited. The mechanism behind the refractive index change is associated with the generation of charges upon photo-excitation of the impurities within the crystal followed by transport and recombination of such charges under the influence of an external electric field. The separation of charges creates an electric field within the crystal known as space-charge field which produces a refractive index change due to the linear electro-optic effect (Pockels effect) which is described by the second order nonlinear susceptibility ($\chi^{(2)}$). The formation of spatial solitons in photorefractive crystals was predicted in 1992 by Segev et al.³⁴ and demonstrated for the first time the year after in a strontium

barium niobate (SBN) crystal.¹⁸ Since the refractive index change in a photorefractive crystal depends on charge separation, they are nonlocal and non instantaneous with response times depending on the intensity used (mW/cm^2 to MW/cm^2).

1.2.4 Liquid crystals

The refractive index change in nematic liquid crystals has its origin in the reorientational effect of elongated pre-oriented molecules. Such pre-orientation is carried out either with an AC^{35,36} or DC^{37,38} electric field. When a polarized beam is launched through a LC sample, a torque is induced in the medium that changes the orientation of the molecules that were previously aligned.^{39,40} Most nematic crystals are uniaxial which means they have one orientation where molecules are arranged symmetrically. The orientation of the optical field with respect to the symmetric axis determines the speed of the optical waves and therefore, the refractive index in that direction n_e . Nematic crystals have two different indices of refraction $n_e \equiv c/v_{\perp}$ and $n_o \equiv c/v_{\parallel}$. The difference between these two refractive indices is known as birefringence⁴¹ and its usually ~ 0.01 and the intensities required to start observing soliton formation are in the mW range.⁴⁰ Since reorientation of LC affects neighbouring molecules, refractive index changes have a strong nonlocality and a delayed response (usually in the order of tens of seconds).

1.2.5 Photopolymerization reactions

All the refractive index changes described so far are based on physical mechanisms. Inducing a refractive index change by starting a chemical transformation is also possible since the products in a chemical transformation have a different refractive index than the reactants. These changes can be reversible or irreversible.⁴² This thesis focuses on photopolymerization reactions. In a typical photopolymerization reaction, molecules known as photoinitiators produce reactive species (radicals or ions) upon absorption of a photon (initiation), although multiphoton absorp-

tion of a photon (initiation), although multiphoton absorption can also be achieved using tightly focused laser beams. These radical/ions react with monomers to generate new reactive species that keep reacting with new monomers (propagation) forming a polymer network. This growing process continues until a termination step takes place. Since monomers are joined together by chemical bonds, there is a contraction in the material and an increase in density which results in a positive refractive index change. The refractive index of a polymer can be approximated Lorentz-Lorenz equation:⁴⁴

$$n = \sqrt{\frac{\frac{2R\rho}{M} + 1}{1 - \frac{R\rho}{M}}} \quad (1.6)$$

Where $R(\text{cm}^3/\text{mol})$ is the molar refraction, $M(\text{g/mol})$ is the polymer molecular mass, and $\rho(\text{g/cm}^3)$ is the density of the polymer. The time evolution of the refractive index change in a photopolymerizable medium can be described by the following empirical equation:²²

$$\Delta n'(x, y, z, t) = \Delta n_s \left\{ 1 - \exp \left[\frac{-1}{U_o} \int_0^{t-\tau} |E(t)|^2 dt \right] \right\} \quad (1.7)$$

where Δn_s is the maximum index change (at saturation when most monomers have reacted), U_o is the minimum energy required to initiate polymerization, $E(t)$ is the optical field amplitude as a function of time and τ , the monomer radical lifetime. A plot of Eq. 1.7 shows 3 distinct zones for any monomer undergoing radical photopolymerization (Figure 1.2). At early stages, no changes in the refractive index are observed since the polymerization reaction is inhibited by oxygen dissolved in the monomer. During the second stage when larger light doses have been delivered, large polymer chains start to form and the density of the materials increases, a sharp increase in refractive index is observed. At the third stage, the reaction reaches completion and $\Delta n'$ saturation.

This transition is generally accompanied by a change of state from liquid (monomers) to solid (polymer).

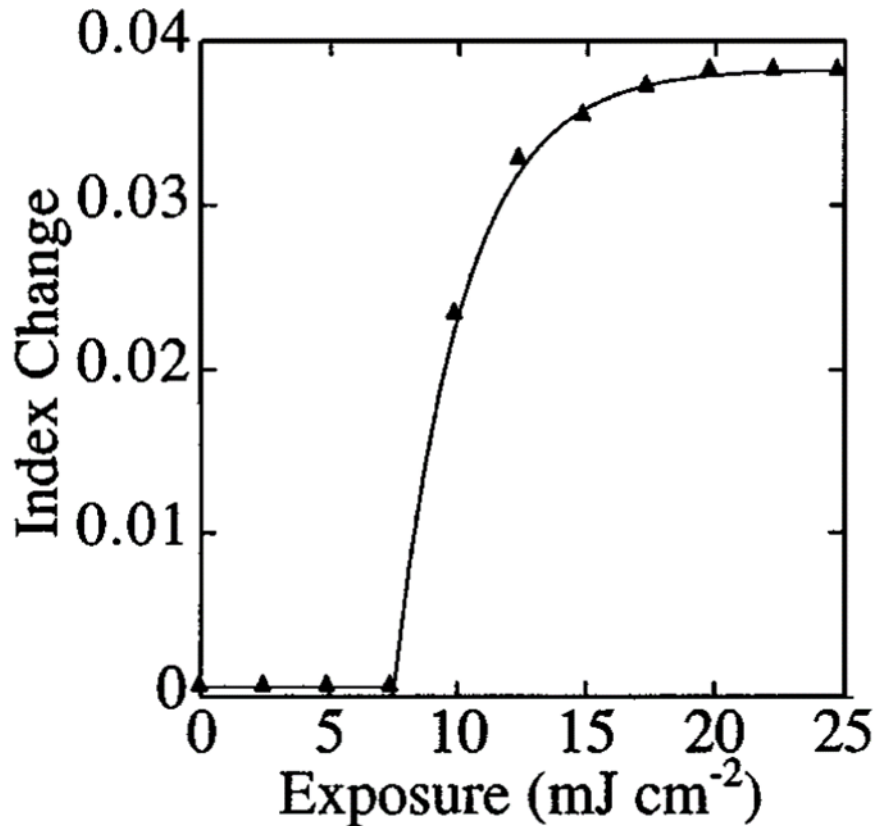


Figure 1.2 General evolution of the refractive index change in a photopolymerizable sample. Reproduced with permission from Kewitsch, A. S.; Yariv, A. Self-focusing and self-trapping of optical beams upon photopolymerization. *Opt. Lett.* **1996**, *21*, 24-26. Copyright 1996 Optical Society of America.²²

1.3 Photopolymerization reaction mechanisms

As mentioned earlier photopolymerization reactions are carried out by radicals or ions that are created upon absorption of light usually through chain growth polymerization. In the case of ionic polymerization, the reactive species can be either cations (cationic polymerization) or anions (anionic polymerization). Cationic polymerization is the only ionic polymerization that will be discussed.

1.3.1 Radical photopolymerization

In the initiation step of free-radical polymerization, radicals (atoms or molecules with an unpaired electron) are formed through photolysis of photoinitiator molecules.

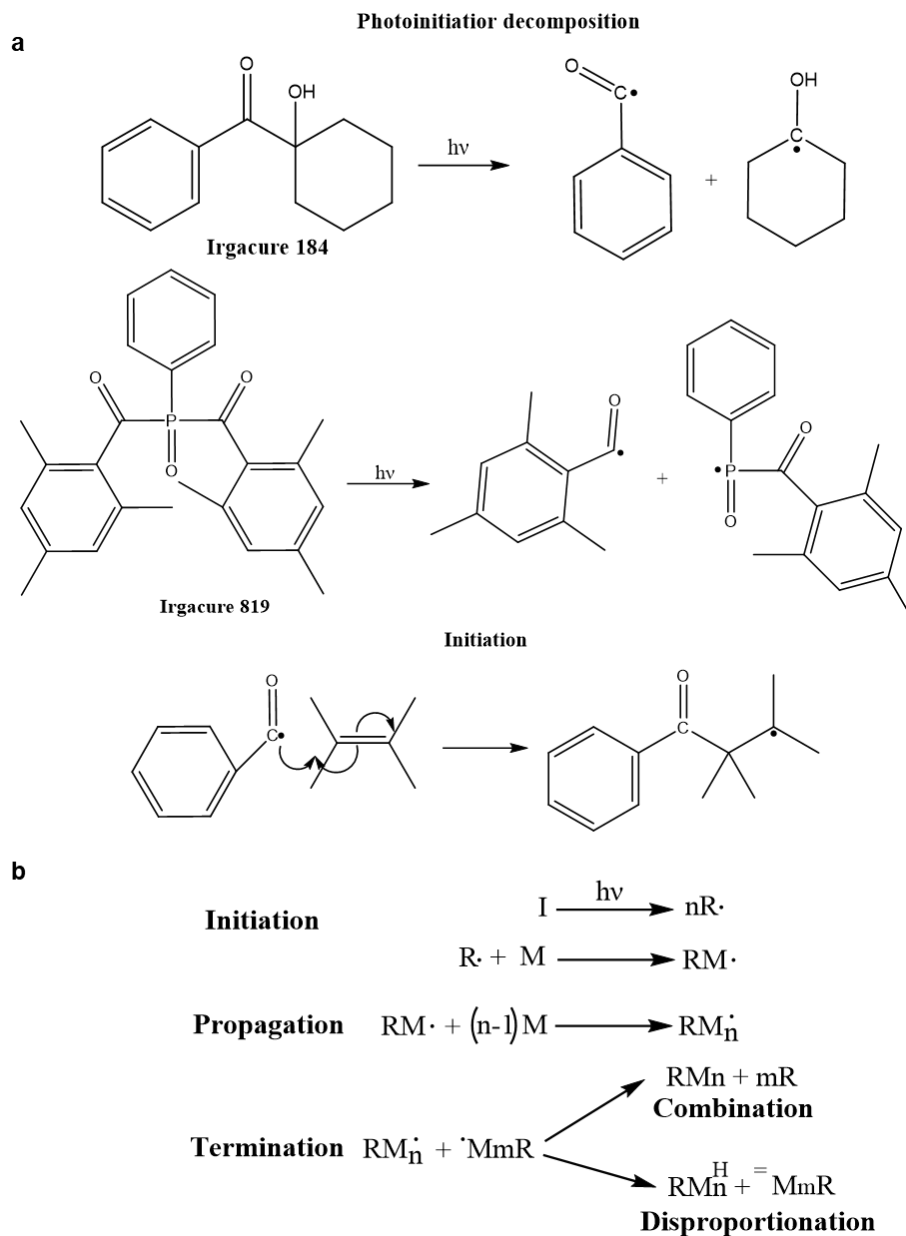


Figure 1.3 a) Photolysis of initiators Irgacure 184 (1-Hydroxycyclohexyl phenyl ketone) and Irgacure 819 (Bis(2,4,6-trimethylbenzoyl)-phenylphosphine oxide).^{45,46} Example of an initiation step. A radical attacks the carbon-carbon double bond creating a new radical one monomer longer. **b)** General steps in any radical polymerization reaction.⁴⁷

An example of this process is illustrated in Figure 1.3a with the photoinitiators Irgacure 184⁴⁵ and Irgacure 819⁴⁶ which were used in several polymerization reactions described in this thesis. These radicals attacked the carbon-carbon double bond C=C of a monomer forming a new radical (initiation) that keeps growing by adding monomers creating a chain (propagation). This process continues until two radical chains collide creating a covalent bond between them (combination) or when a reaction takes place between two radicals creating products that are not radicals (disproportionation). These steps are illustrated in a general manner in Figure 1.3b. Another possibility is that the unpaired electron is transferred from a macro radical to a new specie that can incorporate more monomer (transfer reaction). Figure 1.4 shows the reaction to obtain a widely used organosiloxane photopolymer by our group through free radical photopolymerization.

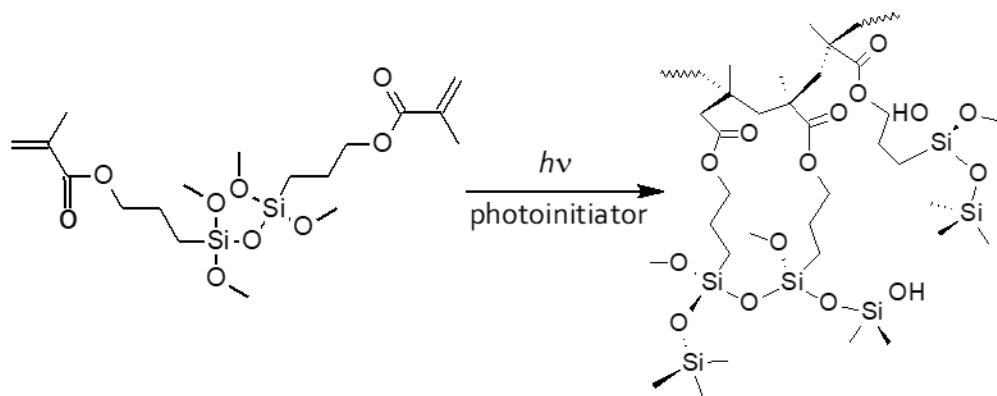


Figure 1.4 Radical photopolymerization of 3-(trimethoxysilyl)propyl methacrylate using Irgacure[®] 784.

1.3.2 Cationic photopolymerization

Cationic polymerizations also involve a chain mechanism in which positively charged monomers are the active species. The former kind of polymerization is known as cationic ring-opening polymerization (ROP). Unlike radical polymerization, there are no actual termination reactions such as combination since all chains are positively charged so the charged sites do not come to a

close proximity due to electrostatic repulsion. In general, cationic polymerization can be described as shown in Figure 1.5.⁴⁷ We have previously shown that it is possible to induce the formation of nonlinear light waves in media undergoing cationic polymerization of epoxide moieties.^{32,48-51}

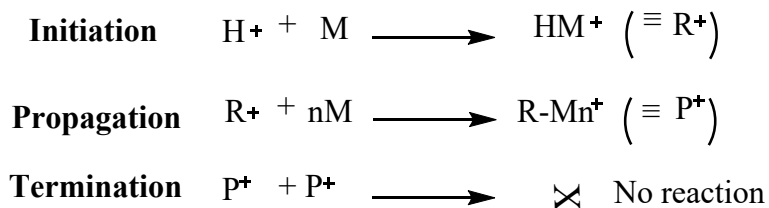


Figure 1.5 Basic steps in a cationic polymerization.⁴⁷ The initial step involves the protonation of the monomer. This new cation keeps adding more monomer until all monomer is depleted or until the growing chain reacts with a contaminant.

Sulfonium and iodonium salts are the most common photoinitiators to induce cationic polymerization.⁴⁷ These photoinitiators absorb in the UV region. The photolysis of the photoinitiator and the protonation of the monomer when UV light is used it takes place as illustrated in (3) of Figure 1.6. However, photopolymerization can be initiated using visible light by the use of a photosensitizer that promotes radical decomposition reactions. This is illustrated for a iodonium salt in (1) and (2) in the same Figure. The first step consists of generating radicals upon absorption of visible light by a photoinitiator (1). Oxidation of one of the radicals by the diaryliodonium salt produces a cation R^+ that is involved in the cationic polymerization in a direct or indirect manner (2). The diaryliodonium free radicals produced in the last step can be used again in the same reaction to continue the cation generation which results in the production of several cations for each photon absorbed. Upon absorption of a photon, an aryl- and a diaryliodonium radical are produced. It is well known that alcohol accelerate the photopolymerization process when diaryliodonium salts are employed as photoinitiators.⁵² The mechanism proposed to explain

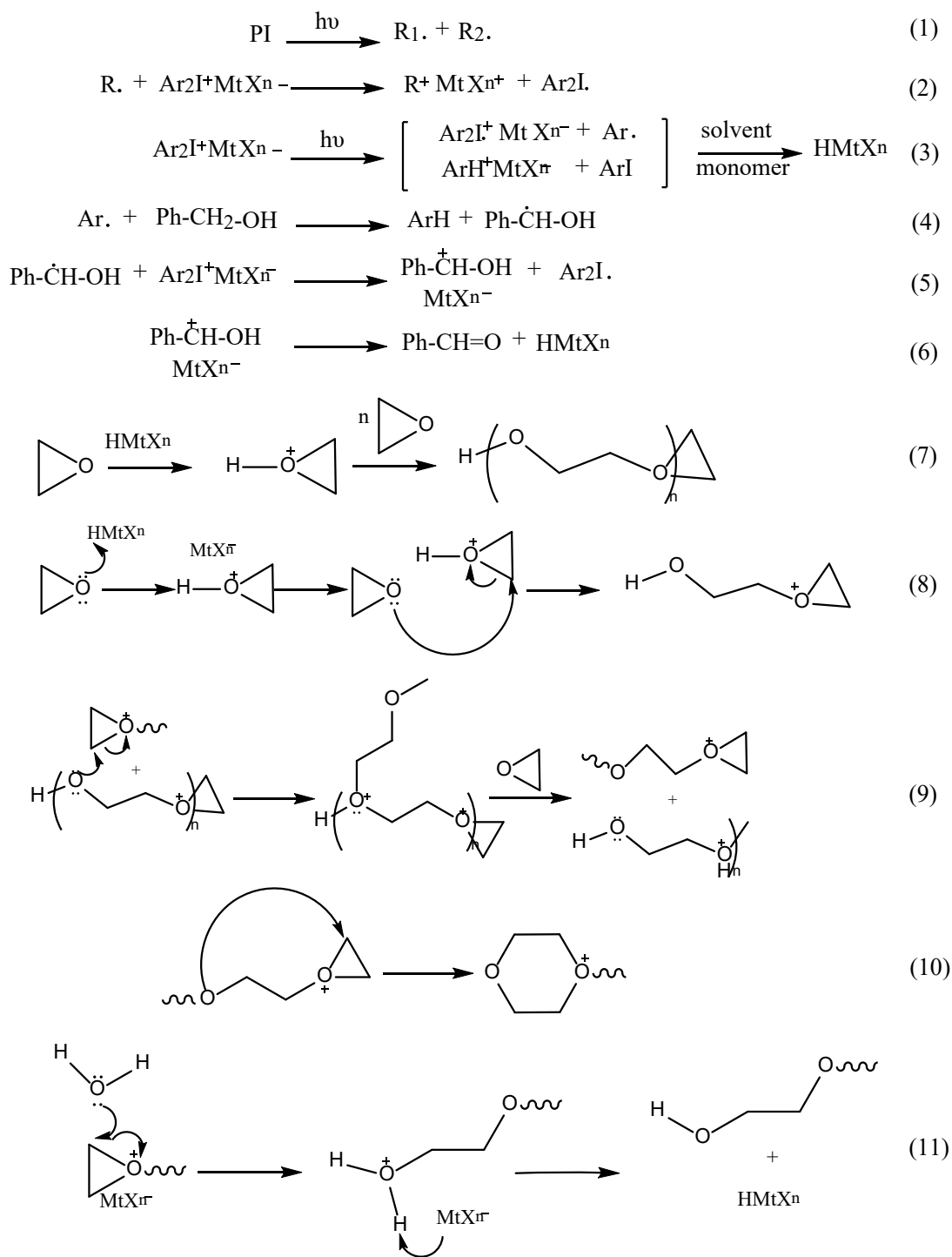


Figure 1.6 (1) and (2) show the generation of a cation R^+ assisted by a photosensitizer that produces radicals upon absorption of light. (3) Light absorption and proton abstraction of a monomer/solvent molecule by a diaryliodonium salt. (4), (5) and (6) show the reactions that are part of the mechanism to explain the acceleration of a photopolymerization reactions when alcohols are used with a diaryliodonium salt photoinitiator. (8) shows the propagation mechanism of ring-opening polymerization. (9), (10) and (11) show some of the reactions that lead to termination in ring-opening polymerization.

In addition to forming protonic acids when they react with solvents or monomers that can initiate polymerization, aryl radicals can abstract hydrogen atoms to form alkyl radicals (4) that can reduce diaryliodonium salts to produce α -hydroxybenzyl cations and diaryliodine radicals (5). A Brønsted acid (HMtX_n) is produced from the spontaneous deprotonation of α -hydroxybenzyl cations as well as the corresponding aldehyde (6). The Brønsted acid protonates the oxygen atom of an epoxide monomer starting ring opening polymerization (7). The propagation mechanism is shown in (8). In the case of ring opening polymerization, some transfer reactions such as inter- or intramolecular reactions become termination reactions when the majority of the monomer has been depleted. Alkylation is one example of intermolecular reaction that is general a termination step (9). A ring expansion produced by back-biting (10) and the reaction with some impurity as water are also possible (11).

1.4 Self-trapped beams

1.4.1 Self-trapping of coherent beams

The first demonstration of soliton formation was done in 1974 with a circular laser beam in sodium vapor as saturable nonlinear medium.⁴ The next demonstration was carried out in 1985 using liquid CS₂ as the nonlinear medium⁵³. It was originally thought that the formation of self-trapped beams was only possible using coherent sources^{54,55} since incoherent ones have random fluctuations that occur in the femtosecond time scale that are captured by instantaneous nonlinear media which were the kind of materials studied at the early stages of this field.^{18,56-62} As a result, incoherent beams break into small fragments in instantaneous nonlinear media. Therefore, having a nonlinear response slower (noninstantaneous) than the random fluctuations taking place in the incoherent beam is the main requirement to elicit self-trapped beams using incoherent light.⁶³ The first

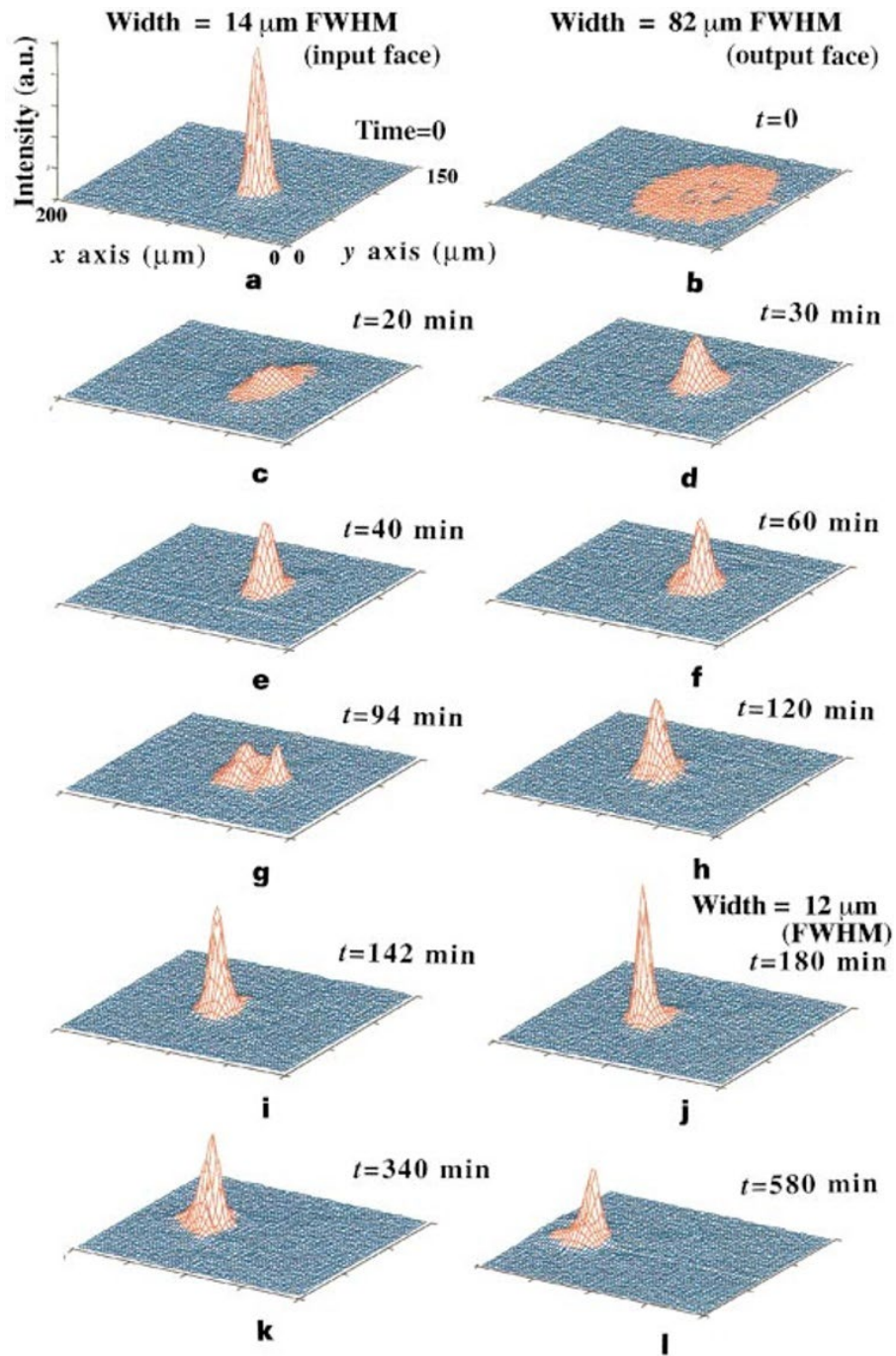


Figure 1.7 Time evolution of the 3-D intensity profile of an incoherent white beam traveling in a crystal. At $t = 0$ s, the width of the beam at the entrance and exit faces of the sample are 14 and 82 μm , respectively. After 180 min, the width of the beam at the exit face got reduced to 12 μm . Reproduced with permission from Mitchell, M.; Segev, M. Self-Trapping of Incoherent White Light. *Nature* **1997**, 387, 880-883 Copyright 1997, Macmillan Magazines Ltd.⁶⁵

demonstration of soliton formation was done with a partially incoherent laser beam in a photorefractive crystal in 1996 by Mitchel et al.⁶⁴ Since the response time (0.1 s for an intensity of 1 W/cm²) of photorefractive crystals can be controlled with the intensity of the beam, using low intensities allows an incoherent beam to self-trapped because it is perceived as uniform by the medium. Self-trapping of a totally incoherent white beam (temporally and spatially) was carried out one year after by the same group.⁶⁵ Experimental demonstration of self-trapping in a photorefractive crystal is shown in Figure 1.7. Photopolymers are another nonlinear media whose response can be tuned with the intensity of the propagating beam. Therefore, self-trapping can be obtained with different light sources. An example of self-trapping of a blue laser beam in a photopolymerizable medium is illustrated in Figure 1.8. Unlike photorefractive crystals, the refractive index changes in photopolymers are permanent. The propagation of laser beams in photopolymerizable media is an efficient method to obtain self-written waveguides.^{22,66-70} Figure 1.9 shows a polymer waveguide fabricated using light from an optical fiber. Such waveguide connects to another opti-

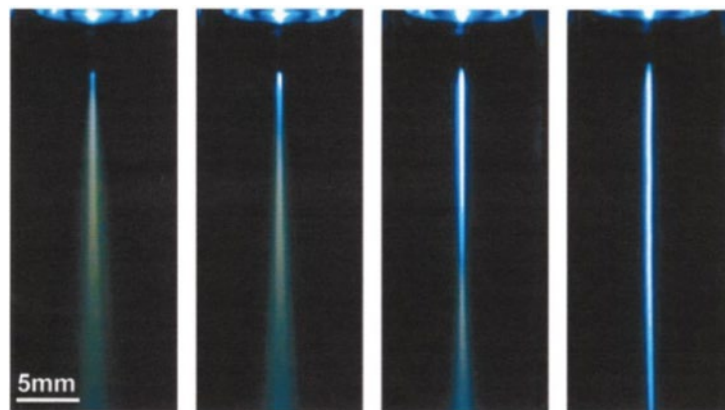


Figure 1.8. Evolution of the self-trapping process of a blue laser beam ($\lambda=488$ nm) in a photopolymerizable medium. As photopolymerization takes place, a permanent optical waveguide is formed in the medium with a core diameter of 100 μm and a length of 40 mm. Reprinted with permission from Kagami M.; Yamashita, T.; Ito, H. Light-induced self-written three-dimensional optical waveguide. *Appl. Phys. Lett.* 2001, 79, 1079–1081. Copyright 2001, AIP Publishing.⁷⁰

cal fiber. The acceptance angle of a self-written waveguide depends on the difference between the refractive index of the core and the cladding:⁷¹

$$\theta_A < \sin^{-1} \left(\sqrt{n_{core}^2 - n_{clad}^2} \right) \quad (1.8)$$

The modes that are supported in a waveguide also depend on the refractive index difference between core and cladding but also on the core size (a) and the wavelength of the light λ :⁷²

$$V = \frac{2\pi}{\lambda} a \sqrt{n_{core}^2 - n_{clad}^2} \quad (1.9)$$

When the parameter $V < 2.405$, only the fundamental mode is supported. Our group has studied the

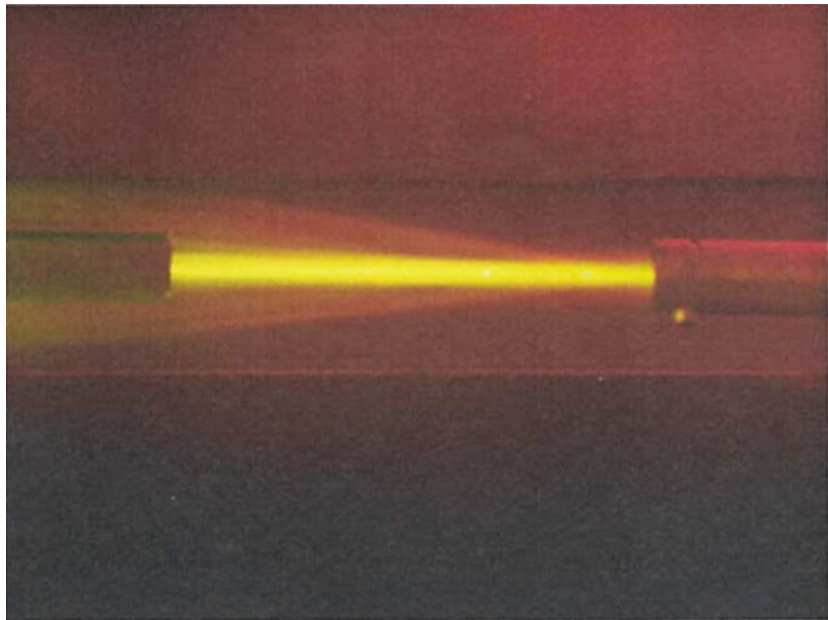


Figure 1.9 Polymeric waveguide obtained through photopolymerization by a self-trapped beam connecting two optical fibers placed 1 mm apart. Reprinted with permission from Dorkenoo, K.; Crégut, O.; Mager, L.; Gillot, F.; Carre, C.; Fort, A. Quasi-solitonic behavior of self-written waveguides created by photopolymerization. *Opt. Lett.* 2002, 27, 1782–1784. Copyright 2002 Optical Society of America.⁶⁸

propagation of coherent and incoherent light in different reversible and irreversible soft photochemical systems. We studied the propagation dynamics of a laser beam in an organosiloxane polymer over intensities ranging from 3.2×10^{-5} to 12732 W/cm^2 .⁷³ In this wide

range of intensities many phenomena can occur. At low intensities, from 3.2×10^{-5} to 1.6×10^{-2} W/cm^2 self-trapping is observed at early stages of the experiment. Figure 1.10A shows the self-trapping process of a laser beam at 1.6×10^{-2} W/cm^2 . During the first at the exit face to $26 \mu\text{m}$ while 3 seconds, a beam that is $20 \mu\text{m}$ at the entrance face and $118 \mu\text{m}$ at the exit face reduces its

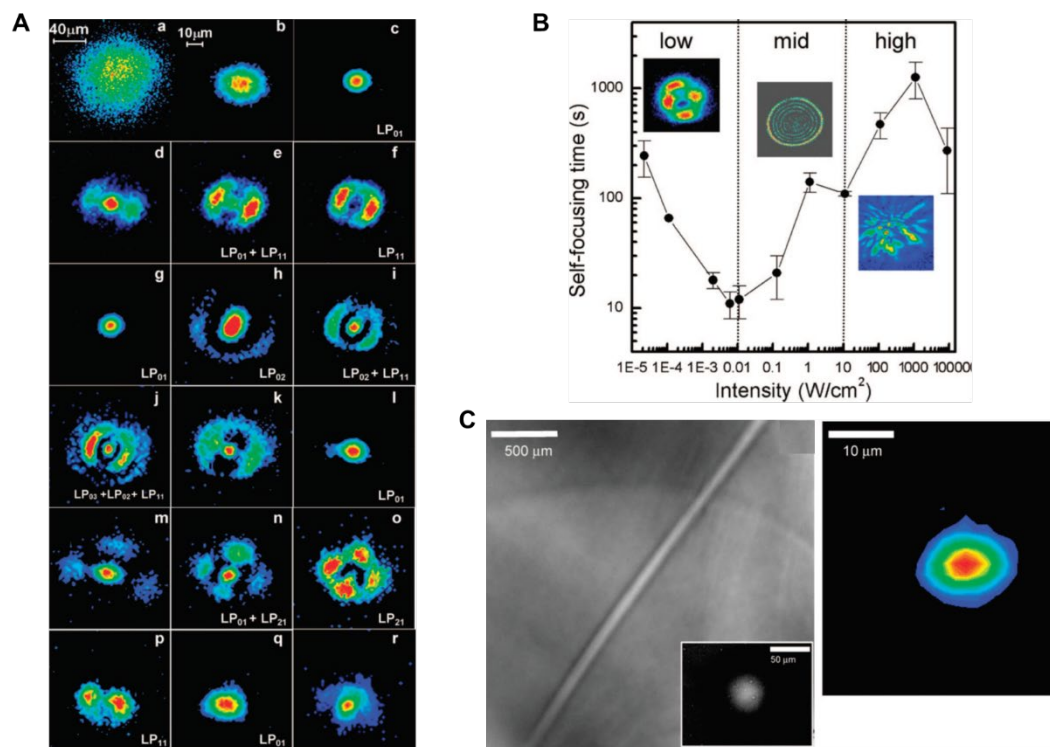


Figure 1.10 **A)** Temporal evolution at the exit face of the 2-D intensity profile of a green laser beam at 1.6×10^{-2} traveling through a sample 6 mm long that contains 3-(trimethoxysilyl)propyl methacrylate (left). Image (a) shows the 2-D intensity profile of the beam under linear conditions. Images (b)-(r) were acquired after 3 s, 27 s, 30 s, 30 s, 32 s, 35 s, 41 s, 47 s, 55 s, 57 s, 61 s, 116 s, 123 s, 129 s, 134 s, 141 s, 156 s and 163 s. **B)** Representation of the three typical results obtained at the three different intensity regimes observed during the nonlinear propagation of a green laser beam in the organosiloxane sample (Left). The low intensity regime is dominated by self-trapping. Self-diffraction rings and beam filamentation are observed at mid- and high intensities. **C)** Optical micrographs (x,z and x,y) of a waveguide obtained in a organosiloxane sample 6 mm long at 1.6×10^{-2} W/cm^2 . At the right, the 2-D intensity profile of a probe laser beam is shown. Reprinted with permission from Villafranca, A. B.; Saravanamuttu, K. An experimental study of the dynamics and temporal evolution of self-trapped laser beams in a photopolymerizable organosiloxane. *J. Phys. Chem. C* **2008**, 112, 17388–17396. Copyright 2008, American Chemical Society.⁷³

diameter while increasing its intensity from 0.133 to 0.46 mW/cm². The beam further narrowed down to 18 μm after irradiating the sample for 27 s. As the refractive index change increases over time, higher order modes are excited and clearly observed (LP₁₁, LP₀₂ and LP₂₁). These experiments confirmed the excitation of higher order modes in cylindrical waveguides and allowed their observation in real time. At medium intensities (from 19 x 10⁻² to 16 W/cm⁻²), diffraction rings emerged due to self-phase modulation. At high intensities (159 to 1.2732 x 10⁴ W/cm⁻²) the beam undergoes filamentation without self-focusing or self-trapping being observed. A representation of a typical result obtained at each intensity regime is shown in Figure 1.10B. The mechanism responsible for this filamentation is similar to modulation instability where the random noise in a broad beam becomes amplified by the nonlinearity which eventually leads to filamentation.⁷⁴ At intensities at which self-trapping is observed, a 3-D waveguide is permanently inscribed in the medium (Figure 1.10C). This approach can be extended to the fabrication of metallodielectric waveguides by doping this organosiloxane photopolymer with Ag nanoparticles.⁷⁵ The refractive index changes originated in this material not only induced self-trapping; attraction and spiraling are also observed when two non-coplanar gaussian beams are launched to the organosiloxane polymer.⁷⁶ Figure 1.11 shows the interactions of two beams labeled as A and B. In the absence of polymerization, the beams do not interact. Instead, they follow their original trajectories while broadening. Reversible self-trapping of a gaussian beam and spiraling as in the organosiloxane photopolymer is also possible in a hydrogel doped with NaI and Ru(bpy)₃Cl₂ in which the Δ*n* is originated by oxidation of I⁻ by [Ru(bpy)₃]²⁺ in the presence of light to produce I₃⁻ ions. Attraction and spiraling in these two systems are observed in the short-

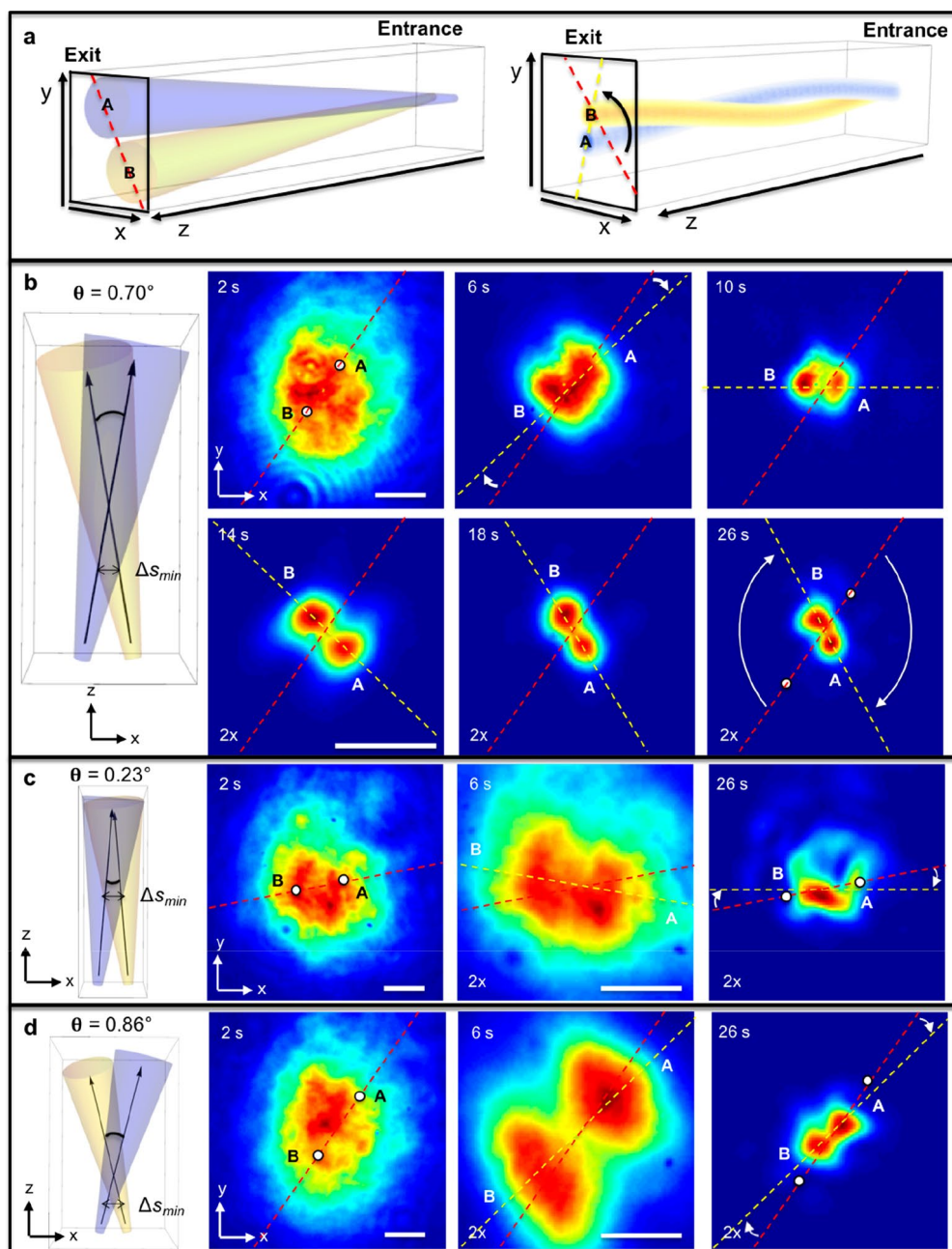


Figure 1.11 a) Representation of the linear propagation of a beam pair (A and B) under linear(left) and nonlinear conditions in which self-trapping and spiraling takes place. Time evolution of the beam output of the beam pair traveling through an organosiloxane sample at **b)** $\theta = 0.70^\circ$, **c)** 0.23° , and **d)** 0.86° . Centers of the beams under linear conditions are highlighted with white dots. The trajectories of each beam at these angles under linear conditions are shown at the left in b-d. Reprinted with permission from Morim, D. R.; Bevern, D.; Vargas-Baca, I.; Saravanamuttu, K. 3-D Spiraling Self-Trapped Light Beams in Photochemical Systems. *J. Phys. Chem. Lett.* **2019**, *10*, 5957–5962. Copyright 2019, American Chemical Society.⁷⁶

term range when the distance between beams is equal or smaller than the beams width which was $\sim 20 \mu\text{m}$ in these experiments. Most interactions between beams take place only when there is a significant overlap between their optical field. In most photopolymers, there are not interactions between self-trapped beams when the separation between them is four times the beam width.⁷⁷ Most interactions between self-trapped beams take place only when there is a significant overlap of their optical fields. Our group showed recently that long-range interactions among self-trapped

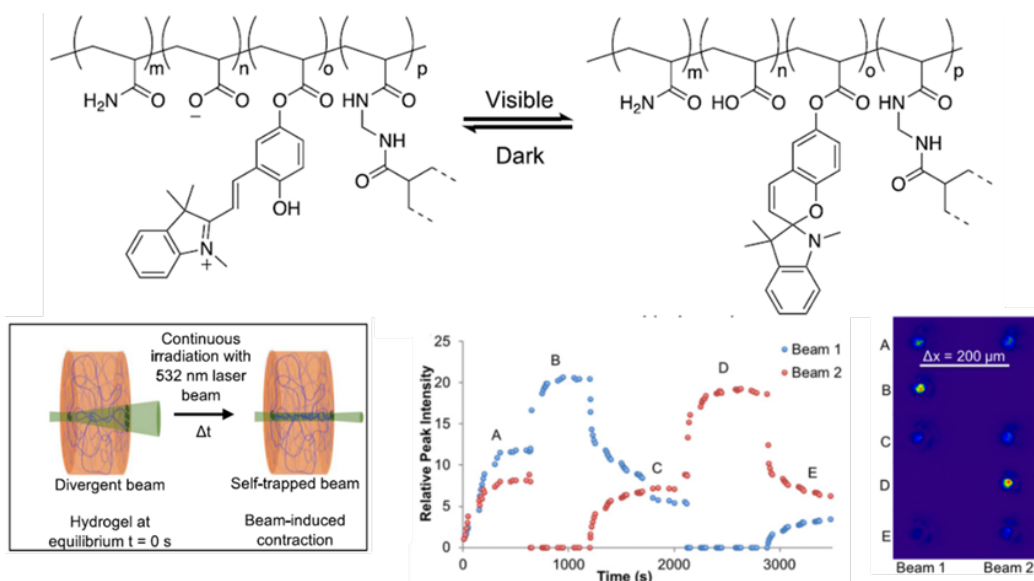


Figure 1.12. Photoisomerization reaction of merocyanine substituents in a methylenebis(acrylamide) cross-linked p(AAm-co-AAc) hydrogel. Upon absorption of visible light, the merocyanine moieties switch to their closed-ring spiropyran form (top). This chemical change increases the hydrophobicity in the irradiated area which causes the water in the irradiated zone to be expelled which leads to a contraction of the hydrogel network. The refractive index change originated by such contraction produces a temporal waveguide. The graph shows the peak intensities of two self-trapped beams separated by $200 \mu\text{m}$ while they interact remotely. The 2-D intensity profile of the beams at selected times is shown at the bottom right. When both beams are launched simultaneously, they self-trapped increasing their intensity (from an initial value of 1) to 12 and 9 (beam 1 and beam 2, respectively) with the final width of both beams being $\sim 40 \mu\text{m}$ (region A). When beam 2 was intentionally blocked, the intensity of beam 1 increased to 20 while its beam width decreased to $28 \mu\text{m}$ (region B). When beam 2 was launched again to the hydrogel, the peak intensity of beam 1 decreased to 5.3 while the size of the beam increased to $\sim 40 \mu\text{m}$ (region C). The opposite effect is observed when beam 1 is blocked and then reintroduced (region D). Reproduced with permission from Morim, D. R.; Meeks, A.; Shastri, A.; Tran, A.; Shneidman, A. V.; Yashin, V. V.; Mahmood, F.; Balazs, A. C.; Aizenberg, J.; Saravanamuttu, K. Opto-chemo-mechanical transduction in photoresponsive gels elicits switchable self-trapped beams with remote interactions. *Proc. Natl. Acad. Sci. U. S. A.* **2020**, 117, 3953-3959. Copyright 2020 National Academy of Sciences.⁷⁸

beams take place in a hydrogel polymer bearing merocyanine moieties that undergo an isomerization reaction that produces their closed-ring spiropyran form upon the absorption of visible light.⁷⁸ This change increases the hydrophobicity in the irradiated area which leads to the expulsion of water and contraction of the polymeric network in the irradiated area (Figure 1.12 top). A temporal waveguide is produced because of the refractive index change originated by this contraction (Figure 1.12 bottom left). When two beams (1 and 2) are launched simultaneously to this hydrogel with distances between beams at least ten times the beam's width, the extend of self-trapping of both beams is smaller than when each of them is launched individually (Figure 1.12 bottom right, region A in graph and in the 2-D intensity profile images). When beam 2 is removed, beam 1 increases its intensity and reduces its diameter (Figure 1.12 bottom right, region B). When beam 2 is reintroduced again, the intensity of beam decreases while increasing its diameter (Figure 1.12 bottom right, region C). This effect can be explained in the following way: since water is expelled due the isomerization reaction in the irradiated areas by both beams, opposing forces of expansion prevent the contraction in the irradiated areas to the same extend as when only one beam is traveling in the medium.

1.4.2 Self-trapping of incoherent beams

Self-trapping of incoherent light has also been extensively studied by our group in different photopolymers. Our first demonstration of this phenomenon was done in an organosiloxane photopolymer using white light.^{79,80} Figure 1.13 shows the time evolution of the intensity profile of a white beam with a 45 μm width at the entrance face generated with QTH lamp traveling in a sample 6 mm long. In addition to self-trapping, other interesting phenomena are elicited when an incoherent beam travels in a photopolymerizable medium such as modulation instability.⁸¹

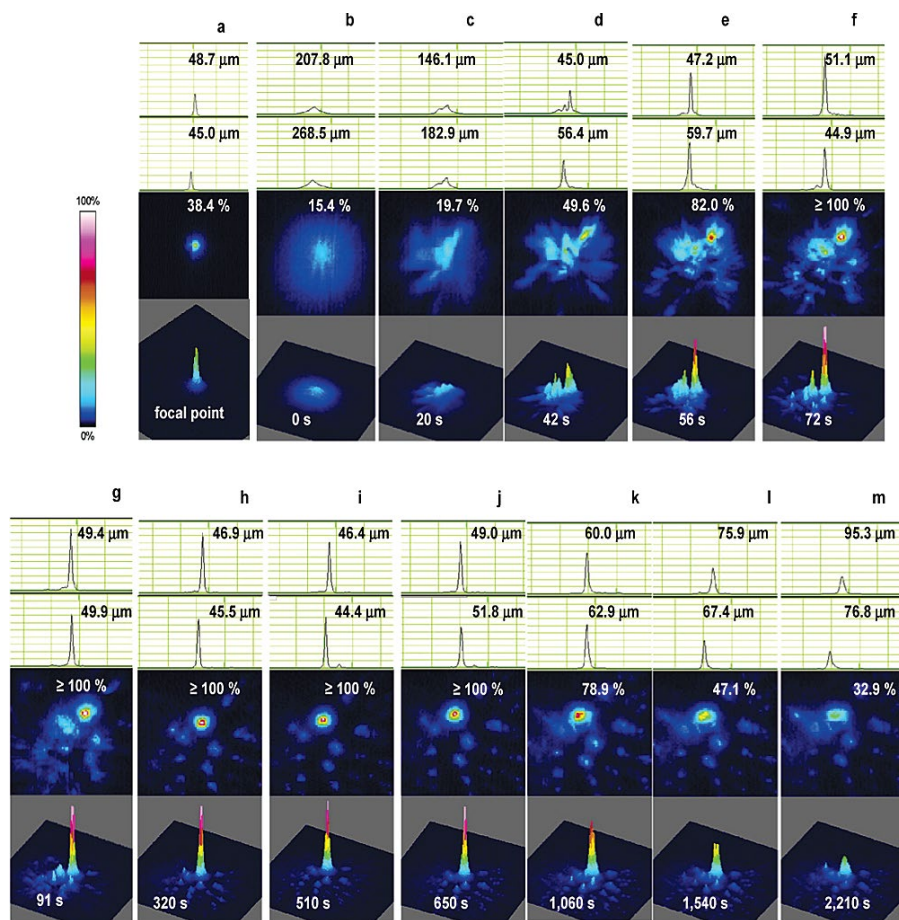


Figure 1.13 Time evolution of the 1-D, 2-D and 3-D intensity profiles of a white beam with a width of 45 μm at the entrance face traveling through an organosiloxane sample 6 mm long. Section **a** shows the intensity profile of the beam at the entrance face. Section **b** shows the intensity profile of the beam at the exit face of the sample under linear conditions. The size of the beam increases to 268.5 μm due to diffraction with a relative intensity of 15.4 %. As polymerization and the increase of refraction index takes place, there is a 5.4-fold decrease in the beam's width and at least a 6.5-fold increase in the intensity of the beam before it slightly widens at the end of the experiment. However, the width of the beam remained smaller than its value under linear conditions. Reprint with permission from Zhang, J.; Kasala, K.; Rewari, A.; Saravanamuttu, K. Self-trapping of spatially and temporally incoherent white light in a photochemical medium. *J. Am. Chem. Soc.* **2006**, 128, 406–407. Copyright 2006, American Chemical Society.⁷⁶

This phenomenon occurs when variations in the intensity of a beam leads to different rates of photopolymerization in the irradiated area. Regions with higher rates of polymerization have a

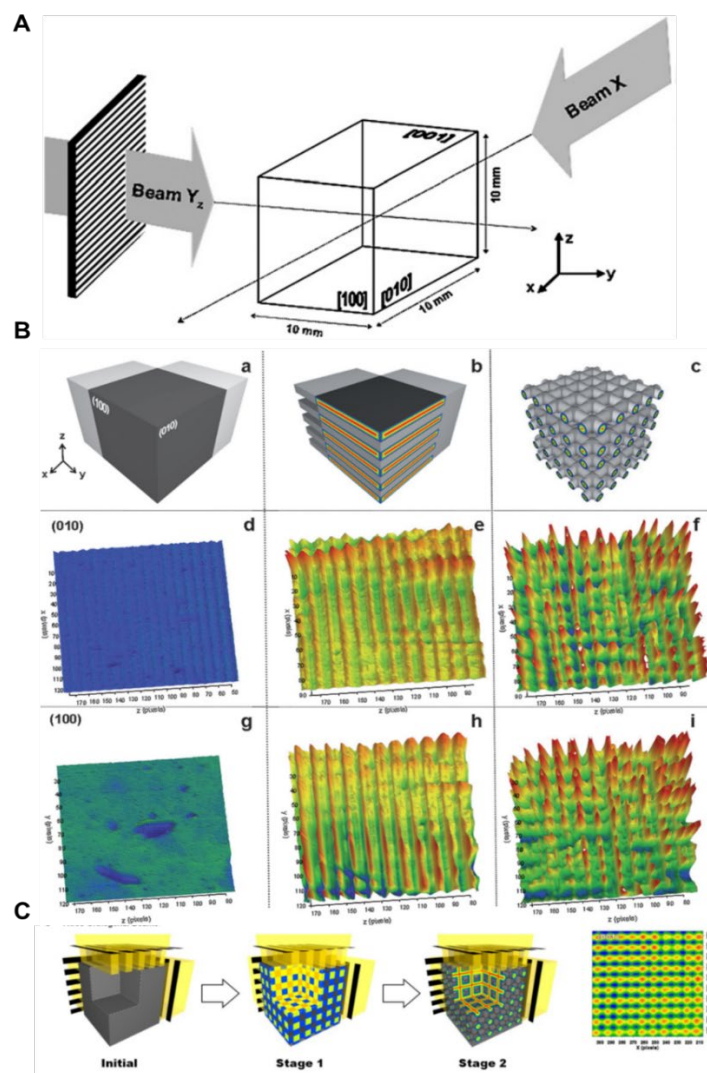


Figure 1.14 A Optical set up used to obtain a lattice by launching two orthogonal white beams to an organosiloxane sample. Capital letters show the direction of the beam propagation. The subscript in Y indicates the direction of the modulation. Only beam Y carried a modulation. The top images in **B** (a, b, and c) are a representation of the evolution of lattice formation. Under linear conditions, the modulation vanishes as the beam travels in the medium (a). Once the photopolymerization reaction takes place rectangular self-trapped filaments emerged (b) which eventually become unstable creating a lattice of self-trapped filaments (c). The bottom at **B** shows the time evolution of the experimental 2-D intensity profiles at the exit face of the lattice side in which the modulated beam is launched ([010] plane). **C** Scheme showing the fabrication of a lattices with primitive cubic symmetry using three perpendicular incoherent modulated beams. **A** and **B** were reprint (adapted) with permission from Burgess I. B.; Ponte M.; Saravanamuttu K. Spontaneous formation of 3-D optical and structural lattices from two orthogonal and mutually incoherent beams of white light propagating in a photopolymerisable material. *J. Mater. Chem.* **2008** 18, 4133–4139. Copyright 2008, ROYAL SOCIETY OF CHEMISTRY.⁸² **C** was reproduced with permission from Ponte, M. R.; Welch, R.; Saravanamuttu, K. An optochemically organized nonlinear waveguide lattice with primitive cubic symmetry. *Opt. Express* **2013**, 21, 4205-4214. Copyright 2013 Optical Society of America.⁸³

higher refractive index. Since light prefers to travel in regions of high refractive index, the beam eventually breaks into many filaments randomly oriented in space that behave themselves as self-trapped beams. Our group showed that is possible to create ordered lattices through modulation instability by using two orthogonal white light beams with one of them bearing a 1-D weak modulation (Figure 1.14A).⁸² The modulated beam produces an array of self-trapped rectangular beams that eventually transform into a 2-D array of filaments. Surprisingly, the second beam also creates a 2-D filament array despite not having any pre-seeded modulation. Poor alignment is observed when none of the beams are modulated. This is remarkable since both beams are mutually incoherent which makes interference impossible. Lattices with primitive cubic symmetry can be obtained by using three perpendicular incoherent beams in which each of them carries a weak 1-D periodic modulation.⁸³ These findings represent a significant reduction of complexity in the fabrication of 3-D photonic lattices since to obtain these kind of lattices 4 in-phase laser beams are required for such process. In addition to transferring patterns to orthogonal beams, it is also possible to encode data in lattices of this kind and perform binary arithmetic (addition and subtraction).⁸⁴ Periodic lattices with different geometries can be obtained using periodic amplitude masks that create well-defined periodic arrays of bright spots (Figure 1.15). In the following examples as well as in the fabrication of prisms with micro-waveguides embedded described in Chapter 2 and 3, the same periodic amplitude mask was employed. The first example consists of a free-standing square array of filaments obtained by launching a collimated white beam to a silicone-acrylate-based photopolymer that was patterned with the periodic amplitude mask described above.⁸⁵ The resulting arrays are flexible and can be compressed up to 70 % of the lattice periodicity while retaining waveguiding capacity. Slim polymer films with a radial distribution of cylindric waveguides can be obtained by launching a converging population of bright spots that

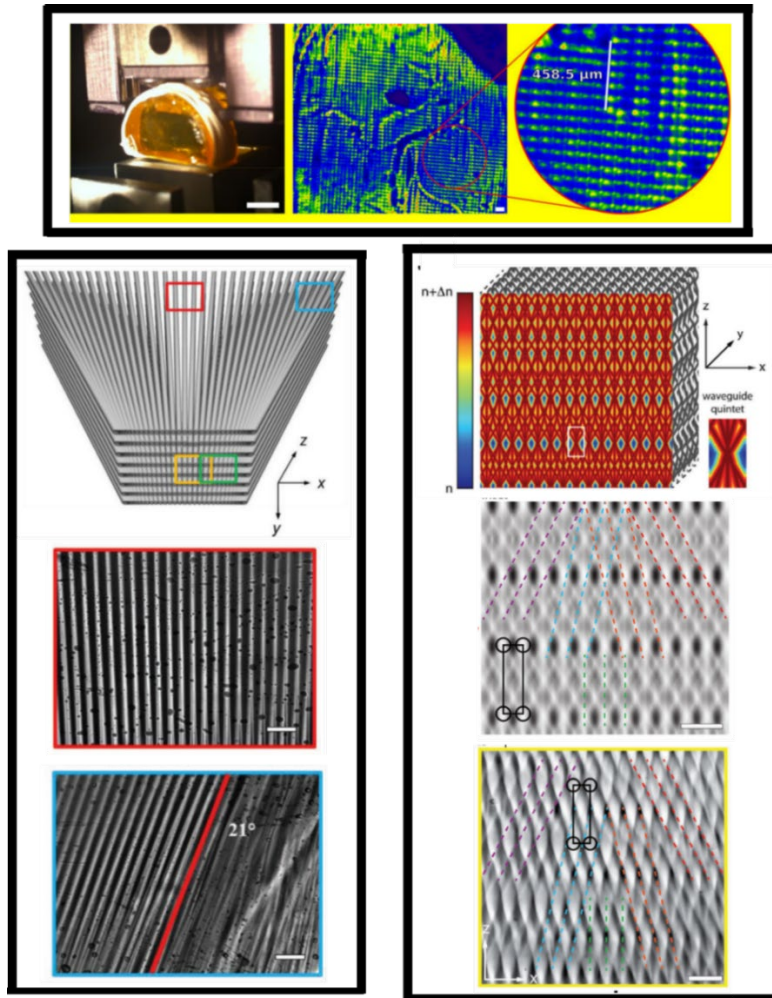


Figure 1.15 Free-standing array of flexible square lattice of micro-waveguides made of a silicone-based acrylate polymer. Reprinted with permission from ref. 85. Copyright 2018 WILEY-VCH Verlag GmbH & Co. KGaA, Weinheim.⁸⁵ Scheme of a polymer film with a radial distribution of micro-waveguides that focuses light or increases its divergence depending on its orientation. These films possess a field of view of 115° for wavelengths in the visible spectrum. Optical micrographs obtained through transmission microscopy of the highlighted red and blue area in the scheme of the polymer film are shown at the middle and bottom in the left rectangle. Reprint with permission from ref. 86. Copyright 2019 WILEY-VCH Verlag GmbH & Co. KGaA, Weinheim.⁸⁶ 3-D lattice fabricated by launching five beams from different orientations. The top image in the rectangle at the right shows a representation of the resulting intersecting lattice while the bottom images show micrographs of such lattice. Reprint with permission from ref. 87. Copyright 2018 WILEY-VCH Verlag GmbH & Co. KGaA, Weinheim.⁸⁷

create a radial distribution of cylindrical waveguides which gives these films a field of view (FOV) of 115° for all visible wavelengths.⁸⁶ Depending on the orientation of the film, they can increase the divergence of a LED or cause the beam to focus. 3-D lattices with higher complexity capable

of performing multiple operations can be obtained by launching 5 collimated beams from different angles.⁸⁷ Each square spot in the amplitude mask produces five micro-waveguides that intersect multiple times without any cross-talking observed among them. Such intersecting geometry not only gives this film a panoramic field of view of 120° but also the ability to perform divergence free transmission, focusing and inversion. In all these examples, the entire sample is polymerized. The fabrication process usually takes several minutes. In this thesis, improvements to the photopolymers are presented that make the fabrication of these lattices possible within seconds and with well-defined shapes that do not require polymerization of the whole sample (molding).

1.5 Volumetric 3-D printing

3-D printing was introduced for the first time by Charles W. Hull in the 1980s.⁸⁸ The new technology immediately attracted the attention of the automotive industry to accelerate design cycles since time-to-market was extremely slow at that time. Since then, several techniques have been developed including inkjet printing, fused depositing modeling, selective laser sintering and stereolithography.⁸⁹ Most of these techniques are based on a layer-by-layer approach. These processes create objects with resolutions ranging from 1 to 100 μm .⁹⁰ However, printing times usually require hours. In addition to being a time consuming process, the presence of layers, introduces fracture planes that make these objects mechanically unstable.^{91,92} Support structures are generally required during the printing process as well. A huge improvement in terms of speed was achieved by a method termed continuous liquid interface production of 3D objects (CLIP).⁹³ The set up used for CLIP is similar to the one used in a bottom-up stereolithographic printer but includes a permeable membrane at the bottom that allows a flux of oxygen to the resin which creates a “dead” zone to inhibit polymerization at the bottom of the bath. Above this dead zone, a

slice of the object is cured by projecting a UV pattern. The layer thickness can be controlled by the intensity used, irradiation time, photoinitiator coefficient, and resin absorption coefficient. Once this layer is cured, the built support plate with the incomplete object is pulled out of the resin. New resin fills the space left and a new layer is cured in a nonstop fashion producing seamless objects at a faster rate (500 mm/hour) than traditional stereolithography (few mm/hour). A similar approach is known as volumetric polymerization inhibition patterning.⁹⁴ In this case, two different light sources are used simultaneously. A UV light source is responsible for activating an inhibitor near the transparent window at the bottom of the bath that creates a dead zone similar to the oxygen inhibition zone in CLIP. Unlike the dead zone created in CLIP that is ten of micrometers thick, the dead zone created in polymerization inhibition patterning can be in the hundreds of micrometers. Having a higher dead zone allows a faster resin flow below the object that is being printed without sacrificing printing speed and it is particularly important when using resins with high viscosity. This method can achieve printing speeds of 2000 mm/h. Another method that uses two light sources to create 3-D objects is xolography.⁹⁵ In this case, a photoswitchable initiator is employed. Upon absorption of UV light, the photoinitiator is taken from a dormant state to a latent state with a half-lifetime of 6 s that is capable of initiating free-radical polymerization in the presence of a coinitiator (Figure 1.16, top rectangle). The printing process is carried out in the following way using a horizontal configuration: a UV light sheet is generated within the vessel that contains the resin by focusing a diverging beam that was previously collimated. In the irradiated area, the photoinitiator, a spiropyran molecule that absorbs only in the UV region, is converted to its merocyanine form. This molecule has a strong absorption in the visible region. Orthogonal from the “latent” sheet produced by the first wavelength, a projector generates visible light images that are focused within the latent sheet. In combination with a coinitiator, the merocyanine form

triggers polymerization upon absorption of visible light in this cross-section. A movie of images is launched to this spot while a linear stage moves the vessel away from the visible light source until the whole object is printed. The resolution obtained by this technique is 25 μm in the x and y directions and 50 μm in the z direction. Methods that do not involve continuous layering but instead instantaneous solidification of the resin into the desired object have also been demonstrated. One of them is based on the superposition of three orthogonal laser beams patterned using holographic beam shaping.⁹⁶ The superimposed intensity profile accumulates simultaneously reaching the required dose distribution to deplete the oxygen dissolved in the resin initially and then to trigger photopolymerization (Figure 1.16, left rectangle). Volumetric printing can be achieved using the same principles that governed computed tomography; an imaging technique widely used in medicine (Figure 1.16, right rectangle). In this technique, cross-sectional images are obtained after x-rays are absorbed by different tissues.⁹⁷ The information obtained is used either for diagnosis or therapy. A reversed process known as intensity modulated radiation therapy is used for cancer treatment.⁹⁸ A volume targeting a tumor is irradiated with a critical dose to eliminate it while minimizing the intensity in the healthy areas. The same principle can be used for 3-D printing. This method is known as Computed Axial Lithography (CAL).⁹⁹ 3-D objects are obtained by launching a movie of images that reconstruct the digital 3-D model to a rotating vessel that contains the photopolymer. Such images are retrieved from a standard stereolithography file format (.stl) The free radicals generated initially are consumed by the oxygen present in the medium. Once the resin has been exposed by every angle, a critical dose threshold is achieved which leads to depletion of the local oxygen and the solidification of the resin with the shape of the target object. The resolution of CAL (300 μm) can be improved by using a feedback system

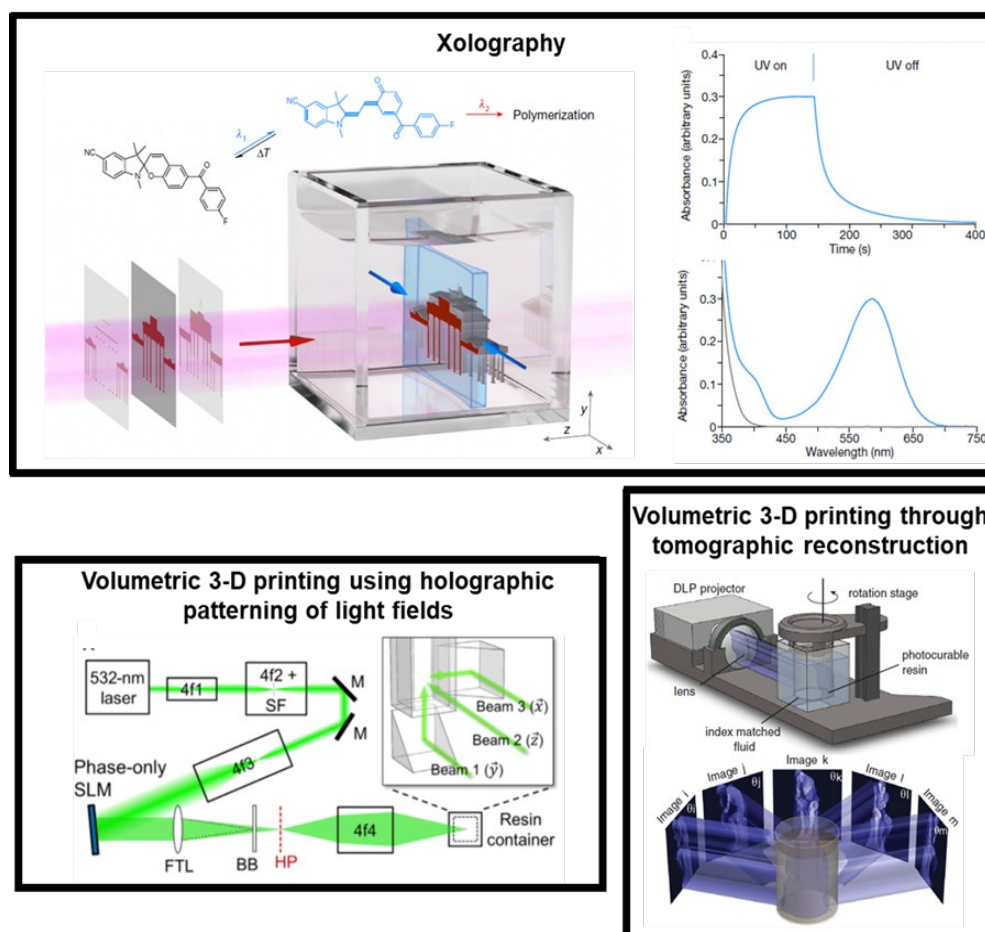


Figure 1.16. The top rectangle shows the two processes the photoinitiator undergoes to trigger free radical polymerization. The first step consists of absorption of UV light to form a latent state with a lifetime of 6 s. The graph at the top shows the photoswitching kinetics. Irradiation for 145 s generates the latent state. Once the UV light is removed, the latent state decays with a lifetime of 6 s. The graph at the bottom shows the absorption spectrum of the photoinitiator in its spiroiran (black line) and merocyanine form (blue line). A representation of the set up used in xolography is shown at the bottom left. The blue area represents the sheet in which solidification takes place. Reprinted with permission from ref. 95. Copyright 2020, Springer Nature Limited.⁹⁵ Bottom left rectangle: Set up used in holographic volumetric 3-D printing. Three orthogonal patterned beams generated using subregions of an image were launched into the sample using 45° mirrors. A spatial light modulator was used to create the image. The 3 beams intersected inside the bath to form the target object. Reprinted with permission from ref 96. Copyright 2017, American Association for the Advancement of Science. Bottom right rectangle: Set up used for Computed Axial Lithography printing. It consists of a Digital Light Projector, and a rotating stage immersed in a fluid. Reprint with permission from ref. 99. Copyright 2019, American Association for the Advancement of Science.

that consists of a camera placed perpendicular to irradiation source that monitors the rotating vessel while getting images during the printing process.¹⁰⁰ The image provide useful information to improve the resolution since they show the order in which each part of the object solidifies. Such information is used to stop the illumination of parts that are already formed or to increase the light dose in areas that take longer to cure. High resolution is achieved by printing an object a second time using the information obtained from a first print. CAL has been applied to obtain hydrogel cell-laden tissue constructs¹⁰¹ and has also been extended to thiole-ene formulations in addition to acrylate-based resins.¹⁰² The first volumetric approach was proposed by our group in 2016. We termed this method 3-D Nonlinear inscription of complex micro-components (3D NSCRIPT).³² The basic 3-D unit operation in this technique consists of launching a LED beam that is patterned with an amplitude mask. The beam inscribes a polymeric structure in a continuous way without layering artifacts as illustrated in the fabrication of the cone in Figure 1.17 (top rectangle). Objects with higher complexity in situ can be obtained by launching two counter-propagating beams. The cup in the rectangle at the bottom in the same figure was obtained this way. Each beam carried the same cross-sectional profile. However, one of the beams carried a dark circular area that was generated by blocking the beam at the center. This leads to an unpolymerized volume in the middle of the cup. When the structures generated by each beam fused, a cup with the respective hole in the middle was created. Metal nanoparticles can be incorporated in situ to the printed objects. Salts containing the desired metal can be reduced in the medium upon exposure to light. The dark colour of the gear in Figure 1.17 is originated by the presence of Au nanoparticles which were incorporated by adding H₂AuCl₄ to the resin. This salt was reduced to Au nanoparticles by the radicals generated by the photoinitiator (camphorquinone) in the presence of the hydrogen donor

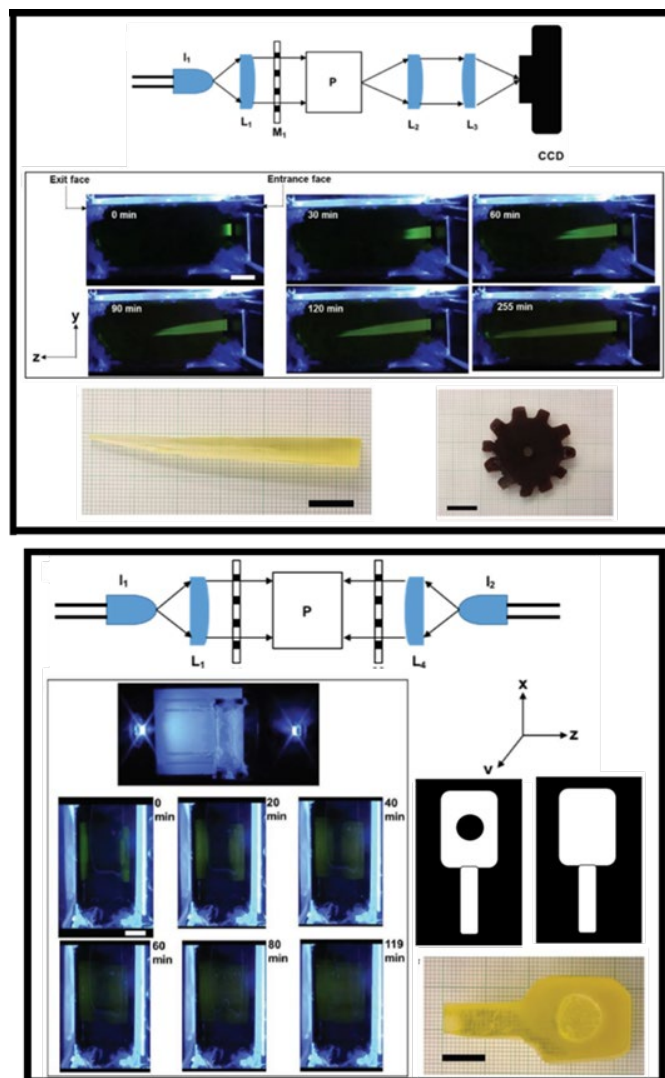


Figure 1.17. Optical set up employed in 3D NSCRIP. A blue LED beam (I_1) is collimated by a planoconvex lens and then launched to an amplitude mask placed at the entrance face of a sample cell that contains the resin (P). The rest of the set up consists of a pair of planoconvex lens and a CCD camera used to monitor the intensity profile of the beam. Time evolution of the printing process of a cone monitored through side view pictures (middle). The resulting cone after being isolated and polished is shown at the bottom left. The gear at the bottom right was obtained in the same manner but using an amplitude mask that produces a beam with cross sectional profile of the gear. HAuCl_4 was added to the resin that, upon irradiation, produces gold nanoparticles. **b** Optical set up used to print the cup shown at the bottom right. Two counter-propagating beams were launched simultaneously to the sample, each of them patterned with the amplitude masks shown at the right. Each of the beams acquired the shape of the white area in the amplitude mask. The time evolution of the printing process of the cup was monitored by imaging the sample cell from the top of the set up. Reprinted with permission from Basker, D. K.; Cortes, O. A. H.; Brook, M. A.; Saravanamuttu, K. 3D Nonlinear Inscription of Complex Microcomponents (3D NSCRIP): Printing Functional Dielectric and Metallodielectric Polymer Structures with Nonlinear Waves of Blue LED Light. *Adv. Mater. Technol.* **2017**, 2, 1600236-n/a. Copyright 2017 WILEY-VCH Verlag GmbH & Co. KGaA, Weinheim.

poly(1,4 butanediol). This clearly shows that we can incorporate different properties or functionalities by adding to the formulation the right compound or precursor. In addition to the gear and the cup, we printed all the components of the da Vinci catapult using a single amplitude mask. We assembled all these parts to create a working catapult. Although this was an excellent proof of concept, the process was lengthy due to the slow polymerization rate in cationic polymerization reactions (Figure 1.18). For example, the cup was obtained in almost two hours even though two different light sources were used simultaneously.

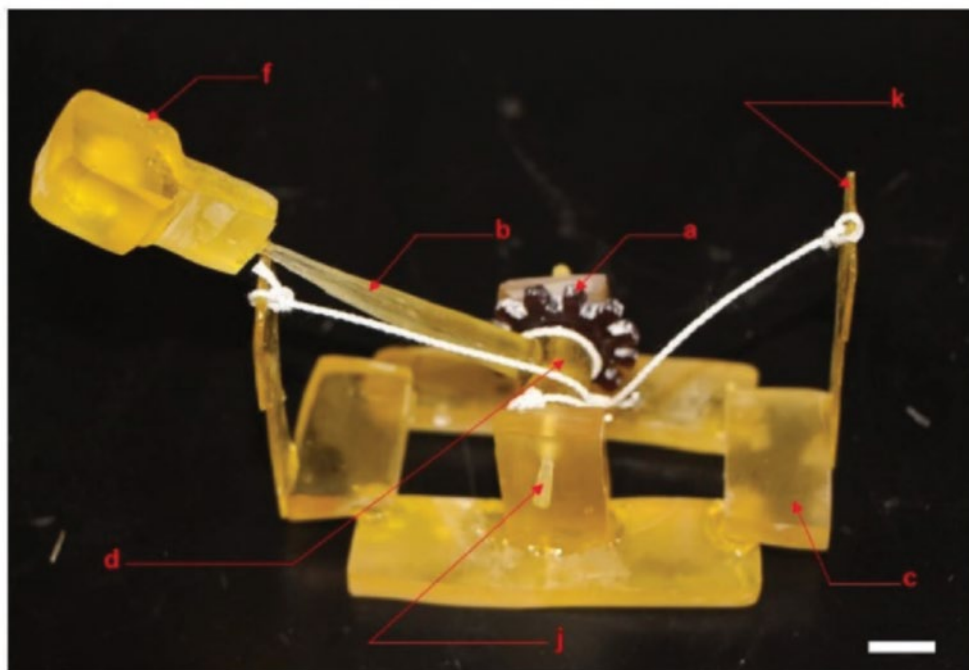


Figure 1.18 Assembled catapult. All the components were obtained through 3D NSCRIPT except for the tension spring (k). Reprinted with permission from Basker, D. K.; Cortes, O. A. H.; Brook, M. A.; Saravanamuttu, K. 3D Nonlinear Inscription of Complex Microcomponents (3D NSCRIPT): Printing Functional Dielectric and Metallodielectric Polymer Structures with Nonlinear Waves of Blue LED Light. *Adv. Mater. Technol.* **2017**, *2*, 1600236-n/a. Copyright 2017 WILEY-VCH Verlag GmbH & Co. KGaA, Weinheim.

Therefore, photopolymers based on cationic polymerization only are not a viable choice for practical applications. Solution Mask Liquid Lithography (SMaLL) is a similar approach in the sense that also employs LED sources to induce continuous inscription of polymeric structures, but

photochromic molecules are used to improve the printing resolution.¹⁰³ When the sample is irradiated, light is absorbed by the photochromic molecules in the medium at the entrance face of the vessel. Therefore, not photopolymerization is initiated at early stages. However, the photochromic species undergo a transformation from an absorbing state to a non absorbing state. As this transformation takes place, photopolymerization is initiated in a continuous way in the same way that occurs in 3D NSCRIPT. This process was also demonstrated with moving parts. However, only simple geometries were fabricated. In addition to printing macroscopic objects,

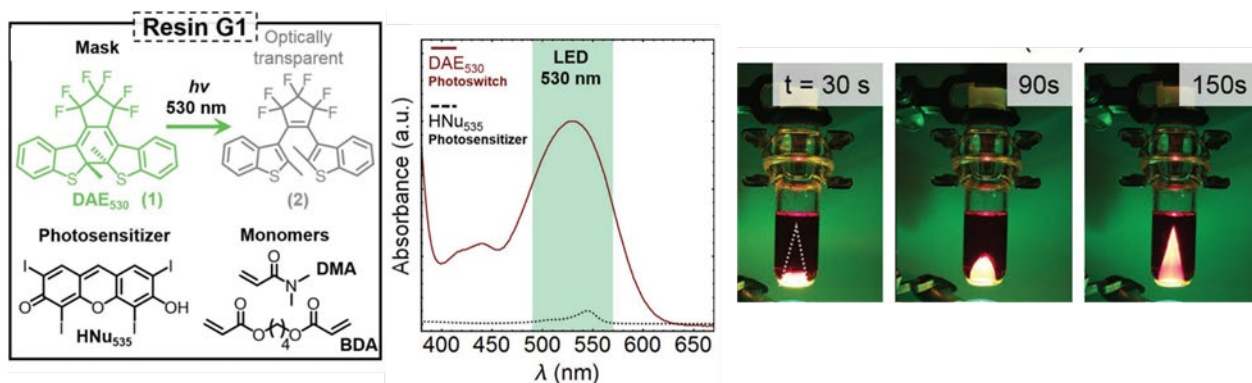


Figure 1.19 Components of Resin G used in SMA_{LL}(left). The ring-opening reaction of the photochromic molecule (DAE530) used in this method produces an optically transparent solution upon absorption of visible light ($\lambda = 530 \text{ nm}$). The masking effect is clearly observed in the absorption spectra in the middle. Before the ring opening reaction of the photochromic molecule takes place, the absorption of the solution is dominated by the former. After this transformation, light can be absorbed by the photosensitizer. Printing process of a cone through the SMA_{LL} principle (right). Reprint with permission from ref. Dolinski, N. D.; Page, Z. A.; Callaway, E. B.; Eisenreich, F.; Garcia, R. V.; Chavez, R.; Bothman, D. P.; Hecht, S.; Zok, F. W.; Hawker, C. J. Solution Mask Liquid Lithography (SMaLL) for One-Step, Multimaterial 3D Printing. *Adv. Mater.* **2018**, *30*, 1800364. Copyright 2018 WILEY-VCH Verlag GmbH & Co. KGaA, Weinheim.

our group has also shown that periodic microscopic features such as arrays of micro-waveguides can be embedded in polymers using nonlinear waves.⁸⁵⁻⁸⁷ These arrays are fabricated by polymerizing the whole sample. A particular shape to the final polymer monolith can only be given by using a mold. Additionally, the fabrication of these arrays is usually carried out at low intensities ($1\text{-}17 \text{ mW/cm}^2$) since the whole sample is polymerized and no micro-features are observed when

higher powers such as the ones in 3D NSCRIPT are used. Microscopic objects and nanometric features have also been obtained through two-photon polymerization.¹⁰⁴ However, it is still mostly limited to laboratory setups rather than real life applications since the printing times are slow for most practical applications ($1\text{-}20\text{ mm}^3\text{h}^{-1}$).^{105,106}

1.6 3-D printing with functional materials

In addition to create objects with high resolution and mechanical stability in a short period of time, another goal of 3-D printing is to create functional objects that can be integrated into working devices. Different variations of this approach have emerged such as the creation of 3-D objects using magnetic inks,¹⁰⁷⁻¹⁰⁹ conductive inks,¹¹⁰⁻¹¹² thermo-responsive materials,^{113,114} metals,^{115,116} and fluorescent inks.¹¹⁷ For example, chemical reactors have been fabricated using metal 3-D printing (Selective Laser Sintering).¹¹⁶ A frequency tunable patch antenna was obtained through inkjet printing using an iron oxide nanoparticle-based magnetic ink.¹⁰⁸ The same technique was used to print a capacitive touch sensor that acted as a computer mouse from a stretchable composite ink made of Ag flakes, silicon rubbers and a solvent.¹¹⁸ Electronic circuits, electrodes, and even a soft neural probe were printed using the conductive polymer poly(3,4-ethylenedioxythiophene: polystyrene sulfonate (PEDOT:PSS)).¹¹⁰ Combining different functional inks have also been done to 3-D print quantum-dot light-emitting diodes (QD-LEDs).¹¹⁷ In addition to this, objects made of soft materials with the ability to deform has also been obtained using shape memory alloys¹¹⁹, inorganic and polymer piezoelectrics^{120,121}, liquid crystal elastomers¹²²⁻¹²⁵, dielectric elastomers^{126,127}, ionic electroactive polymers^{128,129}, shape memory polymers¹³⁰⁻¹³², hydraulics^{133,134} and pneumatics^{135,136}, and hydrogels.¹³⁷⁻¹⁴³ Hydrogels are polymers that are capable of incorporating large amounts of solvent within their network. Because of this ability to incorporate a solvent such as water, some functionalities can be easily incorporated by dissolving

species of interest such as salts¹⁴⁴ or charged nanoparticles¹⁰⁹ to make them conductive or dyes to incorporate fluorescence.¹⁴⁵ Additionally, hydrogels are flexible and can be biocompatible which makes them great candidates the fabrication of artificial skins^{146,147}, optical waveguides that can be incorporated into the human body^{148,149}, and artificial organs.^{101, 150-152}

1.7 Electroactive hydrogels

As mentioned above, hydrogels can also deform in response to some stimuli such as changes in temperature¹⁵³, heat^{154,155}, pH¹⁵⁶⁻¹⁵⁸, magnetic^{159,160} and electric fields.^{145,146,161,162} In order to have a strong response to electric fields, the polymeric network of hydrogels has to have charged monomers. Since some hydrogels respond to electric fields, they have been proposed for the fabrication of artificial muscles¹⁶² and electroactive soft robots.^{144,160} These soft robots are only show unidirectional motion towards the position of one of the electrodes. Hydrogels with positively charged monomers bend towards the another while negatively charged networks bend towards the cathode. When an electric field is applied to a charged hydrogel in solution, the counterions within the hydrogel are the ones responsible for transporting the current inside the gel because of its permselectivity to counterions. The hydrogel used in this work is negatively charged. Therefore, only cations are transporting the current within the hydrogel In the solution near the gel surface facing the cathode, there is a depletion of positively charged ions which creates a higher osmotic pressure on the anode side of the gel than in the cathode side giving as a result swelling on the anode side and deswelling on the cathode side (Eq. 1.10). A positive pressure difference (Eq. 1.11) is created which makes the gel bend towards the cathode :¹⁶⁹

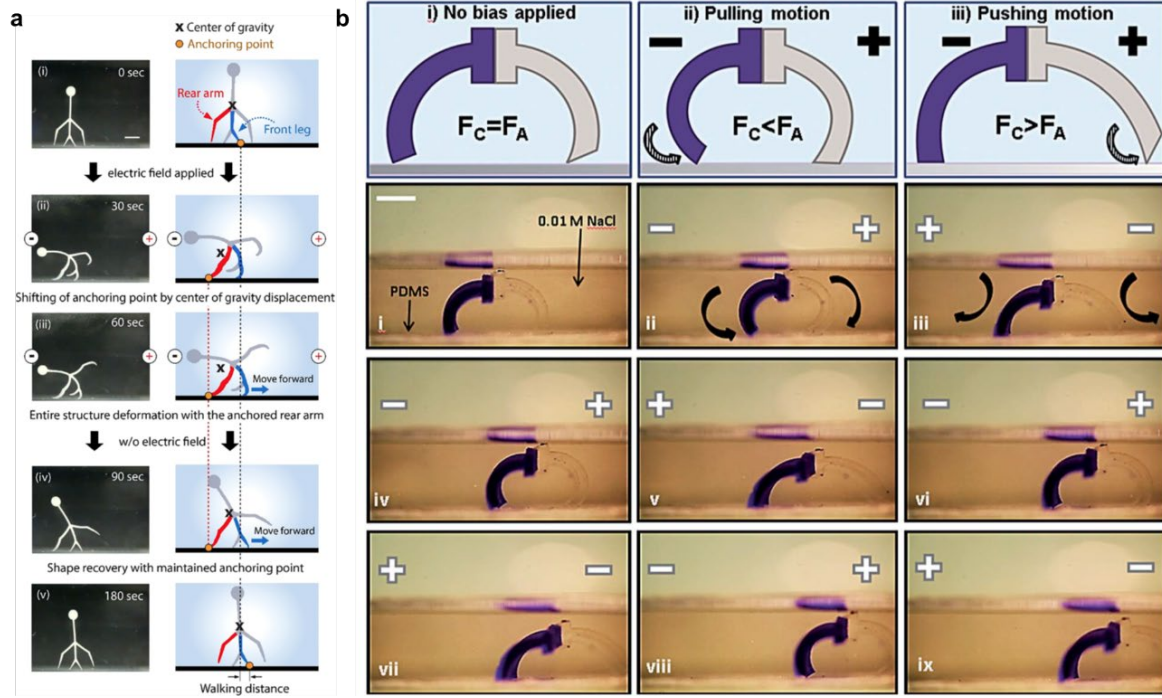


Figure 1.20 a) “Walker” robot made of negatively charged monomers under the effect of an electric field. Reprinted with permission from ref. Han, D.; Farino, C.; Yang, C.; Scott, T.; Browe, D.; Choi, W.; Freeman, J. W.; Lee, H. *Soft Robotic Manipulation and Locomotion with a 3D Printed Electroactive Hydrogel*. *ACS Appl. Mater. Interfaces* **2018**, 10, 21, 17512-17518. Copyright 2018, American Chemical Society.¹⁴⁴ b) Walking robot made of two legs. The purple leg is made of a hydrogel with positively charged monomers (right) while the grey leg (left) contains negatively charged monomers. In the initial configuration, the cathode is next to the positively charged hydrogel while the anode is next to the anionic hydrogel. Once an electric field is applied, both legs bend inward in opposite directions. The whole system moves toward the right since the anionic leg has a larger surface area than the cationic counterpart. Reversing the fields stretches the anionic leg toward the cathode while the cationic leg moves towards the anode but to a lesser extent due to its higher friction force with the substrate which results in unidirectional motion of the two-leg robot. Reprinted with permission from ref. Morales, D.; Palleau, E.; Dickey, M. D.; Velev, O. D. *Electro-actuated hydrogel walkers with dual responsive legs*. *Soft Matter* **2014**, 10, 1337. Copyright 2014, Royal Society of Chemistry.¹⁶⁰

$$\pi_{ion} = RT \sum_i (C_i^h - C_i^s) \quad (1.10)$$

$$\Delta\pi_{ion} = \pi_1 - \pi_2 \quad (1.11)$$

Where π_{ion} is the osmotic pressure difference at an interface hydrogel-solution, R is the ideal gas constant, T is the temperature, C_i^h is the concentration of ions inside the gel and C_i^s is the

concentration of ions in the solution outside the gel. The osmotic pressure difference between both interfaces ($\Delta\pi_{ion}$) is obtained by subtracting the osmotic pressure of the cathode (π_2) from the one of the anode (π_1). Based on a three-point test, such pressure difference is equal to the maximum tensile strength σ :^{160,161}

$$\Delta\pi_{ion} = \sigma = 6DEY/L^2 \quad (1.12)$$

Where D and L are the thickness and the length of the gel, E is the Young modulus and Y is the degree of bending (the difference between the distance of the hydrogels ends before and after bending). When the electric field is removed, the hydrogel returns to its original position over time. If the polarity of the electrodes is inverted, the bending takes place in the opposite direction. Bending an electroactive hydrogel from one direction to another can be done over multiple cycles until some irreversible changes start to be observed due to cyclic fatigue damage.¹⁶³ Even though the sample might not completely fracture, some of its properties might change irreversibly. The hydrogel waveguides described in ref. 148 and 149 are biocompatible and biodegradable which makes them excellent candidates for light-based-therapies inside the human body such as drug release, to trigger migration of cells and photocleavage chemical reactions. Optical fibers can perform complex motions and deliver light towards specific target areas when incorporated into a continuum soft robot.¹⁶⁴ Navigation of such robot was demonstrated in a tortuous cerebrovascular phantom with multiple aneurysms. However, the fabrication process of such robot is rather complex. Since our printing method produces a polymeric waveguide in each step, we used a precursor of an electroactive hydrogel to produce electroactive waveguides that can be controlled remotely. Actuation of electroactive hydrogels mostly involves bending or displacement from right to left or viceversa. For this reason, we built an array of electrodes that makes possible to combine electric fields to bend waveguides towards specific directions and to make them rotate.

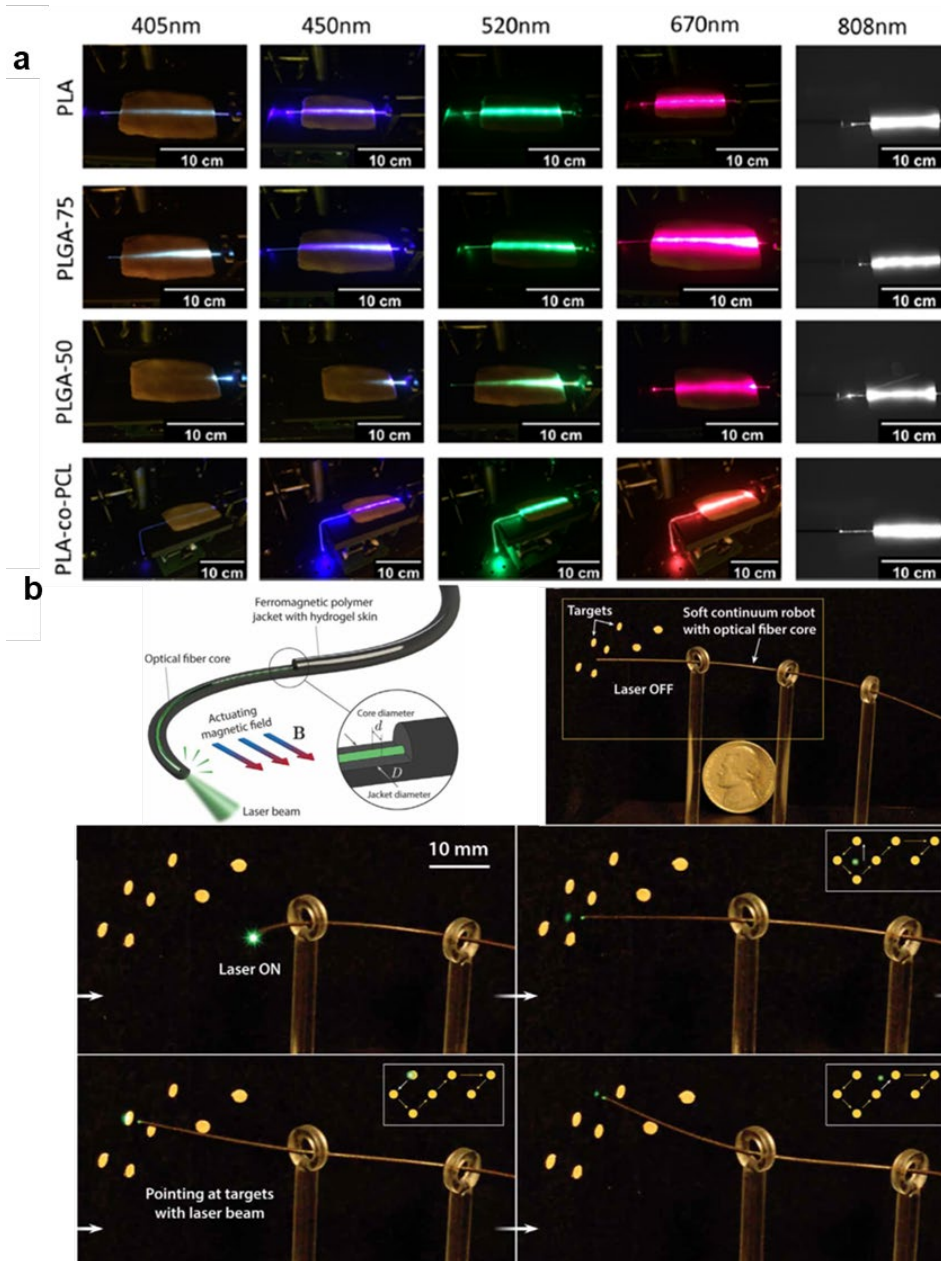


Figure 1.21 a) Images of light of different wavelengths traveling through printed waveguides within tissue. Reprint from Feng, J.; Jiang, Q.; Rogin, P.; De Oliveira, P. W.; Del Campo, A. Printed Soft Optical Waveguides of PLA Copolymers for Guiding Light into Tissue. *ACS Appl. Mater. Interfaces* **2020**, *12*, 20287–20294. Copyright 2020 American Chemical Society. b) The top-left image is a representation of a continuum soft robot composed of an optical fiber wrapped with a ferromagnetic polymer jacket with hydrogel skin. The top-right image shows the experimental set up used to demonstrate steerable light delivery. The four images below show the magnetic soft robot initially traveling through a set of rings while directing light and then directing light towards specific areas (yellow dots). Reprint with permission from Kim, Y.; Parada, G. A.; Liu, S.; Zhao, X. Ferromagnetic soft continuum robots. *Sci. Robot* **2019**, *4*, eaax7329. Copyright 2019, American Association for the Advancement of Science.

1.8 Vortex beams

In addition to linear momentum, light can also carry angular momentum. The angular momentum can have two contributions. The first one is known as spin angular momentum (SAM) which is originated from the light polarization. The second one is known as orbital angular momentum (OAM) which is associated with the spatial distribution of the optical field. The total angular momentum in one photon is equal to the sum of spin and orbital angular momentum:

$$J = (l + s)\hbar \quad (1.13)$$

Optical fields with a phase singularity known as optical vortices have been the focus of intense research since they were introduced in 1974 for Nye and Berry.¹⁶⁵ They possess a helical wavefront and when projected onto a surface, they look like a ring of light with a dark region in the center (Figure 1.22).

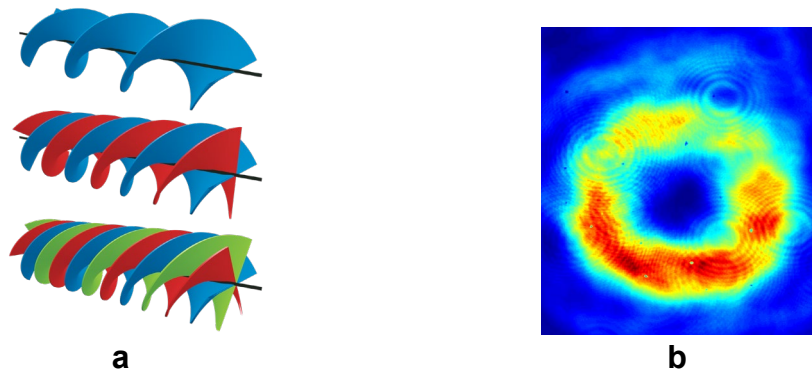


Figure 1.22. a) Phase surfaces of vortex beams with $l = 1, 2$ and 3 .¹⁶⁶ b) Transverse profile of a vortex beam.

Because of their helical wavefront, vortex beams, vortex beams carry orbital angular momentum equal to $l\hbar$.¹⁶⁷ The optical field has an azimuthal component ($e^{il\varphi}$) in which l is an integer known as topological charge which defines the handedness of the spiraling wavefront and φ is the azimuthal angle. The ability to carry OAM open the possibility of using optical vortices in different fields. One of the most known applications is their use as optical traps.^{168,169} Vortex beams have

also used to improve the image resolution in microscopy¹⁷⁰, for the detection of spinning bodies¹⁷¹, to enhance internet data traffic capacity in optical fibers¹⁷² and also, in free-space data transmission.¹⁷³ Vortex beams also form solitons when traveling in nonlinear media.¹⁷⁴ As pointed out earlier, the diffraction of light is suppressed in a nonlinear medium undergoing a Δn . A soliton is formed when there is a balance between the natural diffraction of light which are stationary solutions of the NLSE. A general way to describe a soliton is:¹⁷⁵

$$E = (x, y, z) = U(x, y)e^{i\phi(x,y)+ikz} \quad (1.14)$$

U is the real amplitude, ϕ is the phase and k is the soliton propagation constant. For a soliton with radial symmetry, $U(x, y) = R(r)$ which can be obtained only through numerical methods:¹⁷⁵

$$\frac{\partial R}{\partial r^2} + \frac{1}{r} \frac{\partial R}{\partial r} - \frac{m^2}{r^2} R - kR + N(R^2)R = 0 \quad (1.15)$$

The phase of vortex solitons is described as $l\phi$. When a vortex beam is projected, the transverse shape is similar to a ring of light with a singularity. The soliton envelope $R(r)$ vanishes at the center since $R \sim r^{|l|}$ at $r \rightarrow 0$ while the soliton tail decays as $R(r) \sim e^{-\frac{(r\sqrt{k})}{\sqrt{r}}}$ at $r \rightarrow \infty$. Radially symmetric vortices can be described by:¹⁷⁵

$$E_0 = R(r)e^{il\phi+ikz} \quad (1.16)$$

which is a solution of the NLSE. Vortex solitons undergo azimuthal instability in nonlinear media which is a kind of transverse modulation instability analogous to the one experienced by regular gaussian or incoherent beams. Such instability is caused by the amplification of a perturbation in the medium. Equation 2.3 remains stable as long as $[p] \ll [E_0]$ where p is the perturbation causing MI. Such perturbation can be presented as Fourier series:¹⁷⁵

$$p(r, \phi, z) = \sum p_s(r, z)e^{is\phi} \quad (1.17)$$

Where s is an integer. The only two modes coupled for each s that create a closed eigenvalue p_{l+s} and p_{l-s} . We make sure all perturbations are taken into account by writing the perturbation as:¹⁷⁵

$$p(r, \varphi, z) = e^{ilk+ikz} \{u_s(r)e^{is\varphi+\gamma_s z} + v_s^*(r)e^{-is\varphi+\gamma_s^* z}\} \quad (1.18)$$

The magnitude of perturbation modes $p_{l\pm s}$ increases exponentially when the eigenvalue has a positive real part (grow rate $\text{Re } \gamma_s > 0$). E_0 is linearly stable when p does not increase with propagation distance. The index s of the instability with the fastest grow rates determines the number of filaments that are formed after the ring breaks up. Such grow rate depends mostly in 3 factors: the topological charge, the nature of the nonlinearity and the power of the beam. Vortex beams with $l = 1$ in saturable media tend to split into $2l$ filaments. Since the photopolymers used in our experiments are saturable, we will focus on discussing mostly previous work in saturable nonlinear media in which the nonlinearity is originated from both physical and chemical mechanisms. The filaments from after a vortex beam break behave as fundamental solitons. The centrifugal force among solitons is always repulsive with the nature of the nonlinearity being heavily involved in the outcome. However, solitons pairs with nonzero OAM in which there is an attractive interaction, the centrifugal repulsive force can be balanced out giving as a result a spiraling pair of solitons. Such spiraling was observed using rubidium vapor as the nonlinear system.¹⁷⁶ In this system, the laser frequency detuning was 0.5 GHz close to the rubidium atomic D_2 line at $\lambda \sim 780$ nm. This resulted in the formation of two spiraling solitons that were out of phase. As a result, there is a repulsive force between the formed solitons. However, since the pair of solitons has a nonzero OAM, they rotate around the beam axis while their distance between the solitons increases. The speed of such separation and rotation increased with the concentration of Rb atoms, the reduction of the detuning and the increase of the intensity. Nonrotating solitons were also obtained in sodium vapor with the number of solitons formed following the $2l$ trend previously

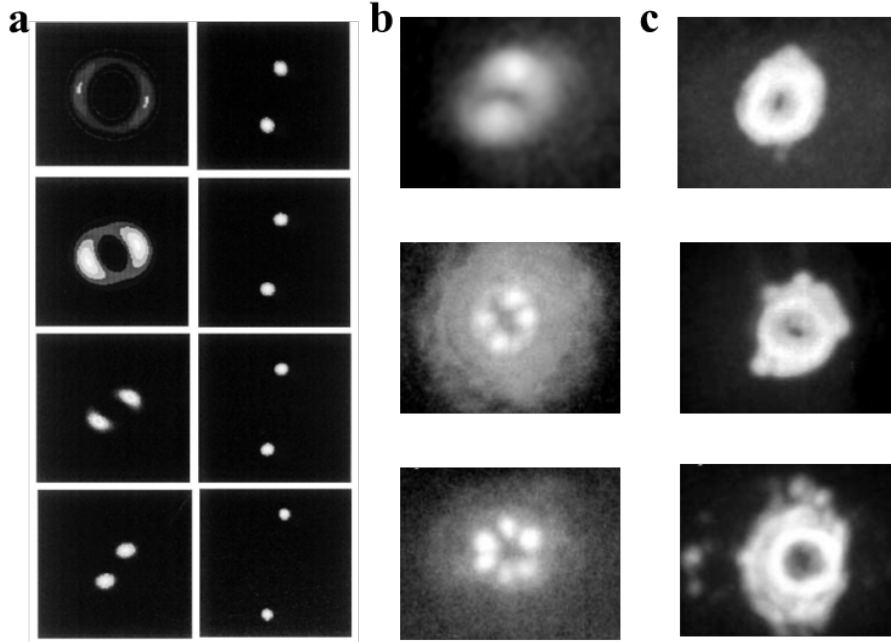


Figure 1.22 **a)** Beam profile at the exit face of a cell containing different concentrations of Rb atoms at a power of 20 mW at the entrance face. Detuning= 0.56 GHz. Concentrations ($10^{11}/\text{cm}^3$) in the first column from top to bottom: 0.03, 1.0, 2.1, 3.1. The concentrations in the second column also from top to bottom were 5.2, 6.2, 7.2 and $8.3 \cdot 10^{11} \text{ cm}^{-3}$. The separation and the rotation angle between the two solitons increases with the concentration of Rb atoms. Reprinted with permission from Tikhonenko, V.; Christou, J.; Luther-Daves, B. Spiraling bright spatial solitons formed by the breakup of an optical vortex in a saturable self-focusing medium. *J. Opt. Soc. Am. B* **1995**, *12*, 2046-2052. Copyright 1995 Optical Society of America **b)** Modulation instability of vortex beams with $l = 1, 2, 3$ traveling through sodium vapor as the nonlinear medium with pulse energies of 76, 234 and 359 nJ respectively. The beams break into 2, 4 and 6 filaments. **c)** When the pulse energy of these beams is increased to 9.1, 24.1 and 6.63 μJ for each topological charge ($l = 1, 2, 3$), they no longer break since the nonlinearity is immediately saturated. **b** and **c** were reprinted with permission from Bigelow, M. S.; Zerom, P.; Boyd, R. W. Breakup of Ring Beams Carrying Orbital Angular Momentum in Sodium Vapor. *Phys. Rev. Lett.* **2004**, *92*, 083902. Copyright 2004 American Physical Society.

described for vortex beams with $l = 1, 2, 3$.¹⁷⁷ These experimental observations can be simulated by propagating randomly perturbed Laguerre-Gaussian beams propagating in a two-level homogeneously broadened system. The breakup of the vortex beam no longer takes place at intensities above 9.1 μJ . It is believed such stability is caused by the saturation of the nonlinearity which suppresses filamentation. Formation of stationary solitons after MI in vortex beams has also

been observed in other kind of nonlinear media such as quadratic nonlinear crystal¹⁷⁸ and Kerr media. Optical vortices with $l = 1$ in a quadratic nonlinear form 3 solitons.¹⁷⁹ In Kerr media, the number of solitons depends on the power and the topological charge.¹⁸⁰ Before discussing vortex beams in nonlinear media where there are chemical reactions involved, the effect of vortex beams in some films elicited by physical mechanisms will be discussed. Vortex beams have shown the capacity of creating chiral micro and nano- structures in which the handedness of the beam is transferred to the material. Such process has been observed in the fabrication of silver¹⁸¹, tantalum¹⁸² and Cr/Au¹⁸³ helical needles and silicon chiral cones.¹⁸⁴ In these cases, the material that was on some support was irradiated. Mass transport can also be created by irradiating materials from the backside. A micro- scale spin jet is created due to the forward and inward mass transfer towards the center of a vortex beam when this one is launched through the backside of a glass plate containing a film of a highly viscous material (4 PS).¹⁸⁵ Such jet is not created when a circularly polarized beam is launched to the medium. Instead, droplets of the viscous material are ejected from the film. In all these cases, the handedness of the vortex beam was transferred to the patterned that were created. Manifestations of the properties of light beams are also observed when the light field induces a photochemical reaction. Many studies of this kind were done in azo-polymers films. Upon absorption of light, azobenzene molecules undergo cis-trans polymerization. The optical scattering force creates a surface relief due to mass transport from bright to dark regions along the polarization of light. When a vortex beam with $l = 10$ was launched to an azopolymer film, a spiral-shaped relief pattern on the polymer film with a shallow depth of 10-20 nm was obtained.¹⁶⁶ Conch-shaped relief with a height above 1 μm can be obtained using vortex beam with circularly polarized light. Such reliefs are only formed when the total angular momentum $J \neq 0$.¹⁸⁷ Relief formation was not observed when launching higher order vortices to the film.¹⁶⁷ Omatusu *et al.*

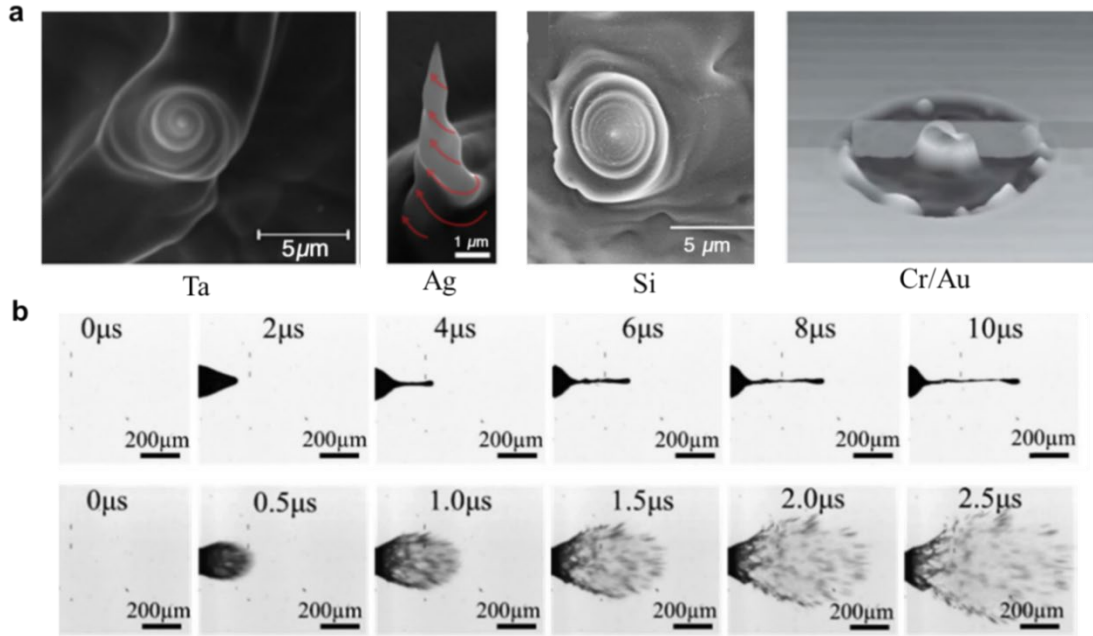


Figure 1.23. a) Chiral structures obtained upon vortex irradiation of thin films made of tantalum, silver, silicon, and chromium/gold. Images (left to right) reprinted with permission from ref. 181,182,183 and 184. Copyright 2017 Optical Society of America. Copyright 2012 American Chemical Society. Copyright 2018 AIP Publishing. Copyright 2017 AIP Publishing. Chiral structures can also be obtained when the sample is irradiated from the substrate side rather than the film side. The top images in **b)** show the time evolution of a spin jet created upon irradiation of a viscous ink with a vortex beam. When the viscous ink is irradiated with a circularly polarized beam, scattered droplets are formed which confirms a vortex beam is necessary for the formation of the spin jet. Reprint with permission from ref. 185. Copyright 2019 Optical Society of America.

recently carried out experiments where vortex beams induced permanent changes in photopolymers. It was observed that the vortex beam initially self-focused creating an annular-shape vortex soliton at exposures times < 0.2 s. For longer exposures times, the hollowed center disappears forming a fiber that breaks into $|l|$ solitons or fibers. A theory to describe these experimental observations is based on a coarse-grained particle model in which the primitive growth mechanism of the particles is addressed.¹⁸⁸ There are two forces acting in the particles formed at early stages of the photopolymerization: the gradient force F_{grad} and the scattering force F_{scat} . F_{grad} is expressed by the following equation:

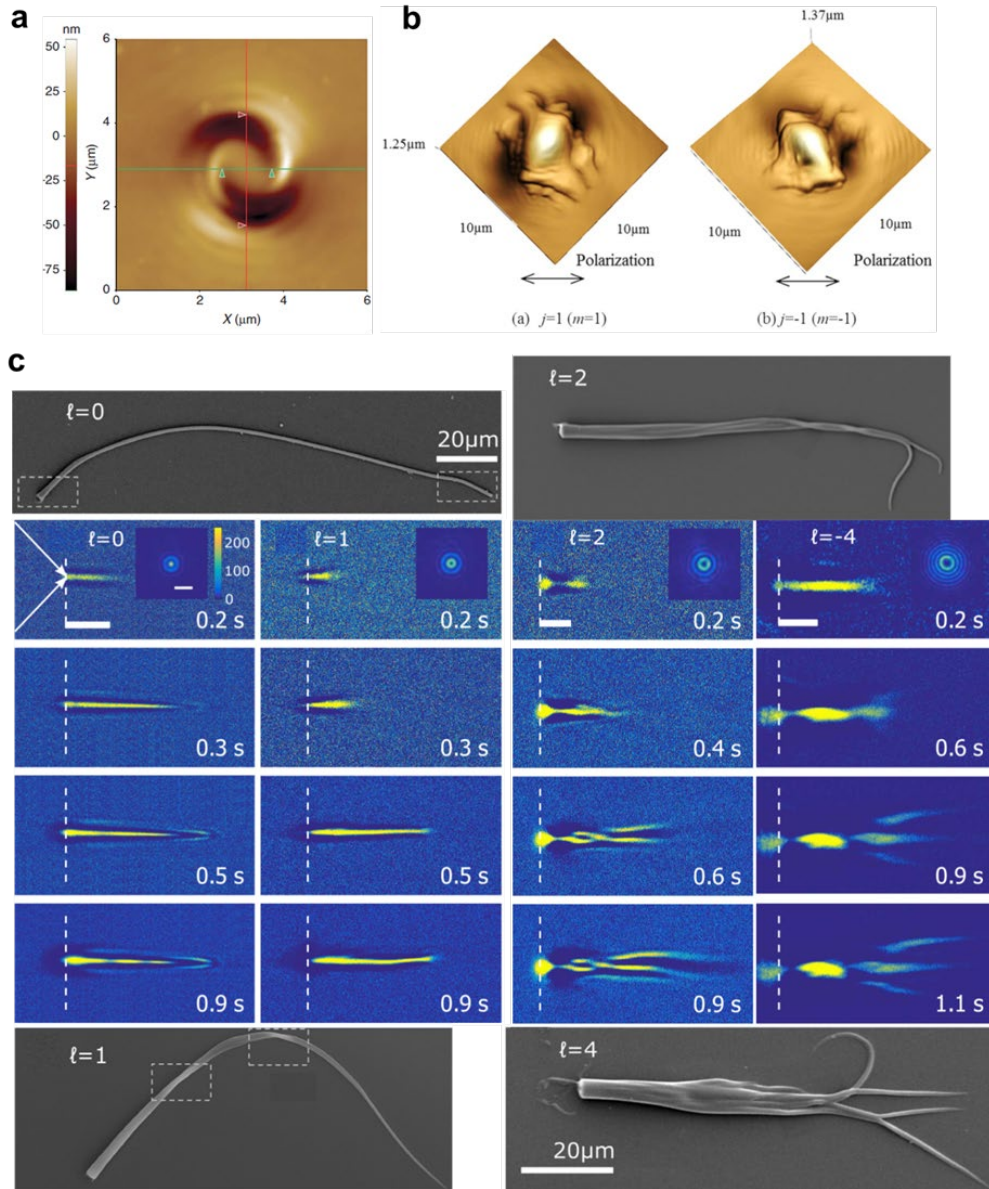


Figure 1.24 a) Surface relief pattern generated with a vortex beam with $l = 10$. Reprint with permission from ref. Ambrosio, A.; Marrucci, L.; Borbone, F.; Roviello, A.; Maddalena, P. Light-induced spiral mass transport in azo-polymer films under vortex-beam illumination. *Nat Commun* **2012**, 3, 989. Copyright 2012, Springer Nature. **b)** Conch-shape reliefs created through the irradiation of a circularly polarized vortex beam with total angular momentum of ± 2 Reprinted with permission from Watabe, M.; Juman, G.; Miyamoto, K.; Omatsu, T. Light induced conch-shaped relief in an azo-polymer film. *Sci Rep* **2014**, 4, 4281. Copyright 2014, Springer Nature. **c)** Each column in the middle shows the time evolution of the fabrication of polymer fibers with $l = 0, 1, 2, 4$ (left to right). Images of the fibers obtained in the experiments are shown on the top ($l = 0, 2$) and bottom ($l = 1, 4$). Reprinted with permission from Lee, J.; Arita, Y.; Toyoshima, S.; Miyamoto, K.; Panagiotopoulos, P.; Wright, E. M.; Dholakia, K.; Omatsu, T. Photopolymerization with Light Fields Possessing Orbital Angular Momentum: Generation of Helical Microfibers. *ACS Photonics* **2018**, 5, 4156–4163. Copyright 2018 American Chemical Society.

$$F_{grad} = \frac{1}{2} \alpha \nabla \left| \frac{1}{t_p} \int_0^{t_p} E(r, \theta, z, t) dt \right| \quad (1.19)$$

Where α is the polarizability of the coarse-grained particles, t_p is the period of the Pointing vector $S(r, \theta, z, t) \equiv E(r, \theta, z, t) \times H(r, \theta, z, t)$ where E and H are the electric and magnetic field. Due to F_{grad} , a coarse-grained particle is trapped and attracted to the focal plane. In this model, it is assumed that the particles are not absorbing. After this consideration, F_{scat} can be obtained as follows:

$$F_{scat} = \frac{n_f}{c} C_{scat} I = C_{scat} \frac{\varepsilon_f E_0^2}{z} \frac{w_0^2}{w^2(z)} \frac{2r^2}{w^2(z)} \exp\left(-\frac{2r^2}{w^2(z)} - \eta^2\right) \left(\frac{1}{k_f r} e_\theta + e_z\right) \quad (1.20)$$

n_f is the refractive index of the fluid, c is the speed of light, C_{scat} is the scattering cross-section defined as $C_{scat} = \frac{\pi}{24} k_f^4 d^6 \left(\frac{\varepsilon_p - \varepsilon_f}{\varepsilon_p + 2\varepsilon_f}\right)^2$ where k_f is the wavenumber of light in the liquid resin, d is the diameter of the particle, ε_p and ε_f are the dielectric constant of the particle and the resin respectively. η is the absorption coefficient of the resin. The scattering force consists of both θ and z components. Therefore, a coarse-grained particle experiences a force along a helical orbit. The intensity of a vortex beam becomes 0 at $r = 0$ and reaches a maximum at $r = w(z)/\sqrt{2}$. At the focal point, the optical forces can be written as follows:

$$F_{grad,z} = -\frac{1}{8} \pi \varepsilon_f d^3 \frac{\varepsilon_p - \varepsilon_f}{\varepsilon_p + 2\varepsilon_f} E_0^2 \eta e^{-1} \quad (1.21)$$

$$F_{scat,z} = \frac{1}{48} \pi \varepsilon_f k_f^4 d^6 \left(\frac{\varepsilon_p - \varepsilon_f}{\varepsilon_p + 2\varepsilon_f}\right)^2 E_0^2 e^{-1} \quad (1.22)$$

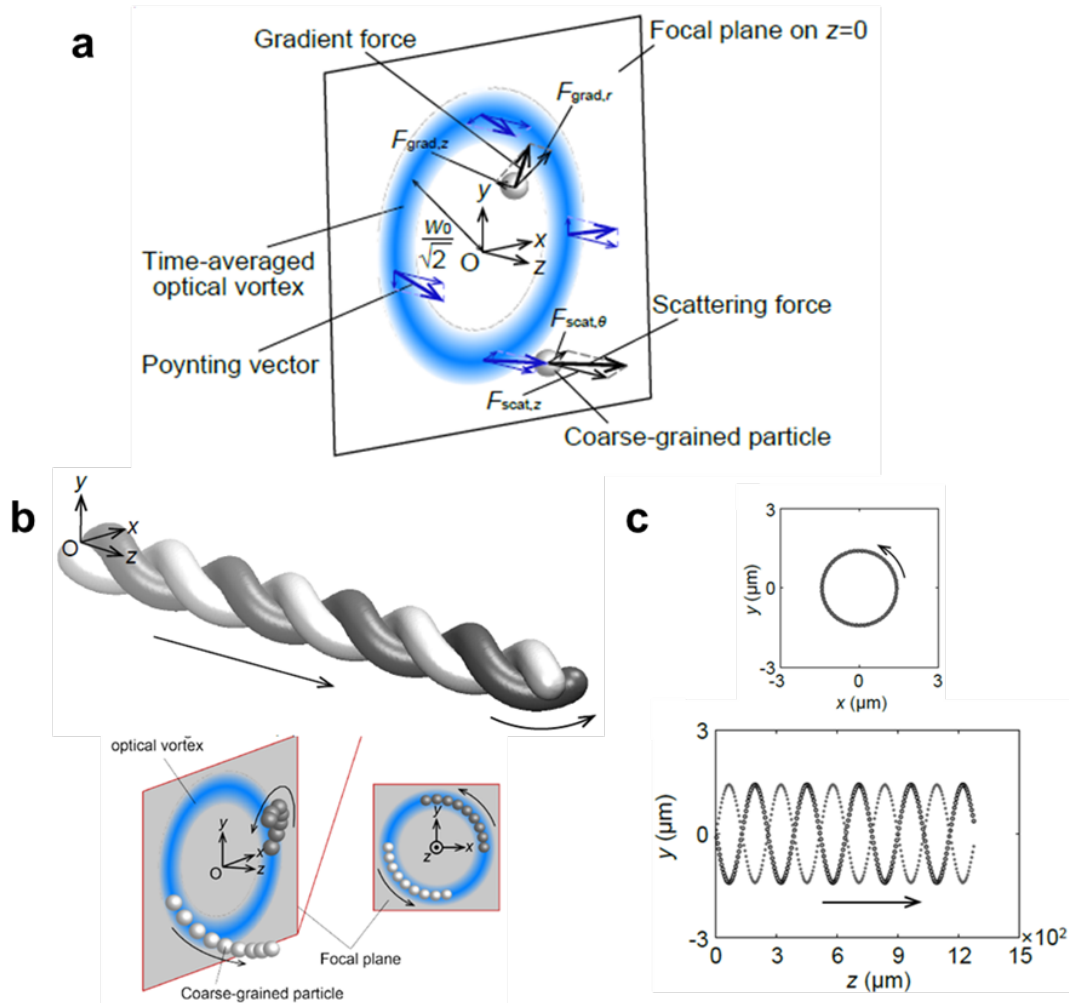


Figure 1.25 a) Diagram of optical forces acting on a particle generated by a vortex beam. Force vectors are represented as bold black arrows while the narrow black arrows correspond to r and z components. b) Scheme of the model proposed to explain polymer fiber formation upon irradiation of a vortex beam based on a coarse-grained particle model. c) Simulated dynamics of a coarsed grained particle with $d = 50 \text{ nm}$ in a medium where the absorption is $\eta=9.24 \times 10^3 \text{ m}^{-1}$. The top graph shows the trajectory of the particle on the xy plane while the graph at the bottom shows the same trajectory of the particle on the yz plane (the z direction is compressed by 100 fold). Reprinted with permission from Lee, J.; Arita, Y.; Toyoshima, S.; Miyamoto, K.; Panagiotopoulos, P.; Wright, E. M.; Dholakia, K.; Omatsu, T. Photopolymerization with Light Fields Possessing Orbital Angular Momentum: Generation of Helical Microfibers. *ACS Photonics* **2018**, 5, 4156–4163. Copyright 2019 Optical Society of America.

When $F_{scat,z} > F_{grad,z}$, a coarse-grained particle could be launched into an orbit. The resulting particle trajectory resembles a helix with a period defined as:

$$L_p = 2\pi r \frac{F_{grad,z} + F_{scat,z}}{F_{scat,\theta}} = \pi k_f w_0^2 - \left[\frac{6\pi w_0^2}{k_f^3} \left(\frac{\epsilon_p - \epsilon_f}{\epsilon_p + 2\epsilon_f} \right) \right] \frac{\eta}{d^3} \quad (1.23)$$

where w_0 is the beam waist. The period of the fibers obtained by Omatsu *et al.* and the one obtained after plotting the experimental conditions in the equation for L_p are in good agreement so the model seems to describe the formation of twisted fibers created by vortex beams.^{188,189} The fiber soliton formation has only been demonstrated in a photopolymer that undergoes free-radical polymerization. We previously demonstrated that it is possible to soliton-like beams in different photopolymers in which the changes originated by the beam can be both reversible or irreversible. So far, the fiber/soliton formation has only been demonstrated in a photopolymer that undergoes free-radical polymerization. In addition, other parameters that can influence the dynamics of fiber/soliton formation such as absorption, have not been studied yet. We studied the effect of vortex beams in a photopolymer that undergoes cationic radical photopolymerization. Our findings are reported in Chapter 4 of this thesis.

1.8 Contributions

Chapter 2

I was responsible for adapting the resins to our 3-D printed method as well as for printing some of the objects. Derek R. Morim was responsible for writing the segmentation algorithm to decompose all objects. We both contributed equally to this work. Diego Colin, Eduardo Alonso Martinez and Ramon Arora printed some of the objects and also helped to make some of the images. Derek R. Morim and K. Saravanamuttu and I wrote the manuscript. Part of this chapter was included in Derek Morim's Ph.D. Thesis: (Morim, D. (2019). Harnessing Optochemical

Waves in Polymers: From Beam Interactions to Inscription of Prismatic Elements [Doctoral dissertation, McMaster University]. Macsphere. <http://hdl.handle.net/11375/24750>

Chapter 3

I proposed Prismatic 3-D printing for the fabrication of electroactive waveguides based on observations from the work described in Chapter 2. I also developed the hydrogel formulations with Derek R. Morim and did the presented simulations. I proposed the set up to carry out multidirectional bending. Natalie Blanchard carried out early experiments with the waveguide lattices. Tomas Omasta did some analysis to quantify bending angles of slab waveguides Kathryn A. Benincasa carried out the tracking of position and intensity of individual micro-waveguides in the waveguide lattices. Kevin Vaughan and I carried out the experimental work analyzed by Kathryn A. Benincasa. K. Saravanamuttu guided the project.

Chapter 4

I carried out early experiments with Derek R. Morim, Alejandro Vazquez and Fariha Mahmood in different photochemical systems. I then focused on the epoxide system and obtained and analyzed the results presented in the Chapter. Karen Volke-Sepúlveda and Kalaichelvi Saravanamuttu provided guidance and suggested experimental work.

1.10 References

- 1) He, G. S.; Nonlinear Optics and Photonics; OXFORD UNIVERSITY PRESS: Oxford, **2015**.
- 2) Chiao, R. Y.; Garmire E.; Townes C. H. Self-Trapping of Optical Beams. *Phys. Rev. Lett.* **1964**, *13*, 479-482.
- 3) Biria, S.; Morim, D. R.; Tsao, F. A.; Saravanamuttu, K.; Hosein, I. D. Coupling nonlinear optical waves to photoreactive and phase-separating soft matter: Current status and perspectives. *Chaos* **2017**, *27*, 104611.

- 4) Bjorkholm J. E.; Ashkin, A. A. cw Self-Focusing and Self-Trapping of Light in Sodium Vapor. *Physical Review Letters* **1974**, *32*, 129–132.
- 5) Maneuf, S.; Desailly, R.; Froehly, C. STABLE SELF-TRAPPING OF LASER BEAMS: OBSERVATION IN A NONLINEAR PLANAR WAVEGUIDE. *Opt. Commun.* 1998, *65*, 193-198.
- 6) De La Fuente, R.; Barthelemy, A.; Froehly, C. (1991). Spatial-soliton-induced guided waves in a homogeneous nonlinear Kerr medium. *Opt. Lett.* **1991**, *16*, 793-795.
- 7) Lawrence, B. L.; Stegeman, G. I. Two-dimensional bright spatial solitons stable over limited intensities and ring formation in polydiacetylene para-toluene sulfonate. *Opt. Lett.* **1998**, *23*, 591-593.
- 8) Pasquazi, A.; Stivala, S.; Assanto, G.; Gonzalo, J.; Solis, J.; Afonso, C. N. Near-infrared spatial solitons in heavy metal oxide glasses. *Opt. Lett.* **2007**, *32*, 2103-2105.
- 9) Torruellas, W. E.; Wang, Z.; Hagan, D. J.; VanStryland, E. W.; Stegeman, G. I.; Torner, L.; Menyuk, C. R. Observation of two-dimensional spatial solitary waves in a quadratic medium. *Phys. Rev. Lett.* **1995**, *74*, 5036–5039.
- 10) Canva, M. T. G.; Fuerst, R. A.; Baboiu, D.; Stegeman, G. I.; Assanto, G. Quadratic spatial soliton generation by seeded down conversion of a strong pump beam. *Opt. Lett.* **1997**, *22*, 1683-1685.
- 11) Bourliaguet, B.; Couderc, V.; Barthélemy, A.; Ross, G. W.; Smith, P. G. R.; Hanna, D. C.; De Angelis, C. Observation of quadratic spatial solitons in periodically poled lithium niobate. *Opt. Lett.* **1999**, *24*, 1410-1412.
- 12) Malendevich, R.; Jankovic L.; Polyakov, S.; Fuerst, R.; Stegeman, G., Bosshard, C.; Gunter, P. Two-dimensional type I quadratic spatial solitons in KNbO₃ near noncritical phase matching. *Opt. Lett.* **2002**, *27*, 631-633.
- 13) Minardi, S.; Sapone, S.; Chinaglia, W.; Di Trapani, P.; Beržanskis, A. Pixellike parametric generator based on controlled spatial-soliton formation. *Opt. Lett.* **2000**, *25*, 326-328.
- 14) Peccianti, M.; De Rossi, A.; Assanto, G.; De Luca, A.; Umeton, C.; Khoo, I. C. Electrically assisted self-confinement and waveguiding in planar nematic liquid crystal cells. *Appl. Phys. Lett.* **2000**, *77*, 7–9.
- 15) Peccianti, M.; Conti, C.; Assanto, G.; De Luca, A.; Umeton, C. Routing of anisotropic spatial solitons and modulational instability in liquid crystals. *Nature* **2004**, *432*, 733–737.
- 16) Henninot, J. F.; Blach, J. F.; Warenghem, M. The investigation of an electrically stabilized optical spatial soliton induced in a nematic liquid crystal. *J. Opt. A: Pure Appl. Opt.* **2008**, *10*, 085104.
- 17) Peccianti, M.; Brzdakiewics, K. A.; Assanto, G. Nonlocal spatial soliton interactions in nematic liquid crystals. *Opt. Lett.* **2002**, *27*, 2103-2105.
- 18) Duree, G. C.; Shultz, J. L.; Salamo, G. J.; Segev, M.; Yariv, A.; Crosignani, B.; Di Porto, P.; Sharp, E. J.; Neurgaonkar, R. R. Observation of self-trapping of an optical beam due to the photorefractive effect. *Phys. Rev. Lett.* **1993**, *71*, 533–536.
- 19) Iturbide-Castillo, M. D.; Marquez-Aguilar P. A.; Sanchez-Mondragon J. J.; Stepanov S.; Vysloukh V. Spatial solitons in photorefractive Bi 12 TiO 20 with drift mechanism of nonlinearity Spatial solitons of nonlinearity. *Appl. Phys. Lett.* **1998**, *64*, 408-410.
- 20) Shih, M.; Leach, P.; Segev, M.; Garrett, M. H.; Valley, G. C. Two-dimensional steady-state photorefractive screening solitons. *Opt. Lett.* **1996**, *21*, 324-326.
- 21) Kos, K.; Salamo, G.; Segev, M. High-intensity nanosecond photorefractive spatial solitons. *Opt. Lett.* **1998**, *23*, 1001-1003.

- 22) Kewitsch, A. S.; Yariv, A. Self-focusing and self-trapping of optical beams upon photopolymerization. *Opt. Lett.* **1996**, *21*, 24-26.
- 23) Kagami, M.; Yamashita, T.; Ito, H. Light-induced self-written three-dimensional optical waveguide. *Appl. Phys. Lett.* **2001**, *79*, 1079–1081.
- 24) Jacobsen, A. J.; Barvosa-Carter, W.; Nutt, S. Micro-scale truss structures formed from self-propagating photopolymer waveguides. *Adv. Mater.* **2007**, *19*, 3892–3896.
- 25) Bachelot, R.; Ecoffet, C.; Deloëil, D.; Royer, P.; Lougnot, D. J. Integration of polymer elements at the end of optical fibers by free-radical photopolymerization. *Appl. Opt.* **2001**, *40*, 5860–5871.
- 26) Dorkenoo, K.; Crégut, O.; Mager, L.; Gillot, F.; Carre, C.; Fort, A. Quasi-solitonic behavior of self-written waveguides created by photopolymerization. *Opt. Lett.* **2002**, *27*, 1782-1784.
- 27) Shoji, S.; Kawata, S.; Sukhorukov, A. A.; Kivshar, Y. S. Self-written waveguides in photopolymerizable resins. *Opt. Lett.* **2002**, *27*, 185-187.
- 28) Shoji, S.; Kawata, S. Optically-induced growth of fiber patterns into a photopolymerizable resin. *Appl. Phys. Lett.* **1999**, *75*, 737–739.
- 29) Jacobsen, A. J.; Barvosa-Carter, W.; Nutt, S. N. Micro-scale truss structures with three-fold and six-fold symmetry formed from self-propagating polymer waveguides. *Acta Materialia* **2008**, *56*, 2540–2548.
- 30) Zhang, J.; Kasala, K.; Rewari A. and Saravanamuttu K. Self-trapping of spatially and temporally incoherent light in a photochemical system. *J. Am. Chem. Soc.* **2006**, *128*, 406-407.
- 31) Zhang, J.; Saravanamuttu, K. The Dynamics of Self-Trapped Beams of Incoherent White Light in a Free-Radical Photopolymerizable Medium. *J. Am. Chem. Soc.* **2006**, *128*, 14913-14923.
- 32) Basker, D. K.; Cortes, O. A. H.; Brook, M. A.; Saravanamuttu, K. 3D Nonlinear Inscription of Complex Microcomponents (3D NSCRIPT): Printing Functional Dielectric and Metallodielectric Polymer Structures with Nonlinear Waves of Blue LED Light. *Adv. Mater. Technol.* **2017**, *2*, 1600236-n/a.
- 33) Di Trapani, P.; Valiulis, G.; Chinaglia, W.; Andreoni, A. Two-Dimensional Spatial Solitary Waves from Traveling-Wave Parametric Amplification of the Quantum Noise. *Phys. Rev. Lett.* **1998**, *80*, 265-268.
- 34) Segev, M.; Crosignani, B.; Yariv, A.; Fischer, B. Spatial solitons in photorefractive media. *Phys. Rev. Lett.* **1992**, *68*, 923-926.
- 35) Naumov, A. F.; Loktev, M. Y.; Guralnik, I. R.; Vdovin, G. Liquid-crystal adaptive lenses with modal control. *Opt. Lett.* **1998**, *23*, 992-994.
- 36) White, T. J.; Bricker, R. L.; Natarajan, L. V.; Vincent, P.; Green, L.; Li, Q.; Bunning, T. J. Electrically switchable, photoaddressable cholesteric liquid crystal reflectors. *Opt. Express* **2010**, *18*, 173-178.
- 37) Mada, H.; Osajima, K. Time response of a nematic liquid-crystal cell in a switched dc electric field. *J. Appl. Phys.* **1986**, *60*, 3111-3113.
- 38) Chen, H. Y.; Lee, W. Electro-optical characteristics of a twisted nematic liquid-crystal cell doped with carbon nanotubes in a DC electric field. *OPT REV* **2005**, *12*, 223–225.
- 39) Peccianti, M.; Assanto, G. Signal Readdressing by Steering of Spatial Solitons in Bulk Nematic Liquid Crystals. *Opt. Lett.* **2001**, *26*, 1690–1692.
- 40) Assanto, G.; Peccianti, M. Spatial Solitons in Nematic Liquid Crystals. *IEEE J. Quantum Electron.* **2003**, *39*, 13–21.
- 41) Hecht, E. Optics, 5th ed.; Pearson: USA, 2017.

- 42) Morim, D. R.; Vargas-Baca, I.; Saravanamuttu, K. Reversibly Trapping Visible Laser Light through the Catalytic Photo-oxidation of I⁻ by Ru(bpy)₃²⁺. *J. Phys. Chem. Lett.* **2016**, *7*, 1585–1589.
- 43) Morim, D. R.; Meeks, A.; Shastri, A.; Tran, A.; Shneidman, A. V.; Yashin, V. V.; Mahmood, F.; Balazs, A. C.; Aizenberg, J.; Saravanamuttu, K. Opto-chemo mechanical transduction in photoresponsive gels elicits switchable self-trapped beams with remote interactions. *Proc. Natl. Acad. Sci. U. S. A.* **2020**, *117*, 3953.
- 44) Huang, Y.; Paul, D. R. Physical Aging of Thin Glassy Polymer Films Monitored by Optical Properties. *Macromolecules* **2006**, *39*, 1554–1559.
- 45) Cho, J. D.; Ju, H. T.; Hong, J. W. (2005). Photocuring kinetics of UV-initiated free-radical photopolymerizations with and without silica nanoparticles. *J. Polym. Sci., Part A: Polym. Chem.* **2005**, *43*, 658-670.
- 46) Neumann, M. G.; Schmitt, C. C.; Ferreira, G. C. The initiating radical yields and the efficiency of polymerization for various dental photoinitiators excited by different light curing units. *Dental Materials* **2006**, *22*, 576–584.
- 47) Koltzenburg, S.; Maskos, M.; Nuyken, O. *Polymer Chemistry*; Springer: eBook 2017.
- 48) Basker, D. K.; Brook, M. A.; Saravanamuttu, K. Spontaneous Emergence of Nonlinear Light Waves and Self-Inscribed Waveguide Microstructure during the Cationic Polymerization of Epoxides, *J. Phys. Chem. C* **2015**, *119*, 20606–20617.
- 49) Hosein, I. D.; Lin, H.; Ponte M. R.; Basker, K. D.; Brook. M. A.; Saravanamuttu, K. Waveguide Encoded Intersecting (WIDEI) Lattices: Slim Polymer Films with Panoramic Fields of View (FOV) and Multiple Imaging Functionality. *Adv. Funct. Mater.* **2017**, *27*, 1702242.
- 50) Lin, H.; Hosein, I. D.; Benicasa K. A.; Saravanamuttu, K. Slim Films with Seamless Panoramic Fields of View: The Radially Distributed Waveguide Encoded Lattice (RDWEL). *Adv. Optical Mater.* **2019**, *7*, 1801091.
- 51) Lin, H.; Benincasa, K.; Fredin. C.; Saravanamuttu, K. Shaping LED beams with Radially Distributed Waveguide Encoded Lattices (RDWELs). *Adv. Optical Mater.* **2019**, *7*, 1801091.
- 52) Crivello, J. V.; Acosta Ortiz, R. Benzyl Alcohols as Accelerators in the Photoinitiated Cationic Polymerization of Epoxide Monomers. *J. Polym. Sci., Part A: Polym. Chem.* **2002**, *40*, 2298–2309.
- 53) Barthelemy, A.; Maneuf, S.; Froehly, C. Propagation Soliton et Auto-Confinement de Faisceaux Laser Par Non Linearité Optique de Kerr. *Opt. Commun.* **1985**, *55* (3), 201–206.
- 54) Segev, M. Optical Spatial Solitons. *Opt. Quantum Electron.* **1998**, *30*, 503–533.
- 55) Trillo, S.; Torruellas, W. *Spatial Solitons* (Springer Series in Optical Sciences); Springer, 2001.
- 56) Bespalov, V. I.; Talanov, V. I. Filamentary Structure of Light Beams in Nonlinear Media. *JETP Lett.* **1966**, *3*, 307–310.
- 57) Wabnitz, S. Modulational Polarization Instability of Light in a Nonlinear Birefringent Dispersive Medium. *Phys. Rev. A* **1988**, *38*, 2018–2021.
- 58) Zakharov, V. E.; Ostrovsky, L. A. Modulation Instability: The Beginning. *Phys. D Nonlinear Phenom.* **2009**, *238*, 540–548.
- 59) Iturbe-Castillo, M. D.; Torres-Cisneros, M.; Sánchez-Mondragón, J. J.; Chávez-Cerda, S.; Stepanov, S. I.; Vysloukh, V. A.; Torres-Cisneros, G. E. Experimental Evidence of Modulation Instability in a Photorefractive Bi₁₂TiO₂₀ Crystal. *Opt. Lett.* **1995**, *20*, 1853.
- 60) Wabnitz, S. Modulational Polarization Instability of Light in a Nonlinear Birefringent Dispersive Medium. *Phys. Rev. A* **1988**, *38*, 2018–2021.

- 61) Aitchison, J. S.; Weiner, A. M.; Silberberg, Y.; Oliver, M. K.; Jackel, J. L.; Leaird, D. E.; Vogel, E. M.; Smith, P. W. E. Observation of spatial optical solitons in a nonlinear glass waveguide. *Opt. Lett.* **1990**, *15*, 471-473.
- 62) Torruellas, W. E.; Wang, Z.; Hagan, D. J.; VanStryland, E. W.; Stegeman, G. I.; Torner, L.; Menyuk, C. R. Observation of Two-Dimensional Spatial Solitary Waves in a Quadratic Medium William. *Phys. Rev. Lett.* **1967**, *73*, 1632–1635.
- 63) Mitchell, M.; Segev, M.; Coskun, T.; Christodoulides, D. Theory of Self-Trapped Spatially Incoherent Light Beams. *Phys. Rev. Lett.* **1997**, *79*, 4990–4993.
- 64) Mitchell, M.; Chen, Z.; Shih, M. Segev, M. Self-trapping of partially spatially-incoherent light. *Phys. Rev. Lett.* **1996**, *77*, 490–493.
- 65) Mitchell, M.; Segev, M. Self-Trapping of Incoherent White Light. *Nature* **1997**, *387*, 880-883.
- 66) Shoji, S.; Kawata, S. Optically-induced growth of fiber patterns into a photopolymerizable resin. *Appl. Phys. Lett.* **1999**, *75*, 737–739.
- 67) Shoji, S.; Kawata, S.; Sukhorukov, A. A.; Kivshar, Y. S. Self-written waveguides in photopolymerizable resins. *Opt. Lett.* **2002**, *27*, 185-187.
- 68) Dorkenoo, K.; Crégut, O.; Mager, L.; Gillot, F.; Carre, C.; Fort, A. Quasi-solitonic behavior of self-written waveguides created by photopolymerization. *Opt. Lett.* **2002**, *27*, 1782–1784.
- 69) Bachelot, R.; Ecoffet, C.; Deloail, D.; Royer, P.; Lougnot, D. J. Integration of polymer elements at the end of optical fibers by free-radical photopolymerization. *Appl. Opt.* **2001**, *40*, 5860–5871.
- 70) Kagami M.; Yamashita, T.; Ito, H. Light-induced self-written three-dimensional optical waveguide. *Appl. Phys. Lett.* **2001**, *79*, 1079–1081.
- 71) Hecht, E. *Optics*, 4th ed.; Addison-Wesley, 2002.
- 72) Fischer-Hirschert, U. H. P. Optical Waveguides BT - Photonic Packaging Sourcebook: Fiber-Chip Coupling for Optical Components, Basic Calculations, Modules; Fischer-Hirschert, U. H. P., Ed.; Springer Berlin Heidelberg: Berlin, Heidelberg, 2015; pp 23–55.
- 73) Villafranca, A. B.; Saravanamuttu, K. An experimental study of the dynamics and temporal evolution of self-trapped laser beams in a photopolymerizable organosiloxane. *J. Phys. Chem. C* **2008**, *112*, 17388–17396.
- 74) Burgess, I. A.; Shimmell, W. A.; Saravanamuttu, K. Spontaneous Pattern Formation Due to Modulation Instability of Incoherent White Light in a Photopolymerizable Medium. *J. Am. Chem. Soc.* **2007**, *129*, 4738-4746.
- 75) Qiu, L.; Franc, J.; Rewari A.; Blanc D.; Saravanamuttu K. Photolytic formation of Ag nanoparticles in oligomeric organosiloxanes: new photolithographic routes to metallodielectric microperiodic structures. *J. Mater. Chem.* **2009**, *19*, 373-378.
- 76) Morim, D. R.; Bevern, D.; Vargas-Baca, I.; Saravanamuttu, K. 3-D Spiraling Self-Trapped Light Beams in Photochemical Systems. *J. Phys. Chem. Lett.* **2019**, *10*, 5957–5962.
- 77) Malallah, R.; Cassidy, D.; Muniraj, I.; Ryle, J. P.; Healy, J. J.; Sheridan, J. T. Controlling the trajectories of self-written waveguides in photopolymer. *J. Opt. Soc. Am. B* **2018**, *35*, 2046–2056 (2018).
- 78) Morim, D. R.; Meeks, A.; Shastri, A.; Tran, A.; Shneidman, A. V.; Yashin, V. V.; Mahmood, F.; Balazs, A. C.; Aizenberg, J.; Saravanamuttu, K. Opto-chemo-mechanical transduction in photoresponsive gels elicits switchable self-trapped beams with remote interactions. *Proc. Natl. Acad. Sci. U. S. A.* **2020**, *117*, 3953-3959.
- 79) Zhang, J.; Kasala, K.; Rewari, A.; Saravanamuttu, K. Self-trapping of spatially and temporally incoherent white light in a photochemical medium. *J. Am. Chem. Soc.* **2006**, *128*, 406–407.

- 80) Zhang, J.; Saravanamuttu, K. The dynamics of self-trapped beams of incoherent white light in a free-radical photopolymerizable medium. *J. Am. Chem. Soc.* 2006, *128*, 14913–14923.
- 81) Burgess, I. B.; Shimmell, W. E.; Saravanamuttu, K. Spontaneous pattern formation due to modulation instability of incoherent white light in a photopolymerizable medium. *J. Am. Chem. Soc.* **2007**, *129*, 4738–4746.
- 82) Burgess I. B.; Ponte M.; Saravanamuttu K. Spontaneous formation of 3-D optical and structural lattices from two orthogonal and mutually incoherent beams of white light propagating in a photopolymerisable material. *J. Mater. Chem.* **2008** *18*, 4133–4139.
- 83) Ponte, M. R.; Welch, R.; Saravanamuttu, K. An optochemically organized nonlinear waveguide lattice with primitive cubic symmetry. *Opt. Express* **2013**, *21*, 4205-4214.
- 84) Hudson, A. D.; Ponte, M. R.; Mahmood, F.; Pena Ventura, T.; Saravanamuttu, K. A soft photopolymer cuboid that computes with binary strings of white light. *Nat. Commun.* **2019**, *10*, 1–9.
- 85) Hudson, A. D.; Bacus, C.; Whinton, M.; Brook, M. A.; Saravanamuttu, K. Single-Step Generation of Flexible, Free-Standing Arrays of Multimode Cylindrical Waveguides. *Adv. Eng. Mater.* **2019**, *21*, 1800875.
- 86) Lin, H.; Benincasa, K. A.; Fradin, C.; Saravanamuttu, K. Shaping LED Beams with Radially Distributed Waveguide-Encoded Lattices. *Adv. Optical Mater.* **2019**, *7*, 1801487.
- 87) Lin, H.; Hosein, I. D.; Benincasa, K. A.; Saravanamuttu, K. A Slim Polymer Film with a Seamless Panoramic Field of View: The Radially Distributed Waveguide Encoded Lattice (RDWEL). *Adv. Optical Mater.* **2019**, *7*, 1801091.
- 88) Hull, C. W. The birth of 3D printing. *Research Technology Management* **2015**, *58*, 25–29.
- 89) Truby, R. L.; Lewis, J. A. Printing soft matter in three dimensions. *Nature* **2016**, *540*, 371–378.
- 90) Wallin, T.J.; Pikul, J.; Shepherd, R.F. 3D printing of soft robotic systems. *Nat Rev Mater* **2018**, *3*, 84–100 (2018).
- 91) Dizon, J. R. C.; Espera, A. H.; Chen, Q.; Advincula, R. C. Mechanical Characterization of 3D-Printed Polymers. *Addit. Manuf.* **2018**, *20*, 44–67.
- 92) Gojzewski, H.; Guo, Z.; Grzelachowska, W.; Ridwan, M. G.; Hempenius, M. A.; Grijpma, D. W.; Vancso, G. J. Layer-by-Layer Printing of Photopolymers in 3D: How Weak Is the Interface? *ACS Appl. Mater. Interfaces* **2020**, *12*, 8908–8914.
- 93) Tumbleston, J. R.; Shirvanyants, D.; Ermoshkin, N.; Januszewicz, R.; Johnson, A. R.; Kelly, D.; Chen, K.; Pinschmidt, R.; Rolland, J. P.; Ermoshkin, A.; et al. Continuous Liquid Interface Production of 3D Objects. *Science (80-.)*. **2015**, *347*, 1349–1352.
- 94) de Beer, M. P.; van der Laan, H. L.; Cole, M. A.; Whelan, R. J.; Burns, M. A.; Scott, T. F. Rapid, Continuous Additive Manufacturing by Volumetric Polymerization Inhibition Patterning. *Sci. Adv.* **2019**, *5*, eaau8723.
- 95) Regehly, M.; Garmshausen, Y.; Reuter, M.; König, N. F.; Israel, E.; Kelly, D. P.; Chou, C. Y.; Koch, K.; Asfari, B.; Hecht, S. Xolography for linear volumetric 3D printing. *Nature* **2020**, *588*, 620–624.
- 96) Shusteff, M.; Browar, A. E. M.; Kelly, B. E.; Henriksson, J.; Weisgraber, T. H.; Panas, R. M.; Fang, N. X.; Spadaccini, C. M. One-Step Volumetric Additive Manufacturing of Complex Polymer Structures. *Sci. Adv.* **2017**, *3*, eaao5496.
- 97) US3778614-Method and apparatus for measuring x- or g-radiation absorption or transmission at plural angles and analyzing the data, 1973.

- 98) Bortfeld, T.; Bürkelbach, J.; Boesecke, R.; Schlegel, W. Methods of image reconstruction from projections applied to conformation radiotherapy. *Phys. Med. Biol.* **1990**, *35*, 1423–1434.
- 99) Kelly, B. E.; Bhattacharya, I.; Heidari, H.; Shusteff, M.; Spadaccini, C. M.; Taylor, H. K. Volumetric Additive Manufacturing via Tomographic Reconstruction. *Science (80-.)*. **2019**, *363*, 1075 LP – 1079.
- 100) Loterie, D.; Delrot, P.; Moser, C. High-resolution tomographic volumetric additive manufacturing. *Nat. Commun.* **2020**, *11*, 1–6.
- 101) Nunez, B. P.; Delrot, P.; Loterie, D.; Li, Y.; Malda, J.; Moser, C.; Levato, R. Volumetric Bioprinting of Complex Living-Tissue Constructs within Seconds. *Adv. Mater.* **2019**, *31*, 1904209.
- 102) Cook, C. C.; Fong, E. J.; Schwartz, J. J.; Porcincula, D. H.; Kaczmarek, A. C.; Oakdale, J. S.; Moran, B. D.; Champley, K. M.; Rackson, C. M.; Muralidharan, A.; McLeod, R. R.; Shusteff, M. Highly Tunable Thiol-Ene Photoresins for Volumetric Additive Manufacturing. *Adv. Mater.* **2020**, *32*, 1–6.
- 103) Dolinski, N. D.; Page, Z. A.; Callaway, E. B.; Eisenreich, F.; Garcia, R. V.; Chavez, R.; Bothman, D. P.; Hecht, S.; Zok, F. W.; Hawker, C. J. Solution Mask Liquid Lithography (SMaLL) for One-Step, Multimaterial 3D Printing. *Adv. Mater.* **2018**, *30*, 1800364.
- 104) Maruo, S.; Nakamura, O.; Kawata, S. Three-dimensional microfabrication with two photon-absorbed photopolymerization. *Opt. Lett.* **1997**, *22*, 132–134.
- 105) Saha, S. K.; Wang, D.; Nguyen, V. H.; Chang, Y.; Oakdale, J. S.; Chen, S. C. Scalable submicrometer additive manufacturing. *Science* **2019**, *366*, 105–109.
- 106) Geng, Q.; Wang, D.; Chen, P.; Chen, S. C. Ultrafast multi-focus 3-D nano-fabrication based on two-photon polymerization. *Nat. Commun.* **2019**, *10*, 1–7.
Sundaram, S.; Skouras, M.; Kim, D. S.; van den Heuvel, L.; Matusik, W. (2019). Topology optimization and 3D printing of multimaterial magnetic actuators and displays. *Sci. Adv.* **2019**, *5*, eaaw1160.
- 107) Podstawczyk, D.; Nizioł, M.; Szymczyk, P.; Wiśniewski, P.; Guiseppi-Elie, A. 3D printed stimuli-responsive magnetic nanoparticle embedded alginate-methylcellulose hydrogel actuators. *Additive Manufacturing*, 2020, *34* 101275.
- 108) Vaseem, M.; Ghaffar, F. A.; Farooqui, M. F.; Shamim, A. Iron Oxide Nanoparticle-Based Magnetic Ink Development for Fully Printed Tunable Radio-Frequency Devices. *Adv. Mater. Technol.* **2018**, *3*, 1700242.
- 109) Odent, J.; Wallin, T. J.; Pan, W.; Kruemplestaedter, K.; Shepherd, R. F.; Giannelis, E. P. Highly Elastic, Transparent, and Conductive 3D-Printed Ionic Composite Hydrogels. *Adv. Funct. Mater.* 2017, *27*, 1701807.
- 110) Yuk, H., Lu, B., Lin, S., Qu, K., Xu, J., Luo, J.; Zhao, X. 3D printing of conducting polymers. *Nat. Commun.* 2020, *11*, 1604.
- 111) Chizari, K.; Daoud, M. A.; Ravindran, A. R.; Therriault, D. 3D Printing of Highly Conductive Nanocomposites for the Functional Optimization of Liquid Sensors. *small* **2016**, *12*, 6076–6082.
- 112) Tan, H. W., An, J., Chua, C. K., Tran, T. Metallic Nanoparticle Inks for 3D Printing of Electronics. *Adv. Electron. Mater.* **2019**, *5*, 1800831.
- 113) Hua, M.; Wu, D.; Wu, S.; Ma, Y.; Alsaid, Y.; He, X. 4D Printable Tough and Thermoresponsive Hydrogels. *ACS Appl. Mater. Interfaces* **2021**, *13*, 12689–12697.

- 114) Davidson, E. C., Kotikian, A., Li, S., Aizenberg, J., Lewis, J. A. 3D Printable and Reconfigurable Liquid Crystal Elastomers with Light-Induced Shape Memory via Dynamic Bond Exchange. *Adv. Mater.* **2020**, 32, 1905682.
- 115) Panwisawas, C.; Tang, Y. T.; Reed, R. C. Metal 3D printing as a disruptive technology for superalloys. *Nat Commun* **2020**, 11, 2327.
- 116) Wei, Q.; Li, H.; Liu, G.; He, Y.; Wang, Y.; Tan, Y. E.; Wang, D.; Peng, X.; Yang, G.; Tsubaki, N. Metal 3D printing technology for functional integration of catalytic system. *Nat Commun* **2020**, 11, 4098.
- 117) Kong, Y. L.; Tamargo, I. A.; Kim, H.; Johnson, B. N., Gupta, M. K., Koh, T. W., Chin, H. A., Steingart, D. A., Rand, B. P., & McAlpine, M. C. 3D printed quantum dot light-emitting diodes. *Nano Lett.* **2014**, 14, 7017–7023.
- 118) Yoon, I. S., Oh, Y., Kim, S. H., Choi, J., Hwang, Y., Park, C. H., Ju, B. 3D Printing of Self-Wiring Conductive Ink with High Stretchability and Stackability for Customized Wearable Devices. *Adv. Mater. Technol.* **2019**, 4, 1900363.
- 119) Huang W. M.; Ding Z.; Wang C. C.; Wei J.; Zhao Y.; H. Purnawali H. Shape memory materials. *Mater. Today* **2010**, 13, 54.
- 120) J. S. Pulskamp, R. G. Polcawich, R. Q. Rudy, S. S. Bedair, R. M. Proie, T. Ivanov, G. L. Smith. Piezoelectric PZT MEMS technologies for small-scale robotics and RF applications. *MRS Bull.* **2012**, 37, 1062.
- 121) Dharmawan A. G.; Hariri H. H.; Foong S.; Soh G. S.; Wood K. L. Steerable miniature legged robot driven by a single piezoelectric bending unimorph actuator. *Proc. - IEEE Int. Conf. on Robotics and Automation*, IEEE, Piscataway, NJ, USA 2017, p. 6008-6013.
- 122) Kuenstler, A. S.; Kim, H.; Hayward, R. C. Liquid Crystal Elastomer Waveguide Actuators. *Adv. Mater.* **2019**, 31, 1901216.
- 123) Li, S.; Bai, H.; Liu, Z.; Zhang, X.; Huang, C.; Wiesner, L. W.; Silberstein, M.; Shepherd, R. F. Digital light processing of liquid crystal elastomers for self-sensing artificial muscles. *Sci. Adv.* **2021**, 7, eabg3677.
- 124) Shahsavan, H.; Aghakhani, A.; Zeng, H.; Guo, Y.; Davidson, Z. S.; Priimagi, A., Sitti, M. Bioinspired underwater locomotion of light-driven liquid crystal gels. *Proc. Natl. Acad. Sci.* **2020**, 117, 3953.
- 125) Kuenstler, A. S.; Kim, H.; Hayward, R. C. Liquid Crystal Elastomer Waveguide Actuators. *Adv. Mater.* **2019**, 31, 1901216.
- 126) Keplinger, C.; Kaltenbrunner, M.; Arnold, N.; Bauer, S. Röntgen's electrode-free elastomer actuators without electromechanical pull-in instability. *Proc. Natl. Acad. Sci.* **2010**, 107, 4505-4510.
- 127) Gu, G.; Zhu, J.; Zhu, L.; Zhu, X. A survey on dielectric elastomer actuators for soft robots. *Bioinspir. Biomim.* **2017**, 12, 011003.
- 128) Shahinpoor, M. Ionic polymer-conductor composites as biomimetic sensors, robotic actuators and artificial muscles-a review. *Electrochim. Acta* **2003**, 48, 2343-2353.
- 129) Bar-Cohen, Y. Electroactive polymers as an enabling materials technology. *Proc. Inst. Mech. Eng., Part G* **2007**, 221, 553-564.
- 130) Mao, Y.; Yu, K.; Isakov, M. S.; Wu, J.; Dunn, M. L.; Qi, J. H. Sequential Self-Folding Structures by 3D Printed Digital Shape Memory Polymers. *Sci Rep* **2015**, 5, 13616.

- 131) Ge, Q.; Sakhaei, A. H.; Lee, H.; Dunn, C. K.; Fang, N. X.; Dunn, M. L. Multimaterial 4D Printing with Tailorable Shape Memory Polymers. *Sci Rep* **2016**, *6*, 31110.
- 132) Zarek, M.; Layani, M.; Cooperstein, I.; Sachyani, E.; Cohn, D.; Magdassi, S. 3D Printing of Shape Memory Polymers for Flexible Electronic Devices. *Adv. Mater.* **2016**, *28*, 4449–4454.
- 133) Chiolerio, A.; Quadrelli, M. B. Smart Fluid Systems: The Advent of Autonomous Liquid Robotics. *Adv. Sci.* **2017**, *4*, 1700036.
- 134) Overveldea, J. T. B.; Kloeka, T.; D’Haena, J. J. A.; Bertoldia, K. Amplifying the response of soft actuators by harnessing snap-through instabilities. *Proc. Natl. Acad. Sci.* **2015**, *112*, 10863-10868.
- 135) Ilievski, F.; Mazzeo, A. D.; Shepherd, R. F.; Chen, X.; Whitesides, G. M. Soft robotics for chemists. *Angew. Chem. Int. Ed.* **2011**, *50*, 1890–1895.
- 136) Verma, M. S.; Ainla, A.; Yang, D.; Harburg, D.; Whitesides, G. M. A Soft Tube-Climbing Robot. *Soft Rob.* **2018**, *5*, 133-137.
- 137) Lim, H. L.; Hwang, Y.; Kar, M.; Varghese, S. Smart hydrogels as functional biomimetic systems. *Biomater. Sci.* **2014**, *2*, 603–618.
- 138) Jeon, S. J.; Hauser, A. W. Hayward, R. C. Shape-Morphing Materials from Stimuli-Responsive Hydrogel Hybrids. *Acc. Chem. Res.* **2017**, *50*, 161–169
- 139) Peng, X.; Wang, H. Shape changing hydrogels and their applications as soft actuators. *J. Polym. Sci., Part B: Polym. Phys.* **2018**, *56*, 1314-1324.
- 140) Le, X.; Lu, W.; Zhang, J.; Chen, T. Recent Progress in Biomimetic Anisotropic Hydrogel Actuators. *Adv. Sci.* **2019**, *6*, 1801584.
- 141) Shang, J.; Theato, P.; Chen, T. Polymer Chemistry Trends in polymeric shape memory hydrogels and hydrogel actuators. *Polym. Chem.* **2019**, *10*, 1036–1055.
- 142) Erol, O.; Pantula, A.; Liu, W.; Gracias, D. H. Transformer Hydrogels: A Review. *Adv. Mater. Technol.* **2019**, *4*, 1900043.
- 143) Ionov, L. Biomimetic Hydrogel-Based Actuating Systems. *Adv. Funct. Mater.* **2013**, *23*, 4555–4570.
- 144) Han, D.; Farino, C.; Yang, C.; Scott, T.; Browe, D.; Choi, W.; Freeman, J. W.; Lee, H. Soft Robotic Manipulation and Locomotion with a 3D Printed Electroactive Hydrogel. *ACS Appl. Mater. Interfaces* **2018**, *10*, 21, 17512-17518.
- 145) O’Grady M. L.; Kuo, P. L.; Parker, K. K. Optimization of electroactive hydrogel actuators. *ACS Appl. Mater. Interfaces* **2010**, *2*, 2, 343–346.
- 146) Ryplida, B.; Lee, K. D.; In, I.; Park, S. Y. Light-Induced Swelling-Responsive Conductive, Adhesive, and Stretchable Wireless Film Hydrogel as Electronic Artificial Skin. *Adv. Funct. Mater.* **2019**, *29*, 1903209.
- 147) Larson, C.; Peele, B.; Li, S.; Robinson, S.; Totaro, M.; Beccai, L.; Mazzolai, B.; Shepherd, R. Highly stretchable electroluminescent skin for optical signaling and tactile sensing. *Science* **2016**, *351*, 1071–1074.
- 148) Feng, J.; Zheng, Y.; Bhusari, S.; Villiou, M.; Pearson, S., del Campo, A. Printed Degradable Optical Waveguides for Guiding Light into Tissue. *Adv. Funct. Mater.* **2020**, *30*, 2004327.
- 149) Feng, J.; Jiang, Q.; Rogin, P.; De Oliveira, P. W.; Del Campo, A. Printed Soft Optical Waveguides of PLA Copolymers for Guiding Light into Tissue. *ACS Appl. Mater. Interfaces* **2020**, *12*, 20287–20294.

- 150) Skylar-scott, M. A.; Uzel, S. G. M.; Nam, L. L.; Ahrens, J. H.; Truby, R. L.; Damaraju, S.; Lewis, J. A. Biomanufacturing of organ-specific tissues with high cellular density and embedded vascular channels. *Sci. Adv.* **2019**, 5: eaaw2459.
- 151) Kolesky, D. B.; Homan, K. A.; Skylar-scott, M. A.; Lewis, J. A. Three-dimensional bioprinting of thick vascularized tissues. *Proc. Natl. Acad. Sci.* 2016, 113, 3179–3184.
- 152) Kolesky, D. B.; Truby, R. L.; Gladman, A. S.; Busbee, T. A.; Homan, K. A.; Lewis, J. A. 3D Bioprinting of Vascularized, Heterogeneous Cell-Laden Tissue Constructs. *Adv. Mater.* **2014**, 26, 3124–3130.
- 153) Kim, Y. S.; Liu, M.; Ishida, Y.; Ebina, Y.; Osada, M.; Sasaki, T.; Hikima, T.; Takata, M.; Aida, T. Thermoresponsive actuation enabled by permittivity switching in an electrostatically anisotropic hydrogel. *Nature Mater* **2015**, 14, 1002–1007.
- 154) Dong, L.; Agarwal, A. K.; Beebe, D. J.; Jiang, H. Variable-focus liquid microlenses and microlens arrays actuated by thermoresponsive hydrogels. *Adv. Mater.* **2007**, 19, 401–405.
- 155) Beebe, D. J.; Moore, J. S.; Bauer, J. M.; Yu, Q.; Liu, R. H.; Devadoss, C.; Jo, B. H. Functional hydrogel structures for autonomous flow control inside microfluidic channels. *Nature* **2000**, 404, 588–590.
- 156) Zarzar, L. D.; Kim, P.; Aizenberg, J. Bio-inspired design of submerged hydrogel-actuated polymer microstructures operating in response to pH. *Adv. Mater.* **2011**, 23, 1442–1446.
- 157) Korevaar, P. A.; Kaplan, C. N.; Grinthal, A.; Rust, R. M.; Aizenberg, J. Non-equilibrium signal integration in hydrogels. *Nat Commun* **2020**, 11, 386.
- 158) Li, M.; Wang, X.; Dong, B.; Sitti, M. In-air fast response and high-speed jumping and rolling of a light-driven hydrogel actuator. *Nat Commun* **2020**, 11, 3988.
- 159) Goudu, S. R.; Yasa, I. C.; Hu, X.; Ceylan, H.; Hu, W.; Sitti, M. Biodegradable Untethered Magnetic Hydrogel Milli-Grippers. *Adv. Funct. Mater.* **2020**, 30, 2004975.
- 160) Morales, D.; Palleau, E.; Dickey, M. D.; Velez, O. D. Electro-actuated hydrogel walkers with dual responsive legs. *Soft Matter* **2014**, 10, 1337.
- 161) Jin, S.; Gu, J.; Shi, Y.; Shao, K.; Yu, X.; Yue, G. Preparation and electrical sensitive behavior of poly (N-vinylpyrrolidone- co-acrylic acid) hydrogel with flexible chain nature. *European Polymer Journal* **2013**, 49, 1871–1880.
- 162) Bassil, M.; Davenas, J.; EL Tahchi, M. Electrochemical properties and actuation mechanisms of polyacrylamide hydrogel for artificial muscle application. *Sensors and Actuators B* **2008**, 134, 496–501.
- 163) Bai, R.; Yang, J.; Suo, Z. Fatigue of hydrogels. *European Journal of Mechanics A/Solids* **2019**, 74, 337–370.
- 164) Kim, Y.; Parada, G. A.; Liu, S.; Zhao, X. Ferromagnetic soft continuum robots. *Sci. Robot* **2019**, 4, eaax7329.
- 165) Nye J. F.; Berry M. V. Dislocations in Wave Trains. *Proc. R. Soc. Lond. A* **1974**, 336, 165–190.
- 166) Ambrosio, A.; Marrucci, L.; Borbone, F.; Roviello, A.; Maddalena, P. Light-induced spiral mass transport in azo-polymer films under vortex-beam illumination. *Nat Commun* **2012**, 3, 989.
- 167) Allen L.; Beijersbergen M. W.; Spreeuw R. J. C.; Woerdman J.P. Orbital angular momentum of light and the transformation of Laguerre-Gaussian laser modes, *Phys. Rev. A* **1992**, 45, 8185-8189.
- 168) Gahagan, K. T., Swartzlander, G. A. Optical vortex trapping of particles. *Opt. Lett.* **1996**, 21, 827–829.

- 169) Ng, J.; Lin, Z.; Chan, C. T. Theory of optical trapping by an optical vortex beam. *Phys. Rev. Lett.* **2010**, 104, 103601.
- 170) Gu, M.; Kang, H.; Li, X. Breaking the diffraction-limited resolution barrier in fiber-optical two-photon fluorescence endoscopy by an azimuthally polarized beam. *Sci Rep* **2014**, 4, 3627.
- 171) Lavery M.; Speirts F.; Barnett S.; Padgett M. Detection of a Spinning Object Using Light's Orbital Angular Momentum. *Science* **2013**, **341**, 537-540
- 172) Bozinovic, N.; Yue Y.; Ren Y.; Tur M.; Kristensen P.; Huang H.; Willner A.; Ramachandran, S. Terabit-Scale Orbital Angular Momentum Mode Division Multiplexing in Fibers. *Science* **2013**, 340, 1545-1548.
- 173) Wang, J.; Yang, J. Y.; Fazal, I. M.; Ahmed, N.; Yan, Y.; Huang, H.; Ren, Y.; Yue, Y.; Dolinar, S.; Tur, M.; Willner, A. E. Terabit free-space data transmission employing orbital angular momentum multiplexing. *Nature Photon* **2012**, 6, 488–496.
- 174) Firth, W. J.; Skryabin, D. V. Optical solitons carrying orbital angular momentum. *Phys. Rev. Lett.* **2016**, 79, 277–280.
- 175) Andrews, D.; Babiker, M. *The Angular Momentum of Light*; Cambridge University Press. Cambridge, 2012.
- 176) Tikhonenko, V.; Christou, J.; Luther-Daves, B. Spiraling bright spatial solitons formed by the breakup of an optical vortex in a saturable self-focusing medium. *J. Opt. Soc. Am. B* **1995**, 12, 2046-2052.
- 177) Bigelow, M. S.; Zerom, P.; Boyd, R. W. Breakup of Ring Beams Carrying Orbital Angular Momentum in Sodium Vapor. *Phys. Rev. Lett.* **2004**, 92, 083902.
- 178) Petrov, D. V.; Torner, L.; Martorell, J.; Vilaseca, R.; Torres, J. P.; Cojocar, C. Observation of azimuthal modulation instability and formation of patterns of optical solitons in a quadratic crystal. *Opt. Lett.* **1998**, 23, 1444-1446.
- 179) Skryabin, D. V.; Firth, W. J. Dynamics of self-trapped beams with phase dislocation in saturable Kerr and quadratic nonlinear media. *Phys. Rev. E* **1998**, 58, 3916–3930.
- 180) Vuong, L. T.; Grow, T. D.; Ishaaya, A.; Gaeta, A. L.; Hoof, G. W.; Eliel, E. R.; Fibich, G. Collapse of optical vortices. *Phys. Rev. Lett.* **2016**, 96, 133901.
- 181) Syubaev, S.; Zhizhchenko, A.; Kuchmizhak, A.; Porfirev, A.; Pustovalov, E.; Vitrik, O.; Kulchin, Y.; Khonina, S.; Kudryashov, S. Direct laser printing of chiral plasmonic nanojets by vortex beams. *Opt. Express* **2017**, 25, 10214–10223.
- 182) Toyoda, K.; Miyamoto, K.; Aoki, N.; Morita, R.; Omatsu, T. Using optical vortex to control the chirality of twisted metal nanostructures. *Nano Lett.* **2012**, 12, 3645–3649.
- 183) Kohmura, Y.; Zhakhovskiy, V.; Takei, D.; Suzuki, Y.; Takeuchi, A.; Inoue, I.; Inubushi, Y.; Inogamov, N.; Ishikawa, T.; Yabashi, M. Nano-structuring of multi-layer material by single x-ray vortex pulse with femtosecond duration. *Appl. Phys. Lett.* **2018**, 112, 123103.
- 184) Rahimian, M. G.; Bouchard, F.; Karimi, E.; Corkum, P. B.; Bhardwaj, V. R. Polarization dependent nanostructuring of silicon with femtosecond vortex pulse. *APL Photonics* **2017**, 2, 086104.
- 185) Nakamura, R.; Kawaguchi, H.; Iwata, M.; Kaneko, A.; Nagura, R.; Kawano, S.; Toyoda, K.; Miyamoto, K.; Omatsu, T. Optical vortex-induced forward mass transfer: manifestation of helical trajectory of optical vortex. *Opt. Express* **2019**, 27, 38019–38027.
- 186) Watabe, M.; Juman, G.; Miyamoto, K.; Omatsu, T. Light induced conch-shaped relief in an azo-polymer film. *Sci Rep* **2014**, 4, 4281.

- 187) Lee, J.; Arita, Y.; Toyoshima, S.; Miyamoto, K.; Panagiotopoulos, P.; Wright, E. M.; Dholakia, K.; Omatsu, T. Photopolymerization with Light Fields Possessing Orbital Angular Momentum: Generation of Helical Microfibers. *ACS Photonics* **2018**, *5*, 4156–4163.
- 188) Nagura, R.; Tsujimura, T.; Tsuji, T.; Doi, K.; Kawano, S. Coarse-grained particle dynamics along helical orbit by an optical vortex irradiated in photocurable resins. *OSA Continuum* **2019**, *2*, 400-415.
- 189) Haugh, N.; Chirality, M.; Korea, S. Photopolymerization with high-order Bessel light beams. *Opt. Lett.* **2020**, *45*, 4080–4083.

2 Decomposition and 3D Printing of Volumetric Prismatic Elements using Nonlinear Optochemical Waves*

2.1 Abstract

Prismatic 3D printing exploits the use of nonlinear waves from light-emitting diodes (LEDs) to create volumetric micro- and macroscopic structures. This technique harnesses the process of optical self-trapping that occurs in the presence of photo-induced refractive index changes from the free-radical photopolymerization of acrylate monomers. Unlike traditional layer-by-layer 3D printing, this approach creates a prism in a single step using a patterned optical profile. Objects were decomposed into eligible prismatic fragments using a segmentation algorithm that converts a three-dimensional mesh into volumetric prisms. The resulting prisms were fused either during or after the printing process to assemble the final object. Fusing of intersecting prisms during the printing process was achieved by launching different optical profiles at different angles by rotating the sample. Prismatic 3D printing offers increased printing speeds, improved mechanical properties and the ability to impart the elements with different functionalities.

2.2 Introduction

3D printing has been harnessed for the fabrication of a variety of objects for applications ranging from biomedical materials to smart robotics — these processes convert digital designs into a physical form.¹⁻⁴ A large assortment of printing techniques have emerged over the years including inkjet printing,⁵ fused deposition modeling,⁶ selective laser sintering,⁷ and stereolithography.⁸ Many of these technologies are based on the sequential printing of layers of patterned material and boast faster production times⁹ and lower production costs¹⁰ than traditional

*I was responsible for adapting the resins to our 3-D printed method as well as for printing some of the objects. Derek R. Morim was responsible for writing the segmentation algorithm to decompose all objects. We both contributed equally to this work. Diego Colin, Eduardo Alonso Martinez and Ramon Arora printed some of the objects and also helped to make some of the images. Derek R. Morim and K. Saravanamuttu and I wrote the manuscript. Part of this chapter was included in Derek Morim's Ph.D. Thesis: (Morim, D. (2019). Harnessing Optochemical Waves in Polymers: From Beam Interactions to Inscription of Prismatic Elements [Doctoral dissertation, McMaster University]. Macsphere. <http://hdl.handle.net/11375/24750>.

manufacturing approaches. For example, stereolithographic 3D printers write a 2D pattern into a thin layer of photopolymer attached to a stage.⁸ The stage is then translated to expose another layer of resin to a new pattern of light, and the process repeated until the object is fabricated.

3D printing techniques that rely on the layer-by-layer assembly of polymer objects can have long printing times and can impart mechanical weakness along the planes of the printed layers.^{11,12} To circumvent these limitations of printing with layers, continuous printing methods have been introduced which mitigate these weaknesses while obtaining reasonable resolutions. These techniques include continuous liquid interface production (CLIP),¹³ volumetric methods that rely on tomographic reconstruction^{14,15} and those that rely on the propagation of nonlinear photochemical waves.^{16,17}

Continuous liquid interface production (CLIP) is analogous to stereolithographic printing but uses a resin bath containing an oxygen-permeable window that inhibits photopolymerization, creating a polymerization dead zone that allows the object to be translated more rapidly within the resin.¹³ This process is significantly faster (500 mm/hour) than conventional stereolithography (few mm/hour) as the layers are formed continuously and create more seamless objects.

Volumetric methods that rely on tomographic reconstruction overcome the need for layer-by-layer printing by calculating the necessary optical profiles required to generate an object volume instead of the individual layers.^{14,15,18,19} Computed axial lithography (CAL), a technique based on the concept of computed tomography (CT) imaging, calculates the profile required from a digital light processing (DLP) projector at different angles in order to create the object of interest within seconds. While this technique is capable of printing objects in both static¹⁴ and rotating^{18,19} resins, the response of the material is nonlinear and will change more quickly near the front end of the sample. The volumetric printing is also susceptible to gravitational and centripetal forces,

absorbance, scattering, and oxygen inhibition, creating a complex system of variables that needs to be adjusted for each resin.

While the propagation of nonlinear photochemical waves must also consider the same variables seen with volumetric printing methods, the effects of centripetal forces, absorbance, scattering and oxygen inhibition are eliminated, reduced, or even have a positive effect on the printing process. Nonlinear waves produced from optical patterns from light-emitting diodes (LEDs) can trigger the cationic photopolymerization of epoxides to create 3D objects from 2D amplitude masks.¹⁶ Light employed in traditional stereolithographic techniques broadens due to the natural diffraction of an optical beam as it propagates. The divergence of an optical beam will blur the projected image as it travels in space, minimizing the depth at which a pattern will retain its resolution, but nonlinear systems can control the divergence of light as it traverses the resin by taking advantage of the photo-induced changes in refractive index that occur due to photopolymerization, thus allowing an image to retain its shape as it travels. The use of self-propagating beams to create three-dimensional objects has been used to create macroscopic objects,¹⁶ microscopic light-guiding features such as optical waveguides²⁰ and can also take advantage of other properties of the resin to manipulate the polymerization and final objects. For example, polymerization rates and absorbance can be adjusted by adding photochromic molecules that activate at the printing wavelength and improve spatial resolution.²¹ Photoinhibitors that activate with a second wavelength to decrease polymerization rates can be used to enhance resolution by using this wavelength in unwanted regions.^{22,23} This is achieved using a photoinitiator/photoinhibitor system in which polymerization is triggered with blue light and inhibition with UV light. Xolography is another method that uses two different wavelengths simultaneously.²⁴ A sheet of UV light with a specific thickness is launched to a resin with a dual-colour photoinitiator (DCPI) that takes the

photoinitiator from an inactive state to a short-lived ($t_{1/2} = 6$ s) latent state that absorbs in the visible region. A second orthogonal laser projects a slice of a 3D object to be printed in the sheet while exciting the photoinitiator that in combination with a co-initiator triggers free-radical polymerization. After the slice has cured, the resin volume is displaced while keeping the sheet of light in the same position to create a different slice of the object.

Prismatic 3D printing builds on the methods that use nonlinear photochemical waves and focuses on the potential geometries that this technique enables — prisms — polyhedra with two parallel faces. Due to the nature of the propagation of these patterns through the resin, right prisms such as cubes, cylinders, rectangular and triangular prisms are the easiest to print, but oblique prisms such as trapezoidal prisms are also possible by changing the printing intensity. The optical pattern determines the shape of the bases (2 parallel faces) of the prism. We illustrate the buildup of increasingly complex objects composed of prismatic elements using an LED, a series of amplitude masks, and a rotatable sample stage with a fast-curing acrylate photoresin. The intensity-dependence of this process is highlighted, illustrating the ability to create tapered and broadened structures, as well as the prismatic elements that maintain their shape as they propagate. A systematic approach is described that breaks down 3D objects into printable volumetric prismatic elements — these elements are permitted to intersect allowing for further buildup of objects from nonlinear waves.

The formation of structures with nonlinear waves relies on the light-induced positive changes in refractive index (Δn) that arise from photopolymerization to counteract the natural divergence of the beam in the medium.^{25,26} This process can be described by (1) where the electric field amplitude (ε) can be described in terms of the free-space wavenumber of the optical field (k_0), the

attenuation coefficient of the medium (α), and the diffraction of the beam described by the transverse Laplacian (∇_t^2).

$$ik_0n_0\frac{\partial\varepsilon}{\partial z} + \frac{1}{2}\nabla_t^2\varepsilon + k_0^2n_0\Delta n\varepsilon + \frac{i}{2}k_0n_0\alpha\varepsilon = 0 \quad (2.1)$$

As the refractive index increases, the beam will self-focus and narrow, until diffraction is suppressed, and a self-trapped beam is formed.

2.3 Results and Discussion

2.3.1 Prismatic Printing Process and Calibration

The prismatic 3D printing optical apparatus (Figure 2) is calibrated by printing a cylinder using a circular or near-Gaussian beam introduced into a resin. A blue beam ($\lambda = 460$ nm) is launched through an amplitude mask with a circular pattern onto the entrance face of a cell that contains an acrylate photoresin and a visible light photoinitiator system (Figure 2a). A side-view image illustrates the propagation of the polymerization front (Figure 2b) within the photoresin as a 5 mm circular input beam (1.1 mW mm^{-2}) propagates through the 11 mm sample. After a delay time of ~ 10 s from inhibition due to the presence of oxygen,²⁶ the propagating polymerization front can be seen travelling at a linear velocity of ~ 1.3 mm/s, which translates to printing speeds of over 1000 mm/h; speeds faster than traditional SLA methods.

Observation of the spatial intensity profile at the exit face of a separate 11 mm sample with a 2 mm input width (Figure 2c) shows that as photopolymerization and the corresponding positive changes in refractive index occur, the light begins to self-trap causing the diffracted beam to narrow, changing the light distribution and the effective intensity in the central region of printing.

The intensity of the light at the exit plane as visualized by the camera increases by 4.4-fold during the course of the experiment. By controlling the intensity of the incident light, the rate of photopolymerization and the propagation properties change.

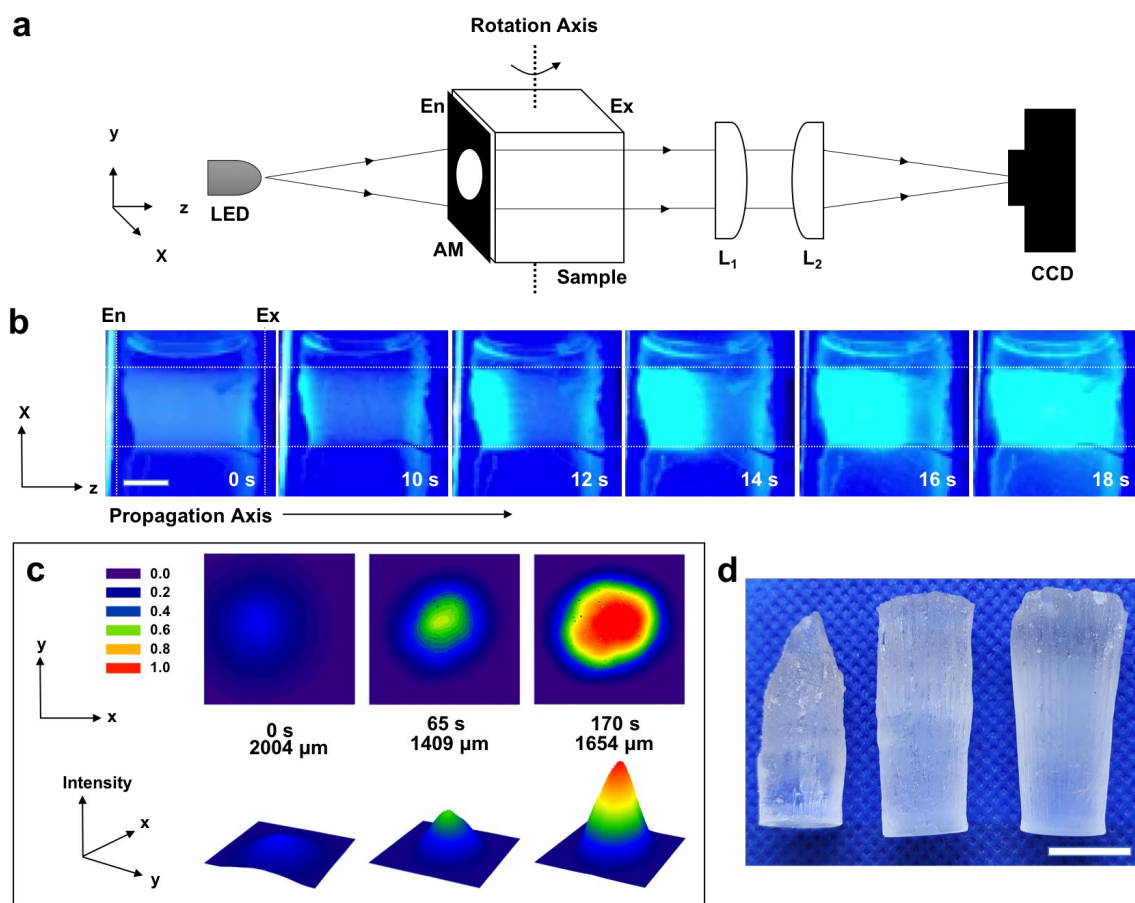


Figure 2.1 (a) Scheme of the optical assembly employed consisting of a blue LED ($\lambda = 460$ nm) and up to 3 amplitude masks (AM) placed at the transparent walls of the rotatable resin cell. Imaging of the optical profile at the exit face of the resin bath during the formation of cylinders was achieved with a planoconvex lens pair (L_1 , f.l. = 250 mm and L_2 , f.l. = 250 mm) and a CCD camera. (b) Side-view images of the growing cylinder with input width = 5 mm, length = 11 mm, intensity = 1.1 mW mm^{-2} and scale bar = 2 cm. The sample cell consisted of a cut syringe with glass cover slips glued to each end. (c) Time evolution of the spatial intensity profile at the exit plane of the sample with a growing cylinder with input width = 2 mm, length = 11 mm (Scale bar = 1 cm). (d) Final printed polymer cylinders with input width = 10 mm, length = 27 mm and obtained with an LED beam at incident intensities from left to right of 0.47 mW mm^{-2} , 1.1 mW mm^{-2} and 1.9 mW mm^{-2} . Scale bar = 1 cm.

In order to identify an appropriate operational intensity, we performed several experiments where we fabricated cylinders at different intensities (Figure 2d). A 10 mm input beam with an intensity of 0.47 mW mm^{-2} launched into a 27 mm long sample resulted in a tapered structure, with a decreasing cross-section as it propagates along z . This behaviour is attributed to the polymerization occurring predominantly in the centre as the outer regions of the beam are not intense enough to overcome inhibition due to oxygen. In contrast, higher intensities of 1.9 mW mm^{-2} produce a large concentration of initial radicals in regions of the diffracted profile which can initiate polymerization in those outer regions before self-trapping has time to occur. This results in an oblique structure that gets larger as the light propagates. It is only at the intermediate intensity of 1.1 mW mm^{-2} that the propagation of the 2D circular beam results in the inscription of a cylinder. The aforementioned calibration must be carried out for all photopolymer systems due to their varying kinetics. While this calibration may seem tedious, the printing of a prism during the calibration confirms that the intensity, absorbance, oxygen content and polymerization rate are collectively at their necessary amounts to obtain a right-angled prism.

Prismatic 3D printing can be used to sequentially print individual prisms with nonlinear waves using separate amplitude masks placed on the sides of the resin cell. The prisms can be combined within the same sample cell or glued together separately if the prisms do not intersect. Each prism is fabricated with a unique optical pattern imposed to the LED beam to create the desired part of the object by propagating through the sample – the beam is then blocked, and the resin bath rotated to launch the beam through another amplitude mask to create a different prismatic element. The propagating element must connect with the previous element when this in situ process is implemented, rotating the sample each time and repeating the process until the full object is

complete. In order to identify prismatic elements within a 3D object, a manual method for mesh segmentation was implemented.

2.3.2 Decomposition of Objects into Prismatic Elements

The systematic decomposition or segmentation of complex objects into separate elements is based on pattern recognition and specific criteria. Mesh segmentation can occur based on comparison to known models such as geometric primitives²⁷⁻³⁰ or even based on parameters such as surface topology,³¹ hidden lines and internal faces,³²⁻³⁶ or printing volume.³⁷

Our manual approach to mesh segmentation is based on the identification of hidden lines and concealed internal faces to partition an object into prisms.³³ The printing of an object, O , requires that it can be decomposed into prisms, P_n , such that the union of all prismatic elements results in the formation of the object (2).

$$O = P_1 \cup P_2 \cup \dots P_n \quad (2.2)$$

This approach begins by taking a 3D mesh — a file comprised of the vertices, edges and faces that define a 3D object — and sequentially performing operations until prismatic elements are formed. Due to the nature of the printing process, it is necessary that each element takes the shape of a prism (e.g., rectangular, triangular and trapezoidal prisms, cylinders, etc.) and prohibits some geometric features based on 2 basic rules:

Rule 1: If two triangular faces share an edge, the mesh is not printable.

Rule 2: Two non-rectangular/non-trapezoidal faces cannot share an edge.

Each right-angled prism will have rectangles orthogonal to the propagation direction and each oblique prism (e.g., trapezoidal prism) will have trapezoids orthogonal to the propagation axis. These rules prevent the prismatic printing of spheres, cones and pyramids, for example.

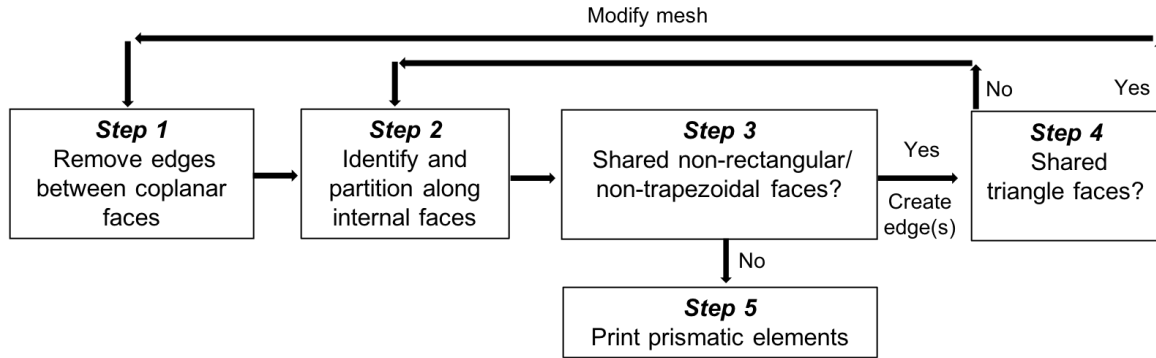


Figure 2.2 Flowchart depicting the decomposition steps that were carried out to convert mesh files into printable prismatic elements and the decomposition of 3 objects. Algorithm written by Dr. Derek Morim.

Figure 2.2 shows a flow chart that includes the necessary steps for the decomposition of objects into prismatic elements:

Step 1: Edges between attached coplanar faces are removed. This step is taken to ensure that an object is broken down into the fewest number of possible fragments to reduce the number of printing steps.

Step 2: Internal faces are identified within the mesh.³³ These internal faces are comprised of visible edges and vertices, and do not intersect with any other edges within the object. Partitioning along these internal faces creates 2 fragments, each possessing a copy of the internal face and its associated vertices and edges.

Step 3: The geometric requirement for printable prisms is the presence of rectangular or trapezoidal faces adjacent to each base. There can therefore be no two adjacent faces that are not rectangular or trapezoidal. If two such faces share an edge, then one must modify the object by creating new edges until this is no longer true. The new edge should be drawn on the face comprised of more edges and it should be drawn either parallel or orthogonal to the shared edge; this process reduces the final number of components by breaking down the more complex polygon.

Step 4: If at any point during the decomposition there exist two adjacent triangles that share an edge, the object is not printable via prismatic 3D printing and the mesh must be modified before returning to step 1. While our remeshing was performed manually, there exist interpolating methods and even a polycube mapping method that can change the mesh of an object.³⁸⁻⁴⁰

Step 5: If the reduced elements contain no two adjacent non-rectangular/non-trapezoidal faces, then that prismatic element can be printed via this printing method. Otherwise, repeat steps 2, 3, and 4 until this becomes true.

The manual decomposition was carried out for each object prior to printing, and each prismatic element was assigned a different colour for clarity. The simplest decomposition occurs when the object is already a prism. In these cases, there exist no edges between coplanar faces (*Step 1*), no internal faces (*Step 2*) and no adjacent non-rectangular/non-trapezoidal faces (*Step 3*). The only two faces with more than 4 edges are the bases of the prism and allows the object to be identified as a printable prismatic element (*Step 5*). Figure 2.3 depicts the decomposition of a house with two inequivalent slanted rooftops. Although two triangular prisms and a rectangular prism are clearly visible, the printing of this house would require 3 steps for 3 prisms. The removal of edges shared between the coplanar triangular and rectangular faces (*Step 1*) reduces the overall number of printing steps. No internal faces are present (*Step 2*) but there exist two 6-sided faces that share an edge (*Step 3*), so an additional edge was drawn parallel to the shared edge. With no shared triangular faces (*Step 4*), we proceed to identify an internal face that can be partitioned (*Step 2*). The resulting elements have no adjacent non-rectangular/non-trapezoidal faces (*Step 3*) and can therefore be printed. (*Step 5*). The 2 printed elements were printed in a total of ~55 s.

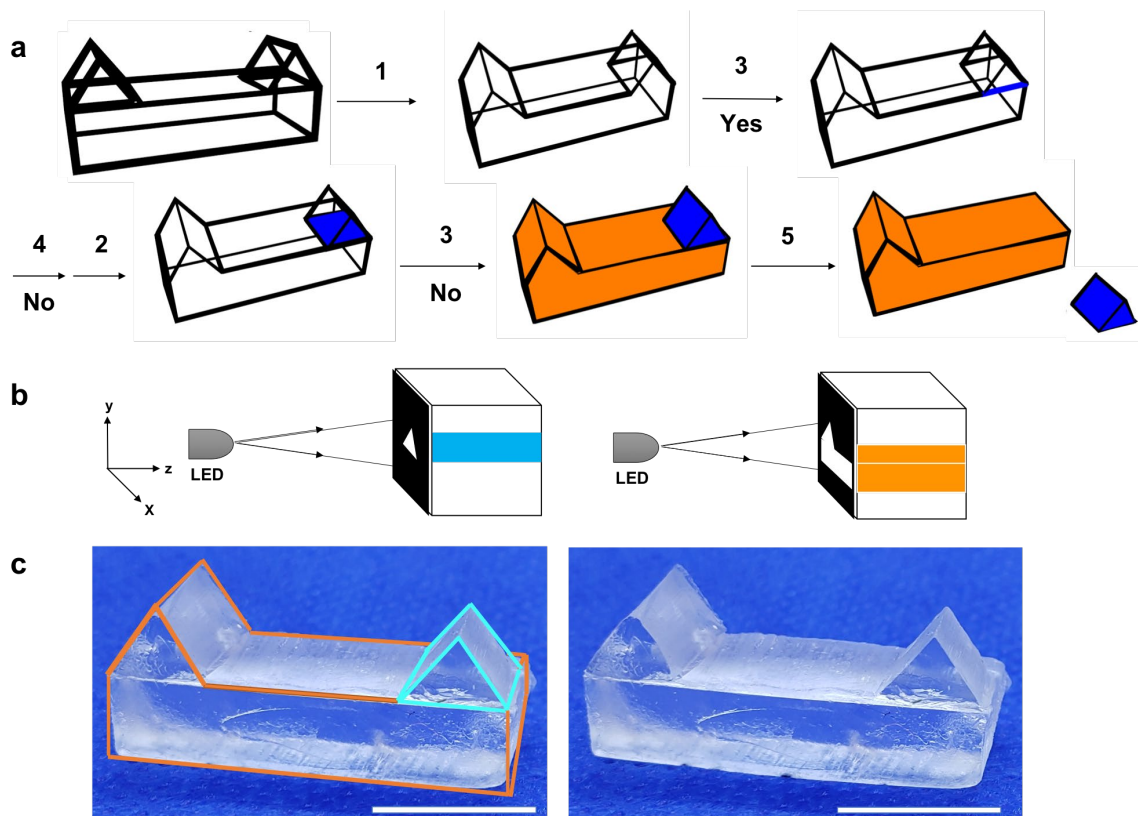


Figure 2.3 (a) Decomposition of a house into 2 separate prismatic elements. (b) Separate printing of each element. (c) House constructed from glued fragments based on the identification of prisms. Scale bar = 1 cm.

The next example (Figure 2.4) illustrates what occurs when the algorithm encounters a non-printable element. There are no shared edges between coplanar faces (*Step 1*) and multiple internal faces (*Step 2*) exist in the object, resulting in several rectangular pyramids after the partitioning. Rectangular pyramids violate *Rule 1* since they possess shared triangular faces (*Step 4*). The only way to mitigate this issue is to convert the rectangular pyramids into trapezoidal prisms and repeating *Steps 1-5*. The resulting trapezoidal prisms were fabricated using higher intensities, capturing and inscribing the diffracted profile (Figure 2.1d). Printing of 5 trapezoidal prisms and one rectangular prism was completed in a total of ~160 s. Additional examples of decomposition

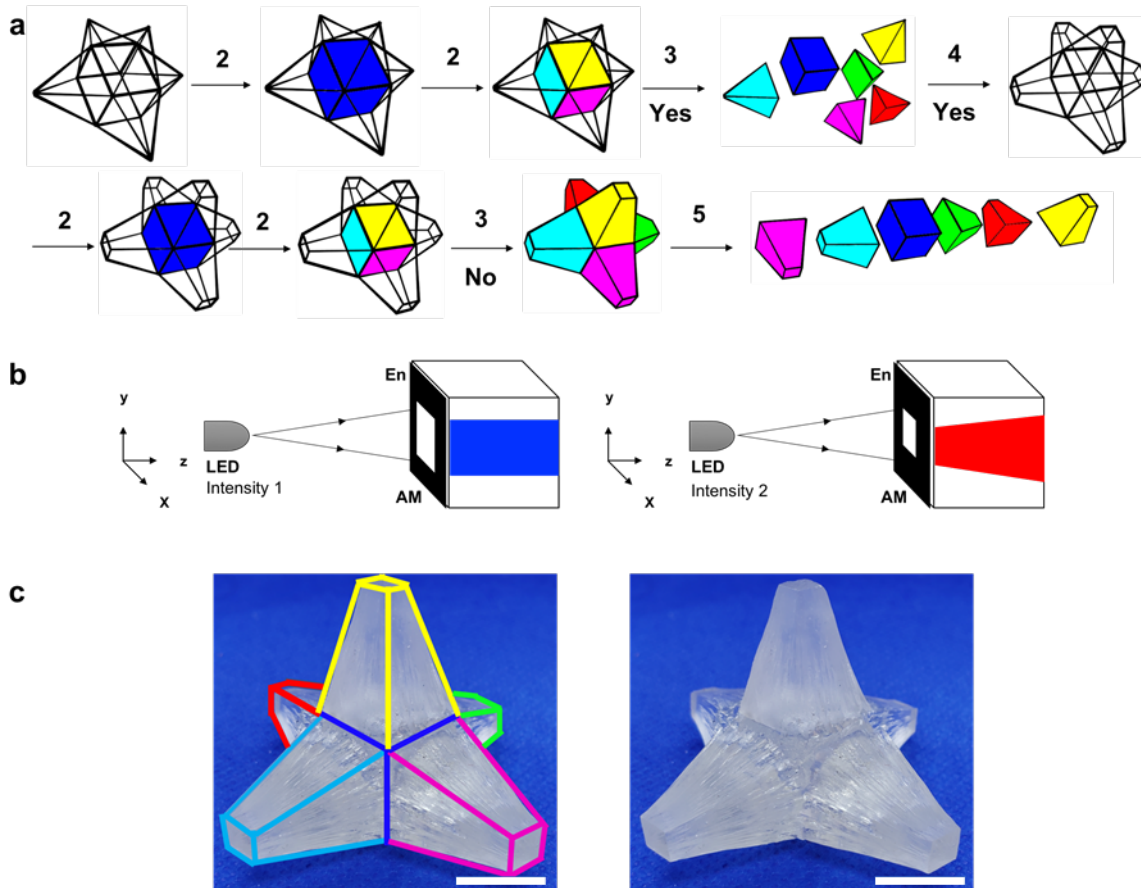


Figure 2.4 (a) Decomposition of an object into separate printable, prismatic elements based on the removal of triangular pyramid volumetric elements. (b) Separate in printing of each element. (c) House constructed from glued fragments based on the identification of prisms. Scale bar = 1 cm.

into prisms and subsequent prismatic 3D printing can be found in Figure 2.5 and the Supplementary Information.

2.3.3 Printing of Intersecting Prismatic Elements

The union of prismatic elements according to *Step 2* remains true in instances when the prismatic elements intersect. The following section highlights our ability to decompose these intersecting prisms, by combining multiple decomposition pathways. Figure 2.5 depicts the decomposition of a runner using the previously described steps (Figure 2.2).

The runner (Figure 2.5) possesses no shared edges between coplanar faces (*Step 1*) but does possess several internal faces (*Step 2*) based on the mesh of the object. Depending on which partition occurs first, one obtains either two prismatic body pieces and one unprintable non-prismatic head OR one prismatic head and two unprintable non-prismatic body pieces. Both routes on their own are unable to create the necessary elements to build the object, but a subset of prismatic elements (P) within that superset (S) exist (*Step 3*) such that those prisms can combine to create an object according to (*Step 2*).

$$P \subseteq S \quad (2.3)$$

As long as there exist enough volumetric prisms to cover the volume of the final object, the object can be printed, even in instances of intersection. This runner is printed using 3 amplitude masks and the sequential rotation of the sample. The LED beam was first launched through a circular mask to create the head. This was followed by a 90-degree rotation and use of one body mask to create half of the body by stopping the polymerization once the propagating wavefront reached halfway. Finally, the resin bath was rotated 180° and the beam was launched through a second body mask until the second half of the runner's body fused with the other half (Figure 2.5). The total printing time of the runner was ~40 s, and the process was extended to fabricate 2 additional runners (Figure 2.6, Supplementary Information). To reaffirm that these intersecting prismatic elements can be created, we printed a lattice of intersecting rods (Figure 2.6) using 3 masks that each contain 9 square apertures. A lattice of 27 intersecting rods was fabricated. The union of prismatic elements to create objects suggests that not only we can break down objects into prismatic elements, but we can build up objects from a set of known prisms by creating meshes that comprise of unified prisms.

In order to compare the quality and speed of our technique with traditional stereolithography, we printed a runner using an SLA printer with the same photoresin (Figure 2.5c). Our technique was significantly faster with a printing time of 40 s compared to 9960 s with the SLA printer. The minimum feature size in the XY direction that can be printed via prismatic printing is on the order of 500 μm while those obtained with a Form 2 SLA printer are on the order of 100 μm .

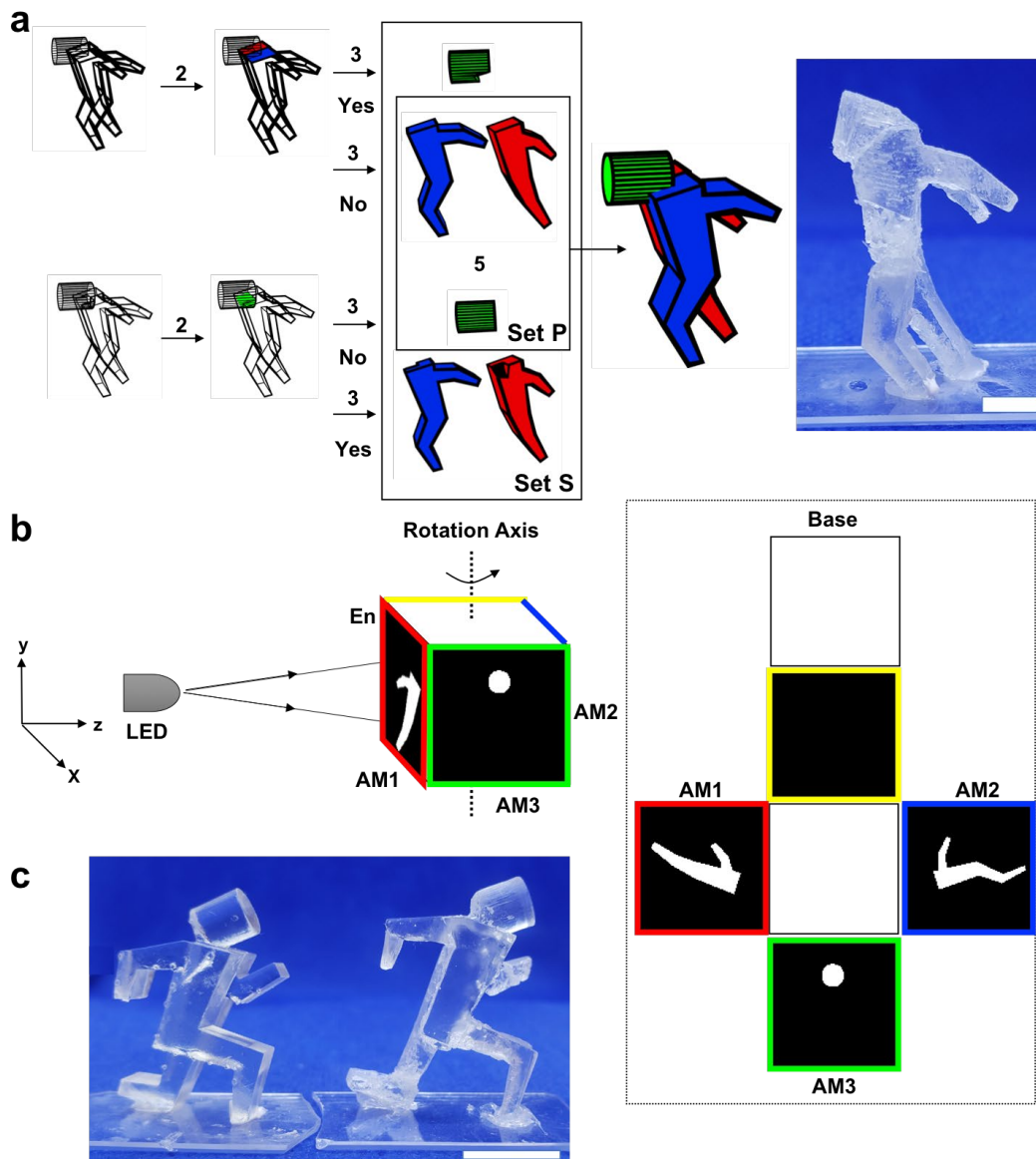
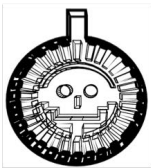


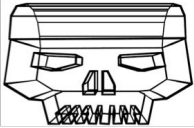


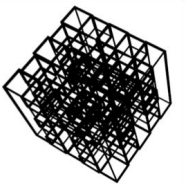
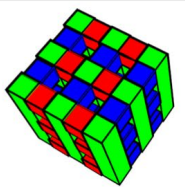


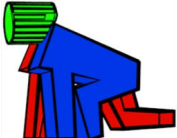
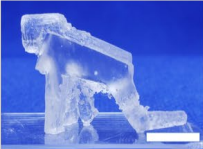








Figure 2.5 (a) Decomposition of a runner using two degenerate methods and the fabrication of a runner. Scale bar = 1 cm. (b) The object was printed by first projecting light onto AM1 of the cell containing photopolymerizable resin, and then subsequently rotating the cell to AM2 and AM3 once each previous element was printed. (c) Images depicting a runner printed using SLA (left) and prismatic 3D printing (right). Scale bar = 1 cm.

A summary of the meshes, fragmented models from the decomposition and the final printed structures are displayed in Figure 2.6.

Mesh	Fragments	Object
		
		
		
		
		
		

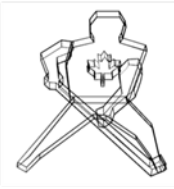

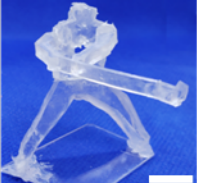
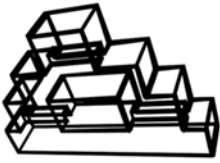
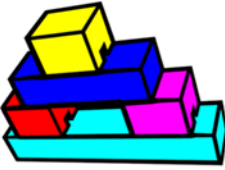


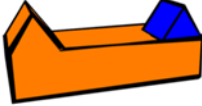
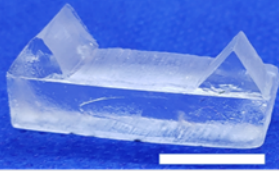

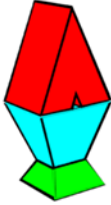
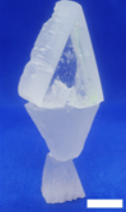
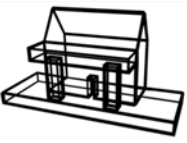

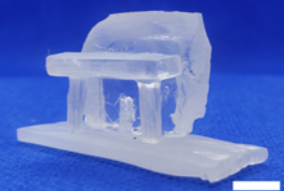


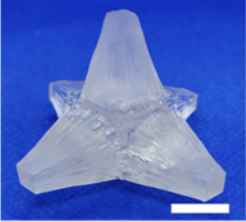
Mesh	Fragments	Object
		
		
		
		
		
		

Figure 2.6 Illustration of fragmented model from various meshes and the resulting printed objects.

2.3.4 Printing Prisms Embedded with Microscopic Waveguide Arrays

We have previously shown that it is possible to generate arrays of micro-waveguides in polymers with periodic amplitude masks.⁴¹⁻⁴³ The fabrication of these micro-arrays is carried out at intensities significantly lower ($\sim 0.01 \text{ mW/cm}^2$) than the ones used for volumetric prismatic elements (1.1 mW/mm^2). When such intensities are used after the LED beam is passed through a periodic amplitude mask, the entire sample cures to the same extent and no periodic microstructure is formed within the polymer.⁴⁴ For example, in our modified version of Autodesk with Irgacure 819 alone or in combination with Irgacure 184 as photoinitiator (s), there is not formation of filaments after the LED beam is launched to an amplitude mask ($\Lambda = 80 \text{ }\mu\text{m}$) with $40 \text{ }\mu\text{m}$ wide square apertures. Even at very low intensities ($\sim 0.01 \text{ mW/cm}^2$), a hard monolith without a periodic microstructure is formed. Irgacure 819 undergoes a fast photolysis that generates up to four radicals⁴⁵. The benzoyl and phosphonyl radicals that are generated are very reactive. The photopolymerization initiated by the light leaking from these micro-filaments through scattering and the diffusion of radicals lead to the same extent of polymerization even in regions that are not irradiated directly. We have extensively studied the formation of self-trapped beams and the permanent inscription of waveguide arrays within an organosiloxane photopolymer^{17,41,46}, so we attempted to create prisms with arrays of micro-channel waveguides embedded in this material. We hypothesized that by having a slower production and a lower concentration of radicals in the surroundings of the square microfilaments would result in a smaller extent of polymerization. This will produce the refractive index contrast needed for the formation of prisms with micro-waveguides embedded. To prove this hypothesis, we used a mixture of Camphorquinone and Irgacure 819. Camphorquinone produces a camphorquinone-derived radical upon absorption of blue light that can undergo different reactions including dimerization, hydrogen abstraction

reactions, radical polymerization or undergo oxidation in the presence of a diaryliodonium salt and oxygen.⁴⁷ Although, it has been reported that this last one accelerates the rate of polymerization of CQ in the absence of coinitiator such as a tertiary amine,⁴⁸ free-radical polymerization is rather slow and proceeds to a limited extent.⁴⁹ Even in the presence of a coinitiator, it was found that the polymerization rate of methyl methacrylate using Irgacure 819 was 1.3×10^{-4} (M s⁻¹) while for CQ in combination with ethyl p-dimethylamino benzoate (EDB) was 1.1×10^{-5} (M s⁻¹).⁴⁹ Based on these results, it can be said that the rate of polymerization with Irgacure 819 as photoinitiator is at least 12 times greater than the rate of polymerization when CQ alone is used. The photon absorption efficiency of CQ in the blue region calculated in that work from the superposition of the emission spectrum of the LED ($\lambda_{\text{max}} = 460$ nm) and the absorption spectra of the photoinitiator, is approximately two times greater than the one of Irgacure 819. Since the emission of our LED is in the same region ($\lambda_{\text{max}} = 445$ nm), it can be assumed that the absorption efficiencies in our system are of the same order. To test the hypothesis that having a slower and a smaller production of free radicals would result in the formation of polymeric prisms with channel waveguides, we used a mixture of CQ and Irgacure 819 as the photoinitiator system in which the concentration of CQ was 5 times larger than the concentration of Irgacure 819. As a result, the absorption of light by CQ in the system is ~ 10 greater than the one of Irgacure 819. The periodic amplitude mask described above ($\Lambda = 80$ μm with 40 μm wide square apertures) was used in conjunction with a second amplitude mask that defined the shape of the prism. The time evolution of an array of beams traveling in a photopolymerizable medium during the printing process of a rectangular prism 3 mm long is shown in Figure 2.18. At $t = 0$ s, under linear conditions, the micro-beams are 42 ± 6 μm in size at the exit face of the sample due to natural divergence. As the polymerization takes place, the size of the filaments decreases since the

divergence is suppressed by the refractive index changes within the medium. The final diameter of the filaments is $37 \pm 9 \mu\text{m}$ after irradiating the sample for 60 s. This is a clear indication that even at high intensities, there is a lower degree of side-polymerization in the areas that are not irradiated directly by each micro-beam. In the irradiated areas, due to the high intensities used, some of the Irgacure 819 molecules absorb light undergoing photolysis and triggering local free-radical polymerization. The light leaking from these filaments through scattering is mostly absorbed by CQ molecules which carry out a slow and inefficient polymerization. The concentration of free radicals generated in the irradiated areas is significantly smaller than when Irgacure 819 is used alone. Therefore, the number of radicals that diffuses to the non-irradiated areas is significantly smaller. These two factors result in a smaller degree of polymerization in the non-irradiated during the printing process. The proposed mechanism is currently being investigated as well as other factors that might play a role in the successful printing of prisms with micro-waveguides embedded. The resulting rectangular prism is shown in Figure 2.7a. Optical micrographs of the rectangular prism at the entrance and exit face show that a periodic array of waveguides with square symmetry was inscribed in the rectangular prism of Figure 2.7b. Each prismatic element created with this technique, with or without micro-waveguides embedded, has a higher refractive index than their surroundings and since they are printed in a continuous manner, these prisms possess excellent light-guiding properties. A proof of the light-guiding properties of the rectangular prism with channel waveguides is shown in Figure 2.7c; when a red LED beam is launched to the prism, the micro-structure in the prism patterns the beam since light prefers to travel in regions of high refractive index. These regions are the ones in which the filaments induced local polymerization. The LED beam is divided into an array of filaments, each with a diameter of $37 \pm 7 \mu\text{m}$ at the exit face of the sample which is commensurate with the size of the aperture of the

periodic amplitude mask used to pattern the prism. The far-field output of a red laser beam is also shown at the right. The beam turns into a square array of bright spots as when a LED is launched. This shows that Prismatic 3D printing is a fast route to obtain polymeric prisms embedded with waveguide circuitry. The light-guiding properties of these prisms could be combined with others by using stimuli-responsive materials for mechanical light manipulation.

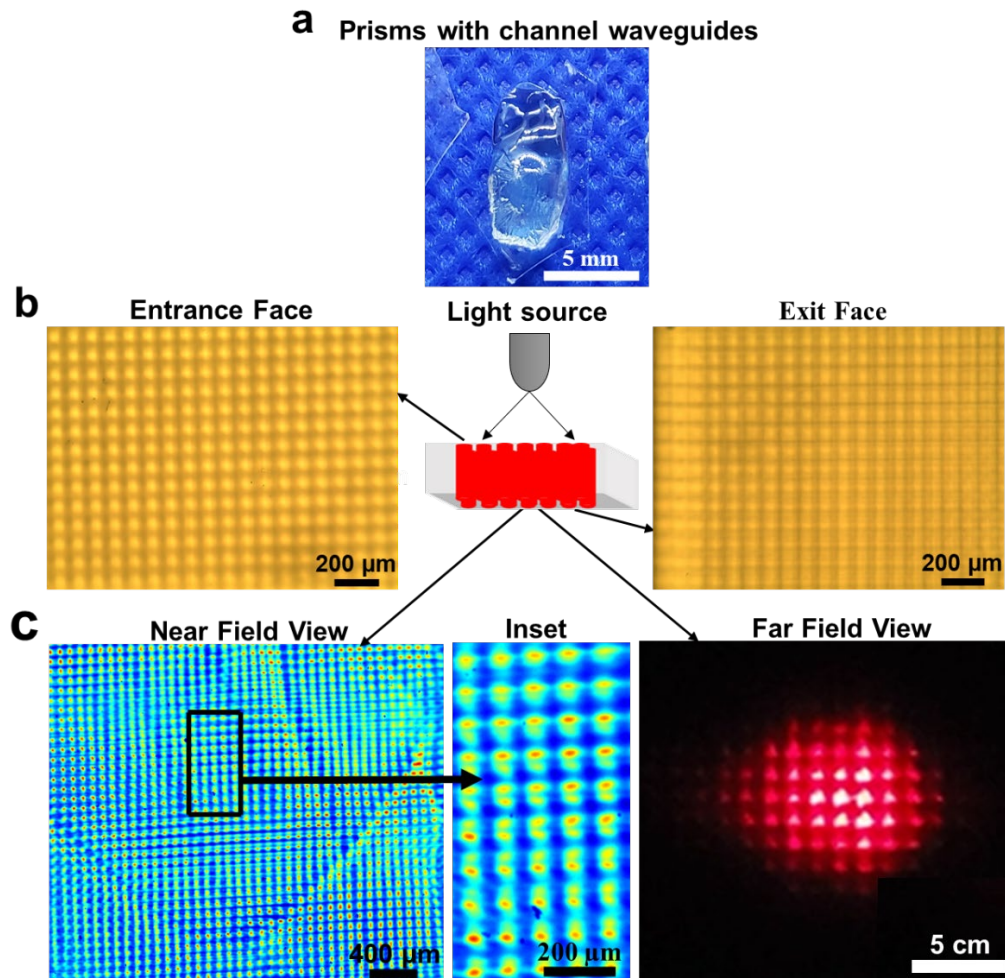


Figure 2.7 a) Rectangular prism (Width x Height x Length= 4 x 8 x 3 mm) with waveguide circuitry. b) Optical micrographs of the entrance (right) and exit face (left) of a rectangular prism with waveguide circuitry. c) Near-Field view of a red LED beam that propagates through the rectangular prism with waveguide circuitry at the exit face of the sample (left). A magnification of the filaments formed is shown in the middle. c) Far-Field view of a laser beam propagating through the same prism.

2.4 Conclusions and Outlook

The prismatic 3D printing of three-dimensional objects using nonlinear waves offers a facile and rapid, room temperature method of printing objects that are comprised of multiple prisms using inexpensive, incoherent LED sources. The ability to manipulate both light and photopolymerizable system provides several parameters that can be adjusted to influence the development of the propagating wave. The decomposition of these objects into prisms have been determined using a manual algorithm that reduces the object into smaller elements. The reverse process of building objects starting from prismatic elements can be done by unifying multiple prisms to build an initial mesh. As proof of concept, we showed that self-trapped beams sequentially launched through 3 amplitude masks and 3 directions can inscribe prismatic elements in situ to make objects including a series of runners, a lattice, and a skull. The higher refractive index of these written structures relative to their surroundings may offer these materials light-guiding properties, allowing us to print different waveguide array architectures into different elements.²⁰ The speed and light-guiding characteristics of these printed elements offer many possibilities for materials embedded with waveguides. Prismatic 3D printing of functional materials with stimuli-responsive polymer elements may allow the build-up of more complex, smart polymers for various applications.⁵⁰ Future work may also entail creating software capable of identifying prisms including microstructured optical waveguides formed within the resin, software that allows scanning of objects and conversion into a printable mesh comprised of prisms and formation of functional materials such as scaffolds for photocatalysis, LEDs and sensing.

2.5 Methods

2.5.1 Materials

Abecryl® 8210, Genomer* 1122TF and Sartomer SR 494 were donated from Allnex, Rahn USA Corp. and Arkema Inc, respectively. Photoinitiators Irgacure® 184 and Irgacure® 819 were obtained from Ciba Specialty Chemicals. Coumarin 6 and N,N'-methylenebis(acrylamide) were obtained from Sigma-Aldrich. 3-(Trimethoxysilyl) propyl methacrylate (MAPTMS) and 0.1 N hydrochloric acid were purchased by Millipore Sigma.

2.5.2 Preparation of photopolymer

Resin 1 was used in most objects except for the prism in **Figure 2.7**. It is a modified version of Autodesk Standard clear prototyping Resin (PR48). It was obtained by mixing Abecryl® 8210 (39.134 %), Sartomer SR 494 (39.134 %), Genomer* 1122TF (19.567 %), Irgacure® 819 (0.197 %) and Irgacure® 184 (1.968 %). The mixture was stirred for 48 hours before using it. For the disk of the death, coumarin 6 was added to resin 1 prior to stirring for 48 hours. The organosiloxane sample used to 3-D print the prism in Figure 2.7 was obtained by combining 1.1000 g (5.5×10^{-5} mol) of 0.05 N hydrochloric acid (diluted from a standardized 0.1 N HCl aqueous solution), 17.6000 g (0.0708 mol) of 3-methacryloxypropyltrimethoxysilane, 0.0400 g of camphorquinone (0.241 mmol), 0.0200 g of Irgacure 819 (0.0477 mmol) and 0.3000 g (1.95 mmol) of N,N'-methyleylenebis(acrylamide). The sample was stirred for 24 hours. The undissolved crosslinker was separated by the solution by decanting.

2.5.3 Optical Apparatus and Imaging

A blue LED ($\lambda_{\max} = 460$ nm, Kerber Applied Research Inc.) was used as the main light source. Tapered objects were fabricated at 2.33 mW mm^{-2} with a separate mounted LED ($\lambda_{\max} = 470$ nm, Thorlabs). The dimensions of each cell varied depending on the target size for each object.

Amplitude masks with the desired pattern to be imposed on the beam were placed at the entrance face of the sample cell. Vinyl amplitude masks were printed using a Graphtec Craft ROBO vinyl cutter. A plano-convex lens pair (L1, f.l. = 250 mm and L2, f.l. = 250 mm) and a CCD camera (WinCamD XHR, DataRay Inc.) were used for monitoring the spatial intensity profile at the exit face when printing cylindrical rods during calibration. A Samsung Galaxy S6 phone camera was used for side imaging of the propagating structures.

To obtain prisms with waveguide circuitry, a LED beam ($\lambda_{\max} = 445$ nm, Thorlabs) was passed through a 2D periodic amplitude mask ($\Lambda = 80$ μm , ≈ 0.94 mW mm⁻², power measured after periodic mask) before being launched to the rectangular amplitude mask that defines the shape of the prism and a cell 3 mm long containing the organosiloxane solution.

2.5.4 Structural characterization of prisms with waveguide circuitry

A transmission microscope (Olympus BH2-UMA, Upright) coupled with a MOTICAM 3+ camera was used to acquire micrographs of the channel waveguides at the entrance and exit face of the prisms.

2.5.5 Optical characterization of the channel waveguides

Right after printing, the periodic amplitude mask was removed from the set up. The sample was illuminated with a Compact Laser Module with USB Connector (635 nm, 0.9 mW). The light output was monitored at the exit face of the prism with the same optical apparatus describe above. Photographs of the Far Field profile were obtained by launching a hand-held red laser beam ($\lambda_{\max} = 635$ nm, Thorlabs) through the rectangular prism 3 mm long.

2.5.6 Post-Processing of Structures

Large elements were sanded due to excess side polymerization during the photoreaction. Prismatic elements printed separately were glued together using 0.3 mL of photoresin and subsequently irradiating with the LED.

2.5.7 Decomposition of Mesh

Mesh files were created in Blender (v.2.79) and manually modified using the decomposition steps (*vide supra*) (prismatic elements coloured differently once decomposed).

2.5.8 SLA Printing

SLA printing of the runner was carried out using a Form 2 printer from Formlabs.

2.6 Acknowledgements

We thank Ciba Specialty Chemicals, Allnex, Rahn USA Corp. and Arkema Inc for the generous donation of photoinitiator and resin components. We thank the Moran-Mirabel group for access to the vinyl cutter and The Forge at McMaster Innovation Park for use of the SLA printer. OAH and DRM acknowledge financial support from the National Council of Science and Technology of Mexico and the Natural Sciences and Engineering Research Council, respectively. Finally, we acknowledge funding from the Natural Sciences and Engineering Research Council and Canadian Foundation for Innovation.

2.7 References

- (1) Stevens, A. G.; Oliver, C. R.; Kirchmeyer, M.; Wu, J.; Chin, L.; Hart, A. J.; Stevens, A. G.; Oliver, C. R.; Polsen, E. S.; Archer, C.; Boyle, C.; Garber, J.; Hart, A. J. Conformal Robotic Stereolithography. *3D Print. Addit. Manuf.* **2016**, *3*, 226–235.
- (2) Vithani, K.; Boyd, B. J.; Goyanes, A.; Basit, A. W.; Gaisford, S.; Jannin, V.; Basit, A. W.; Gaisford, S.; Boyd, B. J. An Overview of 3D Printing Technologies for Soft Materials and Potential Opportunities for Lipid-Based Drug Delivery Systems. *Pharm. Res.* **2018**, *36*, 4.
- (3) Liska, R.; Schuster, M.; Inführ, R.; Turecek, C.; Fritscher, C.; Seidl, B.; Schmidt, V.; Kuna, L.; Haase, A.; Varga, F.; Lichtenegger H.; Stampfl, J. Photopolymers for Rapid Prototyping.

- J. Coatings Technol. Res.* **2007**, *4*, 505–510.
- (4) Melchels, F. P. W.; Feijen, J.; Grijpma, D. W. A Review on Stereolithography and Its Applications in Biomedical Engineering. *Biomaterials* **2010**, *31*, 6121–6130.
 - (5) de Gans, B.-J.; Duineveld, P. C.; Schubert, U. S. Inkjet Printing of Polymers: State of the Art and Future Developments. *Adv. Mater.* **2004**, *16*, 203–213.
 - (6) Hutmacher, D. W.; Schantz, T.; Zein, I.; Ng, K. W.; Teoh, S. H.; Tan, K. C. Mechanical Properties and Cell Cultural Response of Polycaprolactone Scaffolds Designed and Fabricated via Fused Deposition Modeling. *J. Biomed. Mater. Res.* **2001**, *55*, 203–216.
 - (7) Williams, J. M.; Adewunmi, A.; Schek, R. M.; Flanagan, C. L.; Krebsbach, P. H.; Feinberg, S. E.; Hollister, S. J.; Das, S. Bone Tissue Engineering Using Polycaprolactone Scaffolds Fabricated via Selective Laser Sintering. *Biomaterials* **2005**, *26*, 4817–4827.
 - (8) Choong, Y. Y. C.; Maleksaeedi, S.; Eng, H.; Wei, J.; Su, P.-C. 4D Printing of High Performance Shape Memory Polymer Using Stereolithography. *Mater. Des.* **2017**, *126*, 219–225.
 - (9) Esmaeilian, B.; Behdad, S.; Wang, B. The Evolution and Future of Manufacturing: A Review. *J. Manuf. Syst.* **2016**, *39*, 79–100.
 - (10) Thomas, D. Costs, Benefits, and Adoption of Additive Manufacturing: A Supply Chain Perspective. *Int. J. Adv. Manuf. Technol.* **2016**, *85*, 1857–1876.
 - (11) Dizon, J. R. C.; Espera, A. H.; Chen, Q.; Advincula, R. C. Mechanical Characterization of 3D-Printed Polymers. *Addit. Manuf.* **2018**, *20*, 44–67.
 - (12) Gojzewski, H.; Guo, Z.; Grzelachowska, W.; Ridwan, M. G.; Hempenius, M. A.; Grijpma, D. W.; Vancso, G. J. Layer-by-Layer Printing of Photopolymers in 3D: How Weak Is the Interface? *ACS Appl. Mater. Interfaces* **2020**, *12*, 8908–8914.
 - (13) Tumbleston, J. R.; Shirvanyants, D.; Ermoshkin, N.; Janusziewicz, R.; Johnson, A. R.; Kelly, D.; Chen, K.; Pinschmidt, R.; Rolland, J. P.; Ermoshkin, A.; et al. Continuous Liquid Interface Production of 3D Objects. *Science (80-.)*. **2015**, *347*, 1349–1352.
 - (14) Shusteff, M.; Browar, A. E. M.; Kelly, B. E.; Henriksson, J.; Weisgraber, T. H.; Panas, R. M.; Fang, N. X.; Spadaccini, C. M. One-Step Volumetric Additive Manufacturing of Complex Polymer Structures. *Sci. Adv.* **2017**, *3*, eaao5496.
 - (15) Loterie, D.; Delrot, P.; Moser, C. High-Resolution Tomographic Volumetric Additive Manufacturing. *Nat. Commun.* **2020**, *11*, 852.
 - (16) Basker, D. K.; Cortes, O. A. H.; Brook, M. A.; Saravanamuttu, K. 3D Nonlinear Inscription of Complex Microcomponents (3D NSCRIPT): Printing Functional Dielectric and Metallodielectric Polymer Structures with Nonlinear Waves of Blue LED Light. *Adv. Mater. Technol.* **2017**, *2*, 1600236-n/a.
 - (17) Burgess, I. B.; Ponte, M. R.; Saravanamuttu, K. Spontaneous Formation of 3-D Optical and Structural Lattices from Two Orthogonal and Mutually Incoherent Beams of White Light Propagating in a Photopolymerisable Material. *J. Mater. Chem.* **2008**, *18*, 4133.
 - (18) Kelly, B. E.; Bhattacharya, I.; Heidari, H.; Shusteff, M.; Spadaccini, C. M.; Taylor, H. K. Volumetric Additive Manufacturing via Tomographic Reconstruction. *Science* **2019**, *363*, 1075–1079.
 - (19) Nunez, B. P.; Delrot, P.; Loterie, D.; Li, Y.; Malda, J., Moser, C.; Levato, R. Volumetric Bioprinting of Complex Living-Tissue Constructs within Seconds. *Adv. Mater.* **2019**, *31*, 1904209.
 - (20) Basker, D. K.; Brook, M. A.; Saravanamuttu, K. Spontaneous Emergence of Nonlinear Light Waves and Self-Inscribed Waveguide Microstructure during the Cationic

- Polymerization of Epoxides. *J. Phys. Chem. C* **2015**, *119*, 20606–20617.
- (21) Dolinski, N. D.; Page, Z. A.; Callaway, E. B.; Eisenreich, F.; Garcia, R. V.; Chavez, R.; Bothman, D. P.; Hecht, S.; Zok, F. W.; Hawker, C. J. Solution Mask Liquid Lithography (SMaLL) for One-Step, Multimaterial 3D Printing. *Adv. Mater. (Weinheim, Ger.)* **2018**, *30*, n/a.
 - (22) de Beer, M. P.; van der Laan, H. L.; Cole, M. A.; Whelan, R. J.; Burns, M. A.; Scott, T. F. Rapid, Continuous Additive Manufacturing by Volumetric Polymerization Inhibition Patterning. *Sci. Adv.* **2019**, *5*, eaau8723.
 - (23) van der Laan, H. L.; Burns, M. A.; Scott, T. F. Volumetric Photopolymerization Confinement through Dual-Wavelength Photoinitiation and Photoinhibition. *ACS Macro Lett.* **2019**, *8*, 899–904.
 - (24) Regehly, M.; Garmshausen, Y.; Reuter, M.; König, N. F.; Israel, E.; Kelly, D. P.; Chou, C. Y.; Koch, K.; Asfari, B.; Hecht, S. Xolography for linear volumetric 3D printing. *Nature* **2020**, *588*, 620–624.
 - (25) Trillo, S.; Torruellas, W. *Spatial Solitons*; Springer: New York, 2001.
 - (26) O'Brien, A. K.; Bowman, C. N. Impact of Oxygen on Photopolymerization Kinetics and Polymer Structure. *Macromolecules* **2006**, *39*, 2501–2506.
 - (27) Lafarge, F.; Keriven, R.; Brédif, M. Insertion of 3-D-Primitives in Mesh-Based Representations: Towards Compact Models Preserving the Details. *IEEE Trans. Image Process.* **2010**, *19*, 1683–1694.
 - (28) Chen, X.; Golovinskiy, A.; Funkhouser, T. A Benchmark for 3D Mesh Segmentation. *ACM Trans. Graph.* **2009**, *28*, 1-12.
 - (29) Kang, Z.; Li, Z. Primitive Fitting Based on the Efficient MultiBaySAC Algorithm. *PLoS One* **2015**, *10*, e0117341.
 - (30) Le, T.; Duan, Y. A Primitive-Based 3D Segmentation Algorithm for Mechanical CAD Models. *Comput. Aided Geom. Des.* **2017**, *52–53*, 231–246.
 - (31) Araújo, C.; Cabiddu, D.; Attene, M.; Livesu, M.; Vining, N.; Sheffer, A. Surface2Volume: Surface Segmentation Conforming Assemblable Volumetric Partition. *ACM Trans. Graph.* **2019**, *38*, 1.
 - (32) Liu, J.; Cao, L.; Li, Z.; Tang, X. Plane-Based Optimization for 3D Object Reconstruction from Single Line Drawings. *IEEE Trans. Pattern Anal. Mach. Intell.* **2008**, *30*, 315–327.
 - (33) Liu, J.; Chen, Y.; Tang, X. Decomposition of Complex Line Drawings with Hidden Lines for 3D Planar-Faced Manifold Object Reconstruction. *IEEE Trans. Pattern Anal. Mach. Intell.* **2011**, *33*, 3–15.
 - (34) Changqing, Z.; Shifeng, C.; Hongbo, F.; Jianzhuang, L. Progressive 3D Reconstruction of Planar-Faced Manifold Objects with DRF-Based Line Drawing Decomposition. *IEEE Trans. Vis. Comput. Graph.* **2015**, *21*, 252–263.
 - (35) Chen, Y.; Liu, J.; Tang, X. A Divide-and-Conquer Approach to 3D Object Reconstruction from Line Drawings. In *2007 IEEE 11th International Conference on Computer Vision*; 2007; pp 1–8.
 - (36) Xue, T.; Liu, J.; Tang, X. Example-Based 3D Object Reconstruction from Line Drawings. In *2012 IEEE Conference on Computer Vision and Pattern Recognition*; 2012; pp 302–309.
 - (37) Luo, L.; Baran, I.; Rusinkiewicz, S.; Matusik, W. Chopper: Partitioning Models into 3D-Printable Parts. *ACM Trans. Graph.* **2012**, *31*, 1-9.
 - (38) He, Y.; Wang, H.; Fu, C.-W.; Qin, H. A Divide-and-Conquer Approach for Automatic Polycube Map Construction. *Comput. Graph.* **2009**, *33*, 369–380.

- (39) Zhang, M.; Huang, J.; Liu, X.; Bao, H. A Divide-and-Conquer Approach to Quad Remeshing. *IEEE Trans. Vis. Comput. Graph.* **2013**, *19*, 941–952.
- (40) Tulsiani, S.; Su, H.; Guibas, L. J.; Efros, A. A.; Malik, J. Learning Shape Abstractions by Assembling Volumetric Primitives. In *Proceedings - 30th IEEE Conference on Computer Vision and Pattern Recognition, CVPR 2017*; 2017.
- (41) Kasala, K.; Saravanamuttu, K. Optochemical Self-Organisation of White Light in a Photopolymerisable Gel: A Single-Step Route to Intersecting and Interleaving 3-D Optical and Waveguide Lattices. *J. Mater. Chem.* **2012**, *22*, 12281.
- (42) Lin, H.; Hosein, I. D.; Benincasa, K. A.; Saravanamuttu, K. A Slim Polymer Film with a Seamless Panoramic Field of View: The Radially Distributed Waveguide Encoded Lattice (RDWEL). *Adv. Opt. Mater.* **2019**, *7*, 1801091.
- (43) Hudson, A. D.; Ponte, M. R.; Mahmood, F.; Pena Ventura, T.; Saravanamuttu, K. A Soft Photopolymer Cuboid That Computes with Binary Strings of White Light. *Nat. Commun.* **2019**, *10*, 2310.
- (44) Kewitsch, A. S.; Yariv, A. Self-focusing and self-trapping of optical beams upon photopolymerization. *Optics Letters* **1996**, *21*, 24–26.
- (45) Neumann, M. G.; Miranda, W. G.; Schmitt, C. C.; Rueggeberg, F. A.; Correa, I. C. Molar extinction coefficients and the photon absorption efficiency of dental photoinitiators and light curing units. *Journal of Dentistry* **2005**, *33*, 525–532.
- (46) Burgess I. B.; Shimmell W. E.; Saravanamuttu K. Spontaneous Pattern Formation Due to Modulation Instability of Incoherent White Light in a Photopolymerizable Medium. *J. Am. Chem. Soc.* **2007**, *129*, 4738–4746.
- (47) Matsumura, S.; Hlil, A. R.; Lepiller, C.; Gaudet, J.; Guay, D.; Shi, Z.; Holdcroft, S.; Hay, A. S. Stability and Utility of Pyridyl Disulfide Functionality in RAFT and Conventional Radical Polymerizations. *J. Polym. Sci. A Polym. Chem.* 2009, *47*, 866–875.
- (48) Andrzejewska, E.; Rabek, J. F. The role of oxygen in camphorquinone-initiated photopolymerization. *Macromolecular Chemistry and Physics* **1998**, *449*, 441–449.
- (49) Cook, W. D. Photopolymerization kinetics of dimethacrylates using the camphorquinone/amine initiator system. *Polymer* **1992**, *33*, 600–609.
- (50) Neumann, M. G.; Schmitt, C. C.; Ferreira, G. C.; Corrêa, I. C. The initiating radical yields and the efficiency of polymerization for various dental photoinitiators excited by different light curing units. *Dental Materials* **2006**, *22*, 576–584.
- (51) Jung, K.; Corrigan, N.; Ciftci, M.; Xu, J.; Seo, S. E.; Hawker, C. J.; Boyer, C. Designing with Light: Advanced 2D, 3D, and 4D Materials. *Adv. Mater.* **2020**, *32*, 1903850.

2.8 SUPPLEMENTARY INFORMATION

2.8.1 Experimental Methods

2.8.1.1 Materials

Abecryl® 8210, Genomer* 1122TF and Sartomer SR 494 were donated from Allnex, Rahn USA Corp. and Arkema Inc, respectively. Photoinitiators Irgacure® 184 and Irgacure® 819 were

obtained from Ciba Specialty Chemicals. Coumarin 6 and N,N'-methylenebis(acrylamide) were obtained from Sigma-Aldrich. 3-(Trimethoxysilyl) propyl methacrylate (MAPTMS) and 0.1 N hydrochloric acid were purchased by Millipore Sigma.

2.8.1.2 Preparation of photopolymer resins

Resin 1

Resin 1 is a modified version of Autodesk Standard clear prototyping Resin (PR48). It was obtained by mixing Abecryl® 8210 (39.134 %), Sartomer SR 494 (39.134 %), Genomer* 1122TF (19.567 %), Irgacure® 819 (0.197 %) and Irgacure® 184 (1.968 %). The mixture was stirred for 48 hours before using it. For the disk of the death, Coumarin 6 was added to the resin prior to stirring for 48 hours.

Resin 2

Resin 2 is an organosiloxane photopolymer obtained by combining 1.1 g (5.5×10^{-5} mol.) of 0.05 N hydrochloric acid (diluted from a standardized 0.1 N HCl aqueous solution), 17.6 g (0.0708 mol) of 3-methacryloxypropyltrimethoxysilane, 40 mg of camphorquinone (0.2406 mmol), 20 mg of Irgacure 819 (0.0477 mmol) and 300 mg (1.9459 mmol) of N,N'-methyleylenebis(acrylamide). The sample was stirred for 24 hours. The undissolved crosslinker was separated from the solution by decanting.

2.8.2 Post-Processing of Structures

Large elements were sanded (sandpaper grit 220) due to excess side polymerization during the photoreaction. Prismatic elements printed separately were glued together using small amounts of photoresin and subsequently irradiating with the LED.

2.8.3 SLA Printing

SLA printing of the runner was carried out using a Form 2 printer from Formlabs.

2.8.4 Optical Assembly for Self-Trapping Experiments

A blue LED ($\lambda_{\text{max}} = 460$ nm, Kerber Applied Research Inc.) was used as the main light source. Tapered objects were fabricated at 2.33 mW mm^{-2} with a separate mounted LED ($\lambda_{\text{max}} = 470$ nm, Thorlabs). The dimensions of each cell varied depending on the target size for each object. Amplitude masks with the desired pattern to be imposed on the beam were placed at the entrance face of the sample cell. Vinyl amplitude masks were printed using a Graphtec Craft ROBO vinyl cutter. A plano-convex lens pair (L1, f.l. = 250 mm and L2, f.l. = 250 mm) and a CCD camera (WinCamD XHR, DataRay Inc.) were used for monitoring the spatial intensity profile at the exit face when printing cylindrical rods during calibration. A Samsung Galaxy S6 phone camera was used for side imaging of the propagating structures. To obtain prisms with waveguide circuitry, an LED beam ($\lambda_{\text{max}} = 445$ nm, Thorlabs) was passed through a 2D periodic amplitude mask ($\Lambda = 80$ μm , $\approx 0.94 \text{ mW mm}^{-2}$, power measured after periodic mask) before being launched to the rectangular amplitude mask that defines the shape of the prism and a cell 3 mm long containing Resin 2.

2.8.5 Calibration of Intensity by Printing Cylinders

Cylindrical rods were printed as a means of calibration (Table S1) and yielded optimal printing conditions at 1.1 mW mm^{-2} . At distances larger than 5 cm, there is greater difficulty in maintaining the beam diameter as the beam propagates, limiting our technique to objects smaller than 5 cm.

Table 2.1 Diameter at the entrance and exit face of cylinders fabricated with a beam 10 mm wide at 0.47, 1.1 and 1.9 mW mm⁻² (3 replicates).

Intensity (mW mm ⁻²)	10 mm Pathlength		27 mm Pathlength	
	Diameter at Entrance (mm)	Diameter at Exit (mm)	Diameter at Entrance (mm)	Diameter at Exit (mm)
0.47	9.4 ± 0.20	5.0 ± 2.0	9.5 ± 0.10	8.5 ± 0.50
1.1	9.9 ± 0.10	10 ± 0.50	9.9 ± 0.10	11 ± 0.30
1.9	10 ± 0.10	11 ± 0.20	10 ± 0.30	13 ± 0.10

2.8.6 Optical and Structural Characterization of Waveguides

A transmission microscope (Olympus BH2-UMA, Upright) coupled with a MOTICAM 3+ camera was used to acquire micrographs of the channel waveguides at the entrance and exit face of the prisms.

Immediately following printing, the periodic amplitude mask was removed from the set up. The sample was illuminated with a Compact Laser Module with USB Connector (635 nm, 0.9 mW). The light output was monitored at the exit face of the prism with the same optical apparatus describe above. Photographs of the far field profile were obtained by launching a hand-held red laser beam ($\lambda_{\text{max}} = 635 \text{ nm}$, Thorlabs) through the rectangular prism 3 mm long.

2.8.7 Decomposition and Printing of Objects

The following section describes the printing of multiple prismatic elements and then separately combining those elements into a single object. The same decomposition steps are applied to break down an object into the corresponding prismatic elements in Figures S1-S5. Mesh

files were created in Blender (v.2.79) and manually modified using the decomposition steps within the text (prismatic elements coloured differently once decomposed).

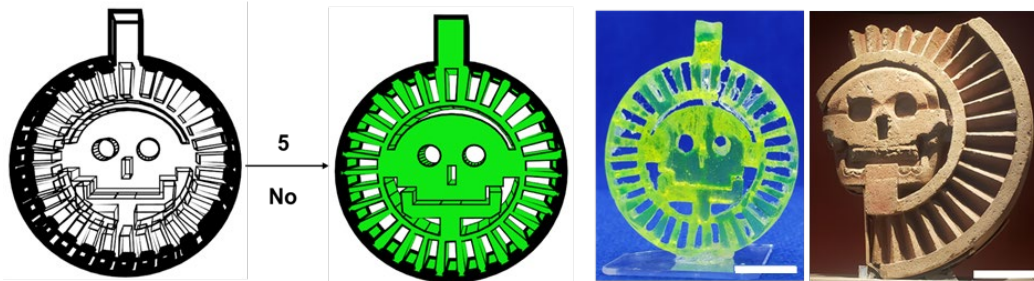


Figure 2.8 Decomposition steps that were carried out to identify a skull medallion mesh is a printable prismatic element and the resulting printed object that resulted. Scale bar = 1 cm. The skull medallion model is a reconstruction of the Mexican sculpture (right). Scale bar = 30 cm.

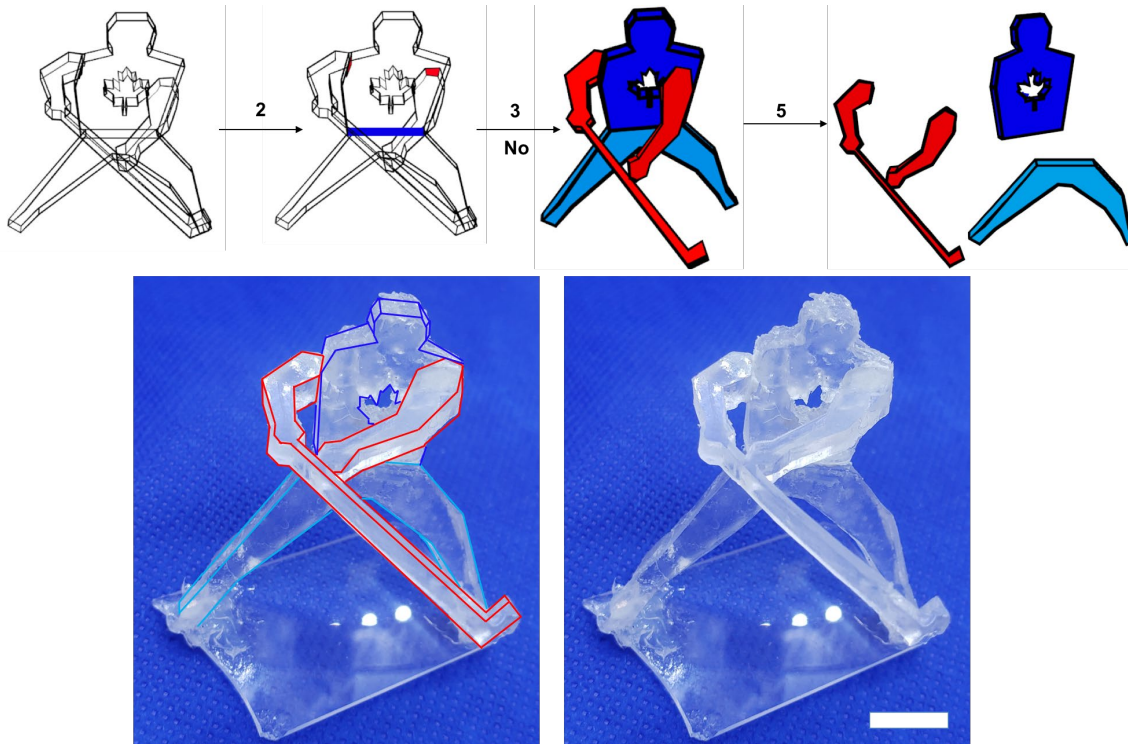


Figure 2.9 Decomposition steps that were carried out to convert a hockey player mesh into printable prismatic elements and the resulting printed object that resulted within 100 s. Scale bar = 1 cm.

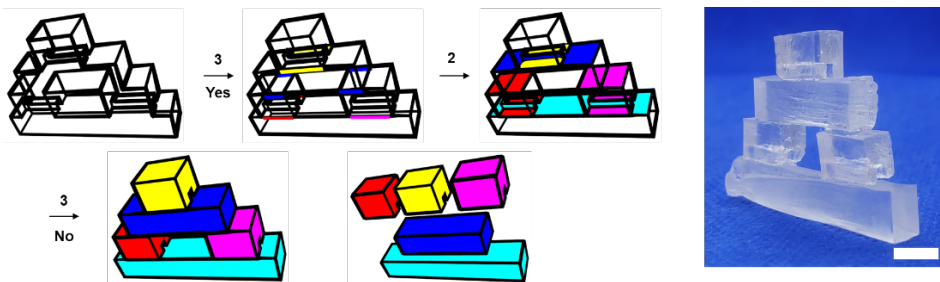


Figure 2.10 Decomposition steps that were carried out to convert an inukshuk mesh into printable prismatic elements and the resulting printed object. Scale bar = 1 cm.

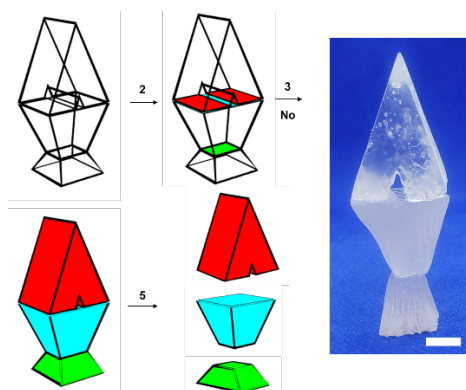


Figure 2.11 Decomposition steps that were carried out to convert a skyscraper mesh into printable prismatic elements and the resulting printed object. Scale bar = 1 cm.

The room of the house (Figure 2.12) (sky blue and red prisms) and the roof (pink prism) were printed in situ as a single piece using the same method described in Figure 2.5b and in the next section using 3 amplitude masks. The red rectangular prism was printed first by launching the beam through a rectangular mask until the polymerization front reached halfway followed by a 180-degree rotation and the use of a second rectangular mask that blocks the beam at the center/bottom creating a rectangular hole to obtain the sky-blue rectangular prism with the door. Finally, the sample was rotated 90° and the beam was launched to a triangular mask to print the roof. The other four pieces were print them individually.

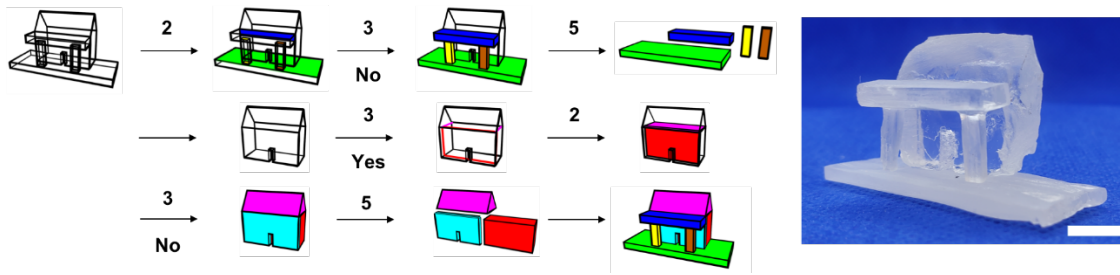


Figure 2.12 Decomposition steps that were carried out to convert a house mesh into printable prismatic elements and the resulting printed object. Scale bar = 1 cm.

Unlike most of the previous examples that looked at printing individual elements and gluing them together, we are also able to create multiple elements by rotating the stage of the sample. By creating multi-element complex objects with amplitude masks (Figure 2.13) placed at the glass walls of the resin cell, we are able to fuse together elements rather than using resin to combine the pieces post-printing. Figures 2.14-2.17 illustrate the decomposition of objects with multiple intersecting prismatic elements which necessitated the use of our decomposition method *in situ* printing.

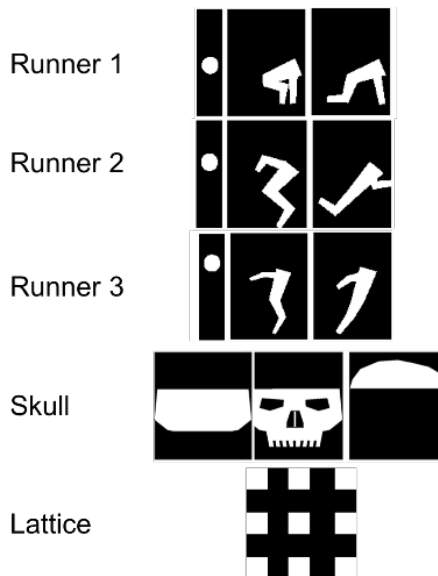


Figure 2.13 Amplitude masks used to print objects *in situ*.

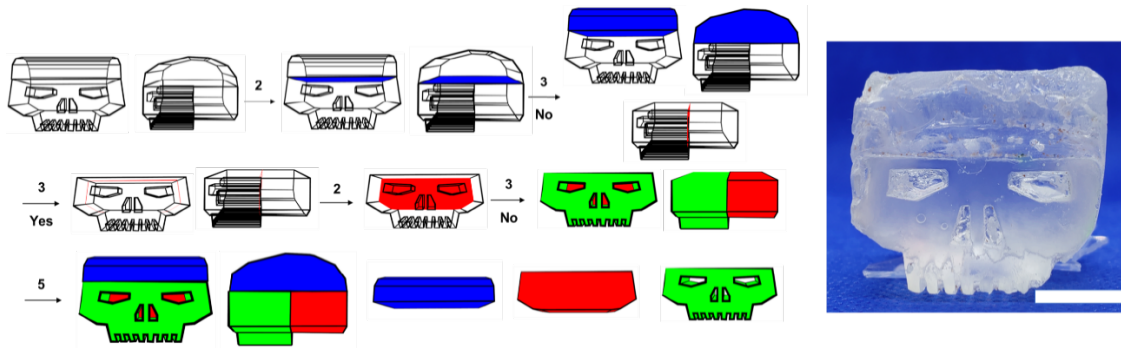


Figure 2.14 Decomposition steps that were carried out to convert a skull mesh into printable prismatic elements and the resulting printed object. Scale bar = 1 cm.

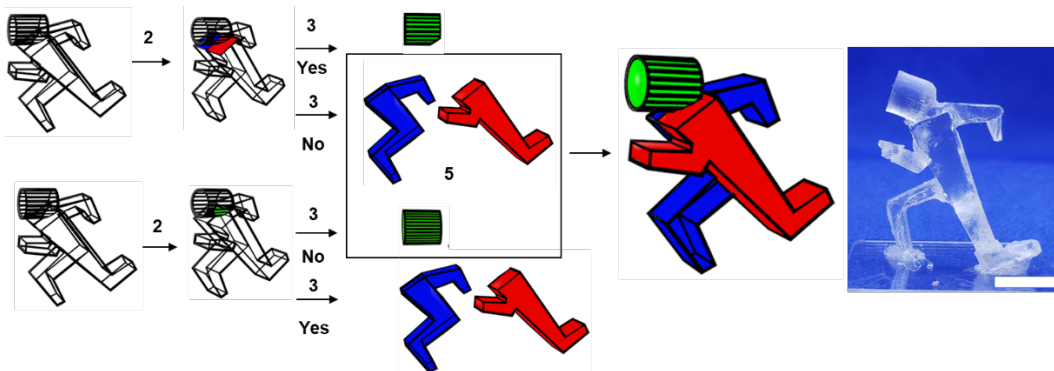


Figure 2.15 Decomposition of a sprinting runner using two methods and the fabrication of the runner. Scale bar = 1 cm.

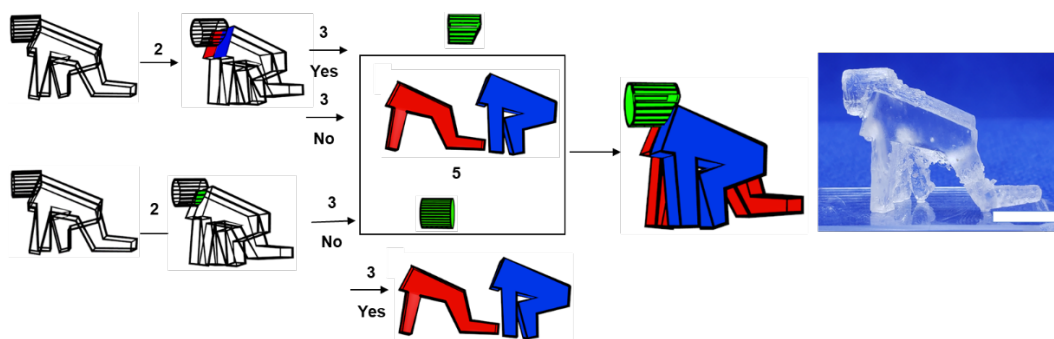


Figure 2.16 Decomposition of a starting runner using two methods and the fabrication of the runner. Scale bar = 1 cm.

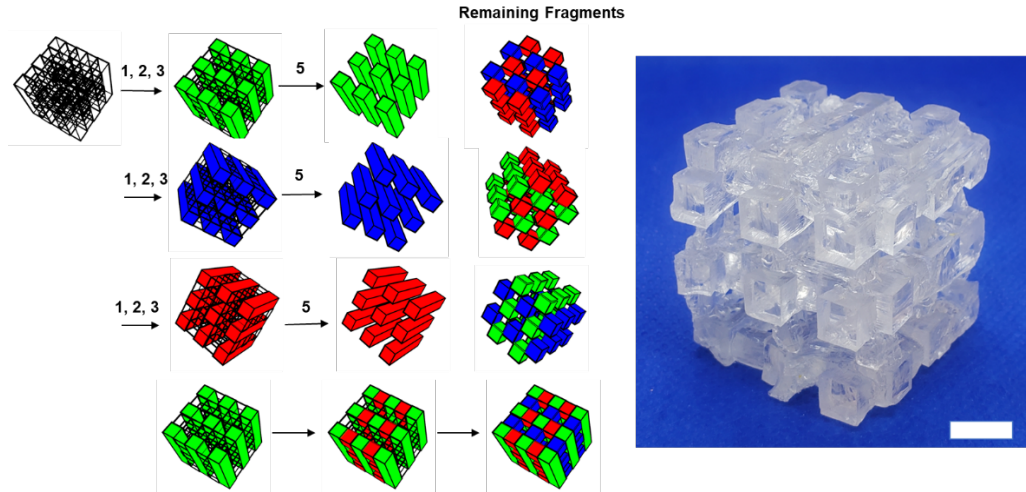


Figure 2.17 Decomposition of a lattice using 3 methods and the fabrication of the lattice in 3 steps with overlapping elements. Scale bar = 1 cm.

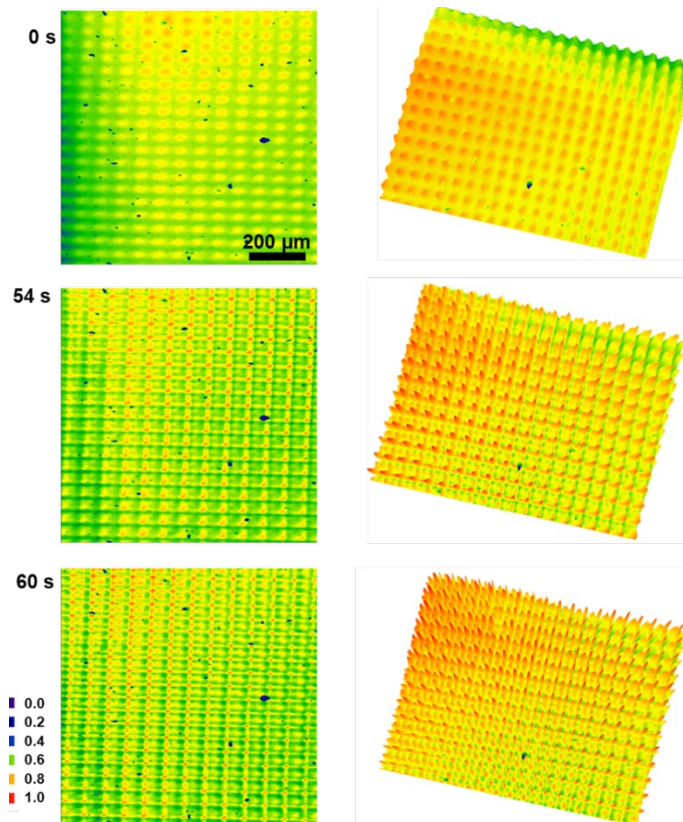


Figure 2.18 2-D and 3-D time evolution of the spatial intensity profile of an array of filaments generated with a periodic amplitude mask ($\Lambda = 80 \mu\text{m}$) with square apertures ($40 \times 40 \mu\text{m}$) during the printing process of a rectangular prism 3 mm long with a waveguide circuitry embedded.

3 Dynamic, remote-controllable bioinspired electroactive hydrogel waveguide architectures*

3.1 Abstract

Electroactive hydrogel light-guiding structures are generated within seconds through Prismatic printing, a volumetric technique that uses self-trapped visible beams from light emitting diodes (LEDs) elicited when photo-induced refractive index changes counteract the natural divergence of light. Due to irreversible refractive index changes experienced by photoinduced reactions, self-trapped beams permanently inscribe cylindrical waveguides along their paths. The waveguides orientation, motion and - thereby the direction of their light output - can be precisely and remotely controlled through external electrical fields. This was achieved with a range of architectures including planar slab waveguides, individual and small arrays of cylindrical waveguides as well as long-range waveguide lattices ($> 10\,000\text{ cm}^{-2}$) that were fabricated taking inspiration from soft bodies/organs such as the lure of the female deep sea angler fish, cilia and squid skin. By applying and varying external electric fields, we can then dynamically control the bending, angular orientation and rotation (up to 360°) of these pliant light-guiding structures.

3.2 Introduction

3-D printing techniques that offer a fast route to create mechanically stable objects have emerged recently. Although some of them rely on layering artifacts similar to the ones used in traditional 3-D printing techniques, they produce seamless objects.¹⁻⁴ One of the best-known 3D printing techniques that creates seamless objects is Continuous Liquid Interface Production (CLIP).¹ Objects are printed by sequentially adding layers above an inert zone created by delivering oxygen to the resin bath through a permeable window placed at the bottom of the bath. After a layer is formed, the building support is pushed out of the resin vat at a faster rate than traditional

*I proposed Prismatic 3-D printing for the fabrication of electroactive waveguides based on observations from the work described in Chapter 2. I also developed the hydrogel formulations with Derek. R. Morim and did the presented simulations. I proposed the set up to carry out multidirectional bending. Natalie Blanchard carried out early experiments with the waveguide lattices. Tomas Omasta did some analysis to quantify bending angles of slab waveguides Kathryn A. Benincasa carried out the tracking of position and intensity of individual micro-waveguides in the waveguide lattices. Kevin Vaughan and I carried out the experimental work analyzed by Kathryn A. Benincasa. K. Saravanamuttu guided the project.

stereolithography. Volumetric polymerization inhibition patterning operates in a similar manner, generating an inhibitor in situ by irradiating the resin in the vat with a second light source.² HARP (light-area rapid printing) eliminates the need of a dead zone by making the resin float on a flowing fluorinated oil that minimizes adhesion of the object being printed with the glass window.³ The flowing oil acts as a cooling system and the absence of an oxygen dead layer makes this technique compatible with a wide range of photopolymers including oxygen-sensitive and -insensitive resins. Xolography is another method that relies on curing layers but this method unlike the ones described previously, uses a horizontal configuration.⁴ A sheet of UV light with a specific thickness is launched to a resin with a dual-colour photoinitiator (DCPI) that takes the photoinitiator from an inactive state to a short-lived ($t_{1/2} = 6$ s) latent state that absorbs in the visible region. A second orthogonal laser projects a slice of a 3D object to be printed in the sheet while exciting the photoinitiator that in combination with a co-initiator triggers radical polymerization. After the slice has cured, the resin volume is displaced while keeping the sheet of light in the same position to create a different slice of the object. Techniques that create objects employing 3D-unit operations have also emerged such as volumetric methods that rely on tomographic reconstruction^{5,6} and those that rely on the propagation of nonlinear photochemical waves.^{7,8} The former method is known as computed axial lithography (CAL).⁵ Objects are created by launching 2D patterns calculated using the same concepts from computed tomography imaging. The combined energy dose from the 2D images solidifies the resin creating the desired object. 3D objects can be created in a single step when patterned blue nonlinear beams from 2D amplitude masks propagate through a photopolymerizable medium.^{8,9} In traditional stereolithographic methods, the thickness is limited to <100 μm since the divergence of beams blur the projected image as it travels in the medium which decreases resolution. The beam divergence can be controlled in nonlinear media such as

photopolymerizable media since the divergence of the beam is counteracted by the photo-induced changes in refractive index originated by the photopolymerization reaction which allows for the creation of 2D images with depth.¹⁰ Since the polymerization is localized, objects obtained through this method have a higher refractive index than their surroundings and since the object is obtained in a continuous manner without layering artifacts, they are homogenous along the propagation front direction. These two properties make these objects light-guiding. Therefore, each element obtained through this method is polymer waveguide. This method can be extended to long-range waveguide lattices ($> 10\ 000\ \text{cm}^{-2}$) embedded in the shape imposed by the 2D amplitude mask. This lattice would be impossible to fabricate with traditional photolithographic methods and even with all the volumetric 3-D printing techniques developed recently. Other 3D-printing techniques such as extrusion-base ink writing,¹¹ direct laser writing¹² and meniscus-guided 3D writing¹³ have also been used to fabricate individual micro- and nano-waveguides. Biocompatible waveguides have potential applications in light-base therapies. For example, del Campo *et al.* demonstrated that it is possible to induce migration of cells within a hydrogel waveguide with light¹⁴ and that drug release can be photo-trigger with the guided light as well as activation of photocleavage reactions.¹⁵

Integrating multiple functions in the same object is a way to carry out multiple operations without additional cost, weight or space. Multifunctional structures often rely on multiple materials to function. For example, multifunctional flexible fibers made of polymer, metal and composite materials are capable of optical stimulation, neural recording and drug delivery in mice.¹⁶ Fibers made of polymers and polymer composites with six electrodes, an optical waveguide and two microfluidics channels that performed similar functions to the ones described previously were also developed by the same group.¹⁷ Niu *et al.* fabricated shape memory polymer waveguides

embedded in $\text{Al}_2\text{O}_3/\text{ZnO}$ photonic shells with the ability to guide light through deep tissues and act as a temperature sensor to monitor in real time mouth respiration, nose breathing and infrared light.¹⁸ However, light delivery using these waveguides is limited to the trajectories that the material experiences to go from the original state to the deformed state. Omnidirectional light steering and navigation in a remotely controlled manner can be achieved by integrating optical fibers into a magnetic soft robot with hydrogel skin that reduces the friction by more than 10 times with their surroundings.¹⁹ There are examples in nature of living organisms with soft bodies/organs from which we can take inspiration to create functional materials and devices for real life applications. The female deep sea angler fish has lure filled with luminescent bacteria that is used to attract prey or mates by moving the back and forth while pulsing the light.²⁰ These creatures also have a muscular skin flap to occult or reveal its bright lure. Motile cilia are hair-like organelles present on the surface of some cells such as the ones present in lungs, respiratory tract, and middle ear.^{21,22} They are generally present in large amounts and have synchronized waving motion. The purpose of their motion varies on the kind of cells they are present which can be to maintain the airways clear of mucus and dirt, to move the ovum from the ovary to the uterus, to propel sperm and so on. Chromatophores are another kind of soft actuators present in the skin of several cephalopods such as squids, cuttlefish and octopuses. These organs are filled with nanostructured pigment granules joined together within an elastic sacculus that expand upon contraction of muscle fibers triggered by an electrical stimulus which makes the chromatophores increase their size temporally.²³ The visual perception of an observer is changeable pattern in the form of an array of coloured dots that seem to migrate in space. Inspired by these three examples of soft structures present in nature, we printed light-guiding structures within seconds including planar slab waveguides, individual and small arrays of cylindrical waveguides as well as long-range

waveguide lattices ($> 10\,000\text{ cm}^{-2}$). We demonstrated that their orientation, motion and - thereby the direction of their light output - can be precisely and remotely controlled through external electrical fields. Through the vectorial sum of external electric fields, we can then dynamically control the bending, angular orientation and rotation (up to 360°) of these pliant light-guiding structures. Reminiscent of the camouflaging techniques of certain marine creatures, this allows precise, remote control of the waveguided light output without the use of computers.

3.3 Horizontal Right-Left beam manipulation with slab electroactive hydrogels inspired by deep sea angler fish lure.

Our hydrogel was developed using as reference two formulations described previously.^{24,25} Slab hydrogel waveguides were obtained by patterning blue LED beams with circular or rectangular masks (Figure 3.1a). Radical polymerization of acrylic acid monomers was initiated launching these patterned beams to cells containing resin **H4** (Figure 3.1b). The refractive index change initiated by the photopolymerization reaction counteracts the natural diffraction of light allowing the patterned beam to travel without diverging while inscribing a polymeric structure in the medium. A 3D-printed rectangular prism waveguide is shown in Figure 3.1c. These prisms remained in the coverslip acting as entrance face of the cell in which they were printed. Such coverslips were placed between two cylindric carbon electrodes that were 7 mm apart from each other in a cage with two open sides that were sealed with coverslips. The slab waveguides were partially immersed in a phosphate buffer solution (pH = 7.4, C = 0.4 M) that acted as electrolyte with the top part of the waveguide above the buffer surface. We first carried out these experiments using a horizontal configuration in which a blue LED beam was launched to the top part of the waveguide before applying an electric field. Our set up is shown in Figure 3.1d. Although there is buffer present in the hydrogel, only 2 % of monomers in the hydrogel are deprotonated

after printing. When the sample is immersed in buffer solution, most acrylic acid monomers lose their acidic proton producing an anionic network (Figure 3.1e, left). When an electric field is applied, the counterions within the hydrogel migrate towards the side closer to the cathode but remain within the network to preserve the electroneutrality inside the gel. The concentration of positive ions at the polymer-solution interface within the hydrogel at the cathode side becomes larger than the one at the anode side.²⁶ In the external solution, there is a greater migration of ions towards the cationic side of the hydrogel because of the gel permselectivity to cations (Figure 3.1e, middle). This concentration gradient generates a higher osmotic pressure on the anode side (π_1) (Swelling) than on the cathode side (shrinks) (π_2) (Eq. 3.1). A positive pressure difference (Eq. 3.2) gives as result swelling on the anode side and bending (Figure 3.1e, right) towards the cathode.²⁷

$$\pi_{ion} = RT \sum_i (C_i^h - C_i^s) \quad (3.1)$$

$$\Delta\pi_{ion} = \pi_1 - \pi_2 \quad (3.2)$$

Based on a three-point bending test, $\Delta\pi_{ion}$ is equal to the tensile strength applied to the gel σ :^{27,28}

$$\Delta\pi_{ion} = \sigma = 6DEY/L^2 \quad (3.3)$$

Where D and L are the thickness and the length of the gel, E the Young modulus and Y the degree of bending. In this instance, Y is defined as the difference between the distance of the hydrogel ends before and after bending. A constant electric force produces a constant pressure difference. Solving **Eq. 3.3** for the degree of bending, we obtain:

$$Y = \sigma L^2 / 6DE \quad (3.4)$$

Since the length of the gel is the parameter that has the biggest impact on the degree of bending, 3D-printed rectangular prisms are fabricated keeping the width and the height constant ($W \times H = 2 \text{ mm} \times 10 \text{ mm}$) while varying their length (6, 9 and 10 mm). Figure 3.2a shows a slab waveguide 10 mm long under the effect of an electric field (1300 V/m). The slab waveguide bends towards the cathode. At the same time, the beam output shifts in the same direction showing that this hydrogel prism can spatially manipulate the beam. As a result, there is a drop in the intensity since most of the light is guided away from the detector. When the polarity of the field is inverted, the bending occurs in the opposite direction. The net effect is a bright sheet with a 2 mm thickness that seems to turn “off” from the point of an observer or light detector. The intensity of the beam is recovered when the waveguide is perpendicular to the optical set up and it decreases again as it keeps bending in the opposite direction. The intensity output of the waveguide decreases $\sim 92 \%$ (Figure 3.2c) when the waveguide reaches its maximum bending angle θ_{max} which is on average $10^\circ \pm 2^\circ$ (Figure 3.2b). Although the waveguide seems to turn “off”, beam propagation simulations show that the acceptance angle of this waveguide is 38° (Figure 3.9). This confirms that the intensity only decreases because light is guided away from the detector. After 5 minutes under the effect of the having the electric field on, the bending equilibrium is achieved faster than at the beginning of the experiment (Figure 2c). This is most likely caused by an increase of charge density in the network (mole fraction of charged species).

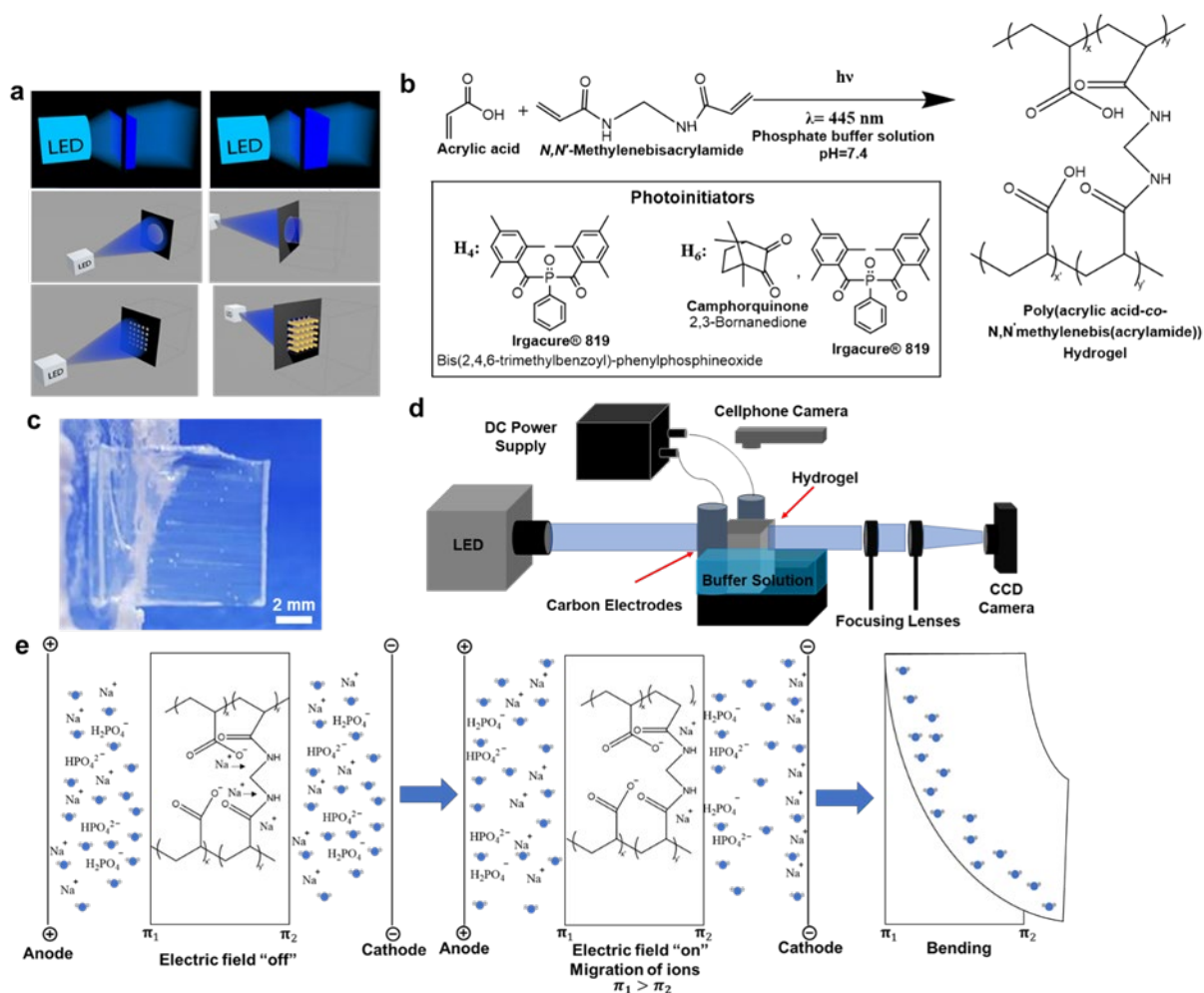


Figure 3.1 a) Slab waveguides were printed by launching a LED beam ($\lambda = 445 \text{ nm}$) through a rectangular or circular mask (top and middle images). The patterned beam was then launched to a cell containing resin **H4**. Micro-patterned prisms were printed by passing the same LED beam through a 2D periodic amplitude mask ($\Lambda = 80 \mu\text{m}$, $\approx 0.94 \text{ mW mm}^{-2}$) before being launched to the amplitude mask that defines the shape of the prism (bottom). In this case the cell contained resin **H6**. **b)** The LED beam induces localized free radical polymerization of acrylic acid monomers resulting in the formation of a prism hydrogel waveguide. **c)** Hydrogel prism 10 mm long (Width= 2 mm, Height= 10 mm). **d)** Optical up used to achieve horizontal right-left beam manipulation with electroactive rectangular waveguides. Samples glued to coverslips placed between two graphite electrodes were partially immersed in a phosphate buffer solution. A blue LED beam was launched to the top part of the sample. Optical profile at the exit face of the gel was monitored with a planoconvex lens pair (L1, f.l. = 250 mm and L2, f.l. = 250 mm) and a CCD camera. **e)** Bending mechanism in electroactive hydrogels. Counterions within the anionic network migrate toward the cathode when an electric field is applied but remain within the polymer to preserve the electroneutrality inside the gel. The local concentration of ions at the cathode increases due to the gel permselectivity to cations (middle). This concentration gradient generates a higher osmotic pressure on the anode side than on the cathode. A positive pressure difference results in swelling on the anode side and bending (right) toward the cathode.

It has been previously shown that the rate of bending increases with the fixed charge density as long as the total charge density is below 70 % in hydrogels with acrylic acid as the monomeric unit.²⁸ The maximum bending angle for the waveguides 9 and 6 mm long is on average $10^\circ \pm 2^\circ$ and $3^\circ \pm 2^\circ$. When such angle is reached, the intensity decreases to ~ 22 and ~ 75 % of its original value. Graphs showing the time evolution of bending angle and beam output can be found in Figure 3.10. Right-left beam manipulation can also be done using a vertical configuration. For this purpose, we 3D-printed a square cage and place two rectangular glassy carbon electrodes 29 mm apart (Figure 3.11). We inserted a cylindrical hydrogel waveguide (Diameter= 2 mm, Length= 12 mm) in the middle of the cage through a 2 mm hole. The effective length of the cylinder was 9 mm. Around 8 of the 9 mm were immersed in a buffer solution while keeping the top of the waveguide above the solution surface. Unlike the horizontal configuration in which light travels through entirely through the top part of a rectangular prism which is not immersed in the buffer solution, ~ 89 % of the cylindric waveguide is immersed in a buffer solution and 11 % is surrounded by air. We applied an electric field of 520 V/m and launched an attenuated green laser beam ($\lambda = 520$ nm). We followed the spatial evolution of the cylinder and the intensity of the beam output with a Moticam 3+ CMOS camera. The polarity of the beam was switched every 180 seconds before reaching equilibrium to keep the tip clean since carbon particles and water droplets are generated in the medium when the electric field is applied. We observed a similar behavior to the horizontal configuration (Figure 3.3a). When the electric field is applied, the cylinder bends towards the cathode and the intensity of the beam output decreases so the waveguide turns into a cylinder with the bright tip seems to turn off and on from the point of view of the detector. In this particular experiment, the intensity of the beam fully recovers during the first 400 seconds when the polarity of the electric field is inverted and the waveguide points

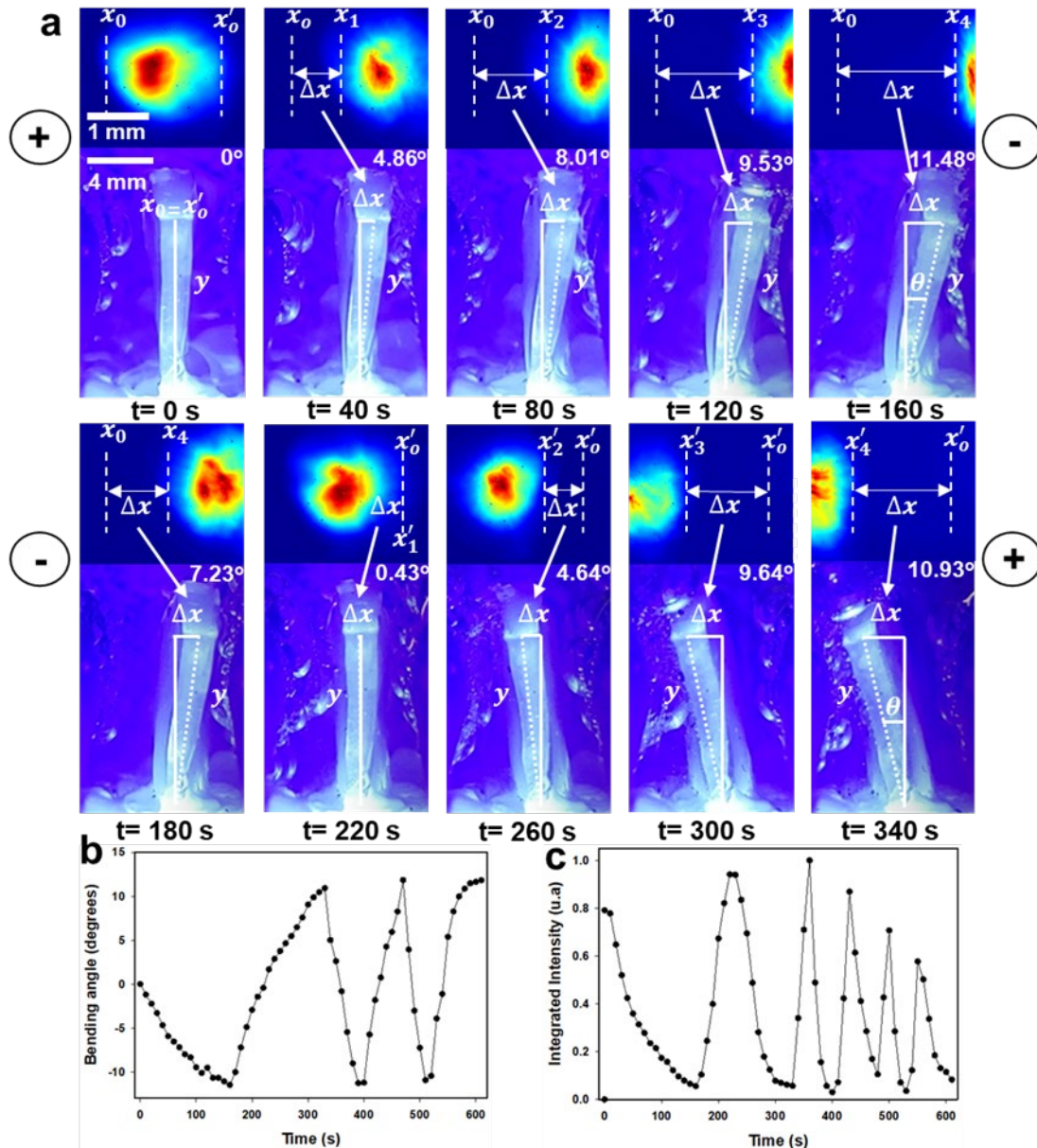


Figure 3.2. **a)** Top view and 2D beam output profile time evolution of a waveguide 10 mm long under the effect of an electric field ($\sigma = 1300$ V/m) when irradiated with a blue LED ($\lambda = 455$ nm). When the electric field is applied, the waveguide bends toward the cathode. At the same time, the beam traveling through the waveguide bends in the same direction. When the polarity of the electric field is reversed, the waveguide and the beam output move in the opposite direction. **b)** Time evolution of the bending angle and integrated intensity of the beam output **c)** As the waveguide bends away from the optical set up, the intensity on the detector decreases $\sim 92\%$ when the maximum bending angle is reached.

directly at the camera again (Figure 3.3c). After 400 seconds of applying the electric field, the intensity of the beam output starts to decrease over time as a result of three factors:

fatigue damage, the fracture plane created by the base surface when the cylinder bends and/or swells and, by the droplets of water with carbon particles that end on the waveguide output that block the laser beam avoiding it to reach the camera that acts as detector.

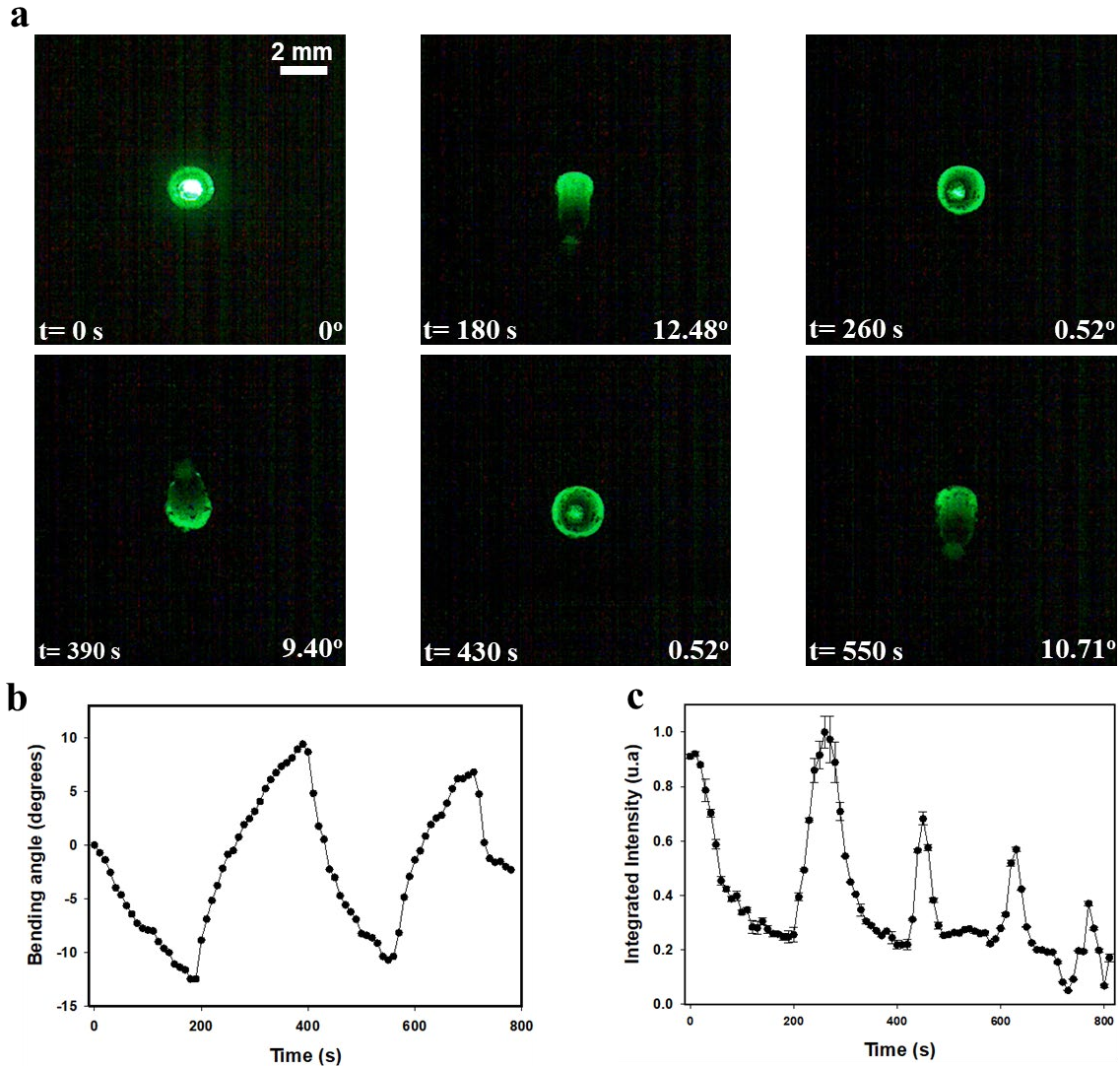


Figure 3.3 a) Top view of the time evolution of a waveguide 9 mm long under the effect of an electric field ($\sigma = 520 \text{ V/cm}$) illuminated with a green laser ($\lambda = 520 \text{ nm}$). When the electric field is applied, the waveguide bends towards the cathode as in the horizontal configuration. When the polarity of the electric field is reversed after 180 s, the waveguide moves in the opposite direction. **b)** Time evolution of the bending angle when the polarity of the electric field is switched every 180 s before reaching equilibrium. A maximum bending angle of $10^\circ \pm 2^\circ$ is achieved. **c)** The intensity of the beam output decreases as it bends since light is guided away from the detector reaching a minimum of $\sim 23\%$ of its original value. The intensity of the beam output is fully recovered during the first 400 s when the polarity of the beam is inverted, and the cylinder points out directly at the camera.

During the first 600 seconds of having the electric field “on”, the maximum bending angle achieved is $10^\circ \pm 2^\circ$ (Figure 3.3b) and the intensity drops to $\sim 23\%$ of its original value when such angle is reached.

3.4 Cilia-inspired array of cylindric electroactive waveguides

The female deep see angler fish is not the only living organism with a stick-like soft structure. Some cells have organelles at their surface known as cilia which also have a periodic motion known as metachronal rhythm in which there is a phase lag that leads to a sequential action similar to a Mexican wave, an example of macroscopic methachronal wave.²⁹ Inspired by these organelles, we printed a large-scale system that consists of arrays of cylindric waveguides that experience coordinated bending towards the cathode. We hypothesized that the cylindric waveguides will be affected in a different way depending on their position relative to the cathode. We carried out bending experiments with square arrays of 4 (2 x 2) and 9 (3 x 3) cylindric waveguides as well as with an individual waveguide. The individual waveguide which was placed at the center of the cage with a distance of 14.5 mm from the edge of the cathode to the center of the hydrogel. In the array of four cylindric waveguides, the first row of two was placed 13 mm away from the cathode while the second row is placed 17 mm away. In the array of 9 waveguides, the first row of 3 cylinders is 11 mm away from the cathode. The second one is right at the center of the cage as in the case of the individual cylinder while the third row is 19 mm away from the electrode. In these experiments, we lead waveguides reached their maximum bending angle θ_{max} . Since significantly damage in the cylinders is observed in the arrays after they bend for the first time, only the first θ_{max} obtained in each experiment was used in the calculations. The polarity of the field was inverted once equilibrium was reached. The individual cylinder achieves a maximum bending

angle of $9^\circ \pm 0^\circ$. (Figure 3.4, left). In the case of the array of 4 cylinders, the two cylinders that are close to the cathode (cylinders 21 and 22) bend on average $12^\circ \pm 1^\circ$ while the two cylinders that are closer to the anode (cylinders 11 and 12) only bend $6^\circ \pm 0^\circ$ (Figure 3.4, center). Finally, in the array of 9 cylinders, the row facing the cathode (11 mm away) bends on average $9^\circ \pm 3^\circ$, the cylinders in the middle of the cell (15 mm away from the cathode) and the row facing the anode bend only $5 \pm 1^\circ$ (Figure 3.4, right). Comparing the individual cylinder and the array of four cylinders, it is clear that the closer the cylinders are to the cathode the more they bend. The closer the cylinder is to the cathode the greater is the force mobile cations experience which results in a higher concentration of mobile cations near the cathode. This produces a higher osmotic pressure on the anode side of each cylinder, having this osmotic pressure a greater magnitude as they get closer to the cathode. A similar trend is observed for the array of 9 cylinders. The second and third row of cylinders have on average the same maximum bending angle of $5^\circ \pm 1^\circ$. The row closer to the cathode, as expected, achieves a greater maximum bending angle ($9^\circ \pm 3^\circ$). However, we can see that the second column which is right at the center of the cage has a significantly smaller bending angle than the individual rod which is placed in the same position which indicates that the outer waveguides exert sort of electric field screening. The waveguides closer to the cathode experienced a faster bending rate ($9 \pm 1 \times 10^{-4}$ rad/s for the 3 x 3 array and $7 \pm 2 \times 10^{-4}$ rad/s for the 2 x 2 array) than the waveguides that are place in the second and third row ($4 \pm 0 \times 10^{-4}$ rad/s for the 2 x 2 array and $4 \pm 0 \times 10^{-4}$ rad/s for the second and third row in the 3 x 3 array). Therefore, at early stages of the experiment the waveguides closer to the anode seemed to experience a delay in their response compared to the waveguides in the first row. Hydrogel arrays with the actual dimensions (typical lengths and thickness are 5-20 μm and 0.25-1 μm) of cilia were fabricated by Mendes et al.³⁰

3.5 Hydrogel waveguide array inspired by squid skin

Squids are soft marine animals that belong to the class Cephalopoda which also includes cuttlefish, octopus and nautilus. The most dynamic camouflage changes in their skin are originated by

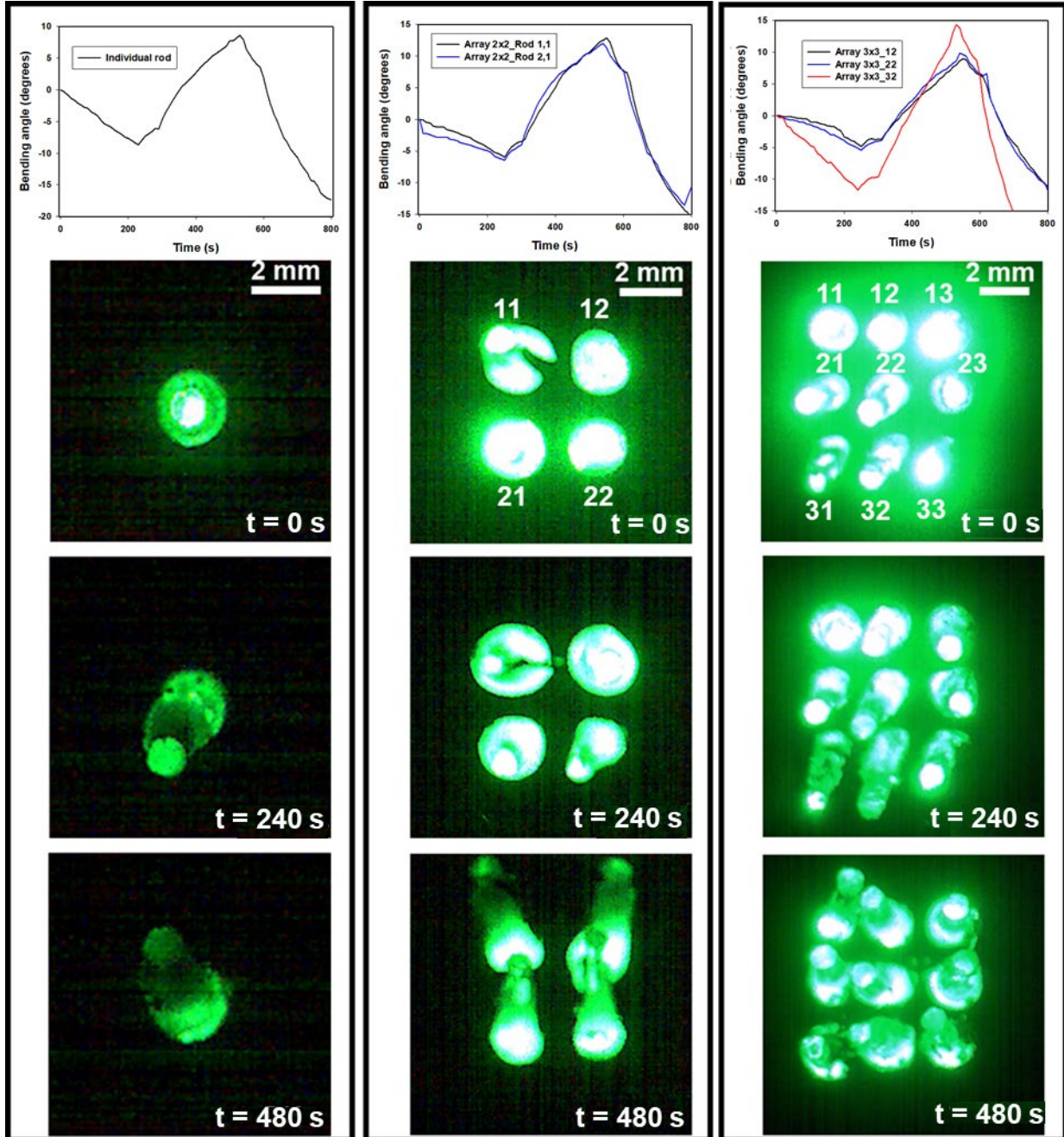


Figure 3.4 Vertical right to left bending of an individual as well as square arrays of 4 (2 x 2) and 9 (3 x 3) cylindric waveguides ($\sigma = 520 \text{ V/cm}$) irradiated with an expanded green laser beam ($\lambda = 520 \text{ nm}$). Graphs at the top show the time evolution of the bending angle of the individual cylinder and of cylinders 11 and 21 of the 2 x 2 array and, cylinders 12, 22 and 32 of the 3 x 3 array.

thousands of dense organs in their skins filled with pigments that have a high refractive index ($n \sim 1.9$) known as chromatophores.³¹ The organ is an elastic sacculus filled with pigment granules with fiber muscles attached to its periphery. Upon a neural signal, the muscle contracts while the sacculus expand which produces a colorful dot which disappears when the neural signal is removed. The net result from the point of view of an observer after a contraction wave is an array of dots that seems to migrate in space. We previously showed that it is possible to print micro-waveguide arrays in an organosiloxane polymer.⁹ We can think about these arrays as polymer fibers embedded in a gel and as high refractive index regions. We hypothesize that creating these arrays using an electroactive hydrogel would allow the formation of a structure with a bright array of dots that would seem to migrate in space from the point of view of an observer. In addition, the light traveling through these microchannels is going to be directed towards the direction in which the waveguide is bending. Our group recently showed that the intensity output and size of a waveguide within a hydrogel network can be affected by contractions produced by the formation of a temporal waveguide generated at a distance at least 10 times the beam width.³² Since the bending in electroactive hydrogels is accompanied by contractions and expansions within the network, we expect complex fluctuations in the intensity of the micro-waveguides embedded within the hydrogel network under the effect of an electric field which will make some waveguides to be expressed while others will turn off just as occurs in squid skin. For this purpose, we printed hydrogel prisms with waveguide lattice embedded. Figure 3.5a shows an example of a hydrogel rectangular prism 6 mm long and 2.5 mm wide with a waveguide lattice embedded that was printed in only 12 seconds. Micrographs of the side view (Figure 5b), as well as entrance and exit face (Figure 5c and d), of this lattice confirm the presence of the waveguides. Imaging with a blue LED

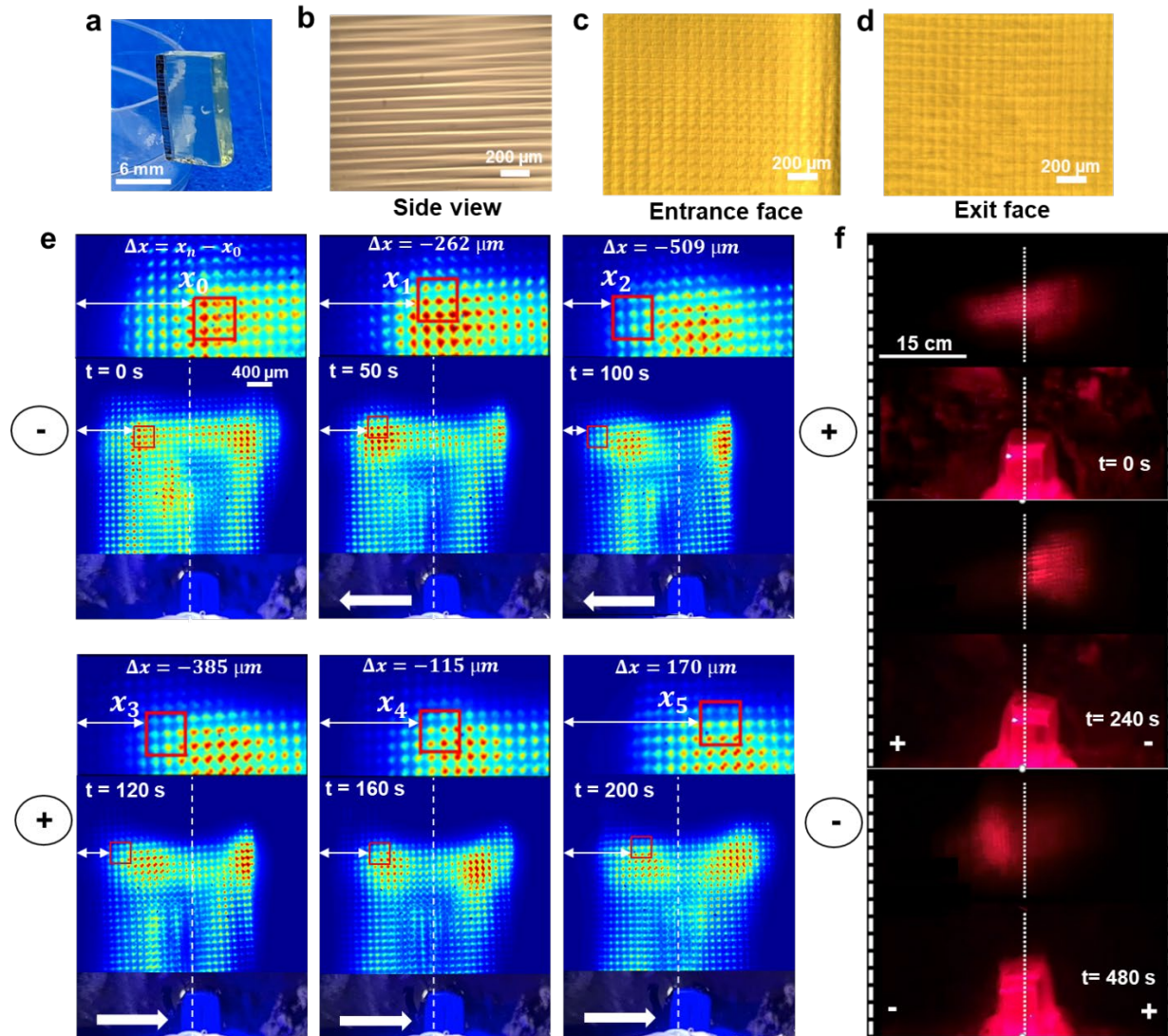


Figure 3.5 a) Hydrogel prism (H x L x W= 10 mm x 6 mm x 2.5 mm) with a waveguide lattice embedded. b) Side view, c) entrance and d) exit faces micrographs of the waveguide lattice. e) Time evolution of the hydrogel waveguide lattice under the effect of an electric field $\sigma = 350 \text{ V/cm}$. The electric field was applied for 100 seconds to keep the lattice within the field of view of the CCD camera. After this period, the electric field was turned off for 60 seconds before inverting the field. The square light pattern generated by the lattice moves towards the cathode. f) Far field view of the light pattern generated by a hydrogel prism (H x L x W= 10 mm x 6 mm x 3.5 mm). The top image shows the hydrogel prism with the waveguide lattice embedded and the light pattern before the electric field was applied. The middle image shows the position of the pattern and the hydrogel lattice after applying the electric field ($\sigma = 350 \text{ V/cm}$) for 240 s. The light pattern is clearly directed to the right. The bottom image shows how light is directed in the opposite direction 240 seconds after the polarity of the field was inverted. Data acquired by Oscar Herrera and Kevin Vaughan.

launched into the sample exit face (at low intensities) shows the presence of an array of bright micro-beams with non-uniform intensity and with the same periodicity of the amplitude mask used to create the pattern. Under the effect of an electric field the waveguide bends towards the cathode while the array of micro-beams also moves in the same direction (Figure 3.5e). Changing the polarity of the electric field after 100 seconds produces the same effect, now in the opposite direction. The ability of the structure to direct light in the same direction of the bending is very evident when the light pattern coming out of the lattice is projected onto a black surface, in conjunction with a semi-coherent laser light source (Figure 3.5f). Positions and intensities of filaments within the hydrogel lattice were analyzed using Trackpy, a Python particle tracking package.³³ Image sets were collected by applying an electric field for 100 seconds in one particular direction before inverting its polarity. In this first trajectory, the whole pattern is initially displaced approximated 509 μm (Figure 3.6). After that, 60 seconds elapsed before applying the electric field with an inversed polarity. The displacement of the hydrogel was only 170 μm in the opposite direction, taking as a reference the initial position. This effect is probably originated by the pH gradient produced by the electrolysis of water.³⁴ OH^- ions are produced in the cathode side while H^+ ions are produced in the anode side. Unlike the slab waveguides, the high porosity of the hydrogel lattice facilitates the penetration of ions from the solution to the polymer network. So as the field is applied, some of the COO^- groups on the anode side get protonated. When the electric field is inverted, the excess of protons on the anode side has to be neutralized first by the OH^- that now are being produced in the former anode side before the COOH groups are deprotonated again. Therefore, the ability of the hydrogel to respond to the applied stimulus decreases temporarily

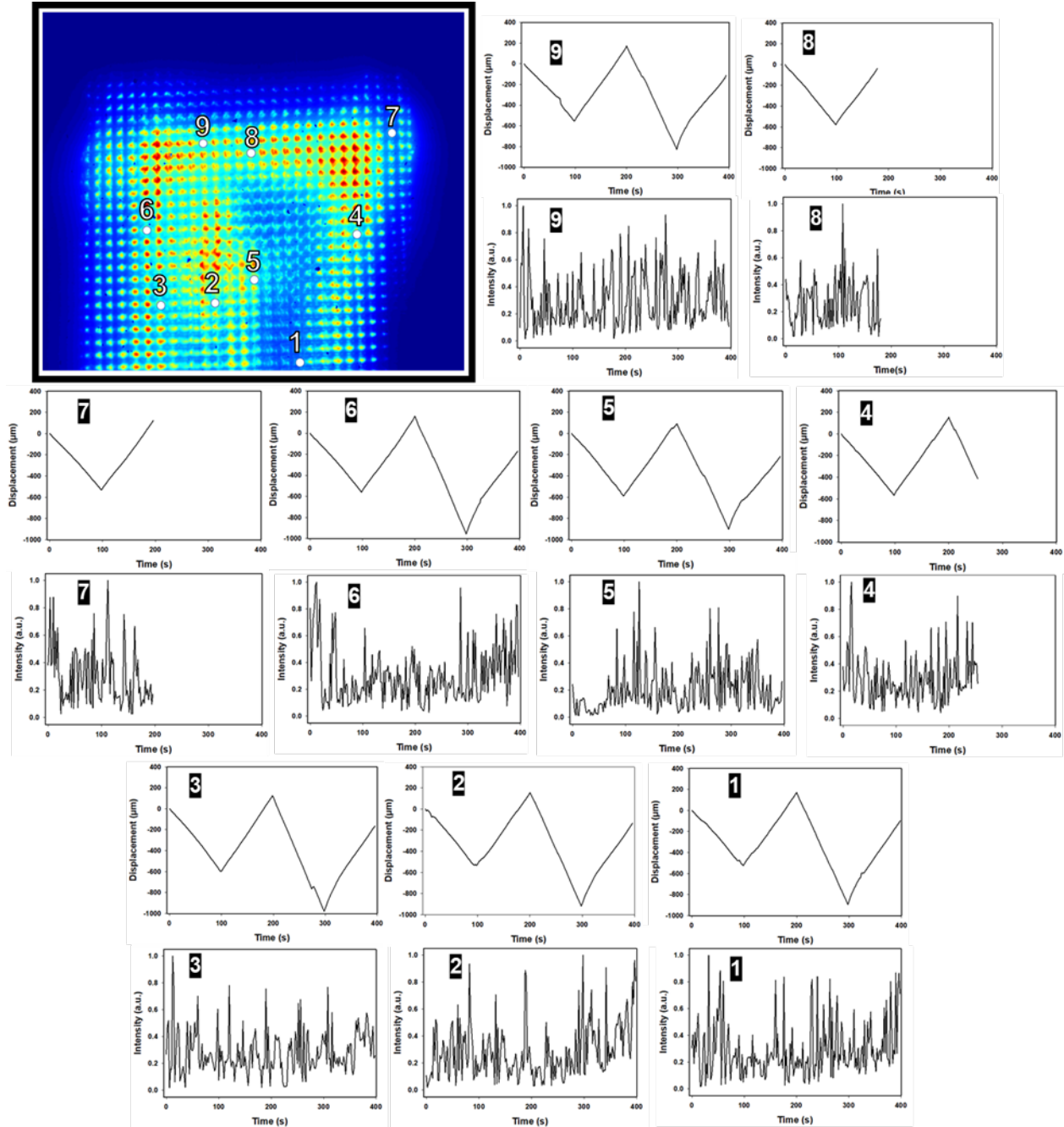


Figure 3.6. Graphs showing the time evolution of the displacement and intensity of the nine waveguides highlighted in the image at the top right while. The electric field was applied for 100 in one direction (μm) before inverting its polarity. As the displacement graphs show, when the polarity was inverted, the waveguides does not bend to the same extend in the opposite. Unlike the intensity output of the slab waveguide, the intensity output of the micro-waveguides shows random fluctuations. Intensity/position filament tracking processing was done by Kathryn Benincasa.

ions facing the cathode. It is also possible that fatigue damaged in immediately manifest in the first 100 s. The intensity of the individual waveguides shows a completely different behavior compared to the intensity output of the slab waveguides. Unlike the slab waveguides in which the intensity decreases when the slab waveguides direct the light output away from the CCD camera and then it is recovered again as goes back to the original position, the intensity output of the micro-waveguides shows random fluctuations which indicates a complex dynamic taking place within the lattice. Since the waveguide lattice is a network of interconnected polymer fibers, contractions and expansions due to the osmotic pressure difference have an impact even in the area that we are monitoring which is not immersed in the buffer solution. Protonation and deprotonation of the COO^- groups due to the pH gradient also induces contractions and expansions due to the increase or decrease of the repulsion among charges of the same sign.³⁵ Local contractions and expansions might affect waveguides that are located at a distance of at least 10 times the beam width of a micro-waveguide.³² The change of the position of the waveguide with respect to the detector (CCD camera) might also have an impact on the intensity output. Further investigation is needed to explain the experimental results obtained through our analysis.

3.6 Multidirectional bending of cylindric hydrogel waveguides

Soft robots made of electroactive hydrogels are only capable of performing unidirectional bending and locomotion.^{25,26} To the best of our knowledge, control over the bending direction of electroactive hydrogels have not been achieved so far. We built a set up with a square geometry made of four rectangular electrodes that can be used to achieve multidirectional bending by combining the electric fields generated by two different power supplies. A scheme of this set up,

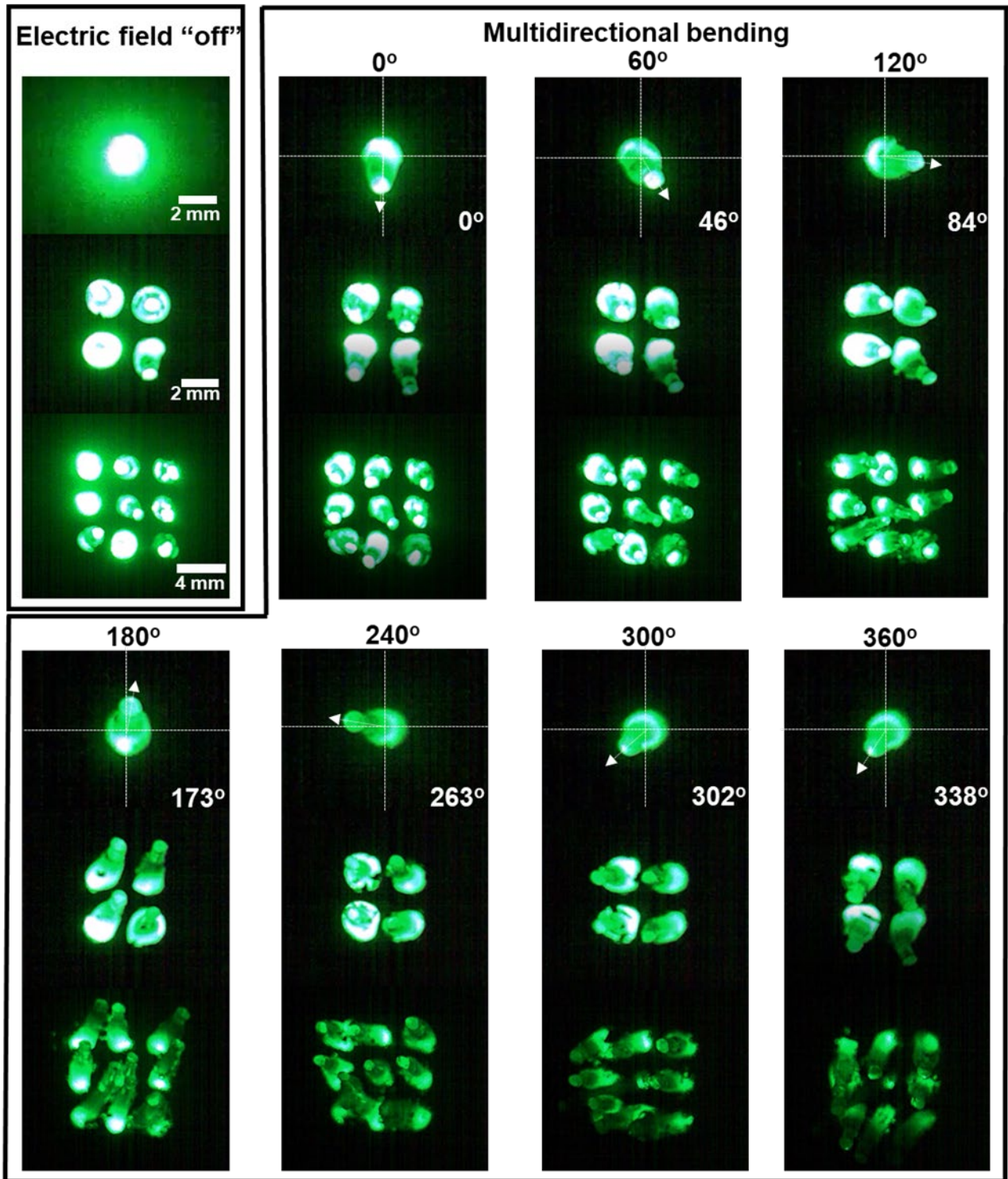


Figure 3.7. Multidirectional bending of cylindrical waveguides illuminated with an expanded green laser ($\lambda = 520 \text{ nm}$). The top left shows an individual waveguide and arrays of 4 and 9 waveguides before the electric field is applied. Target angles are shown above each image. Target angles for the individual waveguide are shown at the right of each image of the individual waveguide. Going through each target angle in a sequence allows the waveguides to rotate.

the vectorial analysis carried out to combine the electric fields and the polarity configuration on the electrodes for each target angle can be found in Figure 3.12. We traced imaginary lines along the direction of the electric field generated by each power supply that were treated like axis. Bending angles were calculated only for individual cylindrical waveguides placed in the center of the square array although we also applied the same combined electric field for each configuration to arrays of 4 (2 x 2) and 9 (3 x 3) cylindrical waveguides. The combined force electric field was kept constant (520 V/m). Our target angles were: 0°, 60°, 120°, 180°, 240°, 300° and 360°. We used the first bending direction of the cylinder as the reference and assigned a 0° value. We used the first bending direction of the cylinder as the reference and assigned a 0° value. For the initial direction, the electric field was applied for 240 s. After that, we switched to the second configuration while applying the electric field for 180 s. This process was repeated until waveguides completed a full cycle. Experimental bending angles for the individual waveguide obtained were 0°, 46°, 84°, 173°, 263°, 302° and 338° (Figure 3.7). A polar plot tracking the position of the waveguide tip and the intensity output is shown in Figure 3.12. This graph shows that the intensity of the waveguide remains steady as it bends to the initial direction. The decrease of the waveguide intensity output overtime is mostly associated with damage of the waveguide. Even though experimental angles show some deviation from target angles, we showed that this approach allows to direct the waveguides towards specific directions and also to achieve rotation. In our multidirectional bending experiments, waveguides were fixed to the base of our set up so only multidirectional bending and rotation are possible. However, this approach could also be used to make soft robots walkers move not only from right to left but also, in multiple directions.

3.7 Conclusions and Outlook

Taking inspiration from organs of living organisms such as the lure of the female angler fish, cilia and squid skin, we fabricated electroactive planar waveguides, individual and small arrays of cylindrical waveguides as well as long range waveguides lattices ($> 10\,000\text{ cm}^{-2}$). We demonstrated that their orientation, motion and -thereby the direction of their light output can be remotely controlled using electric fields. Since both the fabrication and the manipulation of the waveguides is inexpensive, we expect this work to be the benchmark for the fabrication of inexpensive light steering devices for light-based therapies and surgery.³⁶ Regardless of the properties of the photopolymer used, each unit operation of our 3-D printing method produces a light-guiding structure. Therefore, this work also opens the door to print not only electroactive waveguide actuators in a single step but also thermal³⁷ or photoresponsive³⁸ waveguides or even waveguides that can respond to more than one stimulus.

3.8 References

- 1) Tumbleston, J. R.; Shirvanyants, D.; Ermoshkin, N.; Januszewicz, R.; Johnson, A. R.; Kelly, D.; Chen, K.; Pinschmidt, R.; Rolland, J. P.; Ermoshkin, A.; et al. Continuous Liquid Interface Production of 3D Objects. *Science* **2015**, *347*, 1349–1352.
- 2) de Beer, M. P.; van der Laan, H. L.; Cole, M. A.; Whelan, R. J.; Burns, M. A.; Scott, T. F. Rapid, Continuous Additive Manufacturing by Volumetric Polymerization Inhibition Patterning. *Sci. Adv.* **2019**, *5*, eaau8723.
- 3) Walker, D. A.; Hedrick, J. L.; Mirkin, C. A. Rapid, large-volume, thermally controlled 3D printing using a mobile liquid interface. *Science* **2019**, *366*, 360–364.
- 4) Regehly, M.; Garmshausen, Y.; Reuter, M.; König, N. F.; Israel, E.; Kelly, D. P.; Chou, C. Y.; Koch, K.; Asfari, B.; Hecht, S. Xolography for linear volumetric 3D printing. *Nature* **2020**, *588*, 620–624.
- 5) Kelly, B. E.; Bhattacharya, I.; Heidari, H.; Shusteff, M.; Spadaccini, C. M.; Taylor, H. K. Volumetric Additive Manufacturing via Tomographic Reconstruction. *Science (80-.)*. **2019**, *363*, 1075 LP – 1079.
- 6) Loterie, D.; Delrot, P.; Moser, C. High-Resolution Tomographic Volumetric Additive Manufacturing. *Nat. Commun.* **2020**, *11*, 852.

- 7) Dolinski, N. D.; Page, Z. A.; Callaway, E. B.; Eisenreich, F.; Garcia, R. V.; Chavez, R.; Bothman, D. P.; Hecht, S.; Zok, F. W.; Hawker, C. J. Solution Mask Liquid Lithography (SMaLL) for One-Step, Multimaterial 3D Printing. *Adv. Mater.* **2018**, *30*, 1800364.
- 8) Basker, D. K.; Cortes, O. A. H.; Brook, M. A.; Saravanamuttu, K. 3D Nonlinear Inscription of Complex Microcomponents (3D NSCRIPT): Printing Functional Dielectric and Metallo-dielectric Polymer Structures with Nonlinear Waves of Blue LED Light. *Adv. Mater. Technol.* **2017**, *2*, 1600236-n/a.
- 9) Herrera Cortes O. A.; Morim D. R.; Colin D.; Martinez E. A. H., Arora R.; Vargas-Baca I.; Saravanamuttu K. Decomposition and 3D printing of Volumetric Prismatic Elements using Nonlinear Optochemical Waveguides.
- 10) Biria, S.; Morim, D. R.; An Tsao, F.; Saravanamuttu, K.; Hosein, I. D. Coupling Nonlinear Optical Waves to Photoreactive and Phase-Separating Soft Matter: Current Status and Perspectives. *Chaos An Interdiscip. J. Nonlinear Sci.* **2017**, *27* (10), 104611.
- 11) Lorang, D. J.; Tanaka, D.; Spadaccini, C. M.; Rose, K. A.; Cherepy, N. J.; Lewis, J. A. Photocurable Liquid Core – Fugitive Shell Printing of Optical Waveguides. *Adv. Mater.* **2011**, *23*, 5055–5058.
- 12) Gao, H.; Chen, G. F. R.; Xing, P.; Choi, J. W.; Low, H. Y.; Tan, D. T. H. High-Resolution 3D Printed Photonic Waveguide Devices. *Adv. Optical Mater.* **2020**, *8*, 2000613.
- 13) Pyo, J.; Kim, J. T.; Lee, J.; Yoo, J.; Je, J. H. 3D Printed Nanophotonic Waveguides. *Adv. Optical Mater.* **2016**, *4*, 1190–1195.
- 14) Feng, J.; Zheng, Y.; Bhusari, S.; Villiou, M.; Pearson, S., del Campo, A. Printed Degradable Optical Waveguides for Guiding Light into Tissue. *Adv. Funct. Mater.* **2020**, *30*, 2004327.
- 15) Feng, J.; Jiang, Q.; Rogin, P.; De Oliveira, P. W.; Del Campo, A. Printed Soft Optical Waveguides of PLA Copolymers for Guiding Light into Tissue. *ACS Appl. Mater. Interfaces* **2020**, *12*, 20287–20294.
- 16) Canales, A.; Jia, X.; Froriep, U. P.; Koppes, R. A.; Tringides, C. M.; Selvidge, J.; Lu, C.; Hou, C.; Wei, L.; Fink, Y.; Anikeeva, P. Multifunctional fibers for simultaneous optical, electrical and chemical interrogation of neural circuits in vivo. *Nature Biotechnology* **2015**, *33*, 277–284.
- 17) Park, S.; Guo, Y.; Jia, X.; Choe, H. K.; Grena, B.; Kang, J., Park, J., Lu, C., Canales, A., Chen, R., Yim, Y. S., Choi, G. B., Fink, Y., Anikeeva, P. One-step optogenetics with multifunctional flexible polymer fibers. *Nature Neuroscience* **2017**, *20*, 612–619.
- 18) Cheng, J.; Zhang, L.; Zhao, K.; Wang, Y.; Cao, X.; Zhang, S.; Niu, W. Flexible Multifunctional Photonic Crystal Fibers with Shape Memory Capability for Optical Waveguides and Electrical Sensors. *Ind. Eng. Chem. Res.* **2021**, *60*, 8442–8450.
- 19) Kim, Y.; Parada, G. A.; Liu, S.; Zhao, X. Ferromagnetic soft continuum robots. *Sci. Robot* **2019**, *4*, eaax7329.
- 20) Baker, L. J.; Freed, L. L.; Easson, C. G.; Lopez, J. V.; Fenolio, D.; Sutton, T. T.; Nyholm, S. V.; Hendry, T. A. Diverse deep-sea anglerfishes share a genetically reduced luminous symbiont that is acquired from the environment. *eLife* **2019**, *8*:e47606.
- 21) Satir P.; Christensen S. T. Overview of structure and function of mammalian cilia. *Annu Rev Physiol.* **2007**, *69*, 377-400.
- 22) Eggenchwiler, J. T.; Anderson, K. V. Cilia and developmental signaling. *Annu Rev Cell Dev Biol.* **2007**, *23*, 345-373.

- 23) Bell, G. R. R.; Kuzirian, A. M.; Senft, S. L.; Mähger, L. M.; Wardill, T. J.; Hanlon, R. T. Chromatophore radial muscle fibers anchor in flexible squid skin. *Invertebrate Biology* **2013**, 132, 120–132.
- 24) Odent, J.; Wallin, T. J.; Pan, W.; Kruemplestaedter, K.; Shepherd, R. F.; Giannelis, E. P. Highly Elastic, Transparent, and Conductive 3D-Printed Ionic Composite Hydrogels. *Adv. Funct. Mater.* **2017**, 27, 1701807.
- 25) Han, D.; Farino, C.; Yang, C.; Scott, T.; Browe, D.; Choi, W.; Freeman, J. W.; Lee, H. Soft Robotic Manipulation and Locomotion with a 3D Printed Electroactive Hydrogel. *ACS Appl. Mater. Interfaces* **2018**, 10, 21, 17512-17518.
- 26) Morales, D.; Palleau, E.; Dickey, M. D.; Velev, O. D. (2014). Electro-actuated hydrogel walkers with dual responsive legs. *Soft Matter* 2014, 10, 1337.
- 27) Jin, S.; Gu, J.; Shi, Y.; Shao, K.; Yu, X.; Yue, G. Preparation and electrical sensitive behavior of poly (N-vinylpyrrolidone- co-acrylic acid) hydrogel with flexible chain nature. *European Polymer Journal* **2013**, 49, 1871–1880.
- 28) Morales, D.; Palleau, E.; Dickey, M. D.; Velev, O. D. Electro-actuated hydrogel walkers with dual responsive legs. *Soft Matter* **2014**, 10, 1337.
- 29) Gueron, S.; Levit-Gurevich, K.; Liron, N.; Blum, J. J. Cilia internal mechanism and metachronal coordination as the result of hydrodynamical coupling. *Proc. Natl. Acad. Sci. U. S. A.* **1997**, 94, 6001–6006.
- 30) Glazer, P. J.; Leuven, J.; An, H.; Lemay, S. G.; Mendes, E. Multi-stimuli responsive hydrogel cilia. *Adv. Funct. Mater.* **2013**, 23, 2964–2970.
- 31) Dinneen, S. R.; Osgood, R. M.; Greenslade, M. E.; Deravi, L. F. Color Richness in Cephalopod Chromatophores Originating from High Refractive Index Biomolecules. *J. Phys. Chem. Lett.* **2017**, 8, 313–317.
- 32) Morim, D. R.; Meeks, A.; Shastri, A.; Tran, A.; Shneidman, A. V.; Yashin, V. V.; Mahmood, F.; Balazs, A. C.; Aizenberg, J.; Saravanamuttu, K. Opto-chemo-mechanical transduction in photoresponsive gels elicits switchable self-trapped beams with remoteinteractions. *Proc. Natl. Acad. Sci. U. S. A.* **2020**, 117, 3953-3959.
- 33) D. B. Allan, et al. trackpy:Trackpy v0.4.1, <https://zenodo.org/record/3492186>, (2019).
- 34) O’Grady, M. L.; Kuo, P. L.; Parker, K. K. Optimization of electroactive hydrogel actuators. *ACS Applied Materials and Interfaces* **2010**, 2, 343–346.
- 35) Korevaar, P. A.; Kaplan, C. N.; Grinthal, A.; Rust, R. M.; Aizenberg, J. Non-equilibrium signal integration in hydrogels. *Nat. Commun.* **2020**, 11, 386.
- 36) York, P. A.; Peña, R.; Kent, D.; Wood, R. J. Microrobotic laser steering for minimally invasive surgery. *Sci. Robot.* 2021 6, eabd5476.
- 37) Hua, M.; Wu, D.; Wu, S.; Ma, Y.; Alsaid, Y.; He, X. 4D Printable Tough and Thermoresponsive Hydrogels. *ACS Appl. Mater. Interfaces* 2021, 13, 12689–12697.
- 38) Yao, Y.; Waters, J. T.; Shneidman, A. V.; Cui, J.; Wang, X.; Mandsberg, N. K.; Li, S.; Balazs, A. C.; Aizenberg, J. Multiresponsive polymeric microstructures with encoded predetermined and self-regulated deformability. *Proc. Natl. Acad. Sci. U. S. A.* 2018, 115, 12950–12955.

3.9 SUPPLEMENTARY INFORMATION

3.9.1 Resin formulations.

The hydrogel precursor for slab waveguides was obtained by mixing 67.61 mmol of acrylic acid, 6.94 mmol of N,N'-methylethylenebis(acrylamide) as crosslinker, 4.48×10^{-2} mmol of Irgacure® 819 as photoinitiator and 5 mL of sodium phosphate buffer solution 0.4 M (pH= 7.4) (Resin H4). The resin used to fabricate hydrogel prisms micropatterned with waveguide channels was a slightly modification from the previous one. Same amounts of acrylic acid, N,N'-methylethylenebis(acrylamide) and phosphate buffer solution were used. In this case, Irgacure® 819 (2.24×10^{-2} mmol) was used in combination with camphorquinone (1.20×10^{-2} mmol) (Resin H6).

3.9.2 3-D printing of slab hydrogel waveguides and micro-patterned prisms with channel waveguides

The slab waveguides were fabricated by launching a LED ($\lambda = 445$ nm, Thorlabs, $I \approx 0.94$ mW mm⁻²) beam through rectangular or circular amplitude masks placed at the entrance face of cells containing resin **H4** (Figure 3a). The beam propagated through cells with transparent coverslips as exit and entrance face with pathlengths of 6, 9, 10 and 12 mm for 14 - 20 seconds while triggering localized free radical polymerization (Figure 3b). The beam was blocked when the polymeric waveguide reached the exit face of the cell. Once the process was completed, the coverslip at the entrance face was removed with the polymeric structure attached to it. To obtain micro-patterned prisms with channel waveguides the LED beam was collimated using a planoconvex lens (F.L. = 250 mm, d= 25.4 mm) and passed through a 2D periodic amplitude mask ($\Lambda = 80$ μ m, ≈ 0.94 mW mm⁻², power measured after periodic mask) before being launched to the rectangular amplitude

mask that defines the shape of the prism (Figure 3a). In this case the cell contained Resin **H6**. The length of all micro-patterned prisms was 6 mm. The sample was irradiated for 12 seconds.

3.9.3 Horizontal Right to Left beam manipulation with slab electroactive hydrogels

3D-printed rectangular prism waveguides were used right after printing without any further treatment since they get cloudy upon swelling and tend to break easily as their swelling ratio increases. Waveguides (width x height= 2 mm x 10 mm) 6, 9 and 10 mm long were glued to coverslips between two graphite electrodes (diameter =10 mm) placed 7 mm apart. The coverslip was glued to a rectangular cage with two open sides. The other side of the cage was sealed with a coverslip as well. The waveguides were partially immersed in a phosphate buffer solution (pH=7.4, C = 0.4 M) that acted as electrolyte. A blue LED beam ($\lambda = 445 \text{ nm}$) was launched through the top part of the slab waveguides. Imaging of the optical profile at the exit face of the gel was achieved with a planoconvex lens pair (L1, F.L. = 250 mm and L2, F.L. = 250 mm) and a high-resolution charge-coupled device (CCD) camera [1200 horizontal x 1024 vertical pixels; pixel size = 3.2 μm horizontal x 3.2 μm ;]. Images were collected every 10 seconds. Integrated intensity was obtained by adding the intensity of all the pixels in each image. The bending of the hydrogel was monitored with a cellphone camera (Samsung 9) placed at the top of the electrochemical cell. A DC power supply (BK1735A-ND, B&K Precision) was used to generate the electric field. Once the hydrogel reached equilibrium, the polarity of the beam was inverted. We repeated this process until fatigue damaged in the hydrogel was observed. We performed 3 experiments for each different pathlength.

3.9.4 Calculation of bending angles

Since the bending curvature ($1/R$) for the longest waveguide (10 mm) is very small at the maximum bending angle θ_{max} (~ 0.02), it can be assumed that all the waveguides remain a straight line as they bend and that the length of the waveguide (y) remains constant over the experiment.

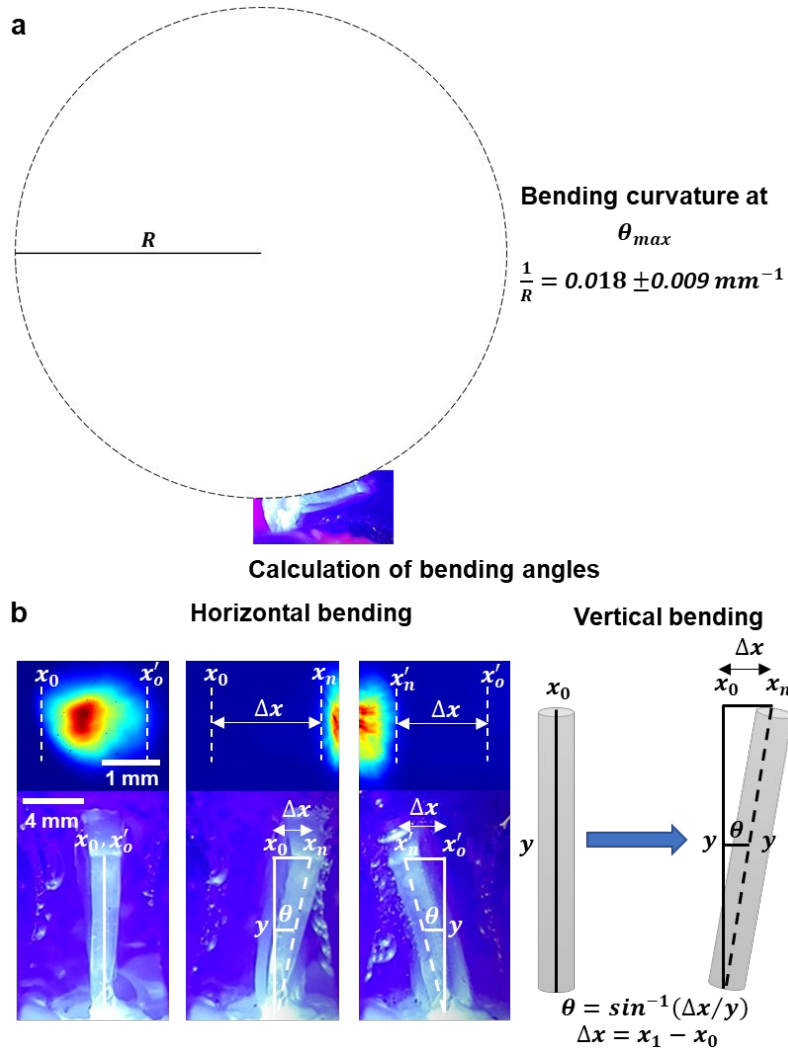


Figure 3.8. **a)** The average bending curvature of the longest waveguide at θ_{max} is ~ 0.02 . Therefore, it can be assumed that the waveguide remains a straight line and that its length does not change during the experiment. **b)** Illustration of how the displacement of the waveguide Δx was calculated for horizontal and vertical bending. Subtracting the initial position of one of the edges of the beam from the of the edge after 10 s. Bending angles were obtained using the inversed sine function.

The displacement of the waveguide Δx was calculated by subtracting the initial position of one of the edges of the beam from its new position after 10 seconds. Bending angles were obtained using the inversed sine function.

3.9.5 Beam Propagation Method (BPM) simulations of light propagation in slab hydrogel waveguides.

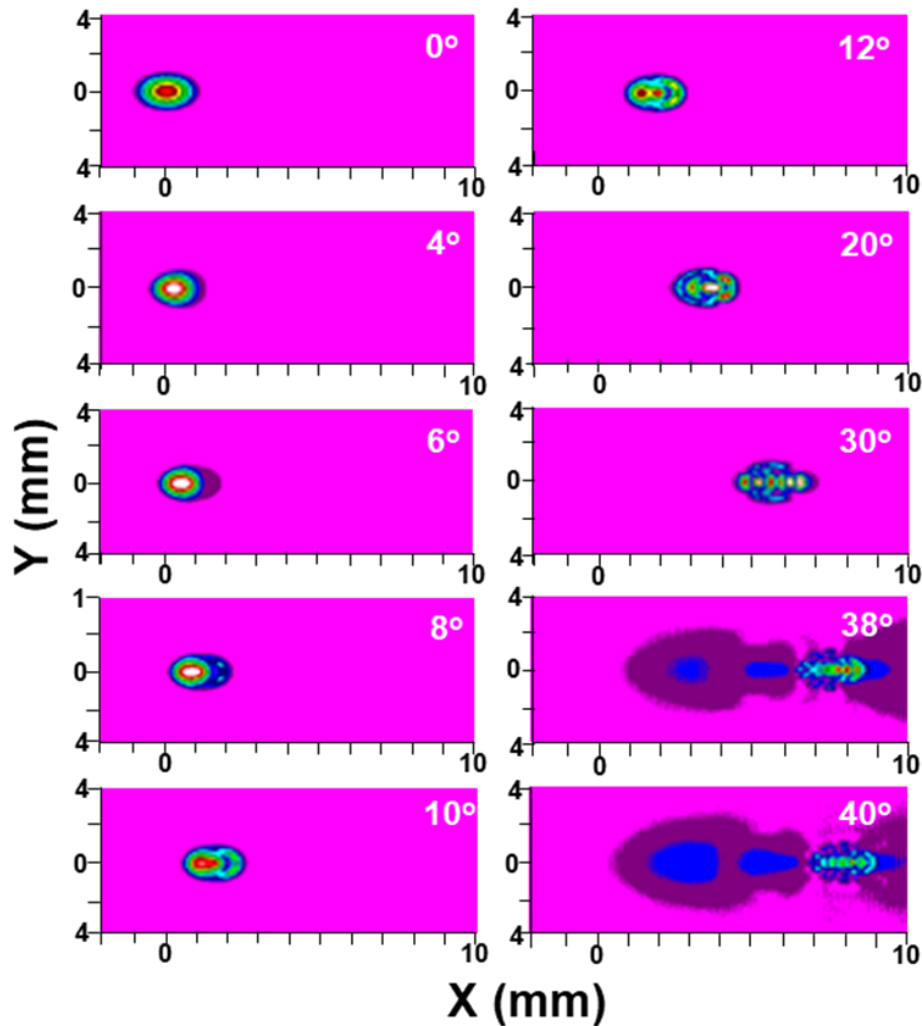


Figure 3.9 Beam propagation method simulations of a beam ($\lambda = 445 \text{ nm}$) traveling through a slab waveguide $10,000 \mu\text{m}$ long ($\Delta n = 0.4$) oriented at $0\text{-}12^\circ$, 30° , 38° and 40° with respect to the x axis. Transverse (xy) cross sections of the beam output are shown. After 38° , the beam output does not follow the trajectory of the waveguide. Instead, the beam is guided at an angle smaller than the angle at which the waveguide is oriented.

To find out the acceptance angle of the waveguide, we carried out simulations using Beam Propagation Method implemented in the BeamPROP software package (RSoft Products, Synopsys, USA). We simulated the hydrogel as a slab waveguide assuming an index step profile. The refractive index of the hydrogel was assumed to be an average between the refractive index of polyacrylic acid and water ($n = 1.4$).

3.9.6 Horizontal Right-Left beam manipulation with slab electroactive hydrogels

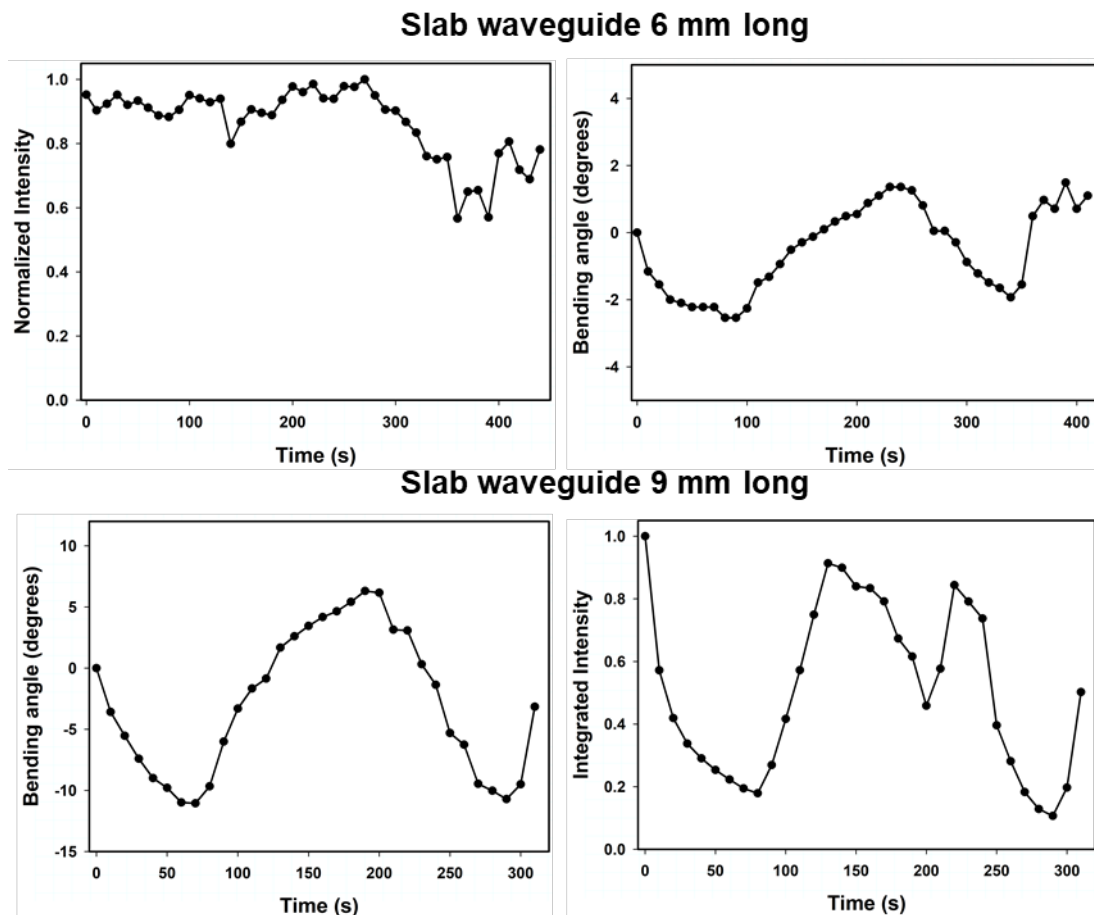


Figure 3.10 Time evolution of the bending angle (left) and integrated intensity of the beam output (right) of slab waveguides 6 and 9 mm long (c). As the waveguide bends away from the optical set up, the intensity on the CCD camera decreases. The maximum bending angle θ_{max} for the waveguides 9 and 6 mm long is on average 10 ± 2 and 3 ± 2 . When θ_{max} is reached, the intensity decreases to ~ 22 and ~ 75 % of its original value.

Since only the part of the hydrogel that is not immersed in water was imaged, the refractive index contrast used was $\Delta n=0.4$. The waveguide was 2 mm wide and 10 mm long. The waveguide was

oriented at 0-12°, 20°, 30°, 38° and 40° with respect to the x axis. The beam was launched parallel to the z axis. Beam profiles were captured at the xy plane.

3.9.7 Vertical right-left bending beam manipulation with slab electroactive hydrogels

We 3D printed a square prism cage (44 x 44 x 25 mm) with 4 electrode holders on each edge. This set up was used for multidirectional bending and rotation of cylindric waveguides as well. We placed 2 rectangular glassy carbon electrodes (25 x 25 x 3 mm) parallel to each other. The cylindric hydrogel (Diameter = 2 mm, Length= 12 mm) were inserted through circular holes in the bottom of the cage. The effective length of the waveguides was 10 mm for most experiments except for the experiments where the intensity was monitored in which the effective length was 9 mm. The cage was sealed with a coverslip glued to the bottom. 8 mm of the waveguides were immersed in buffer solution. We performed these experiments using individual and arrays of 4 and 9 cylindric waveguides. The rods were illuminated with a Compact Laser Module with USB Connector, 520 nm, 0.9 mW placed underneath the cube. A beam expander was used to illuminate the arrays. The time evolution of the waveguide position was followed with a Moticam 3+ camera. We analyzed the intensity of individual waveguides as they bend to compare their behavior with the rectangular prism waveguides. To keep the waveguide tip clean from the carbon particles generated during experiments with individual cylinders, we switched the polarity of the electric field every 180 s before the waveguide reached equilibrium. We tracked the position of the end of the waveguide as well as the intensity of the beam output using ImageJ. Experiments in which the waveguides reached equilibrium were also carried out with individual waveguides and arrays of 4 and 9 cylinders to analyze the relationship between the extend of bending and the distance of the waveguide from the cathode. Bending angles were calculated in the same manner as in the

horizontal experiments: the displacement of the waveguide Δx was calculated by subtracting the initial position of the center waveguide's end from its new position after 10 seconds. It was assumed that the effective length of the waveguide remained constant (9/10 mm) during the experiment. Bending angles were obtained using the inversed sine function. The polarity of the electric field was switched every 240 s. The electric force used was 500 V/m. We performed 3 experiments for each different pathlength.

3.9.8 Horizontal Right-Left beam manipulation with micro-patterned prisms with channel waveguides.

We used a set up for experiments with micro-patterned prisms similar to the one used for horizontal right-left beam manipulation with slab electroactive hydrogels. The only difference between this set up and the previous one is that electrodes were placed 43 mm apart. The field strength used was 350 V/m. The polarity of the electric field was switched every 100 seconds before equilibrium was reached to keep the array of microwaveguides within the camera field of view to monitor the highest number of filaments possible. We analyzed the intensity and tracked the position of each filament in a grid 10x10 filament in 3 different samples using ImageJ.

3.9.9 Structural characterization of prisms with micro-channel waveguides

A transmission microscope (Olympus BH2-UMA, Upright) coupled with a MOTICAM 3+ camera was used to acquire micrographs of the channel waveguides at the entrance and exit face of the prisms.

3.9.10 Tracking and intensity quantification of micro-beams within a hydrogel waveguide lattice

Trackpy¹ is a particle tracking program (PTP) that implements Crocker-Grier algorithm² to follow particles through a series of images. Briefly, the algorithm works in the following way. First, the program allows the user to determine the best parameters to select particles for a single frame - these will later be used for the entire set using a designated function in the package. The particle coordinates are then found in each frame to form particle trajectories. Lastly, the package offers different analysis tools to further compliment the dataset that is acquired, but that is solely up to the experimental design and what information is needed to be obtained. Using Trackpy¹ and other Python¹ programming packages, herein will be discussed the methods used to track filament location and intensity over a series of frames (i.e. time steps). Features are detected based on the local brightness of said feature. As such, particles should be as bright, distinct, and highly contrasted from the background as possible. Trackpy detects filaments by identifying the local brightness maxima within an image. To do this, a series of image filters are applied -to images to help enhance any filament features; are not to create new ones; or amplify noise in the structure. First, a white top hat filter is applied to amplify any small bright features. This is followed by a gaussian filter (also known as a gaussian blur), which reduces noise. Lastly, a maximum filter removes dark spots and widens bright image structures. To absolutely ensure that the highest regions of intensity are being selected, a binary map is created of the maximum filter image.

Crocker and Grier had written their algorithm based on tracking the movement of a suspension of colloidal particles, and thus assumed the particles were following a noninteracting, Brownian motion.¹ As a result of this assumption, if the particle moves significantly from one frame to the next (i.e., larger than the particle radius), the approximation fails and tracks are not correctly

linked.³ Therefore, minimizing the timesteps between frames was optimized by recording multiple logs with as short of time step as possible between frames.

First the raw data (i.e., .wct files acquired from DataRay beam profiling software) and grayscale images (as .png) are used to acquire a binary map of each image in the dataset of interest. From here a function returns a 2D numpy array of filament locations and their specified intensities.

3.9.11 References

- 1) D. B. Allan, et al. trackpy:Trackpy v0.4.1, <https://zenodo.org/record/3492186>, (2019).
- 2) Crocker, J. C.; Grier, D. G. Methods of Digital Video Microscopy for Colloidal Studies. *J. Colloid Interface Sci.* **1996**, *179* (1), 298–310. <https://doi.org/10.1006/jcis.1996.0217>.
- 3) Couédel, L.; Nosenko, V. Tracking and Linking of Microparticle Trajectories during Mode-Coupling Induced Melting in a Two-Dimensional Complex Plasma Crystal. *J. Imaging* **2019**, *5* (3). <https://doi.org/10.3390/jimaging5030041>.

3.9.12 Multidirectional bending of cylindric hydrogel waveguides

To achieve multidirectional bending, we combined electric fields generated from two power supplies connected to four glassy carbon plates. The combined electric field was kept constant (500 V/cm). We traced imaginary lines along the direction of the electric field generated by each power supply that were treated like axis. An example of the vectorial analysis carried out to combine the electric fields is shown in Figure 5a. The voltages employed to achieve each target angle as well as the polarity configurations on the carbon plates are shown in Figure 5b. Our target angles were: 0°, 60°, 120°, 180°, 240°, 300° and 360°. We used the first bending direction of the rod as the reference and assigned a 0° value. For the initial direction, the electric field was applied for 240 s. After that, we switched to the second configuration while applying the electric field for 180 s. This process was repeated until the waveguide completed a full cycle. It was assumed that the length of the cylinders remained 10 mm during the whole experiment. The same procedure was used for the array of 4 and 9 waveguides.

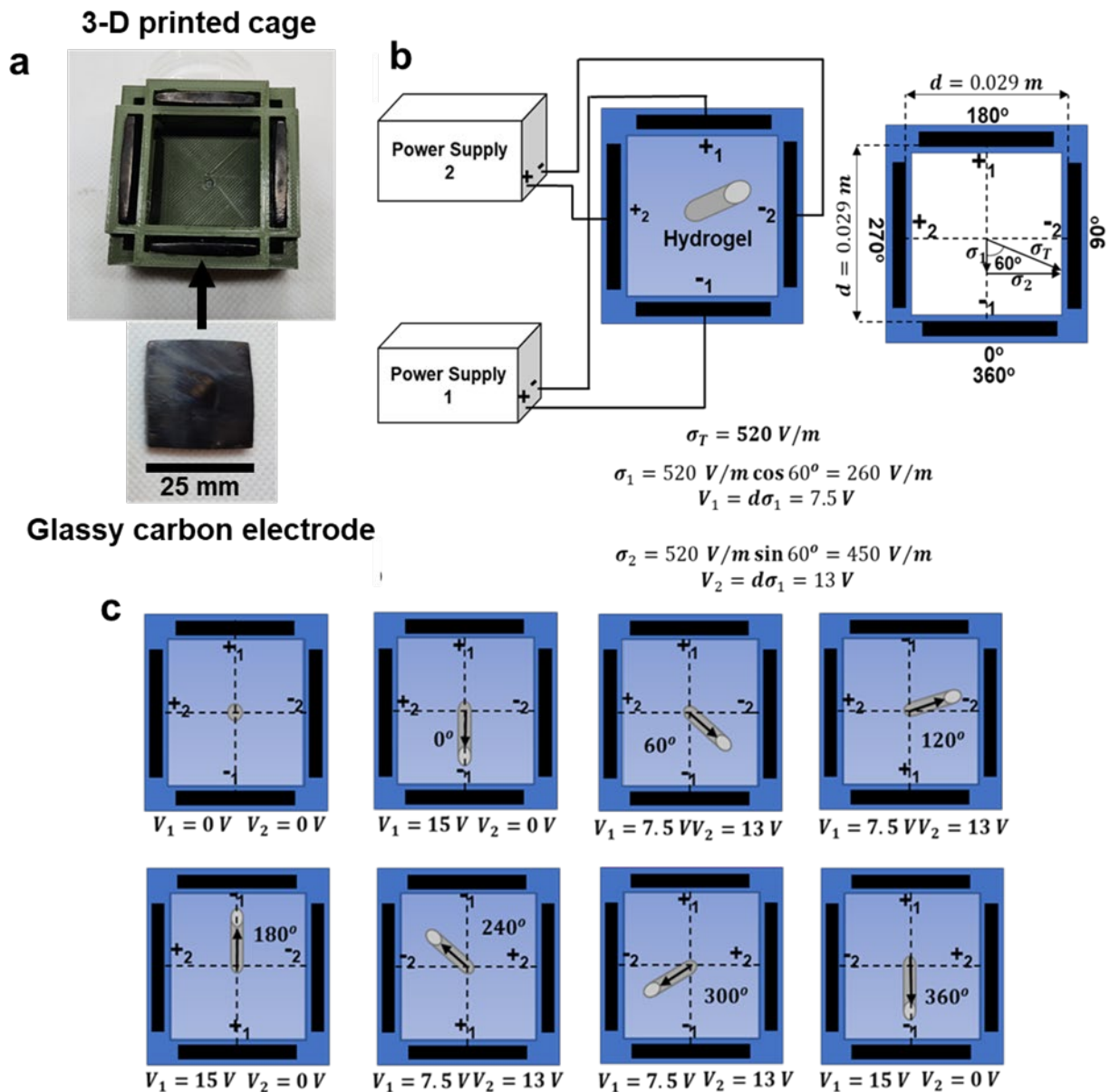


Figure 3.11 a) Top view of the set up to achieve vertical right-left and multidirectional bending of cylindric hydrogel waveguides (left). **b)** An example of the vectoral analysis carried out to combine the electric fields from both power supplies is shown at the right and bottom. To make the waveguide bend 60° taking as a reference a vertical line going through the center of the cage, the voltage from power supply 1 was set at 7.5 V producing a electric field pointing down of 260 V/m. Power supply 2 was set at 13 V with a horizontal field towards the right of 450 V/m. The combined electric field from both power supplies is 520 V/m. The same electric field (500 V/m) is obtained with an individual power supply is set at 15 V. **c)** All configurations used to direct the cylindric waveguide in a circular trajectory.

3.9.12 Trajectory of the end of a cylindric hydrogel waveguide during a multirectional bending experiment.

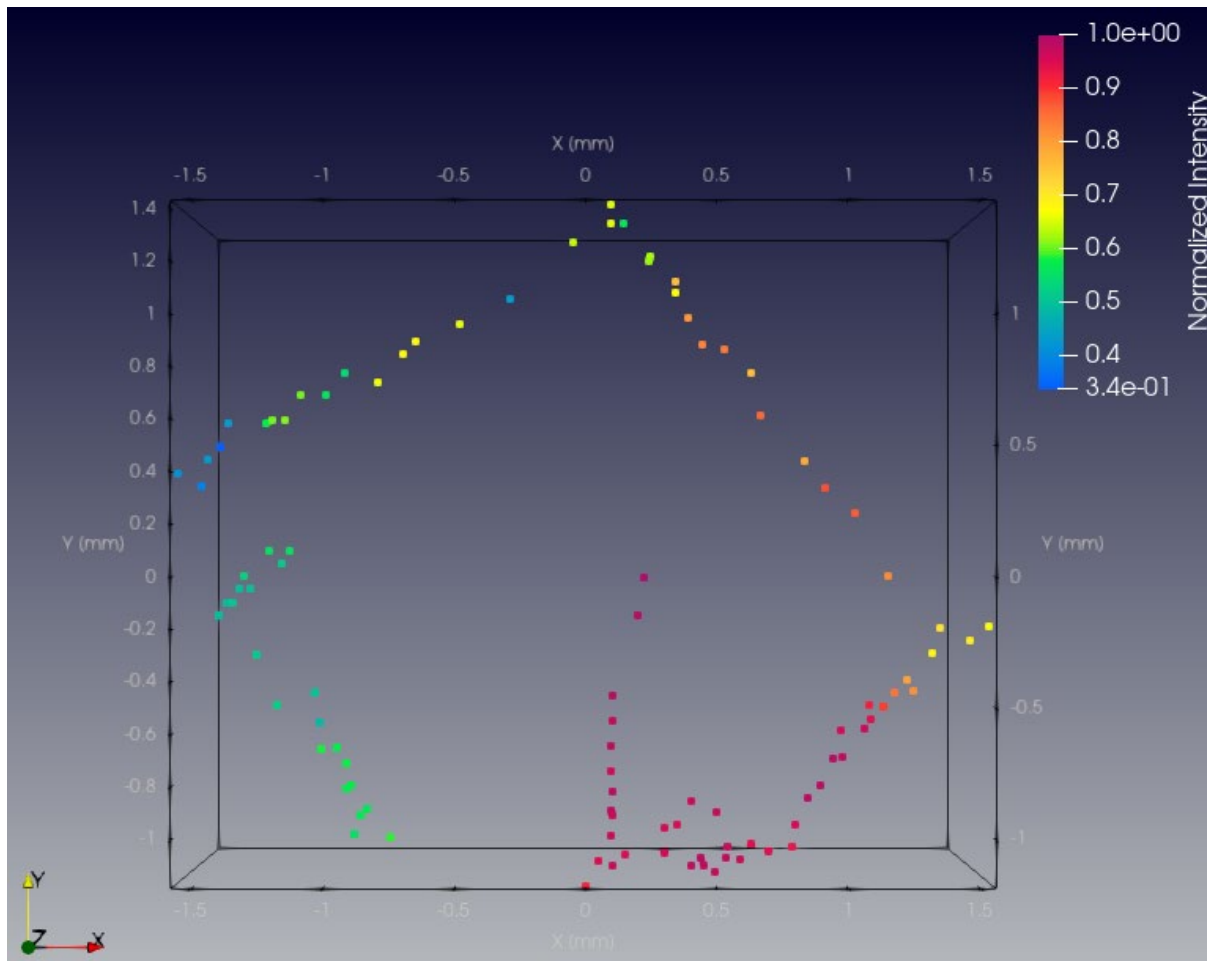


Figure 3.12 Polar plot of the position of a cylindric waveguide 10 mm long and its intensity output during a multidirectional bending experiment. The intensity of the waveguide output remains unchanged as it bends towards the first target angle (0°). Although times are not shown in the polar plot, the intensity of the waveguide output starts to decrease after 7 minutes due to damage within the hydrogel. Data processed by Tomas Omasta.

4 Dynamics of a vortex beam in a medium undergoing cationic photopolymerization

4.1 Abstract

Vortex beams have been shown to form helical fibers upon self-focusing and self-trapping in resins that undergo free-radical polymerization. In those experiments, when monitoring the beam output during fiber formation, rotation of the fiber output is observed. The length of the fibers is limited to $< 200 \mu\text{m}$ for pure vortex beams but it can be extended to $\sim 1 \text{ cm}$ when vortex beams are embedded in a Bessel beam. These beams also remain stable as they propagate in the photopolymerizable media. In this work, we showed that rotational phenomena are also induced by vortex beams in a medium undergoing cationic polymerization. Unlike the rate of rotation, which is proportional to the intensity, the extend of the rotation is independent of the intensity as long as the polymerization reaction does not take place instantaneously. Even though the beam becomes unstable in only a few seconds, a ring-shape polymer fiber with the length of the sample (6 mm) can be obtained when the sample is irradiated for a few minutes. These results indicate rotational phenomena induced by vortex beams can be elicited in a variety of photopolymers with different polymerization mechanisms and that polymer fibers $> 200 \mu\text{m}$ can be fabricated.

4.2 Introduction

Vortex beams have a helical wavefront that produces a ring-like intensity profile when projected onto a surface. Such helical wavefront is described by a phase term ($\exp(il\varphi)$) where φ is the azimuthal angle and l is an integer known as topological charge. The sign of l defines the direction of the twist while its magnitude is associated with the number of twists. They form unstable solitons when traveling in saturable nonlinear media that break into $2l$ filaments that behave as fundamental solitons.¹ Such solitons can be stationary,² or they can orbit around each

I carried out early experiments with Derek R. Morim, Alejandro Vazquez and Fariha Mahmood in different photochemical systems. I then focused on the epoxide system and obtained and analyzed the results presented in the Chapter. Karen Volke-Sepúlveda and Kalaichelvi Saravanamuttu provided guidance and suggested experimental work.

other.³ Vortex beams remain stable when the nonlinearity of the medium is saturated.² Partially incoherent beams were also shown to be stable in nonlinear media as long as certain threshold was exceeded.⁴ Vortex beams have the ability to induce mass transport on thin films made of different materials such as silver,^{5,6} tantalum,⁷ Cr/Au,⁸ Silicon⁹ and azobenzene polymers.^{10,11} This mass transport produces chiral structures with a handedness defined by the sign of l . They also can induce forward mass transfer when the beam is launched from the substrate side.¹² The mass transport in most of these cases involves physical mechanisms except for the azobenzene polymers in which a reversible cis-trans isomerization reaction takes place. Omatsu et al. demonstrated that vortex beams can induce the formation of helical microfibers.¹³ Just like it occurs with gaussian beams in a photopolymerizable medium, the positive Δn originated by the photopolymerization reaction leads to self-trapping and self-focusing.¹⁴⁻¹⁶ The resulting self-trapped beam produces a self-written waveguide. In Omatsu's experiments, a hollowed waveguide with an annular shape is initially formed when the sample is irradiated for < 0.2 s. When the sample is irradiated for longer periods of time, the center gets polymerized so a waveguide that breaks into $|l|$ smaller fibers with a minimum fiber diameter $d_{end} \approx 0.9 \mu m$. The chirality of the fibers is determined with the sign of l . Interestingly, attraction is observed among the two fibers when $l = 2$ which results in the formation of a double helix. The rotation rate is proportional to the power of the beam. The length of these fibers is limited to $< 200 \mu m$. Helical fibers up to ~ 1 cm long can be obtained when an optical vortex is embedded in a Bessel beam.¹⁷ In both cases, the rotation rate during fiber formation is proportional to the power of the beam while the period of the fiber is the same for each wavelength regardless of the power used. Nagura et al. proposed a model to explain the formation of helical fibers based on the formation of coarse-grained polymer nanoparticles generated at the focal plane of the beam.¹⁸ The formation of the polymer creates a refractive index

difference between the resin and the polymer. The initial polymer chain is assumed to have a nanometric size. In this regime, Rayleigh scattering theory applies.¹⁹ The radiation force exerted by the vortex beams has two different contributions: the scattering force F_{scat} and the gradient force F_{grad} . The former one acts in the positive z direction the F_{grad} acts in the negative z direction. When $F_{scat,z} > F_{grad,z}$, the coarse-grained nanoparticle is launched into a helical orbit since F_{scat} has also an azimuthal component ($F_{scat,\theta}$).

The resulting particle trajectory resembles a helix with a period described as:¹⁸

$$L_p = 2\pi r \frac{F_{grad,z} + F_{scat,z}}{F_{scat,\theta}} \quad (4.1)$$

where r is the radius of the nanoparticle. The continuous generation of such nanoparticles produces a helical fiber with a period L_p . The fibers fabricated so far have been fabricated using resins that undergo free radical polymerization. Our group recently proved that phenomena such as self-focusing, self-trapping and modulation instability can also be induced in media undergoing cationic polymerization and not only in media that undergoes free radical polymerization.²⁰⁻²² Despite being significantly slower than free radical polymerization, cationic polymerization offers some advantages over free radical polymerization such as less volume shrinkage, lack of oxygen inhibition and monomers with low toxicity.²³ Inhere, we studied the dynamics of a vortex beam traveling in a medium undergoing cationic polymerization of epoxide moieties. We observed that the area of highest intensity in the nonuniform vortex beam turns into a filament that rotates around the beam axis with a rate proportional to the intensity of the beam output. Followed this rotation process, the whole ring turns into a single filament in at least 67% of the cases in this intensity of

the input beam is between 21 and 63 W/cm². The extend of rotation is not statistically different in this intensity range. When the intensity is raised to 140 W/cm² the rotation does not take place to the same extend but a polymer fiber is formed when the sample is irradiated for 5 minutes.

4.3 Results and Discussion

The set up used is shown in Figure 4.1. A green, continuous-wave laser light ($\lambda = 532$ nm) from a solid state, diode-pumped source (Verdi V5 Coherent, Inc., California) was passed through a $\lambda/2$ waveplate and a series of neutral density filters to attenuate intensity. The resulting linearly-polarized beam was then passed through a spiral phase plate (Holo/Or Ltd., Israel) to generate a vortex beam with $l = \pm 1$. The sign of l was modified through rotation of the phase plate. The vortex beam was then focused onto the entrance face of the sample using a plano-convex lens ($f = 75.6$ mm). The epoxide resin was obtained following a procedure by Crivello at al. Samples were placed in ring cells 6 mm long with optically transparent sides. The evolution of the vortex beam was followed by imaging with a CCD camera at the exit face of the sample or within the sample.

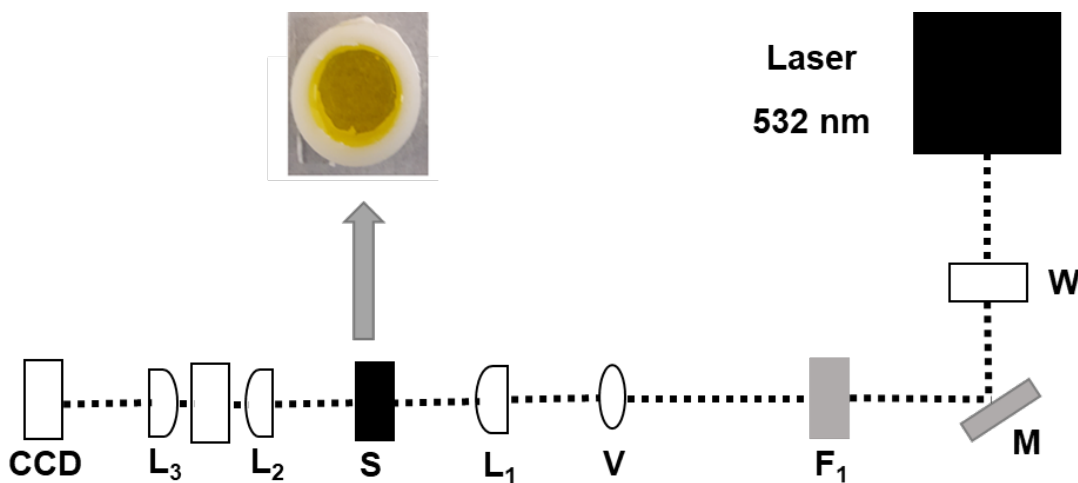


Figure 4.1 The optical assembly consists of a $\lambda/2$ waveplate (W1), a mirror (M), a neutral density filters (F1 & F2), a spiral phase plate (V), a focusing lens (L1), a sample stage (S), imaging lenses (L2 & L3) and a charge-coupled device camera (CCD).

A typical result is shown in Figure 4.2. The focused beam has a 27 μm diameter which increases to 105 μm due to the natural divergence of the beam. As can be seen at $t = 0 \text{ s}$, the intensity around the ring is not homogeneous. The intensity is higher in the red areas and therefore, the rate of polymerization is faster in this region of the beam. As the polymerization process takes place, this area turns into a filament that rotates around the beam axis. The rotating filament is always the one formed at the region of highest intensity. The sense of the rotation depends on the sign of l . For a vortex beam with $l = -1$ (Figure 4.2), a counter-clockwise rotation is observed while for $l = +1$ (Figure 4.4) there is a clockwise rotation. In this system, the area of highest intensity starts to rotate before an “actual” filament is completely formed. Once the filament is formed, no rotation is observed. The extend of the rotation ($\Delta\theta$) (see Figure 3a) was calculated by following the evolution of the rotating filament around the beam axis. We found that $\Delta\theta$ is not statistically different when this intensity of the input beam is between 21 and 63 W/cm^2 . Similar results were obtained by Omatsu when using a pure vortex beam ($\lambda = 405 \text{ nm}$) and when using a vortex beam embedded in a Bessel beam ($\lambda = 532 \text{ nm}$). In both cases, the periodicity of the resulting polymer fiber was independent of the intensity of the beam. In our experiments, we do not observe the formation of a stable polymer fiber but the extend of rotation ($\Delta\theta = 405.73 \pm 68.46, 416.26 \pm 114.26, 379.37 \pm 42.68$) is ~ 1 cycle which corresponds to a period of the helix trajectory before the formed filament breaks into a random pattern. Regardless of the irradiation time, the length of the fiber obtained by Omatsu is limited to $< 200 \mu\text{m}$ when a pure vortex beam is launched to the sample. In both systems, the rotation process associated with the OAM and the helical wavefront is only observed at early stages which indicates the vortex beam is not stable in the self-formed polymer structure. The rate of rotation of the filament is proportional to the intensity (Figure 4.3b) as it has been previously observed in photopolymers and in other nonlinear

media.²⁵ However, the linear relationship between rotation and intensity is lost when the intensity is raised to 140 W/cm^2 . This is mostly caused by the fact the rotation is suppressed in some

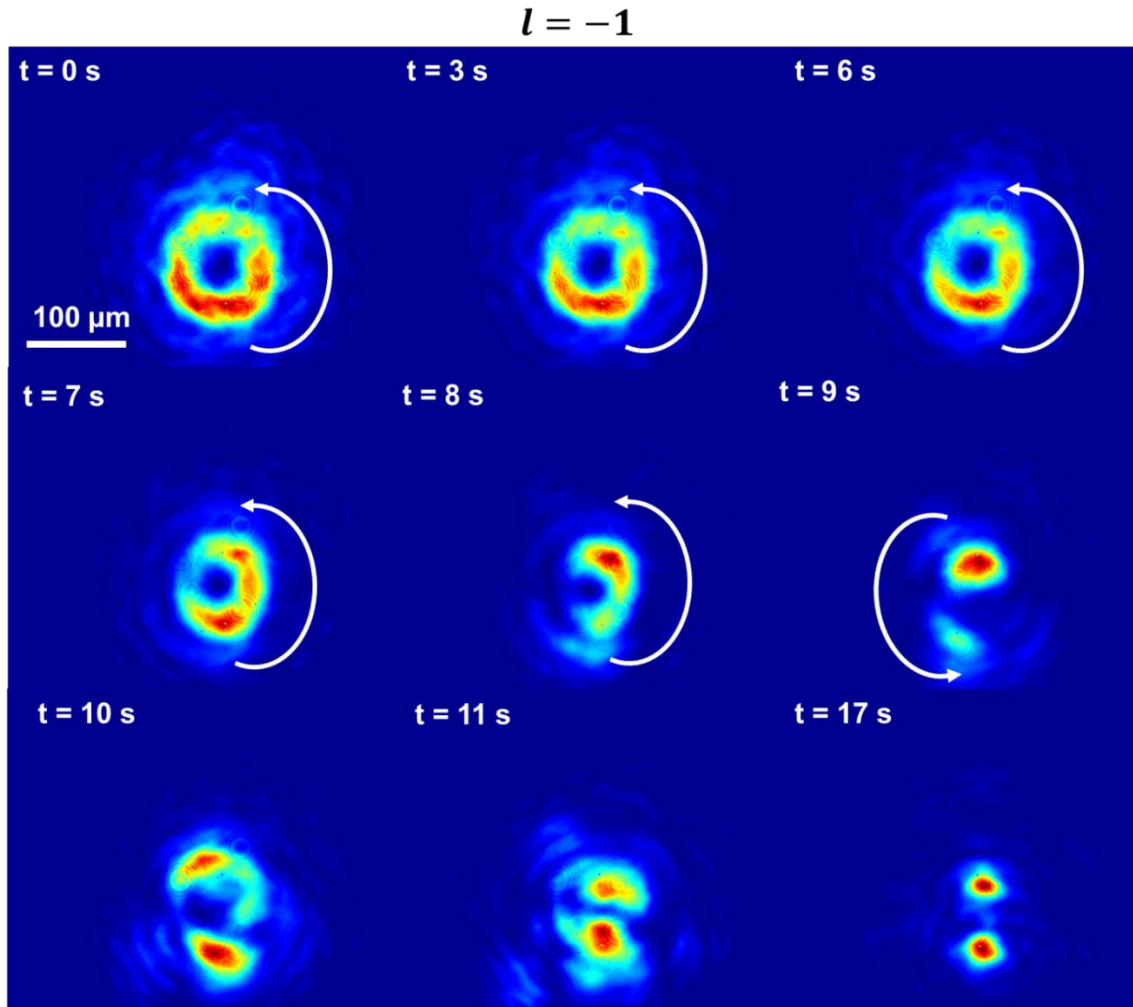


Figure 4.2 Temporal evolution of the vortex beam with $l = -1$ at $I = 42.08 \text{ W/cm}^2$ in the epoxide system. The filament formed at the region of highest intensity rotates counter-clockwise around the beam axis.

experiments due to the fast increase of viscosity in the medium because of the cationic polymerization which results in a $\Delta\theta$ significantly smaller than the $\Delta\theta$ in the experiments with lower intensities and also in a value with a un uncertainty ($211 \pm 176^\circ$). In order to corroborate the hypothesis of the rotation being counteracted, we launched the vortex beam to a prepolymerized sample which resulted in a solid sample rather than a viscous resin. We observed

that the rotation in the prepolymerized sample does not take place to the same extent even when the intensity is within the range at which rotation always takes place. A comparison between and

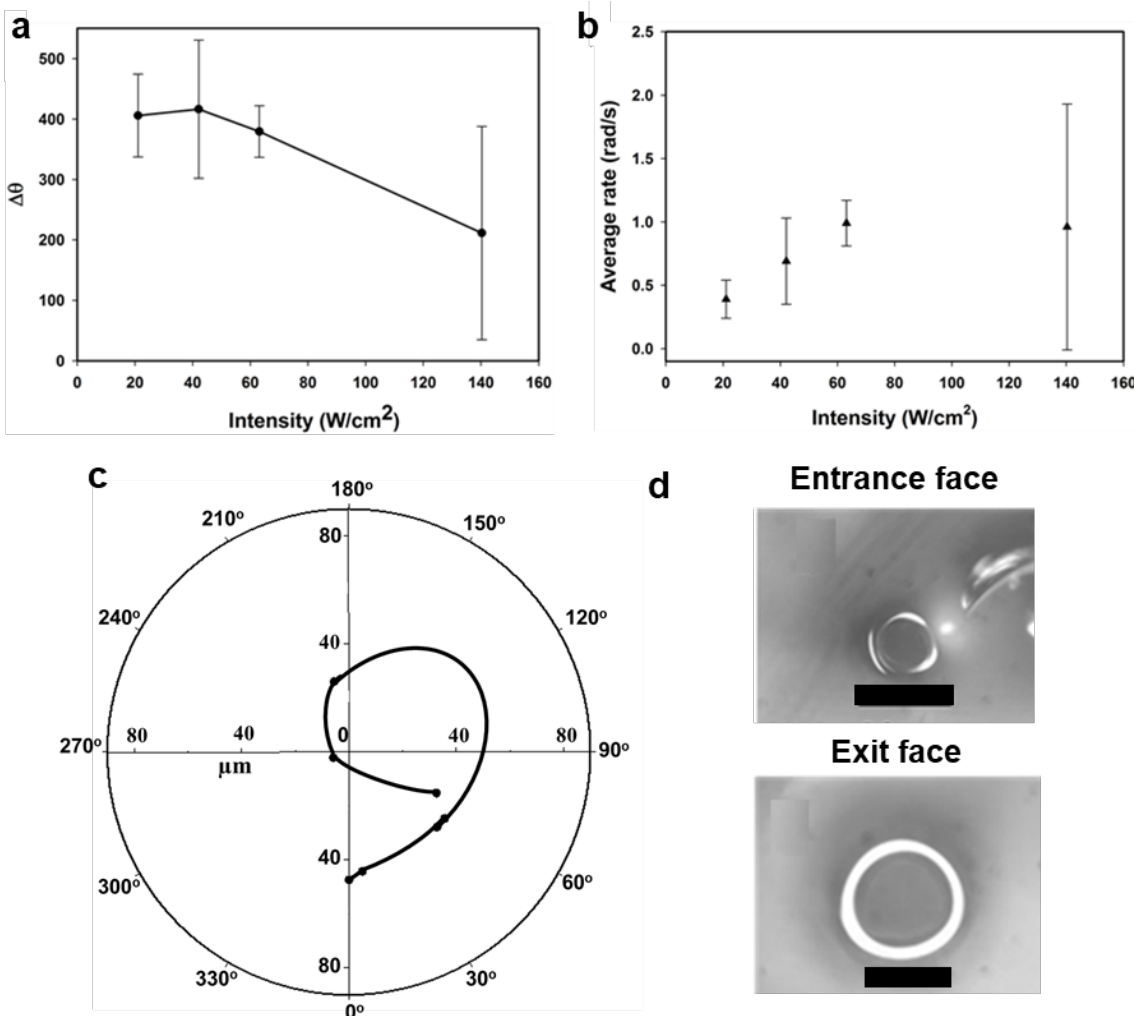


Figure 4.3. a) Extent of the rotation $\Delta\theta$ as a function of intensity. b) Rate of rotation as a function of intensity. c) Polar plot showing the evolution of a rotating filament at $I = 42 \text{ W}/\text{cm}^2$. d) Micrographs of the entrance and exit face of a polymer fiber obtained after irradiating an epoxide sample for 5 minutes at $I = 140 \text{ W}/\text{cm}^2$.

experiment carried out using an intensity of at $140 \text{ W}/\text{cm}^2$ in a regular sample and one in a prepolymerized solid sample at $42 \text{ W}/\text{cm}^2$ (Figure 4.5). At $140 \text{ W}/\text{cm}^2$, it is possible to obtain a polymer fiber 6 mm long when irradiating the sample for 5 minutes (Figure 4. 3d). The effect of Δn in the divergence of the beam is clearly illustrated by measuring the area of the ring before it

breaks, by following the trajectory of the rotating filament and also by analyzing the dimensions of the fiber at the entrance and exit face when the sample is irradiated for 5 minutes using a intensity of 140 W/cm^2 . As illustrated in Table 4.1, the area of the ring for the lowest intensity undergoes a 38 % decrease before breaking up while for the highest intensity the area of the ring only decreases 7 % before breaking up. The polar plot in Figure 4.3c also illustrates the evolution of the rotating filament obtained after launching a vortex beam with an intensity of 42 W/cm^2 which shows an inward spiraling trajectory indicating that the divergence of the beam is counteracted as the magnitude of Δn increases. Finally, the size of the polymer fiber obtained at the exit face when irradiating the sample for 5 minutes has a diameter of $30 \mu\text{m}$ which is slightly greater than the size of the input beam (Diameter= $27 \mu\text{m}$) but significantly smaller than the size of the beam at the exit face (Diameter= $105 \mu\text{m}$) (Figure 4.3d).

4.4 Conclusions and Outlook

We have shown vortex beams induce rotational phenomena in a medium undergoing cationic polymerization. The area with the highest intensity in the non-uniform beam starts rotation around the beam axis once polymerization takes place and eventually turns into a filament in most cases. The extend of the rotation is independent of the intensity of the input beam as long as there is not a fast solidification of the resin and the rate of rotation is proportional to the intensity of the beam. These observations are in agreement with the experiments performed by Omatu at al.^{13,17} and with the model to describe the formation of helical fibers proposed by Kawano at al¹⁸ which indicates the rotation phenomena induced by vortex beams can be elicited in all kinds of photopolymers. Unlike the experiments performed with Omatsu with pure vortex beam in which the length of the fibers is limited to $< 200 \mu\text{m}$, we showed that it is possible to obtain fibers with a ring shape 6 mm

long by irradiating the sample for a few minutes. Such fibers are obtained despite the vortex beam becomes unstable within seconds. Further fiber characterization is needed in order to know whether the fiber has a helical shape or if the circular shape is maintained through its whole length. Helical microfibers 1 cm long were fabricated previously by embedding a vortex beam in a Bessel beam. Although further characterization is pending, we showed it is possible to create fibers of similar lengths only with a vortex beam which suggest fibers with lengths in the cm scale can be obtained under certain conditions which might be dependent on the material, the size of the beam, the irradiation time, etc.

4.5 References

- (1) Firth, W. J.; Skryabin, D. V. Optical Solitons Carrying Orbital Angular Momentum. *Phys. Rev. Lett.* **1997**, *79*, 2450–2453.
- (2) Bigelow, M. S.; Zerom, P.; Boyd, R. W. Breakup of Ring Beams Carrying Orbital Angular Momentum in Sodium Vapor. *Phys. Rev. Lett.* **2004**, *92*, 083902.
- (3) Tikhonenko, V.; Christou, J.; Luther-Daves, B. Spiraling bright spatial solitons formed by the breakup of an optical vortex in a saturable self-focusing medium. *J. Opt. Soc. Am. B* **1995**, *12*, 2046-2052.
- (4) Jeng, C.; Shih, M.; Motzek, K.; Kivshar, Y. Partially Incoherent Optical Vortices in Self-Focusing Nonlinear Media. *Phys. Rev. Lett.* **2004**, *92*, 043904.
- (5) Syubaev, S.; Zhizhchenko, A.; Kuchmizhak, A.; Porfirev, A.; Pustovalov, E.; Vitrik, O.; Kulchin, Y.; Khonina, S.; Kudryashov, S. Direct laser printing of chiral plasmonic nanojets by vortex beams. *Opt. Express* **2017**, *25*, 10214–10223.
- (6) Toyoda, K.; Miyamoto, K.; Aoki, N.; Morita, R.; Omatsu, T. Using optical vortex to control the chirality of twisted metal nanostructures. *Nano Lett.* **2012**, *12*, 3645–3649.
- (7) Toyoda, K.; Miyamoto, K.; Aoki, N.; Morita, R.; Omatsu, T. Using Optical Vortex To Control the Chirality of Twisted Metal Nanostructures. *Nano Lett.* **2012**, *12*, 3645.
- (8) Kohmura, Y.; Zhakhovskiy, V.; Takei, D.; Suzuki, Y.; Takeuchi, A.; Inoue, I.; Inubushi, Y.; Inogamov, N.; Ishikawa, T.; Yabashi, M. Nano-structuring of multi-layer material by single x-ray vortex pulse with femtosecond duration. *Appl. Phys. Lett.* **2018**, *112*, 123103.
- (9) Rahimian, M. G.; Bouchard, F.; Karimi, E.; Corkum, P. B.; Bhardwaj, V. R. Polarization dependent nanostructuring of silicon with femtosecond vortex pulse. *APL Photonics* **2017**, *2*, 086104.
- (10) Ambrosio, A.; Marrucci, L.; Borbone, F.; Roviello, A.; Maddalena, P. Light-induced spiral mass transport in azo-polymer films under vortex-beam illumination. *Nat Commun* **2012**, *3*, 989.

- (11) Watabe, M.; Juman, G.; Miyamoto, K.; Omatsu, T. Light induced conch-shaped relief in an azo-polymer film. *Sci Rep* **2014**, *4*, 4281.
- (12) Nakamura, R.; Kawaguchi, H.; Iwata, M.; Kaneko, A.; Nagura, R.; Kawano, S.; Toyoda, K.; Miyamoto, K.; Omatsu, T. Optical vortex-induced forward mass transfer: manifestation of helical trajectory of optical vortex. *Opt. Express* **2019**, *27*, 38019–38027.
- (13) Lee, J.; Arita, Y.; Toyoshima, S.; Miyamoto, K.; Panagiotopoulos, P.; Wright, E. M.; Dholakia, K.; Omatsu, T. Photopolymerization with Light Fields Possessing Orbital Angular Momentum: Generation of Helical Microfibers. *ACS Photonics* **2018**, *5*, 4156–4163.
- (14) Kewitsch, A. S.; Yariv, A. Self-focusing and self-trapping of optical beams upon photopolymerization. *Opt. Lett.* **1996**, *21*, 24-26.
- (15) Shoji, S.; Kawata, S.; Sukhorukov, A. A.; Kivshar, Y. S. Self-written waveguides in photopolymerizable resins. *Opt. Lett.* **2002**, *27*, 185-187.
- (16) Dorkenoo, K.; Crégut, O.; Mager, L.; Gillot, F.; Carre, C.; Fort, A. Quasi-solitonic behavior of self-written waveguides created by photopolymerization. *Opt. Lett.* **2002**, *27*, 1782–1784.
- (17) Haugh, N.; Chirality, M.; Korea, S. Photopolymerization with high-order Bessel light beams. *Opt. Lett.* **2020**, *45*, 4080–4083.
- (18) Nagura, R.; Tsujimura, T.; Tsuji, T.; Doi, K.; Kawano, S. Coarse-grained particle dynamics along helical orbit by an optical vortex irradiated in photocurable resins. *OSA Continuum* **2019**, *2*, 400-415.
- (19) Harada, Y.; Asakura, T. Radiation forces on a dielectric sphere in the Rayleigh scattering regime. *Optics Communications* **1996**, *124*, 529–541.
- (20) Basker, D. K.; Cortes, O. A. H.; Brook, M. A.; Saravanamuttu, K. 3D Nonlinear Inscription of Complex Microcomponents (3D NSCRIPT): Printing Functional Dielectric and Metallodielectric Polymer Structures with Nonlinear Waves of Blue LED Light. *Adv. Mater. Technol.* **2017**, *2*, 1600236-n/a.
- (21) Basker, D. K.; Brook, M. A.; Saravanamuttu, K. Spontaneous Emergence of Nonlinear Light Waves and Self-Inscribed Waveguide Microstructure during the Cationic Polymerization of Epoxides, *J. Phys. Chem. C* **2015**, *119*, 20606–20617.
- (22) Hosein, I. D.; Lin, H.; Ponte M. R.; Basker, K. D.; Brook. M. A.; Saravanamuttu, K. Waveguide Encoded Intersecting (WIDEI) Lattices: Slim Polymer Films with Panoramic Fields of View (FOV) and Multiple Imaging Functionality. *Adv. Funct. Mater.* **2017**, *27*, 1702242.
- (23) Invernizzi, M.; Suriano, R.; Muscatello, A.; Turri, S.; Levi, M. Near-visible stereolithography of a low shrinkage cationic / free-radical photopolymer blend and its nanocomposite. *J. Appl. Polym. Sci.* **2020**, *137*, 48333.
- (24) Crivello, J. V. A New Visible Light Sensitive Photoinitiator System for the Cationic Polymerization of Epoxides. *J. Polym. Sci., Part A: Polym. Chem.* **2009**, *47*, 866–875.
- (25) Caullet, V.; Marsal, N.; Wolfersberger, D.; Sciamanna, M. Vortex Induced Rotation Dynamics of Optical Patterns. *Phys. Rev. Lett.* **2012**, *108*, 263903.

4.6 SUPPLEMENTARY INFORMATION

4.7 Methods

4.8 Materials

3,4-Epoxy cyclohexylmethyl 3,4-epoxycyclohexanecarboxylate (ERL), camphorquinone (PS), and poly(tetrahydrofuran) (pPTHF) were purchased from Sigma Aldrich. Epoxypropoxypropyl-terminated polydimethylsiloxane (DMS) and bis(4-tert-butyl phenyl)iodonium hexafluoroantimonate (PI) were purchased from Gelest and Hampford Research, respectively. All chemicals were used without further purification.

4.9 Preparation of photopolymer

The epoxy sol was made by mixing and stirring ERL (76 wt %), DMS (10 wt %), pTHF (10 wt %), PS (0.5 wt %) and PI (0.5 wt %) for 48 hours. A viscous, transparent solution was obtained. To obtain the prepolymerized sample, the epoxide sol. was injected in the cell and irradiated for 36 minutes using a white light source.

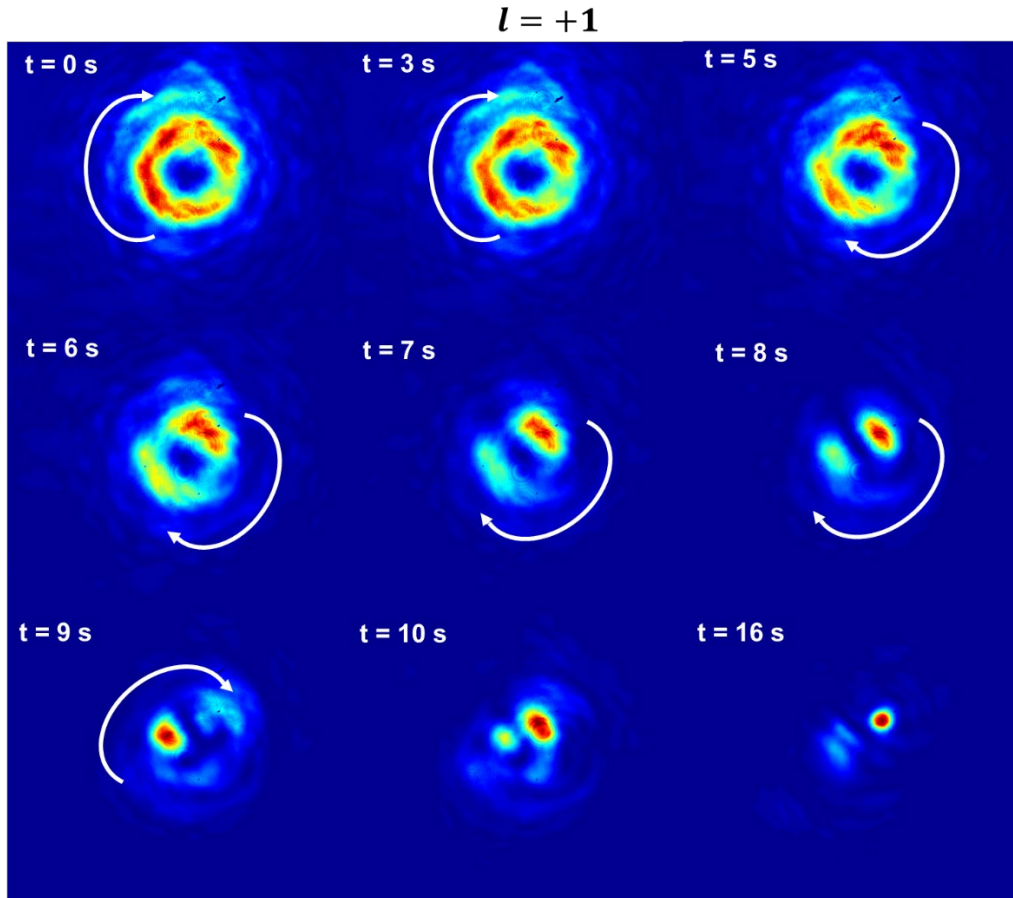


Figure 4.4. Temporal evolution of the vortex beam with $l = +1$ at $I = 42.08 \text{ W/cm}^2$ in the epoxide system. The filament formed at the region of highest intensity rotates counter-clockwise around the beam axis.

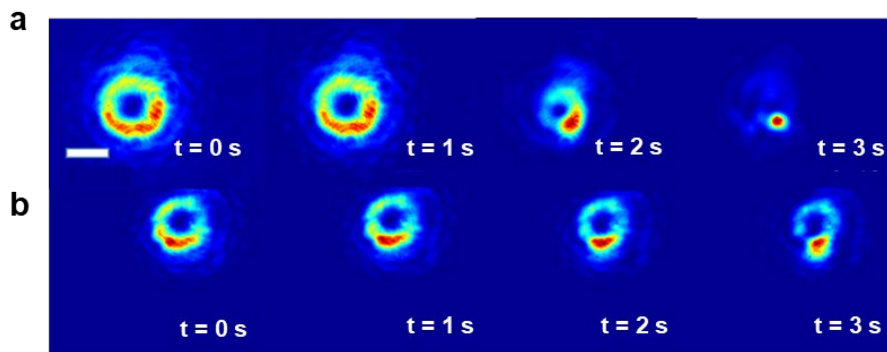


Figure 4.5 a) Typical result in a regular epoxide sample with $l = -1$ at $I = 140.27 \text{ W/cm}^2$ (top) and in a prepolymerized sample (bottom) at $I = 42.08 \text{ W/cm}^2$.

Table 4.1 Area of a vortex beam with $l = -1$ at the exit face at $t = 0$ s (A_o) and before breaking up into filaments (A_f). The calculations were made for each of the intensities used by subtracting the area of the dark center from the area of the whole ring.

Intensity (W/cm²)	A_o (μm²)	A_f (μm²)	ΔA (%)
21	8472	6147	38
42	7931	7162	11
63	8158	7680	6
140	8708	8145	7

5 Conclusions and future work

The propagation of light can be modified and modulated by the refractive index changes that are self-induced in a nonlinear material. This becomes a powerful tool when such changes are induced permanently such as the liquid-solid transition induced by photopolymerization reactions. Taking advantage of this, we developed a new 3-D printing technique that inscribes polymeric structures using nonlinear waves in a time scale ranging from seconds to minutes using inexpensive light sources. Because of the nature of the process, each 3-D unit operation produces a polymer waveguide. We demonstrated that further properties such as electroactuation can be incorporated by using resins that produce functional materials. Inspired by organs presented in a variety of organs present in different living organisms such the lure of the female angler fish, cilia and squid skin, we created electroactive hydrogel architectures in which their angular orientation and waveguided output can be remotely controlled using electric fields. The refractive index changes generated through photopolymerization can also counteract the divergence of nonconventional beams such as vortex beams and induce further transformations until it becomes unstable. Along this process, the properties of the beam such as the helical wavefront and its ability to carry OAM are manifested as rotational phenomena while inscribing its 2D intensity profile in the medium.

5.1.1 Prismatic 3-D printing

We presented several improvements to the volumetric 3-D printing technique we developed in 2016 based on the continuous inscription of polymeric structures using nonlinear waves which includes materials with a fast-curing rate, objects with higher complexity and even with additional features such as the incorporation of waveguide circuitry. The basic 3-D unit operation of our

method consists of patterning a blue LED beam with an amplitude mask placed at the entrance face of a rectangular/cubic resin container. The 2D light image created with the amplitude mask inscribes such image in the medium with certain depth. Due to the nature of the method, our printing technique is limited to objects made of overlapping/intersecting prisms. To aid with the printing process of an existing 3D mesh, we wrote a segmentation algorithm that allows to decompose such mesh into the fewest number of prismatic elements that can be printed individually to be assembled as a form of post processing or fused in situ by rotating the sample after each prism is printed. Due to the nature of the printing process, certain geometries such as spheres, cones and pyramids are forbidden. However, some modifications to these particular shapes can be done in order to obtain objects that resemble the 3-D mesh. Each prismatic element obtained through this method is homogenous along the propagation front direction and also has a higher refractive index than their surroundings. These two properties make each prismatic element light-guiding. We also showed that by using a periodic amplitude mask, micro-waveguides can be embedded in these prisms as long as the side-polymerization is controlled. Most objects presented in Chapter 2 were fabricated in a time scale ranging from seconds to minutes. The method is also unexpensive since it only relies on visible light produced by a LED and vinyl amplitude masks.

5.1.2 Electroactive hydrogel waveguide architectures.

Since prismatic printing creates micro- and macro-waveguides, we realized further properties could be incorporated to these waveguides. We explored electroactuation as the first example which is the ability to deform, under the effect of an electric field. We developed two different hydrogels that produce an anionic network when immersed in a basic solution. Inspired by three different soft organs present in different living organisms such as the lure of the female angler fish,

cilia and chromatophores in squid skin, we created a range of architectures including planar slab waveguides, individual and arrays of cylindrical waveguides as well as long-range waveguide lattices. All these architectures can be remotely control through external electric fields which also means directing the waveguided output towards the bending direction of the waveguide. In the case of the planar slab waveguide, the net result is a bright sheet that seems to turn off from the point of view of a detector when light is directed away from its field of view. For the array of cylindrical waveguides, we used the light output of the waveguide to track the position of each individual waveguide. We observed that the waveguides in the arrays closer to the cathode bend faster and to a greater extend than the ones closer to the anode. The electric field generates a contraction wave in the array that affects each row of waveguides to a different extend producing a sequential motion as it occurs in the metachronal waves motile cilia experience. For our last system, we got inspired by squid skin. The main camouflage mechanism in squids involves thousands of soft actuators present in their skin known as chromatophores which are perceived as colorful dots which are manifested upon a contraction when a neural signal is received. When the neural signal is removed, the chromatophores are not manifested. Contraction waves in their skin are perceived from the point of view of an observer as an array of colourful dots migrating in space. Inspired by chromatophores in squid skin, we printed hydrogel prisms with micro-waveguides embedded. We can think about this system as circular regions of high refractive index embedded in a gel from the surface point of view which turn into a bright spot when light is launched to the lattice. When the electric field was applied, we were able to make these bright spots migrate in space towards the cathode. Just as in the case of slab waveguides, inverting the polarity of the electric field makes the micro-beams and the lattice migrate in the opposite direction. We observed that all the cylindric waveguides do not bend to the same extend in the

opposite direction taking as a reference the initial position of the lattice, but they bend to a greater extend overall every time the field is inverted and tend to bend more towards the first bending direction. The higher porosity of the lattice as well as the lower degree of crosslinking makes the lattice more sensitive to changes of pH which occur due the electrolysis of water and also to fatigue damage. It is possible that fatigue damage is observed since the first time the hydrogel is bended or that the initial pH gradients generated at the beginning of the electro actuation experiments are not immediately reversed.¹ Therefore, the solution at initial cathode side remains mainly basic while the solution at the initial anode side remains acidic which favors bending towards the initial cathode. Unlike the intensity of the slab waveguides that decreases when the waveguide is directed away from the CCD camera and increases again to its original value when the waveguide points directly at the camera after the field is reversed, the beam output in the micro-waveguides show random fluctuations in intensity due to the multiple process taking place within the lattice such as contraction and expansions due to swelling/deswelling because of the osmotic pressure difference created due to the migration of ions when the electric field is applied² and also due to local pH changes that lead to protonation and deprotonation within the hydrogel network.¹ Regardless of the origin of the contractions and expansions, volume changes in the hydrogel network can have a long-range effect impacting neighboring waveguides.³ Additionally, fatigue damage and just the change in position of the micro-waveguides with respect to the detector might affect the intensity detected as well. Finally, we build a set up that consists on a 3-D printed cage with four electrode holders in a quadratic configuration. This system allows to combine perpendicular electric fields to remotely controlled the bending of cylindric waveguides toward target directions. Therefore, we can control their angular orientation and even induce rotation without the use of computers.

5.1.3 Dynamics of a vortex beam in a medium undergoing cationic photopolymerization

We demonstrated that vortex beams can induce rotational phenomena in a medium undergoing cationic polymerization. We observed that the extend of rotation is independent of the intensity used but the rate of rotation is linearly dependent on this parameter. Both observations are true as long as the solidification of the resin does not take place instantaneously. These observations match previous results observed in media undergoing free radical polymerization⁴ and also can be described by the coarse-grained particle model proposed by Nagura at al.⁵ Even though the vortex beam becomes unstable within seconds, it is possible to inscribe polymer fibers with the dimensions of our sample (6 mm) which are significantly longer than the ones obtained by Omatsu at al. which are $< 200 \mu\text{m}$.⁴

5.1.4 General conclusions

This thesis provides several improvements to our volumetric 3-D printing technique developed in 2016 which includes the introduction of resins with fast curing rate as well as functional resins which allows the fabrication of 3-D objects in a time scale ranging from seconds to minutes. We also showed that embedding micro-waveguides lattices within these objects is also possible as long as the side-polymerization in the medium is controlled. Our second contribution illustrates how we can introduce additional functionalities to the light-guiding objects obtained through this technique such as electroactuation which opens the possibility to print waveguides with different properties in a single step and using only one material. This is the first time electroactive hydrogel waveguides have been fabricated. A method to orient electroactive waveguides towards targeted directions and to rotate such waveguides was also proposed. To be best of our knowledge, only

unidirectional bending and locomotion has been achieved in electroactive hydrogels. Our last contribution shows that vortex beams can induce rotational phenomena in a medium undergoing cationic polymerization and that vortex beams can produce fibers with a ring shape with lengths a few mm long. Previous experiments were carried out in media undergoing free radical polymerization and the length of fibers in these experiments was in the μm scale.

5.2 Future work and outlook

5.2.1 Prismatic 3-D printing

Although the field of 3-D printing has undergone tremendous progress in recent years and there are techniques in the market that create all kind of shapes made of a variety of materials, our method offers a cheap yet effective alternative to produce microfluidic devices, waveguides and so on. Printing over existing objects is also a viable alternative with our method. Some properties such as autofluorescence⁶ and conductivity⁷ could be easily incorporated to the 3-D printed objects by adding to the resin the particles of interest. Waveguides that are photo-⁸ and thermo-responsive⁹ could also be fabricated. Automatizing the printing process through the use of a light projector and a rotating stage is also necessary for real life applications. A futuristic vision of this technique would be a combination of prismatic 3-D printing and optical traps to assemble nano and micro patterns¹⁰ in the volume that is to be printed and possible the use of two-photon polymerization and moving waveguides for fine details in the structure.

5.2.2 Electroactive waveguides.

Both hydrogels fabricated contain already 45% (w/w) buffer solution after printed. Therefore, they are conductive. Figure shows a LED that is turned on using a 3-D printed hydrogel waveguide as

a part of the electronic circuit. A potential application would be their incorporation into ionotronic devices.^{11,12} These waveguides could also be printed without buffer solution to be used in combination with the electrode array for educational purposes in physics/chemistry labs. Locomotion of soft robots in multiple directions rather than only bending could also be achieved using our square electrode array. Modifications to the resin in order to eliminate fatigue

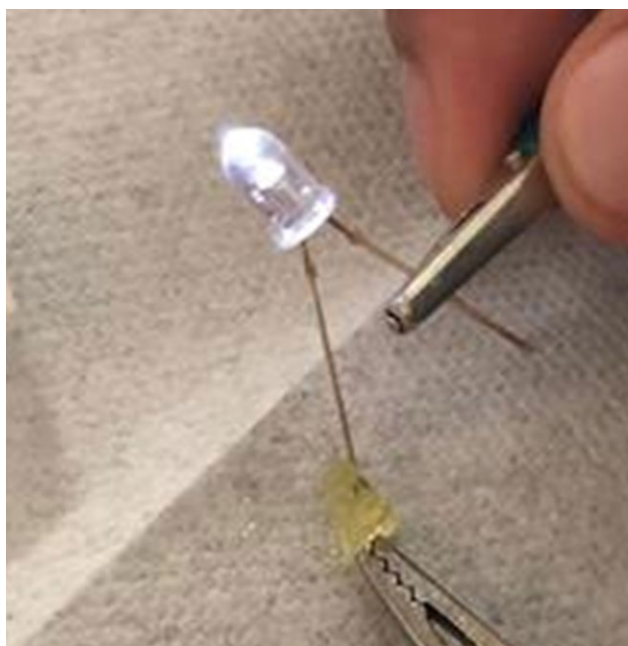


Figure 5.1. LED driven by a 9 V battery with a hydrogel prism acting as a part of the electronic circuit.

damage are also needed. Fatigue damage is a problem in most hydrogels. Increasing the crystallinity of hydrogels proved to be an efficient method to increase fatigue. Increasing the crystallinity of hydrogels proved to be an efficient method to increase fatigue resistant.¹³ Increasing the crystallinity of electroactive hydrogels could also be explored. Multiresponsive waveguides could also be fabricated by using a crosslinker with azobenzene groups while keeping acrylic acid as monomer.¹⁴ In addition to being electroactive, incorporating such crosslinker would give the hydrogel the ability to deform even with guided light. Patterning hydrogel waveguides

with soft electrodes is also worth exploring in order for them to operate in air and not only in aqueous media. Making these electroactive waveguides biocompatible and biodegradable could have potential application in light-based therapies^{15,16} and also for inexpensive devices for minimally invasive surgery¹⁷ since they would allow to deliver light an even cellsm to specific regions rather than a fixed spot.

5.2.3 Dynamics of a vortex beam in a medium undergoing cationic photopolymerization

Even though we demonstrated rotational phenomena can be induced in a vortex beam and that a fiber a few mm long with a ring shape can be created, further characterization of the fiber remains pending, especially a side characterization to know whether the helical wavefront is transferred to the fibers. Such characterization has been challenging since the fiber gets severely disturbed/damaged when isolated from the unpolymerized resin and due to the fact, some side polymerization around the fiber hinders the structure created by the vortex. Twisted photonic crystal fibers can act as optical polarizers and that also preserve the chirality of OAM modes. It is expected fibers fabricated with vortex beams will show similar properties. The behavior of vortex beams in other photochemical systems developed in our lab is being explored.

5.3 References

- (1) O'Grady, M. L.; Kuo, P. L.; Parker, K. K. Optimization of electroactive hydrogel actuators. *ACS Applied Materials and Interfaces* **2010**, 2, 343–346.
- (2) Jin, S.; Gu, J.; Shi, Y.; Shao, K.; Yu, X.; Yue, G. Preparation and electrical sensitive behavior of poly (N-vinylpyrrolidone- co-acrylic acid) hydrogel with flexible chain nature. *European Polymer Journal* **2013**, 49, 1871–1880.
- (3) Morim, D. R.; Meeks, A.; Shastri, A.; Tran, A.; Shneidman, A. V.; Yashin, V. V.; Mahmood, F.; Balazs, A. C.; Aizenberg, J.; Saravanamuttu, K. Opto-chemo-mechanical transduction in photoresponsive gels elicits switchable self-trapped beams with remoteinteractions. *Proc. Natl. Acad. Sci. U. S. A.* **2020**, 117, 3953-3959.

- (4) Lee, J.; Arita, Y.; Toyoshima, S.; Miyamoto, K.; Panagiotopoulos, P.; Wright, E. M.; Dholakia, K.; Omatsu, T. Photopolymerization with Light Fields Possessing Orbital Angular Momentum: Generation of Helical Microfibers. *ACS Photonics* **2018**, *5*, 4156–4163.
- (5) Nagura, R.; Tsujimura, T.; Tsuji, T.; Doi, K.; Kawano, S. Coarse-grained particle dynamics along helical orbit by an optical vortex irradiated in photocurable resins. *OSA Continuum* **2019**, *2*, 400-415.
- (6) Xu, H.; Tan, Y.; Wang, D.; Wang, X.; An, W.; Xu, P.; Xu, S.; Wang, Y. Autofluorescence of hydrogels without a fluorophore. *Soft Matter* **2019**, *15*, 3588–3594.
- (7) Odent, J.; Wallin, T. J.; Pan, W.; Kruemplestaedter, K.; Shepherd, R. F.; Giannelis, E. P. Highly Elastic, Transparent, and Conductive 3D-Printed Ionic Composite Hydrogels. *Adv. Funct. Mater.* **2017**, *27*, 1701807.
- (8) Yao, Y.; Waters, J. T.; Shneidman, A. V.; Cui, J.; Wang, X.; Mandsberg, N. K.; Li, S.; Balazs, A. C.; Aizenberg, J. Multiresponsive polymeric microstructures with encoded predetermined and self-regulated deformability. *Proc. Natl. Acad. Sci. U. S. A.* **2018**, *115*, 12950–12955.
- (9) Hua, M.; Wu, D.; Wu, S.; Ma, Y.; Alsaied, Y.; He, X. 4D Printable Tough and Thermoresponsive Hydrogels. *ACS Appl. Mater. Interfaces* **2021**, *13*, 12689–12697.
- (10) Zhang, S.; Li, W.; Elsayed, M.; Peng, J.; Chen, Y.; Zhang, Y.; Zhang, Y.; Shayegannia, M.; Dou, W.; Wang, T.; Sun, Y.; Kherani, N. P.; Neale, S. L.; Wheeler, A. R. Integrated Assembly and Photopreservation of Topographical Micropatterns. *Small* **2021**, *17*, 2103702.
- (11) Yang, C.; Suo, Z. Hydrogel ionotronics. *Nat Rev Mater* **2018**, *3*, 125–142.
- (12) Chen, B.; Suo, Z. Optoionic Sensing. *Small* **2021**, 2103882.
- (13) Lin, S.; Liu, X.; Liu, J.; Yuk, H.; Loh, H.; Parada, G. A.; Settens, C.; Song, J.; Masic, A.; Mckinley, G. H.; Zhao, X. Anti-fatigue-fracture hydrogels. *Sci. Adv.* **2019**; *5*: eaau8528.
- (14) Lin, S.; Liu, X.; Liu, J.; Yuk, H.; Loh, H.; Parada, G. A.; Settens, C.; Song, J.; Masic, A.; Mckinley, G. H.; Zhao, X. Multiresponsive polymeric microstructures with encoded predetermined and self-regulated deformability. *Proc. Natl. Acad. Sci. U. S. A.* **2018**, *115*, 12950-12955.
- (15) Feng, J.; Zheng, Y.; Bhusari, S.; Villiou, M.; Pearson, S., del Campo, A. Printed Degradable Optical Waveguides for Guiding Light into Tissue. *Adv. Funct. Mater.* **2020**, *30*, 2004327.
- (16) Feng, J.; Jiang, Q.; Rogin, P.; De Oliveira, P. W.; Del Campo, A. Printed Soft Optical Waveguides of PLA Copolymers for Guiding Light into Tissue. *ACS Appl. Mater. Interfaces* **2020**, *12*, 20287–20294.
- (17) York, P. A.; Peña, R.; Kent, D.; Wood, R. J. Microrobotic laser steering for minimally invasive surgery. *Sci. Robot.* **2021**, *6*, abd5476.